

Optimal Tuning of Active Power Gradient Control in Multi-Energy HVAC-HVDC Power Systems

Master Thesis

Georgios Giannakopoulos

Intelligent Electrical Power Grids



Master Thesis

Optimal Tuning of Active Power Gradient Control in Multi-Energy HVAC-HVDC Power Systems

by

Georgios Giannakopoulos

in partial fulfilment of the requirements for the degree of

Master of Science

in Electrical Power Engineering

at the Delft University of Technology,

to be defended publicly on Thursday April 22, 2021 at 13:00 AM.

Supervisor:	Prof. Dr. ir. Jose Rueda Torres	TU Delft
	Arcadio Perilla	TU Delft
Thesis committee:	Prof. Dr. Peter Palensky	TU Delft, IEPG Group
	Prof. Dr. ir. Jose Rueda Torres	TU Delft, IEPG Group
	Prof. Dr. Thiago Batista Soeiro	TU Delft, DCE&S Group

This thesis is confidential and cannot be made public until April 30, 2023.

An electronic version of this thesis is available at <http://repository.tudelft.nl/>.



Power systems nowadays are experiencing a significant energy transition characterized by the progressive increment of power electronic interfaced units. Voltage source converters are extensively utilized to interconnect renewable energy sources at various transmission levels, facilitate the asynchronous interconnection of system areas through HVDC links and enable the installment of responsive demand units into the grid. The latter increase of power electronic interfaced units in the power system has significantly altered its dynamic behavior as the system is characterized by low inertia conditions, fast and more frequent dynamics based on the converters' switching actions, lack of inertial response, limited short circuit capability and uncertain generation and demand mixes. Under these new operating conditions one of the main concerns of TSOs is the ability of the system to withstand active power-frequency imbalances. To cope with the frequency stability issues encountered, power electronic interfaced elements introduced, can be effectively utilized to offer ancillary services such as fast frequency support to the grid due to the high controllability levels and the rapid response capability they exhibit.

This thesis project deals with the optimization of the frequency response of a multi-area, multi-energy HVAC-HVDC power system, representing a power electronic dominated power system. The network analyzed consists of a 3-area system modified so that the areas are electromagnetically decoupled through MMC-based HVDC links and different controllable energy sources such as fully decoupled wind turbines type IV and proton exchange membrane electrolyzers are installed at various points of the system. The modified system exhibits 3 decoupled areas with different generation and demand mixes characterized by different inertia levels and increased controllability due to the converters' capabilities. The outer controllers of the power electronic interfaced elements installed have been modified with the active power gradient control scheme to respond to frequency excursions and provide fast frequency support to the grid in case of commonly occurred active power-frequency imbalances.

However, when multiple elements are simultaneously acting upon the same target variable, such as the system frequency, interactions between the controllers may lead to insufficient or over regulation and thus coordination among the different elements is more than necessary. For this reason, in this study two different problem formulations have been proposed aiming at a coordinated tuning of the parameters of the frequency controllers of the synthetic inertia elements participating in the frequency regulation against critical commonly occurred active power-frequency imbalances. The former one is based on the minimization of the frequency deviation from its nominal value following an active power imbalance and the latter one on the minimization and equalization of the dynamic displacements of the areas' speed following an active power imbalance. To effectively solve the optimization problem and enhance the frequency stability of the system a powerful metaheuristic optimization algorithm, the mean variance mapping optimization (MVMO) algorithm has been utilized.

The optimization results can effectively highlight the tuning strategy that achieves the best frequency response of the system under various commonly occurred active power frequency disturbances. It can also provide further insight on the proper utilization of various sources of synthetic inertia with respect to their response capabilities. Finally, the simulation results can also clarify the importance of the location of installation of converter-based elements providing fast frequency support with respect to the grid node the imbalance occurs.

Contents

1	Introduction.....	1
1.1.	Motivation.....	1
1.2.	Literature review.....	4
1.2.1.	Power system stability.....	4
1.2.2.	Frequency stability in conventional power systems	6
1.2.3.	Frequency stability and issues in power electronics dominated power systems.....	7
1.2.4.	Frequency support alternatives in PE dominated power systems	9
1.3.	Problem definition and previous work	11
1.4.	Objectives, research questions and thesis contribution	12
1.5.	Research approach.....	14
1.6.	Thesis outline.....	15
2	Theoretical background.....	16
2.1.	Frequency in power systems	16
2.1.1.	The importance of frequency in power systems.....	16
2.1.2.	Frequency operational regulations and key performance indicators	17
2.2.	Power electronics in power systems	18
2.2.1.	The role of PEIs and the VSC	18
2.2.2.	Modelling of the MMC	19
2.2.3.	Operation and control of the MMC	22
2.3.	Fundamental concepts of HVDC technology	24
2.3.1.	The advantages of HVDC technology and its applications.....	24
2.3.2.	MMC based HVDC power transmission overview.....	24
2.4.	PEM electrolyzers	27
2.4.1.	Fundamentals of PEM electrolysis.....	27
2.4.2.	Modelling and control of PEM electrolyzers for frequency stability studies	29
2.5.	Wind energy systems.....	31
2.5.1.	Operation overview of wind turbines	31
2.5.2.	Wind energy system configurations	33
2.5.3.	WT type 4: advantages, modelling and control	35
3	Study Case: FFS in Multi-area Multi-energy Power System.....	37
3.1.	Dynamic simulations in DigSILENT PowerFactory	38
3.1.1.	RMS & EMT Simulations.....	38
3.1.2.	Simulation setup	38
3.1.3.	Dynamic models and modelling approach – Use of templates.....	40
3.2.	The original PST 16 benchmark power system.....	41
3.3.	The modified PST 16 benchmark system	43
3.4.	Modifications on the original PST 16 benchmark power system	47

3.4.1.	Synchronous generators modelling and control	47
3.4.2.	Areas' tie-lines, MMC-HVDC interconnection links modelling and control	49
3.4.2.1.	MMC- HVDC interconnection links representation	49
3.4.2.2.	MMC-HVDC interconnection link operational behaviour and control	50
3.4.2.3.	Introducing APG control strategy in the converter control loop.....	53
3.4.3.	Modelling and control of PEM electrolyzers	55
3.4.4.	Introducing, modelling and control of WTs.....	57
3.4.5.	Modelling and control of static compensators	62
4	Optimizing the APG control for FFS	63
4.1.	Introduction	63
4.2.	Problem formulation 1	63
4.3.	Problem formulation 2	66
4.4.	The MVMO algorithm.....	68
4.5.	MVMO algorithm implementation in Python and co-simulation with DPF.....	70
5	Results and performance evaluation	73
5.1.	Introduction	73
5.2.	Results under problem formulation 1	74
5.2.1.	Loss of largest generating unit in area C (C7G).....	74
5.2.2.	Loss of largest generating unit in area A (A1aG)	81
5.2.3.	Loss of largest generating unit in area B (WTB10)	87
5.2.4.	Load event area B.....	92
5.2.5.	Load event area A.....	98
5.2.6.	Load event area C.....	101
5.3.	Results under problem formulation 2	106
5.3.1.	Loss of largest generating unit in area C (C7G).....	107
5.3.2.	Loss of largest generating unit in area A (A1aG)	111
5.3.3.	Loss of largest generating unit in area B (WTB10)	114
5.3.4.	Load event area B.....	118
5.3.5.	Load Event Area C.....	121
5.3.6.	Load event area A.....	125
5.4.	Simulation highlights	127
6	Conclusions & Future Work.....	131
6.1.	Thesis summary.....	131
6.2.	Answers to research questions	132
6.3.	Suggestions for future research	136

List of Tables

Table 3.1: RMS and EMT simulation differences [72] [101].	38
Table 3.2: Element distribution in the original PST 16 benchmark system.	43
Table 5.1: Frequency response results – Loss of SGU C7G - FFS local means.	75
Table 5.2: Frequency response results - Loss of SGU C7G - FFS by local and inter-area means.	78
Table 5.3: Frequency response results -Loss SGU A1aG- FFS by local and inter-area means.	84
Table 5.4: Frequency response results - loss WTB10 - FFS local means.	88
Table 5.5: Frequency response results - Loss of WTB10 - FFS local and inter-area means .	90
Table 5.6: Frequency response results - Load event area B - FFS local means.	93
Table 5.7: Frequency response results - Load event area B - FFS local and inter-area means .	94
Table 5.8: Frequency response results - Load event area A - FFS local and inter-area means .	99
Table 5.9: Frequency response results - Load event area C - FFS local means.	102
Table 5.10: Frequency response results - Load event area C - FFS local and inter-area means.	103
Table 5.11: Frequency response results - Loss of SGU C7G - FFS local and inter-area means (OF2).	107
Table 5.12: Frequency response results -Loss SGU A1aG- FFS by local and inter-area means (OF2).	112
Table 5.13: Frequency response results - Loss of WTB10- FFS local and inter-area means (OF2).	116
Table 5.14: Frequency response results - Load event area B- FFS local and inter-area means (OF2).	119
Table 5.15: Frequency response results - Load event area C- FFS local and inter-area means (OF2).	123
Table 5.16: Frequency response results - Load event area A- FFS local and inter-area means (OF2).	126

List of Figures

Figure 1.1: Global GHG emissions by sector [118].....	2
Figure 1.2: CO ₂ emissions under current, reference and REmap scenarios [9].	2
Figure 1.3: Annual CO ₂ emissions by sector in reference and REmap scenarios [9].	3
Figure 1.4: Frequency response and active power injection following an active power imbalance [26].....	7
Figure 1.5: Time scales of power systems' dynamic phenomena [25].....	8
Figure 2.1: Modular Multilevel Converter (MMC) schematic diagram [71].	19
Figure 2.2: MMC equivalent circuit (AVM type 6) [48].	22
Figure 2.3: MMC steady state schematic diagram [63].....	22
Figure 2.4: 4-Quadrant P-Q circle diagram of VSC [66].	23
Figure 2.5: VSC-HVDC configurations: a) Monopolar b) Bipolar c) Homopolar d) Multiterminal e) Back to back [63].	26
Figure 2.6: MMC-based HVDC interconnection link representation [78].	26
Figure 2.7: MMC station control loop based on current-vector control strategy [48].....	27
Figure 2.8: Main hydrogen production methods [81].	27
Figure 2.9: Schematic diagram of PEM electrolyzer [44].....	29
Figure 2.10: PEM electrolyzer representation [63].....	29
Figure 2.11: Equivalent electrical circuit of electrolysis stack [82].	30
Figure 2.12: Typical set of Cp- λ curves of a WT [91].....	32
Figure 2.13: Typical power curve of a WT [90].	33
Figure 2.14: Type 1: fixed speed WT configuration [93].	33
Figure 2.15: Type 2: Partially variable speed WT configuration [93].....	34
Figure 2.16: Type 3: Variable speed - Partial scale power converter WT configuration [93].	34
Figure 2.17: Type 4: Full scale power converter - Variable speed WT configuration [93].....	35
Figure 2.18 : Generic model structure of WT according to IEC 61400-27 [99].	36
Figure 2.19: WT type 4 control strategy [97].....	36
Figure 3.1: Simulation process in DPF - A flowchart.	39
Figure 3.2: Single model definition-hierarchical modelling approach DPF [102].....	41
Figure 3.3: The original PST 16 benchmark power system [100].	42
Figure 3.4: The modified PST 16 benchmark system.	44
Figure 3.5: Areas' frequency response during steady state conditions.....	46
Figure 3.6: Areas' frequency response under commonly occurred imbalances.....	47
Figure 3.7: SGU Composite Frame.	47
Figure 3.8: Heatmap of the modified PST 16 benchmark system - Load flow & Elements Loading.	48
Figure 3.9: HVDC interconnection link schematic diagram.....	49
Figure 3.10: Modified P/Vdc controller HVDC link with APG control strategy.	53
Figure 3.11: APG Controller HVDC link flowchart.....	53
Figure 3.12: Active power event in the MMC link.....	54
Figure 3.13: APG modification in the P/Vdc controller's common model.	54
Figure 3.14: PEM electrolyzers composite frame.	55
Figure 3.15: PEM electrolyzer model in DPF.....	55
Figure 3.16: PEM electrolyzer dynamic control block diagram.	56
Figure 3.17: APG Controller Electrolyzer – flowchart.	56
Figure 3.18: Parameter modification in the electrolyzer's common model.....	57
Figure 3.19: : WT main control blocks.	58

Figure 3.20: WT model in DPF.	59
Figure 3.21: APG Controller WT – flowchart.....	60
Figure 3.22: WT Common model parameter modification through python.	61
Figure 3.23: WT frequency controller block diagram.	61
Figure 3.24: STATCOM composite frame.	62
Figure 4.1: Schematic interpretation of OF2.	67
Figure 4.2: MVMO algorithm algorithmic process. Fitness evaluation counter denoted by i [114].	69
Figure 4.3: Simulation process flow.	72
Figure 5.1: Areas' frequency response - Loss of SGU C7G - No FFS.....	75
Figure 5.2: Frequency response area C – Loss of SGU C7G - FFS by local means.....	76
Figure 5.3: Frequency response area C - Loss of SGU C7G - FFS by local and inter-area means.	77
Figure 5.4: Areas' frequency response - Loss of SGU C7G - FFS by all SI means.....	79
Figure 5.5 WTs' active power output - Loss of SGU C7G – FFS by all SI means.	80
Figure 5.6: PEM Electrolyzers' power consumption - Loss of SGU C7G -FFS by all SI means.	80
Figure 5.7: Active Power Flows HVDC links – Loss of SGU C7G – FFS by all SI means.	81
Figure 5.8: Areas' frequency response - Loss of SGU A1aG - No FFS.....	81
Figure 5.9: Areas' frequency response - Loss of SGU A1aG - FFS by local electrolyzers.	82
Figure 5.10: Frequency response area A - Loss of SGU A1aG - FFS by local and inter-area means.....	83
Figure 5.11: Areas' frequency response - Loss of SGU A1a - FFS by all SI means.....	84
Figure 5.12: PEM Electrolyzers' power consumption - Loss of SGU A1a -FFS by all SI means.	85
Figure 5.13: Active Power Flows HVDC links – Loss of SGU A1aG - FFS by all SI means.	86
Figure 5.14:WTs' active power output - Loss of SGU A1aG - FFS by all SI means.	86
Figure 5.15: Areas' frequency response - Loss of WTB10 - No FFS.....	87
Figure 5.16: : Frequency response area C – Loss WTB10 - FFS by local means.....	88
Figure 5.17:Frequency response area B - Loss of WTB10 - FFS by local and inter-area means.....	89
Figure 5.18: Areas' frequency response - Loss of W B10 - FFS by all SI means.	90
Figure 5.19: WTs' active power output - Loss of WTB10 – FFS by all SI means.....	91
Figure 5.20:Active Power Flows HVDC links – Loss of WTB10 – FFS by all SI means.	91
Figure 5.21:PEM Electrolyzers' power consumption - Loss of WTB10 -FFS by all SI means.	92
Figure 5.22: Areas' frequency response - Load event area B - No FFS.	93
Figure 5.23: Frequency response area B - Load event area B - FFS by local means.	94
Figure 5.24: Frequency response area B - Load event area B - FFS by local and inter-area means.....	95
Figure 5.25: Areas' frequency response - Load event area B - FFS by all SI means.	96
Figure 5.26: Active Power Flows HVDC links – Load event area B - FFS by all SI means.	96
Figure 5.27: PEM Electrolyzers' power consumption - Load event area B -FFS by all SI means.....	97
Figure 5.28:WTs' active power output - Load event area B – FFS by all SI means.....	97
Figure 5.29: Areas' frequency response- Load event area A - no FFS.....	98
Figure 5.30: Areas' frequency response- Load event area A - FFS by local electrolyzers.....	99
Figure 5.31: Frequency response area A - Load event area A - FFS by local and inter-area means.....	99
Figure 5.32: Areas' frequency response - Load event area A - FFS by all SI means.	100
Figure 5.33: Active Power Flows HVDC links – Load event area A - FFS by all SI means.	100
Figure 5.34: PEM Electrolyzers' power consumption - Load event area A -FFS by all SI means.....	101
Figure 5.35: Areas' frequency response- Load event area C - no FFS.....	102
Figure 5.36: Frequency response area C – Load event area C - FFS by local means.	103
Figure 5.37: Frequency response area C - Load event area C - FFS by local and inter-area means.	104
Figure 5.38: Areas' frequency response - Load event area C - FFS by all SI means.	105

Figure 5.39: Active Power Flows HVDC links – Load event area C - FFS by all SI means.	105
Figure 5.40: WTs’ active power output - Load event area C - FFS by all SI means.	105
Figure 5.41: PEM Electrolyzers’ power consumption - Load event area C -FFS by all SI means.....	106
Figure 5.42: Frequency response area C - Loss of SGU C7G - FFS by local and inter-area means (OF2).....	108
Figure 5.43: Areas' frequency response - Loss of SGU C7G - FFS by all SI means (OF2).....	109
Figure 5.44: Active Power Flows HVDC links – Loss of SGU C7G - FFS by all SI means (OF2).....	109
Figure 5.45: PEM Electrolyzers’ power consumption - Loss of SGU C7G -FFS by all SI means (OF2).....	110
Figure 5.46: WTs’ active power output - Loss of SGU C7G - FFS by all SI means (OF2).....	110
Figure 5.47: Frequency response area A - Loss of SGU A1a - FFS by local and inter-area means (OF2).	111
Figure 5.48: Areas' frequency response - Loss of SGU A1aG - FFS by all SI means (OF2).....	112
Figure 5.49: PEM Electrolyzers’ power consumption - Loss of SGU A1aG -FFS by all SI means (OF2).	113
Figure 5.50: Active Power Flows HVDC links – Loss of SGU A1aG - FFS by all SI means (OF2).....	113
Figure 5.51: WTs’ active power output - Loss of SGU A1aG - FFS by all SI means (OF2).	114
Figure 5.52: Frequency response area B - Loss of WTB10 - FFS by local and inter-area means (OF2).	115
Figure 5.53: Areas' frequency response - Loss of WTB10 - FFS by all SI means (OF2).....	116
Figure 5.55: Active Power Flows HVDC links.....	117
Figure 5.55: WTs’ active power output –	117
Figure 5.56: PEM Electrolyzers’ power consumption - Loss of WTB10 - FFS by all SI means (OF2).	117
Figure 5.57: Frequency response area B - Load event area B - FFS by local and inter-area means (OF2).....	119
Figure 5.58: Areas' frequency response - Load event area B - FFS by all SI means (OF2).....	120
Figure 5.59: Active Power Flows HVDC links – Load event area B - FFS by all SI means (OF2).	120
Figure 5.60: PEM Electrolyzers’ power consumption - Load event area B -FFS by all SI means (OF2).	121
Figure 5.61: Frequency response area C - Load event area C - FFS by local and inter-area means (OF2).	122
Figure 5.62: Areas' frequency response - Load event area C - FFS by all SI means (OF2).....	123
Figure 5.63: Active Power Flows HVDC links – Load event area C - FFS by all SI means (OF2).	124
Figure 5.64: PEM Electrolyzers’ power consumption - Load event area C -FFS by all SI means(OF2).	124
Figure 5.65: WTs’ active power output – Load event area B - FFS by all SI means (OF2).	125
Figure 5.66: Frequency response area A - Load event area A - FFS by local and inter-area means (OF2).....	125
Figure 5.67: Areas' frequency response - Load event area A - FFS by all SI means (OF2).....	126
Figure 5.68: Active Power Flows HVDC links – Load event area A - FFS by all SI means (OF2).	127
Figure 5.69: PEM Electrolyzers’ power consumption - Load event area A -FFS by all SI means (OF2).	127
Figure A.1: Clarke Transformation.....	145
Figure A.2: Park Transformation.....	146
Figure A.3: Reference frames and signals after transformation.	146
Figure B.1: SGU Composite Frame.....	148
Figure B.2: SGU excitation system IEEEAC4A block diagram.	149
Figure B.3: SGU Turbine Model IEEEG1.	150
Figure B.4: SGU Governor Model IEEE G1.....	151
Figure B.5: SGU simple PSS block diagram.....	152
Figure C.1: HVDC interconnection link Composite Frame [72].....	153
Figure C.2: P/Vdc Controller of MMC HVDC link block diagram [72].....	154
Figure C.3:Q/Vac Controller of MMC HVDC link block diagram [72].	155
Figure D.1: WT Composite Frame DPF [115].....	156
Figure F.1: Frequency nadir deviation per event and group of SI sources tuned under problem formulation 1.....	178
Figure F.2: Frequency nadir deviation per event and group of SI sources tuned under problem formulation 2.....	178

Figure F.3: Steady state frequency deviation of the affected area per event and group of SI sources tuned under problem formulation 1 – Loss of generating units' events179

Figure F.4: Steady state frequency deviation of the affected area per event and group of SI sources tuned under problem formulation 1 – Load under-frequency events.179

Figure F.5: Steady state frequency deviation of the affected area per event and group of SI sources tuned under problem formulation 2 – Loss of generating units' events180

Figure F.6: Steady state frequency deviation of the affected area per event and group of SI sources tuned under problem formulation 2 – Load under-frequency events.180

Figure F.7: Maximum initial deviation (nadir) per event and OF under the best achieved frequency response of the affected area.181

Figure F.8: Steady state frequency deviation per event and OF under the best achieved frequency response of the affected area.181

Figure F.9: MVMO algorithm- Objective Functions convergence plot per problem formulation- Loss C7G.....181

Figure F.10: WTs' optimization variables convergence per OF - Loss C7G.182

Figure F.11: Electrolyzers optimization variables convergence per OF - Loss C7G.....182

Figure F.12: HVDC links optimization variables convergence per OF - Loss C7G.....182

List of Abbreviations

AC. *Alternating Current*
AEM. *Anion Exchange Membrane*
APG. *Active Power Gradient*
AVM. *Average Value Model*
AWE. *Alkaline Water Electrolysis*
BoP. *Balance of Plant*
CAES. *Compressed Air Energy Storage*
CCP. *Common Coupling Point*
CE. *Central European*
CIGRE. *French: International Council for Large Electric Systems*
COI. *Center of Inertia*
CSC. *Current Source Converter*
DC. *Direct Current*
DFIG. *Doubly Fed Induction Generator*
DPF. *DigSILENT PowerFactory*
DSL. *DigSILENT Simulation Language*
DSM. *Demand Side Management*
EMT. *ElectroMagnetic Transient*
ENTSO-E. *European Network of Transmission System Operators for Electricity*
EPC. • *Emergency Power Controller*
ESS. *Energy Storage Systems*
EU. *European Union*
EV. *Electric Vehicle*
FACTS. *Flexible AC Transmission System*
FCR. *Frequency Containment Reserve*
FFR. *Fast Frequency Response*
FFS. *Fast Frequency Support*
FLRT. *Fault ride through*
FRR. *Frequency Restoration Reserve*
FRT. *Fault Ride Through*
FSM. *Frequency Sensitive Mode*
GHG. *Greenhouse Gas*
GSC. *Grid Side Converter*
HER. *Hydrogen Evolution Reaction*
HVDC. *High Voltage Direct Current*
IEC. *International Electrical Commission*
IEEE. *Institute of Electrical and Electronics Engineers*
IEPG. *Intelligent Electrical Power Grids*
IGBT. *Insulated Gate Bipolar Transistor*
IRENA. *International Renewable Energy Agency*
KPI. *Key Performance Indicator*
LSC. *Line Side Converter*
LVRT. *Low Voltage Ride Through*
MEC. *Microbial Electrolysis Cell*
MMC. *Modular Multilevel Converter*
MPP. *Maximum Power Point*
MVMO. *Mean Variance Mapping Optimization*
OER. *Oxygen Evolution Reaction*
OF. *Objective Function*
PE. *Power Electronic*
PEC. *Power Electronic Converter*
PEI. *Power Electronic Interface*
PEIL. *Power Electronic Interfaced Loads*
PEM. *Proton Exchange Membrane*
PFC. *Primary Frequency Control*
PHU. *Pumped Hydro Unit*
PI. *Proportional Integral*
PLL. *Phase Lock Loop*
PMSG. *Permanent Magnet Synchronous Generator*

POD. *Power Oscillating Damping*
PSS. *Power System Stability*
PV. *Photovoltaic*
PWM. *Pulse Width Modulation*
RES. *Renewable Energy Sources*
RMS. *Root Mean Square*
RoCoF. *Rate of Change of Frequency*
RR. *Replacement Reserve*
RSC. *Rotor Side Converter*
SC. *Synchronous Condenser*
SCADA. *Supervisory Control And Data Acquisition*
SCIG. *Squirrel Cage Induction Generator*
SFC. *Secondary Frequency Control*
SG. *Synchronous Generator*
SGU. *Synchronous Generating Unit*
SI. *Synthetic Inertia*
SM. *Synchronous Machine, SubModule*
SO. *System Operator*
SOE. *Solid Oxide Electrolysis*
STATCOM. *Static Compensator*
TSO. *Transmission System Operator*
UFLS. *Under Frequency Load Shedding*
UNFCCC. *United Nations Framework Convention on Climate Change*
VSC. *Voltage Source Converter*
VSM. *Virtual Synchronous Machine*
WRIG. *Wound Rotor Induction Generator*
WT. *Wind Turbine*

1 Introduction

The first chapter of this report constitutes a general overview of the content of this thesis project highlighting the author's motivation on the research field. Initially, the current state of art considering the impact of energy transition and the increasing number of power electronic interfaces (PEIs) into the form and operation of power systems is analyzed, mainly focusing on frequency stability challenges encountered. Then, based on the outcomes of a literature study open research gaps are indicated and possible mitigation alternatives are discussed. Afterwards, the main objectives of this study are clearly defined, and research questions are formulated. Finally, a workflow chart depicts the research approach of this study followed by the thesis outline.

1.1. Motivation

Human activity during the past led to the emergence of one of the main battles for modern societies, the climate change. The effects of it in our everyday lives becomes more and more evident, rising the global concern on the current environmental policies and highlighting the necessity of immediate mitigation and prevention measures [1]. That impelled governments around the world to cooperate under the United Nations Framework Convention on Climate Change (UNFCCC) and sign common agreements against the consequences of persistent environmentally harmful emissions such as greenhouse gas (GHG) emissions [2]. The latest and most extended global policy against the climate change is the Paris Agreement, signed in 2016 by 190 parties aiming at a reduction of the global temperature increase by 2°C compared to the preindustrial levels, with the pursuit to contain the increase even further to 1.5°C. It also targets to improve parties' ability to face the consequences of the climate change by supporting their efforts both technically and financially. Through the signing of this agreement, human behavior has been highlighted as the main reason behind the climate change due to the increase of harmful gas emissions like carbon-dioxide, nitrous oxide and methane, responsible for the greenhouse effect and thus the global warming [3] [4].

The European Union (EU) as significant contributor to the signing of the Paris Agreement has prepared the Clean Power Plan and the 2030 and 2050 Climate and Energy Frameworks setting targets for the coming years aiming to become the world's first climate-neutral continent in world [4] [5] [6] [7]. The key objectives for 2030 comprise an at least 40% abatement in the net GHG emissions in comparison to the 1990's levels with an intention to increase to 55%, an increase in the renewable energy sources installed by at minimum 32% and an improvement in the energy efficiency of 32.5% [5].

According to [8], GHG emissions, need to shrink by 50% until 2050 and almost nullify in the second half of the century to fulfil the signed targets. As it can be observed in *Figure 1.1*, energy-related human activities constitute the main liable sector for GHG emissions. Furthermore, it is expected that by 2050, the gross

electricity consumption will significantly increase as electricity would become the main energy carrier for heat and transportation [9].

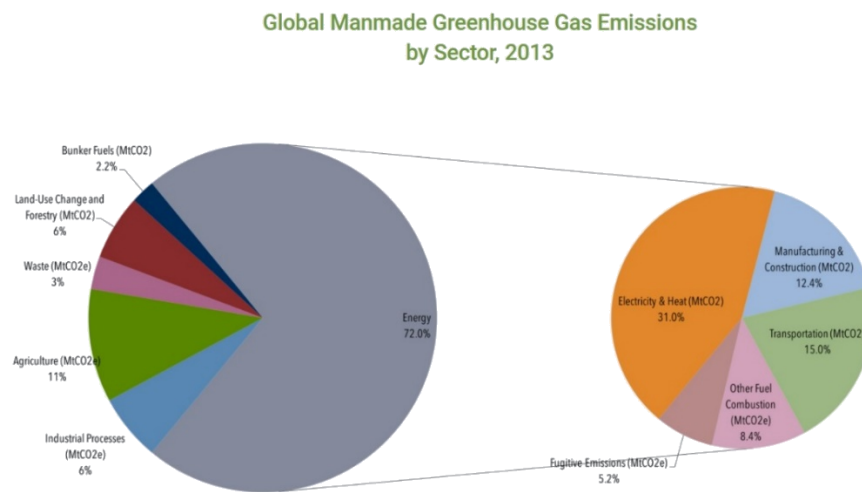


Figure 1.1: Global GHG emissions by sector [118].

To reach the goals of the Paris Agreement and efficiently contain the global temperature, decarbonizing and renewable transformation of the energy sector is essential. In fact, the road to success strongly depends on the fast deployment of renewable energy sources (RES), electrification of highly CO₂ emitting sectors such as transportation and heating and improved energy conversion [9]. According to the International Renewable Energy Agency (IRENA), the currently developed plans, denoted as “Reference Case” in Figure 1.2 and Figure 1.3, would not be adequate to meet the expected results, whereas a proposed strategy, denoted as “REmap Case”, that deploys extensive measures - increase of the renewable share to 66% of the total energy consumption, renewable power generation of more than 85%, accelerated electrification of transportation and heating at higher efficiency rates- would lead to 70% reduction of the GHG emissions and a successful counteracting on climate change.

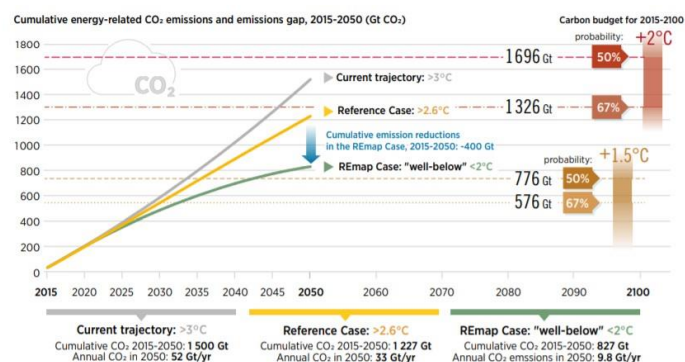


Figure 1.2: CO₂ emissions under current, reference and REmap scenarios [9].

Even at the most conservative plans, the intended energy transition would significantly affect the form and the behavior of power systems. The introduction of RES will significantly increase the PEIs in system both in transmission and distribution levels, as their connection is predominately achieved through power converters [10] [11] [12] [13]. In parallel, modernization of power grids is strongly connected with the transformation of conventional alternating current (AC) networks into hybrid AC/DC networks due to the advantages of the high

voltage direct current (HVDC) technology [14] [15] [16] [17]. Moreover, changes are also expected on the demand side as power electronic interfaced loads (PEIL) offer improved power quality, efficiency and controllability, whereas new technologies like electric vehicles (EVs), hydrogen-based demand such as electrolyzers and energy storage systems (ESS) will form what is called multi-energy power system. As it clear, the energy transition leads to power electronics (PEs) dominated multi energy systems that inherently have completely different behavior.

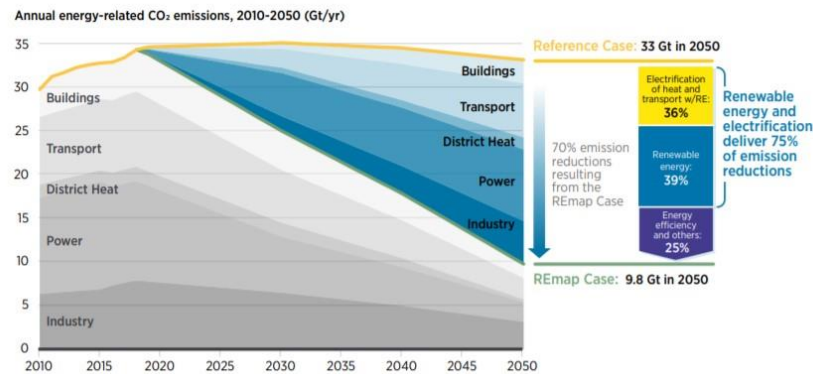


Figure 1.3: Annual CO₂ emissions by sector in reference and REmap scenarios [9].

The future PE dominated multi-energy systems are expected to impose many obstacles in the operation of power systems. According to [18] the latter ones can be split into three categories: a) challenges due to the altered system behavior, b) challenges in the system operation and c) challenges because of the lack of ancillary services. The most significant changes are due to the new variable and uncertain nature encountered both on supply and demand sides and the different dynamic response of the PEIs utilized for the interconnection of the new elements [18] [19]. Furthermore, existing network assets if not improved will experience problems as new power flows and the increased system's complexity will lead them close to their technical limits [18]. Finally, new strategies for ancillary services and protection schemes should be developed according to the electromagnetically decoupled and control-based responses of the new PEI elements characterized by lack of natural response to power changes and limited short circuit support [18].

Among these challenges, the effects of PEIs in the power system stability are of great importance for the ceaseless, reliable and secure system operation. In fact, future power systems are expected to exhibit a completely different dynamic behavior as more regular, faster and not effectively damped dynamic phenomena will emerge. In addition, decommissioning of conventional synchronous generation will alter the system response, leading to reduced inertia levels, limited short-circuit capacity and lack of excitation and stabilizing systems that will put in danger the stability of the system [18] [19]. Preserving the frequency within acceptable limits is highlighted as a critical target of system operators worldwide [18].

Under the new volatile conditions, an increased power system flexibility, observability and controllability is more than necessary. Emerging new technologies connected through PEIs and especially voltage source converters (VSCs) can effectively offer ancillary services to the grid due to their increased levels of controllability and fast responses. The latter support can come from both generation and demand sides and from interconnection links utilizing HVDC technology. However, when facing complex stability phenomena targeting on the same variables such as frequency, coordination among the individual elements is more than necessary to avoid adverse control actions [20].

1.2. Literature review

1.2.1. Power system stability

Based on section 1.1, the energy transformation of power systems leads to new complex, variable and uncertain behavior of the system. Its dynamic response is characterized by the fast and frequent responses based on the switching actions of the PEIs severely affecting the stability margins of the system. However, new technologies introduced in modern systems can provide ancillary services if their controllers are enhanced to respond to grid imbalances offering increased flexibility and fast response. For this reason, creating and utilizing models of the future multi-energy systems can demonstrate the dynamic performance of the system, highlight possible stability issues, and generate ideas on potential solutions. Exploring the feasibility, the efficiency, and potential improvements of control strategies through time-domain simulations and achieving optimal coordination among them is the goal towards the required reliability and security for a stable operation of the power system.

According to [21] and [22] power system stability (PSS) is defined as follows:

“Power System Stability is the ability of an electric power system for a given initial operating condition, to regain a state of operating equilibrium after being subjected to a disturbance with the most system variables bounded so that practically the entire system remains intact.”

PSS is of great importance since it is strongly connected with main operational characteristics of power systems. A stable system has the capability to withstand failures or contingencies of high probability of occurrence ensuring critical operational needs such as continuity of supply, reliability and security [21] [23].

When an event occurs, different forms of instability may be encountered and thus PSS can be classified into groups considering the main variable affected, the intensity of the disturbance and the timespan to which the dynamics extend [21] [24]. Although the definition of the PSS remains intact due to the transformation of the power grids, that is not the case with its classification as the introduction of PEI units led to a new faster dynamic behavior and thus new forms of instability [22]. These new forms occur because of the lower inertia levels, the limited short-circuit capability and interactions among the control systems. As a result, PSS can be classified not only to the 3 original groups -voltage, rotor angle and frequency stability- but also to resonance and converter driven stability [22] briefly explained below:

- **Voltage stability** is related to the ability of the system after experiencing an event to preserve the systems' bus voltages within the acceptable operational limits so that the system remains intact. Voltage instability occurs mainly due to loss of equilibrium of reactive power between supply and demand. Sustained falls or rises of bus voltages may lead from tripping of various elements such as transmission lines, generators or RES from protection devices, to cascading outages and even blackouts. Potential causes of voltage instabilities are the inadequate capacity for power transfer, limited voltage support, restoring load actions, characteristics of compensation devices, actions of control devices and large penetrations of RES with limited supporting capabilities. Voltage stability based on the size of the disturbance can be further

classified on large and small-disturbance voltage stability. Considering the time span of instabilities, distinction into short and long-term instabilities is common. The former one, refers to fast dynamics from PEIL, HVDC converters or induction motors occurring at several seconds, whereas long-term instabilities deal with slower dynamics at the time frame of several minutes [21] [22] [24].

- **Rotor angle stability** deals with the ability of the electromagnetically coupled synchronous generating units (SGUs) to withstand a disturbance and remain in synchronism. In this type of instability, the relative angle of the rotor among the synchronous machines (SMs) is the mainly affected variable. Under steady state, an equilibrium between the electromagnetic and mechanical torques of each synchronous generator (SG) is observed. When a disturbance occurs, this balance is perturbed and SGUs tend to accelerate or decelerate leading to angle separation. This angular difference, with respect to the power angle relationship, will lead faster running machines to an increased active power output able to decelerate them restoring the equilibrium. However, if a threshold is reached a further increase in the angular difference leads to reduced active power output and thus to further acceleration and to loss of synchronism. Converter based units introduced to power systems nowadays are also affecting the rotor angle stability, as the system becomes more prone to rotor swings and to insufficient oscillations damping due to the displacement of SGUs, changes in the main power flows in the links and the low inertia conditions. However, these phenomena can be tuned down if the controllers of converter-based units are effectively designed [22]. With respect to the disturbance, rotor angle stability is further split into small signal stability and transient stability referring to small and large disturbances, respectively. Finally, the time frame of rotor angle instabilities is short referring to fast dynamic phenomena between 3-5s and up to 20s for large systems [21] [22] [24].
- **Frequency stability** refers to the system's capability to preserve the frequency within the allowed operating bounds and restore it to its nominal value, after the occurrence of a severe contingency. Frequency instabilities occur due to the severe perturbation of the active power balance between supply and demand. When due to a contingency in the power system there is an excess in the generated active power, frequency rises, whereas when the required power is greater than the generated one frequency drops. Severe frequency excursions may trigger protection systems and lead to loss of generators or demand centers, cascading outages and even blackouts. In large interconnected systems, in case of severe active power imbalances, system splits commonly occur. The time frame of frequency instabilities is divided into short and long-term instabilities depending on the frequency response and the control actions triggered. The introduction of converter based units in replacement of SGUs in power systems, has significantly affected the system's dynamic response due to the low inertia conditions, the lack of natural inertial response and faster dynamic behavior encountered leading to the emergence of new challenges [21] [22] [24]. Further details about the frequency response in the latter systems are provided in sections 1.2.2 and 1.2.3.
- **Resonance stability** is a new category in the PSS classification and refers to periodical and insufficiently damped oscillations of the voltage and current waveforms occurring when energy is exchanged between elements. It can be split in two categories: the torsional resonance associated with the sub-synchronous oscillations occurring between compensators installed in series to the SGU's shaft and electrical resonance mainly occurring when directly connected to the grid induction machines experience self-excitation because

of resonance among the series capacitors and the effective reactance of the machines. The former type is mainly met in SGUs but is also encountered due to interactions of fast responding devices such as HVDC links, power system stabilizers and compensators, whereas the latter type is met in DFIG leading to large oscillations able to damage the equipment [22].

- **Converter-driven stability** is a new category in the PSS classification associated to interactions between the controllers of the converter-based units introduced and the system dynamics. Converter based units' behavior depends on the time scales and responses of their controllers and the applied algorithms and thus possible interactions can be observed between these elements and either the electromagnetic transients of the grid or the electromechanical dynamics of synchronous elements. Instability occurs mainly in form of frequency oscillations over a wide range and also as limited power transfer capability at specific points. Depending on the frequency of oscillations it can be further split to slow and fast interaction instabilities. The former one refers to the instabilities between slow acting controllers of converter based units and mainly the SGs electromechanical dynamics leading to oscillations below 10Hz, whereas the latter one refers to interactions among fast acting controllers of converters, HVDC links and FACTS and fast responding network elements such as the transmission network, the SMs dynamics and various PEI units leading to oscillations up to hundreds of Hz [22].

1.2.2. Frequency stability in conventional power systems

System operators (SOs) around the world consider frequency response of the system important for the secure and reliable operation of the power grid [18]. For this reason, supervisory control and data acquisition (SCADA) systems are systematically utilized for real time supervising of the frequency so that operators can immediately cope with significant frequency deviations [25].

In conventional power systems characterized by synchronous generation, when a critical disturbance occurs able to perturb the active power equilibrium between supply and power consumption, a series of control actions – primary, secondary and tertiary control – are applied to effectively contain frequency deviations and quickly restore it to its nominal value [24] [25]. The frequency response of a system after an active power imbalance when load frequency control actions are applied can be observed in Figure 1.4.

Before the automatic and manual actions of the controllers of SGUs, the system itself tries to maintain the balance with its inherent inertial or natural response [24]. The latter one is triggered when the imbalance occurs due to the electromagnetic coupling of synchronously rotating elements of the system. These units can absorb or deliver kinetic energy based on the swing equation, Equation 1.1, so as to withstand and limit the imbalance. This action takes place at a time frame of 0.5-1s following the disturbance and significantly affects the rate of change of frequency (RoCof) or df/dt . Strong power systems are characterized of high inertia levels, low RoCofs and high capabilities to withstand and quickly recover from active power imbalances [24] [25] [26].

$$\frac{2H}{f_0} \frac{df}{dt} = P_m - P_e \quad \text{Equation 1.1}$$

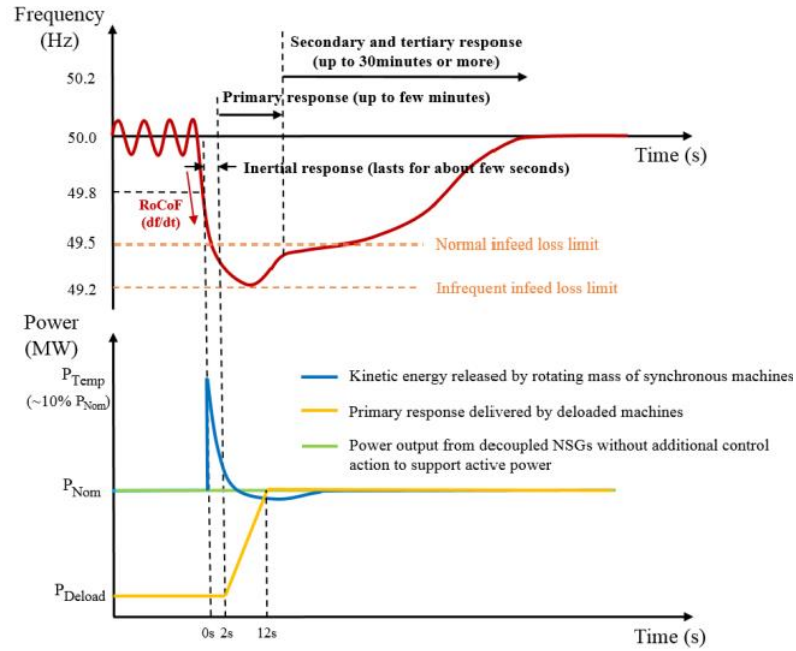


Figure 1.4: Frequency response and active power injection following an active power imbalance [26].

Inertial system response is followed by primary control scheme, activated when a sustained deviation occurs and is responsible to preserve the active power balance of the network within a time frame of several seconds. It regulates the active power output of the SGs proportionally to sensed frequency excursions and thus it is also denoted as frequency-droop control. Each participating unit in the primary frequency control contributes from a new point to the balance according to its droop constant, R , as observed in Equation 1.2 [24] [25].

$$f - f_0 = -R(P - P_0)$$

Equation 1.2

The primary frequency control (PFC) actions, as expected in the case of proportional controllers, cannot restore the target variable to its original value. For this reason, secondary frequency control (SFC) schemes are enabled after 30s for a period up to several minutes. Its goal is to automatically adjust the active power setpoints of all SGUs to sufficiently restore the frequency and release the already deployed PFC reserves. In case of multi-area networks additional attention has to be paid in the flows among the tie lines that have to be also regulated accordingly [24]. Finally, if a steady-state error remains and further manual adjustment in the active power dispatch among the units is required, tertiary control is activated for several minutes up to hours. The new setpoints aim at nominal frequency value, released PFC and SFC reserves and unit participation to the new active power demand according to the economic dispatch of the system [24].

1.2.3. Frequency stability and issues in power electronics dominated power systems

In contrast to the frequency response of synchronously operating systems, future PE dominated systems exhibit a completely different dynamic behavior as the response of its elements is based on the switching actions of the converters and not on the electromagnetic coupling of rotating machines [19] [22]. The new phenomena occur at the time frame of 10^{-6} up to 10^{-4} s whereas conventional electromechanical phenomena

from 10^{-2} up to 10^3 s as it can be observed in Figure 1.5 [25]. Hence, system dynamics become more frequent, fast and complex to be monitored and handled. In fact, fast dynamics may lead to significant challenges on the response of current control structures and to additional stress to remaining SGUs leading to larger frequency deviations and to more frequent participation of reserves [18]. Furthermore, decommissioning of synchronous rotating masses of the system, leads to lower inertia levels, due to the reduced kinetic energy available for inertial response. RES connected through PEIs have no natural inertia capability if no special control actions are applied to their control systems [18][19] [25] [26]. Hence, according to the swing equation, Equation 1.1, the RoCof is expected to significantly increase following a disturbance, while the maximum instantaneous frequency deviation would be greater due to the limited natural and primary frequency support.

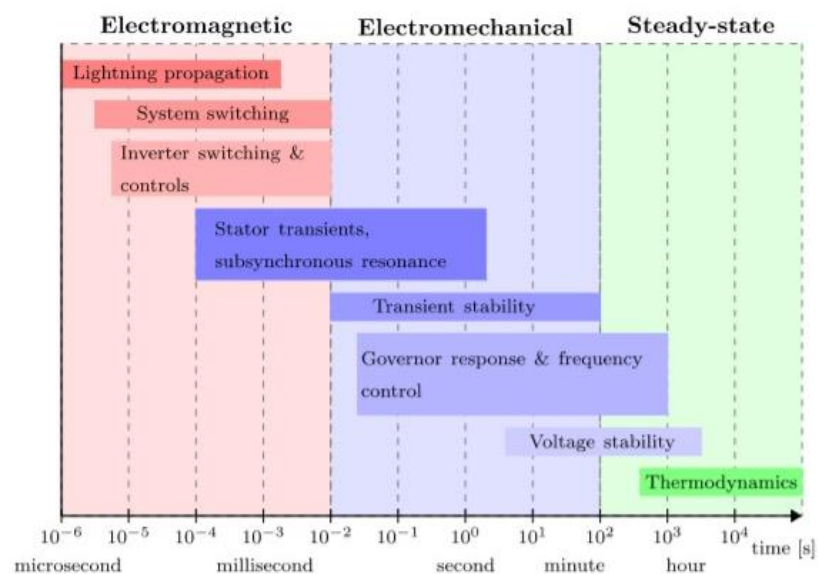


Figure 1.5: Time scales of power systems' dynamic phenomena [25].

An increased RoCof may have significant impact on the system operation, as various protection devices may be triggered to disconnect critical components increasing further the imbalance. As a result, cascading outages of generating units or tie-lines and even blackouts are commonly encountered [27] [28]. Furthermore, in many power systems under frequency load shedding (UFLS) schemes are activated to sustain the deviations and maintain the normal operation to a part of the system. In large interconnected systems like the continental European one, system splits into islands are highly probable to occur. If no anti-islanding protection is activated, the system splits into islands with different frequency levels to continue to operate [18] [27] [29].

Situation is expected to worsen, as PFC may not be adequate to improve the frequency response following a disturbance. As it is stated in [18] and [22], systems with high-RES penetration have volatile prices, which means that ancillary services provided from conventional generation may not be competitive leading to their decommissioning. Replacement of synchronous reserves from variable ones utilizing RES increases the uncertainty in the system [30]. The intermittent nature of RES would impose uncertainty into the availability of reserves due to the weather dependent prime sources and the limited overloading capability of PEI units [18].

Moreover, various control strategies applied to PEI of RES like wind turbines (WTs) may also contribute to frequency problems. Due to the limited overloading capability of PEs, control schemes like fault ride through (FRT) applied to WT interconnections may escalate the reactive power injection in expense of active power,

to deal with voltage instabilities at their common coupling points (CCPs) [25] [31]. Additionally, when the power setpoints are set back to nominal, the time required for WTs to restore their active power injection is significant and may lead to frequency instabilities in the interconnected network. This type of instabilities is denoted as voltage induced frequency dips [18] [19].

Apart from the supply side, changes are also expected on the consumption. Critical loads of the system tend to be connected to the grid through PEIs due to higher efficiencies and constant power needs [19]. Also, new technologies like EVs, ESS and hydrogen-based systems deploy PEIs for their grid connection. As a result, the inherent response of conventional loads to frequency changes as explained in [24] is nonexistent anymore. Furthermore, power grids nowadays tend to transform from the conventional AC networks to hybrid AC/DC networks since more and more HVDC technology is used for remote RES interconnection, transfer of bulk power over long distances and areas interconnection links. As in the previous cases, HVDC technology is based on PEIs which effectively decouple elements from the grid and thus frequency support is absent if not supplementary measures are applied [19] [25].

In a nutshell, the main challenges considering the frequency stability of the PE dominated network originate from the reduced level of inertia, the very fast-dynamic response, the limited overloading capability of the converters, the lack of natural response and the uncertainty over the availability of the primary sources. Frequency response of the system following an imbalance will be characterized by very stiff RoCofs, larger maximum instantaneous frequency deviations, excessive and more frequent oscillations and inability to restore to its nominal value in case of low reserve availability. For this reason, frequency support from the new PEI components of the system and utilization of their fast control capabilities is more than essential for the reliable operation of the system and thus has gained great attention lately.

1.2.4. Frequency support alternatives in PE dominated power systems

The challenges imposed by the transition to the PE dominated energy systems forced TSOs, governments and institutes to search for alternatives to improve the frequency response under the new conditions [32]. To cope with the frequency stability problems encountered, two general group of solutions can be determined: The operational or managing solutions and the adaptation or modernization solutions [33].

The operational solutions are those that SOs can apply when operating the system to preserve the minimum required inertia levels. Among these solutions, SOs may perform grid code modifications to allow extended RoCofs and frequency deviations based on the withstand capabilities of the existing units, leading the system operation close to its limits [33] [34]. Another possible solution is to modify protection settings to adapt to the new operating conditions and avoid activation of generators protection schemes or UFLS [33]. Furthermore, high RoCof events can be avoided if large cross-border exchanges or large loads are limited. Based on the swing equation, Equation 1.1, it is clear that the RoCof is influenced by the size of the imbalance and thus containing the maximum possible imbalance would reduce the possibility of high RoCof events [33] [34]. Also, operating the existing power plants below their rated power would increase the headroom for larger active power imbalances, a solution with significant environmental and financial consequences [32] [33] [35]. Finally, a possible alternative for SOs would be to restrict the amount of PEI elements installed and set a minimum amount of operating or reserve SGUs to ensure the minimum required inertia for normal and reliable

supply. As it is obvious, these solutions can only have a temporary fit before extensive solutions are applied, as they are opposite to environmental and financial targets and policies [33].

On the other side, adaptation and modernization solutions refer to the introduction of new elements enhanced with modern ancillary capabilities and seem more efficient and enduring alternatives [33]. In [32] several technologies have been proposed as alternative sources of inertia. These sources depending on the connection method deployed can be split into synchronous inertia sources and non-synchronous or synthetic inertia (SI) sources. The first ones are electromagnetically coupled sources that offer natural inertial response similar to the conventional SMs, whereas the latter ones offer what is called SI by applying various control strategies in the PEI utilized for their connection [32] [35] [36].

Synchronous inertia sources based on their inherent natural response to active power changes, form a mature yet challenging solution [32] [35]. Among these sources, synchronous condensers (SCs), already utilized for reactive power compensation, is a promising option [37]. In fact, they are electromagnetically coupled free spinning motors that can replace conventional power plants and operate exclusively as ancillary service elements [32] [35]. However, if not equipped with additional rotating masses like flywheels, they are characterized by low inertia constants [36]. Other possible options in this category are AC interconnectors, pumped hydro units (PHUs), compressed air energy storage (CAES) units and rotating stabilizers. However, these solutions are characterized of various disadvantages and they are not considered as extensive or easily applied alternatives in all cases. AC interconnectors suffer from limited power transfer capacity and charging current problems with an increasing distance, PHUs require two large basins to offer adequate support and CAES systems are based on suitable underground caverns. If also, other environmental, financial or constructional issues are considered, their utilization is not worthwhile [32] [35] [36].

Considering the various non-synchronous means of inertia, various technologies can be utilized for frequency support from the demand side [32] [35]. Fully decoupled type 4 WT's and solar photovoltaic (PV) systems with supplementary controllers can use the excess amount of wind or solar irradiation for frequency support when necessary [33] [36]. The limitations that originate from possible unavailability of the prime source can be overcome by operating the system below its maximum power point (MPP) or in combination with various ESS [38]. For RES connected to the grid through HVDC links, the energy stored on the capacitance of the direct current (DC) link can also be utilized if necessary [39]. Non-synchronous ESS such as batteries, flow-batteries, supercapacitors and flywheels can also be integrated to various locations of the grid and act rapidly in case of imbalances [32] [35] [36] [40]. HVDC links used to interconnect different synchronous areas or systems can also exploit the capabilities of VSCs to offer frequency support by controlling their power injection and even share an active power imbalance between areas [41] [42]. Finally, demand side management (DSM) has gained great attention, as the capabilities of new responsive technologies such as EVs or multi-MW scale proton exchange membrane (PEM) electrolyzers can be also considered as alternatives to preserve the network balance [32] [35] [43] [44].

The exploitation of the sources of SI is mainly based on improving the control capabilities of VSCs used for their integration. VSCs can adjust very fast their operating setpoints and inject or absorb power according to various inputs such as the system frequency [45] [46] [47]. Several control methods have been proposed to be enhanced to the current control schemes to enable fast frequency response of these systems. Virtual

synchronous machines (VSMs), for example, can control the converter to fully emulate the behavior of a conventional SM and thus its dynamic response. SI control strategy on the other hand, is based on the measurement of the RoCof that can be used as input to supplementary frequency controllers, whereas fast frequency response (FFR) control schemes use the frequency deviation droop method to sustain the deviations [36]. The performance of these control strategies is based on the key characteristics of the controllers, the RoCof withstand capability, the acceptable frequency deviations, the size and the inertia of the system and finally the availability and the capacity of the source of inertia [36]. The main controllers' characteristics that influence their performance are the input signal measurement strategy, the response time of the controller to measure, process and actuate to control the target variable, the ramp-rate which is the rate the active power output changes, the power amplitude, which is the necessary amount of power for frequency support and the minimum power capacity required [32] [35] [36]. Among these control strategies, VSM is the most complex one to be applied, while difficulties also arise in the enhancement of voltage and current operating limitations of the converters. Regarding the SI control strategy, the main issue concerns the rapid and accurate measurement of the RoCof and the influence of the noise that can significantly affect the controller's performance. However, if these challenges are overcome SI control has remarkable results considering the RoCof containment. FFR control schemes take rid of the issues of RoCof measurement and noise and have a great performance not only in the RoCof containment, but also on achieving reduced maximum instantaneous frequency deviation (nadir) and reduced steady state deviation if properly tuned [36].

Nowadays, active power gradient (APG) control strategy has also been considered as an effective solution. This scheme is able to take advantage of the FFR control strategy characteristics and use the frequency deviation as input to calculate the magnitude of the required active power injection/absorb (ΔP) added to the active power setpoint of the converter, but also controls another critical parameter, the ramp-rate, and thus the rate the active power is injected by the VSC for the active power-frequency control [48].

1.3. Problem definition and previous work

From all the aforementioned, it can be concluded that the energy transition has led to the need to transform the energy system, one of the main contributors to the CO₂ emissions and climate change into a smarter, more flexible, sustainable and green system. However, this transformation entails many operational and technical challenges originating from the fact that the currently forming multi-energy systems depict a large number of PEIs. These devices are based on the semiconductor switching and not on the conventional electromagnetic coupling with the network. Hence, in the new PE dominated systems, most of the elements are fully decoupled from the network dynamics. As a result, the new power systems experience low inertia conditions, high variability and uncertainty both on the supply and demand, reduced short-circuit capacity and very fast and frequent dynamics. Under these new conditions, PSS is highly affected and thus additional measures should be taken to assure it. Especially, preserving the active power balance is among the most challenging tasks under the highly variable and low-inertia conditions and thus frequency stability issues are one of the main concerns of SOs.

To mitigate these arising problems, latest studies have highlighted the potential of frequency support from control schemes attached to VSCs used to integrate RES such as WTs, to form stations of HVDC

interconnection links between synchronous areas and to connect responsive demand units such as PEM electrolyzers. In fact, these converters can be controlled to inject or absorb active power at very fast rates utilizing APG control scheme, through the control of two main parameters the magnitude of the additional active power injection (ΔP) required for ensuring active power balance in the network of interest and the APG or ramp-rate that active power is injected into or absorbed from the grid. These parameters are highlighted as critical and have been incorporated in modified grid codes such as in the UK as part of the connection requirements for frequency support from converter-based elements [32] [35] [49].

Previous work has highlighted the capability of APG control scheme applied to VSC stations of HVDC link between synchronous areas to offer fast frequency support (FFS) following an active power imbalance event when the interconnected systems have different levels of inertia [48]. Also, in [50] has been found that enhanced frequency response is also possible at interconnected systems with similar levels of inertia when optimal tuning of APG control parameters is achieved. Moreover, the effectiveness of the APG control method has been also tested in considering a more complex multi-energy system with simultaneous frequency regulation from both VSC stations of an HVDC link and responsive demand, electrolyzers [20]. In all these later cases, it has been verified that APG control scheme has high potential in achieving frequency support and regulation. Additionally, it has become obvious that optimal tuning of the control parameters is more than necessary to achieve the response of interest. This task becomes more and more challenging when complexity of the system increases, and coordination is required. In fact, in larger meshed systems, with more than two synchronous interconnected areas, high share of RES like WTs and responsive demand units all contributing to the mitigation of active power imbalances, coordination and optimal tuning of the controllers is essential to avoid adverse control actions that could lead to over regulation issues or to oscillating and unstable frequency profiles. Optimal tuning strategy for these complex problems constitutes yet an open research gap that need to be further investigated.

1.4. Objectives, research questions and thesis contribution

The main objective of this thesis report is to develop a generic model of a multi-area multi-energy hybrid HVAC-HVDC power system with RES and responsive demand units and optimally tune the APG control strategy attached to various elements for effective and well-coordinated FFS following a significant active power imbalance. For this reason, various models of SI elements available in the IEPG group of TU Delft such as WTs, PEM electrolyzers and HVDC links that have shown high potential for FFS, will be used as starting point of this thesis. The most suitable ones for stability studies will be selected and modified to be applied to the main system model, the original PST 16 benchmark system, to form the multi-area network of this study. The modelling and the simulation processes in this study have been performed with the aid of a powerful software tool developed by DlgSILENT, PowerFactory 2020, whereas for the development and solution of the optimization problem aiming at the tuning of the controllers Python 3.8 has been utilized.

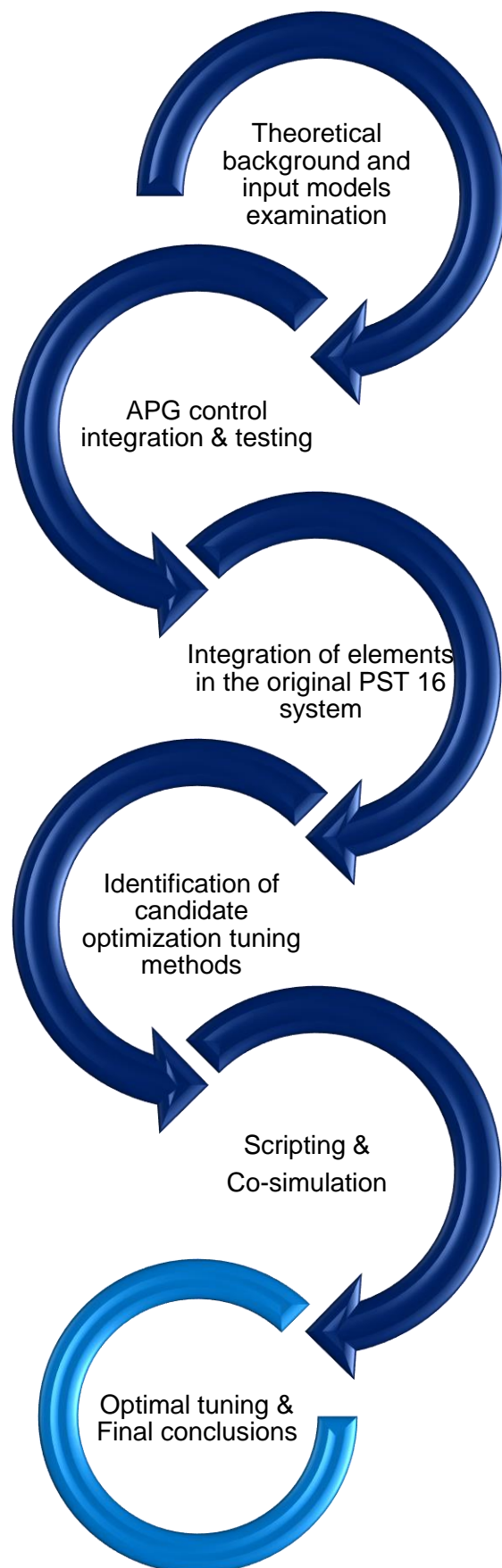
To arrive to the goal of the current study the following questions have been formulated:

- How various PEI elements such as WTs type 4, MMC-based HVDC links and PEM electrolyzers should be modelled for RMS frequency stability studies in DIgSILENT PowerFactory 2020?
- What modifications should be done to enhance the controllers of the newly introduced elements with the APG control scheme to offer FFS?
- Which are the necessary inputs and the most critical parameters of the new controllers?
- What modifications should be done in a multi-area test system like the original PST 16 benchmark system to enable the integration of controllable elements to form a hybrid HVAC-HVDC multi-energy power system?
- How to optimally tune the controllers attached to the PEIs of the introduced elements to offer fast and well-coordinated active power – frequency support with the minimum effort?
- What is the frequency profile of the system before and after applying the tuned control strategy? Has the frequency profile improved and in what ways?

The contribution of this thesis report is enclosed in the following points:

- At the end of this project, a benchmark multi-area, multi-energy, HVDC-HVAC hybrid system suitable for frequency stability studies and RMS simulations in DIgSILENT PowerFactory 2020 will have been developed. In fact, this system would be a representative modification of the original PST 16 system that would contain MMC-based HVDC interconnection links, fully decoupled type 4 WTs and responsive demand units such as PEM electrolyzers.
- The feasibility and performance of extended and simultaneous deployment of APG control scheme in various PEI elements of the new developed network to offer adequate fast active power – frequency support will be examined. It worths pointing out that previous work has shown the potential of this control strategy in smaller systems but not on larger more complex and variable systems.
- Investigation of the performance of different optimization methods to tune the APG parameters and effectively offer frequency support in a complex multi-area, multi-energy system.
- Script development and modifications for APG parameters optimal tuning in different PEI elements introduced and development of a co-simulation environment for the optimization strategy by combining DIgSILENT PowerFactory 2020 and Python 3.8.
- Indepth analysis of the results of extensive RMS simulations on the frequency stability of the new developed system and the proposed optimization strategies utilized to achieve the corresponding results.

1.5. Research approach



- Literature review on PSS in conventional and future PEI dominated power systems.
- APG control strategy for FFS
- PST 16 system model in DigSILENT PowerFactory
- DigSILENT MMC-HVDC link model in DigSILENT PowerFactory
- PEM electrolyzer model in DigSILENT PowerFactory
- WT type IV model in DigSILENT PowerFactory

- Introduction of APG control scheme in MMC-HVDC link
- Introduction of APG control scheme in PEM electrolyzers
- Introduction of APG control scheme in WTs type IV
- Response testing in P setpoint changes and active power – frequency event
- Investigation of key control parameters on the performance of each element

- Utilization of merging tool – Integration of MMC- HVDC links, PEM electrolyzers and WTs Type IV in the original PST 16 system
- Modifications for optimal operation of modified multi-energy PST 16 system
- Testing under normal steady-state conditions

- Extensive RMS simulations before optimization
- Determination of critical issues and parameters in frequency response
- Examination of various optimization algorithms, problem definitions, boundary conditions, constraints

- Development and modification of the script according to the optimization algorithm and its characteristics
- Development of co-simulation environment between DigSILENT PowerFactory and Python

- Identification of the best performing optimization strategy
- Result analysis before and after controlling and optimal tuning
- Conclusions on the elements participation to support according to characteristics and localtion
- Final conclusions of the system's frequency stability

1.6. Thesis outline

The present report covers all the aforementioned topics and is structured as follows:

- **Chapter 2** : This chapter consists of 2 parts. In the first one the importance of the frequency for power systems is described followed by the main requirements and the key performance indicators used to evaluate the frequency stability of a system. In the second part of this chapter the fundamental theory behind all the introduced system elements in this study such as WTs type 4, PEM electrolyzers and MMC-based HVDC links is presented.
- **Chapter 3**: In this chapter the software package, DlgSILENT PowerFactory 2020 and the various tools used in this study are clearly presented. Then the original PST 16 benchmark system, the starting point of the modelling process, is presented followed by the detailed analysis of all the modifications applied to it to form the system of interest. Finally, a summary of the modified system is provided followed by its initialization verification.
- **Chapter 4**: This chapter contains all the information regarding the optimization algorithm, the MVMO algorithm, utilized to solve the optimization problem of interest and tune the corresponding controllers. Furthermore, in this chapter the different problem definitions are presented in detail considering the objective function, optimization vectors and variables definition and the set of the bounds for each of the variables of interest. Finally, the process that needs to be followed to form the co-simulation environment between Python 3.8 and DlgSILENT PowerFactory 2020 and perform the set of simulations of interest is presented.
- **Chapter 5**: In this chapter all the simulation results considering the system's frequency response under commonly occurred active power imbalances and different scenarios of actively supporting means of SI are presented. According to the presented problem formulations in Chapter 4, the results considering the same active power events are set against to evaluate the efficiency of the optimization strategy under different perspectives.
- **Chapter 6**: This final chapter contains the conclusions of the current study, answers to the formulated research questions and recommendations for future research on the same field.

2 Theoretical background

This chapter is a condensed version of the main fields of interest of this project. In the first part, the role of frequency in power systems is presented followed by the regulations and the key performance indicators used to evaluate the system's response to commonly occurred active power imbalances. At the second part of this chapter the fundamental concepts of the new technologies integrated into the original system such as MMC-based HVDC interconnection links, PEM electrolyzers and WTs are briefly explained.

2.1. Frequency in power systems

2.1.1. The importance of frequency in power systems

The main target of a power system is to continuously supply the demand with the required amount of power. To achieve this, the generated power has to sufficiently cover the consumption and the various system losses at every instant. Electrical utility frequency is the global system variable in which every imbalance in the equilibrium between supply and demand is reflected and for normal operation has to be maintained close to its nominal value of 50Hz. To preserve it at these levels, TSOs apply various balancing strategies so that the power equilibrium in each synchronous area is not perturbed as denoted in Equation 2.1. If the latter one is not achieved, frequency drops in case of lack of sufficient generation and rises when an excess amount of generated active power is available in the network [24] [51].

$$\sum P_{generated} = \sum P_{load} + \sum P_{losses} \quad \text{Equation 2.1}$$

Typically, in power systems under normal operation frequency varies close to its nominal value and tends to deviate from it in occurrence of a significant active power imbalance. If the various control strategies applied by TSOs are unable to maintain the frequency within acceptable limits the system becomes unstable. Generally, frequency instabilities are strongly associated with poor inertial response and thus low inertia, inadequate support from elements participating in the PFC, lack of optimal coordination of control actions, protection limitations and insufficient number of available reserves. In case of extensive frequency excursions various protection devices are triggered to isolate important equipment and lead to cascading outages or even blackout events.

Various events during the past confirm the importance of maintaining the frequency within acceptable limits. In 2003, a loss of two 380kV transmission lines interconnecting Italy and Switzerland due to a storm led to overloading and tripping of tie-lines between Italy and France. The Italian system faced a significant loss of

imported power, being separated from the central European (CE) one, that led the frequency to drop at high rates and finally a blackout was not avoided [52]. In 2006, the CE system faced another significant event, when a planned disconnection of a line in Germany has not been correctly evaluated and communicated to other TSOs leading to lines overloading, cascading line tripping and a split of the CE system into 3 islands of different frequencies [53]. In 2015, in Turkey a similar event took place when an important system corridor supplying the western part with power generated in the eastern part of Turkey was disconnected due to maintenance. The parallel interconnection lines were under high stress and one of them finally tripped leading to a system split. The western part faced a significant frequency drop whereas in the eastern part the frequency increased at a rate of 1.6Hz/s. Cascading outages led to a blackout which was not spread in the CE system [54]. In January 2019, the CE system faced the largest frequency deviation since 2006 equal to 49.8Hz. The reason behind it was the simultaneous occurrence of a technical issue due to a frozen measurement in the tie lines between Germany and Austria and a deterministic frequency deviation during the transition to the evening peak load in the system [55]. As it is clear, the impact of frequency instabilities can critically affect the system's secure and reliable operation.

2.1.2. Frequency operational regulations and key performance indicators

To reach the objective of frequency stability, TSOs around the world have set various regulations considering the operational limits and defense and restoration plans to deal with possible events. Hence, the European Commission and the European Network of Transmission System Operators for Electricity (ENTSO-E) have cooperated to establish rules for the European systems. According to [56], the nominal system frequency is set at 50Hz and the normal operational frequency range may vary from 49.5Hz to 50.5Hz. If now the frequency drops below 47.5Hz or rise above 51.5Hz, the system is expected to collapse, and restoration plan needs to be activated. The aim of TSOs is to preserve the frequency within the normal operational range of $\pm 500\text{mHz}$ and to avoid maximum instantaneous frequency deviations larger than $\pm 800\text{mHz}$ and maintain steady state deviations within $\pm 200\text{mHz}$ [56] [57].

To arrive to this goal, defense plans developed, define the operation of frequency containment reserves (FCRs), frequency restoration reserves (FRRs) and replacement reserves (RRs) and set the rules for cooperation among TSOs, DSOs and significant grid users and activation of UFLS and disconnection of generating units when there is no alternative solution [56] [57]. In more detail, when an underfrequency event occurs, FCRs should be enabled when the deviation is larger than 10mHz and provide 50% of their full capacity for frequency support within 15s and their full bid within 30s for deviations above 200mHz [58]. System elements, able to provide FFS have to participate in the frequency containment, based on their technical limitations such as rated capacity, maximum supporting time, overloading capability, RoCof withstand capability. Neighboring systems and TSOs should also support the affected area as long as their operational security is not under threat. As a last resort, UFLS schemes can be activated under specific conditions. In the CE system, automatic UFLS schemes are activated at frequency ranges between 48Hz and 49Hz reaching a maximum level of 45% of total national load allowed to be disconnected. Finally, in case of frequency drops below 47.5Hz system collapse can be hardly avoided [56] [57].

Apart from the rules and plans developed, TSOs have set grid code requirements for all the generating units, demand facilities and HVDC interconnections connected at transmission levels to avoid unexpected disconnections able impose further perturbations in the active power balance. Thus, generating units should remain connected for an unlimited amount of time in frequency ranges of 49Hz-51Hz, for at least 30min in for frequency ranges of 47.5Hz-48Hz and 51Hz-51.5Hz and for a larger than 30min period in the frequency range of 48.5Hz-49Hz. Out of these regions or at RoCofs beyond their withstand capabilities, power generating units are allowed to disconnect from their point of connection for protection reasons [56] [57] [59]. Finally, HVDC facilities and interconnectors are expected to remain connected for an unlimited amount of time for frequency ranges between 49Hz-51Hz and for at least 60s for ranges of 47Hz-47.5Hz [60].

The response of a system following an active power imbalance can be evaluated using some key performance indicators (KPIs). Initially, when performing frequency stability studies, a list of the most frequent contingencies in the system should be specified. Then the frequency stability margin and the effectiveness of the designed control strategy is validated against the most severe of them. Additionally, the system size, structure and initial operating state can severely affect the system's response. Finally, the evaluation of the system's frequency stability margins under an event lies on specific KPIs: The maximum instantaneous frequency deviation during transient period (frequency nadir), the steady state frequency deviation, the rate of change of frequency (RoCof) and the time required to stabilize and restore [56] [61] [62].

2.2. Power electronics in power systems

2.2.1. The role of PEIs and the VSC

As explained in Chapter 1 power systems nowadays are transforming to PEs dominated systems to facilitate the interconnection of RES and new technologies such as HVDC links, ESS and responsive demand units at various voltage levels. The use of power electronic converters (PECs) assures the smooth power conversion process by controlling the power flow through different variables such as the voltage, the frequency and the number of phases and thus modifying the input signals according to the output requirements [10] [63]. This is achieved by controlling the operation of switches, the heart of PECs, in a coordinated way. The energy conversion process may include conversion from DC or AC input to DC or AC output with constant or adjustable voltage magnitudes and frequency and transformation from single to three phase system and vice versa [64]. The evolution of PECs is strongly correlated with the development and the characteristics of semiconductor switching elements such as controllability, voltage blocking capability, voltage drop across the switch, losses and their ability to operate at different frequencies. Hence, depending on the switches utilized different PECs and controls have been proposed [63] [64].

Nowadays, VSCs constitute the most attractive option due to their control features providing the ability to deal with the complex requirements of modern power systems. In fact, they are used in various applications such as HVDC transmission, integration of RES into the grid and also to connect significant demand facilities [48] [65] [66]. VSCs are built from IGBT switching elements whose conduction state is externally controlled through pulses on their gates. Additionally, they have large DC capacitors to preserve the DC voltage constant at a specific polarity, enabling the bidirectional power flow by just reversing the current direction. Due to their

inherent turn-off capability, these devices exhibit an independent from the AC network commutation process and thus they are called self-commutated converters. Their increased controllability enables the fast control of their power output through the control of the current waveform in terms of magnitude and frequency. This can be achieved through pulse width modulation (PWM) techniques applied at the gates of the IGBTs. Finally, as self-commutated devices, they offer connection to weak, highly meshed or even passive networks forming the network's AC voltage and frequency [67] [68] [69].

The simplest three phase VSC is the 2-level VSC that consist of a six-pulse bridge with IGBTs, antiparallel diodes and DC smoothing capacitors and it is characterized by its simple design. However, it exhibits extensive switching losses and significant harmonic distortion as it can only produce 2 voltage levels at its output and not a perfect sinusoidal waveform [66][68]. To get rid of these problems, the modular multilevel VSC (MMC) has been developed. The 3 phase MMC consists of 3 legs of 2 arms, each of which has N series submodules (SMs) and can produce (N+1) voltage levels, as observed in Figure 2.1. A SM has either an IGBT half bridge topology or an IGBT full bridge topology with the required antiparallel diodes and a parallel capacitor. Each SM can be independently controlled through PWM modulation and thus the MMC can produce an almost perfect sinusoidal waveform. This means that the harmonic content induced into the grid can be significantly reduced through the increase of the number of SMs N. Its design allows the utilization of a lower switching frequency leading to effectively reduced losses. Finally, the modular form of the MMC constitutes its design easily scalable so that it can be used in high voltage and power applications [69] [70].

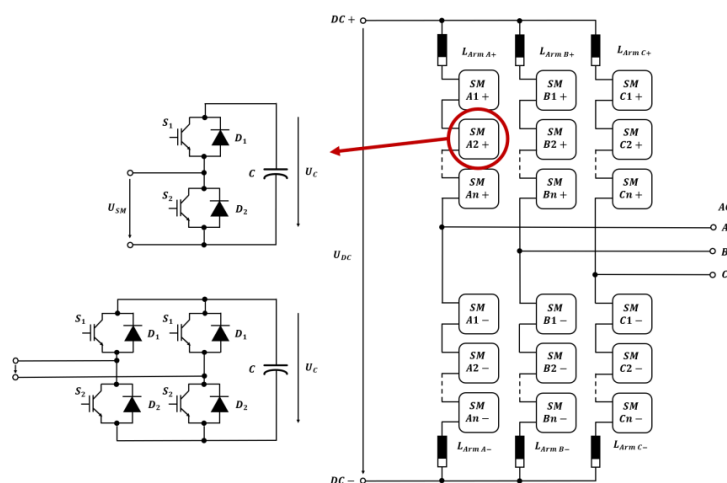


Figure 2.1: Modular Multilevel Converter (MMC) schematic diagram [71].

2.2.2. Modelling of the MMC

In literature different models embodying the behavior of the VSC and thus the MMC have been proposed [71] [72]. The accuracy of the model required, and the time frame of interest determine the suitability of a model for a specific study case. For dynamic stability studies of interest, a simplified model, the average value model (AVM) type 6 can be utilized to represent the MMC as explained in [72] [73]. In this type of model, the switching actions of the IGBTs and the diodes representation are neglected and thus the computational requirements of the model effectively decrease, and larger simulation time steps can be utilized.

The main assumptions of the AVM type 6 model are summarized below:

- The output of the MMC is perfectly sinusoidal and thus no harmonic distortion exists.

- The AC and DC sides of the MMC are modelled as controlled voltage and current sources, respectively.
- The internal variables of the MMC are perfectly controlled and thus the voltages across the capacitors of each SM are balanced and the 2nd harmonic circulating currents are suppressed.
- The total capacitance of the submodules of the MMC is represented as an equivalent capacitance on the DC side of the converter.

According to Figure 2.1 the following set of equations (Equation 2.2 to Equation 2.6) describe the AC side of the MMC [72][74] [75]:

$$U_{upperj} = U_{upperj}^{SM} - L_{arm} \frac{di_{upperj}}{dt} \quad \text{Equation 2.2}$$

$$U_{lowerj} = U_{lowerj}^{SM} - L_{arm} \frac{di_{lowerj}}{dt} \quad \text{Equation 2.3}$$

$$U_{upperj}^{SM} = \sum_{k=1}^N S_{upperjk} U_{C_{upperjk}} \quad \text{Equation 2.4}$$

$$U_{lowerj}^{SM} = \sum_{k=1}^N S_{lowerjk} U_{C_{lowerjk}} \quad \text{Equation 2.5}$$

$$U_j = -U_{upperj} + \frac{V_{dc}}{2} = +U_{lowerj} - \frac{V_{dc}}{2} \quad \text{Equation 2.6}$$

Where U_j is the voltage at each phase of the AC network and $j=A,B,C$, U_{upperj} and U_{lowerj} are the total arm voltages per phase. U_{upperj}^{SM} and U_{lowerj}^{SM} are the total voltages of all the SMs on the arms of each phase as a function of the active capacitors defined by the binary function S and the capacitor voltage U_c of the arms of each phase. The arm current i_{upperj} and i_{lowerj} of each phase can be calculated with respect to the AC current of each phase I_j and the DC current I_{DC} through Equation 2.7 and Equation 2.8 considering that the I_{zj} representing the circulating currents of the 2nd harmonic are assumed to be equal to 0.

$$i_{upperj} = -\frac{I_j}{2} + \frac{I_{DC}}{3} + I_{zj} \quad \text{Equation 2.7}$$

$$i_{lowerj} = +\frac{I_j}{2} + \frac{I_{DC}}{3} + I_{zj} \quad \text{Equation 2.8}$$

Finally, we can conclude to the following set of equations (Equation 2.9 to Equation 2.12) :

$$U_j = \frac{L_{arm}}{2} \frac{dI_j}{dt} + e_j \quad \text{Equation 2.9}$$

$$e_j = \frac{u_{lowerj}^{SM} - u_{upperj}^{SM}}{2} \quad \text{Equation 2.10}$$

$$U_{upperj} + U_{lowerj} = U_{DC} \quad \text{Equation 2.11}$$

$$e_j = U_{refj} \frac{V_{DC}}{2} \quad \text{Equation 2.12}$$

It can be also assumed that each phase has a constant number of SMs and thus the MMC output voltage e_j is considered as in the classic VSC representation as a single voltage source denoted by Equation 2.11.

The DC side of the MMC is represented by a current source determined through equation, Equation 2.13 and Equation 2.14, assuming preserved power balance and an equivalent capacitance of the SM's capacitances determined by Equation 2.15.

$$U_{DC} I_{DC} = \sum_j e_j I_j \quad \text{Equation 2.13}$$

$$I_{DC} = \frac{1}{2} \sum_j U_{refj} I_j \quad \text{Equation 2.14}$$

$$C_{eq} = \frac{6C}{N} \quad \text{Equation 2.15}$$

An inductance equal to $L_{armDC} = (2/3)L_{arm}$ may be also added on the DC side for accuracy reasons [73]. The complete equivalent circuit of the MMC based on AVM type 6 can be observed in Figure 2.2.

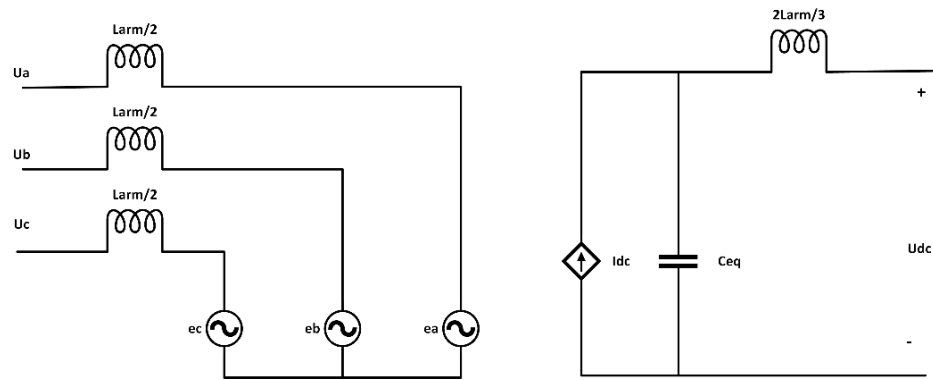


Figure 2.2: MMC equivalent circuit (AVM type 6) [48].

2.2.3. Operation and control of the MMC

As the MMC on the AC side is modelled as a voltage source connected via a phase reactor and a transformer to the network, the amount and direction of the power passing through it can be controlled according to Figure 2.3. In fact, if the AC voltage at the CCP (V_{ac}) is considered as reference, the voltage of the MMC (V_{vsc}) determines the output of the MMC according to Equation 2.16 and Equation 2.17 [63] [69].

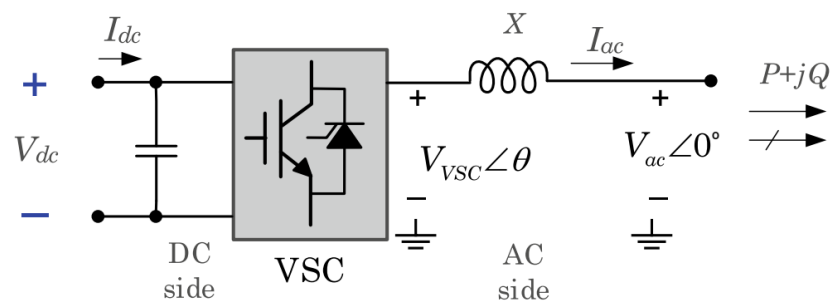


Figure 2.3: MMC steady state schematic diagram [63].

$$P = \frac{|V_{AC}| |V_{VSC}|}{X} \sin \theta \quad \text{Equation 2.16}$$

$$Q = \frac{|V_{AC}| |V_{VSC}| \cos \theta - |V_{AC}|^2}{X} \quad \text{Equation 2.17}$$

Where angle θ is the angular difference of the angle of the AC voltage at the CCP and the voltage phase angle of the MMC output and X is the total reactance between the MMC and the CCP.

The MMC design as it is based on the IGBT technology, offers operation of the converter in four quadrants meaning that it enables bidirectional power flow. The operating mode of the converter can be found via the 4-Quadrant PQ circle diagram shown in Figure 2.4. Thus, depending on the point of operation it can work either as an inverter or a rectifier and can either inject or absorb reactive power from the AC network [66].

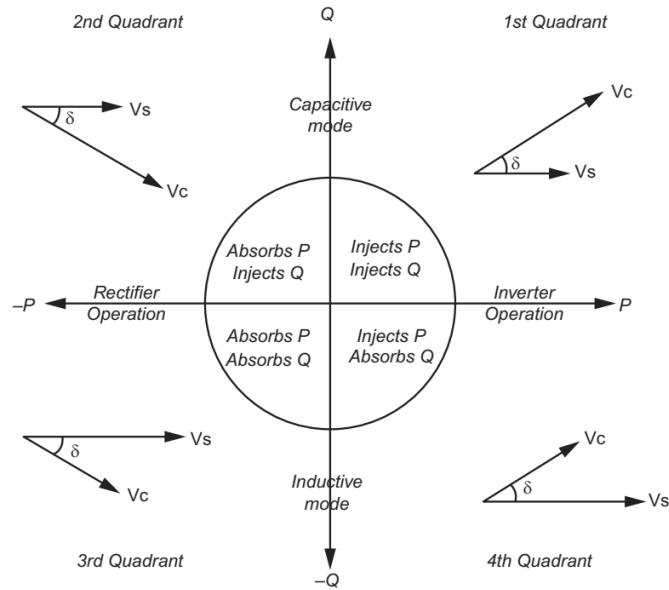


Figure 2.4: 4-Quadrant P-Q circle diagram of VSC [66].

The operating principle of the MMC highlights the importance of creating a suitable voltage waveform at its output. The latter can be facilitated through the control of the IGBTs with an optimum pattern. The most prominent technique to do so, is the pulse width modulation (PWM), in which the firing pulses for the switches are generated with the aid of a reference signal at the desirable grid frequency (modulation frequency) and a carrier signal that mainly has a triangular form at the converter's switching frequency (f_s) and at a constant magnitude. Having determined the switching pattern, the output waveform is characterized by a fundamental frequency component and harmonics, which in case of MMC can be effectively neglected [69].

For the calculation of the output voltage of the MMC converter Equation 2.12 can be used. As it is clear, it depends on the PWM modulation index (M_i) observed in Equation 2.18 and Equation 2.19, which is the fraction among the maximum of the reference signal and the maximum of the carrier signal, the modulation frequency (f_m) provided by the reference signal and the angle θ [66].

$$e_j = V_{VSC} = \frac{1}{2} M_i U_{DC} \sin(2\pi f_m t + \theta) \quad \text{Equation 2.18}$$

$$M_i = \frac{V_{m_peak}}{V_{tri_peak}} \quad \text{Equation 2.19}$$

The last step to control the output is to create the reference signal for the PWM modulation. Various control methodologies have been developed to generate this signal as explained in [69]. Among them the current-vector control strategy is most frequently used for grid-following applications as it offers independent power control. In this method, the control of the converter is achieved through the control of the current in the d-q frame. Initially, voltage and current measurements at the AC side of the converter are measured and transformed to d-q. The fast-inner current control loop is then responsible to modify the measured currents

with respect to setpoints and generate the voltage reference in the d-q frame for the PWM modulation. Phase lock loop (PLL) which is able to align the d axis with the grid voltage vector is utilized to achieve independent active and reactive power control via the direct (i_d) and quadrature (i_q) component of the current respectively. The current setpoints i_{d_ref} and i_{q_ref} are generated in a slower outer control loop and provided to the inner current control loop. In fact, the i_{d_ref} is generated based on either a predefined active power setpoint P_{ref} , a DC voltage setpoint V_{dcref} or the frequency in a P/Vdc controller and the i_{q_ref} is generated with respect to a reactive power reference point Q_{ref} or an AC voltage reference V_{acref} . Finally, the generated voltage references are transferred back to the ABC frame for the PWM technique. The transformation from ABC to d-q frame and vice versa, is achieved through the Clarke-Park transformation also known as d-q-0 transformation. Further details about the d-q-0 transformation can be found in the Appendix A.

2.3. Fundamental concepts of HVDC technology

2.3.1. The advantages of HVDC technology and its applications

In the past 50 years HVDC technology has gained great attention and has been extensively applied in power systems [66]. In fact, it has been used to transfer large amount power remotely, asynchronously interconnect systems, enable power transfer through underground/undersea cables and integrate remotely installed RES to the grid such as offshore WTs [76] [77]. The extensive utilization of this technology lies on its advantages compared to the HVAC one, summarized below [66] [76]:

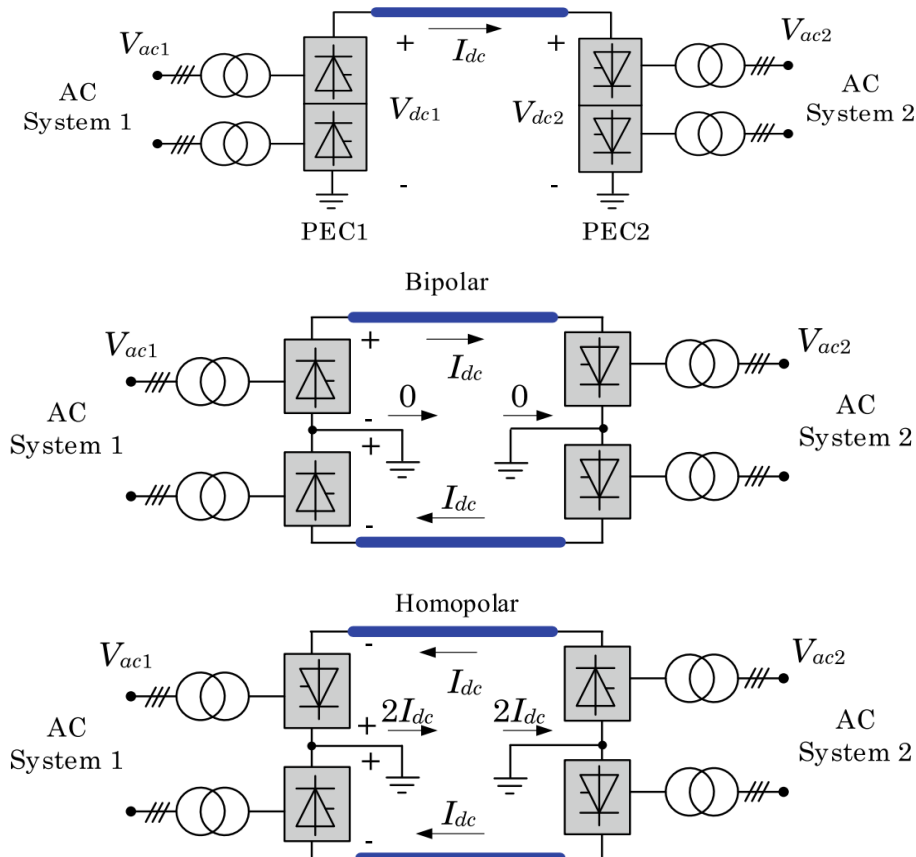
- For a given power level, the capital cost of HVDC systems is much less compared to HVAC systems
- For a given power level, the operational cost of HVDC systems is lower compared to HVAC as:
 - DC systems use 2 conductors instead of 3 in AC
 - Skin effect is absent in DC systems
 - Corona effect is less significant
 - Charging of the lines/cables is not required to enable power transfer
 - No technical limitations exist for power transfer over long distances
- Reactive power compensation is not required in DC systems
- Back-to-back HVDC interconnection offers asynchronous system interconnection.
- HVDC links exhibit high controllability and fast dynamic response due to their PEIs especially when VSC or MMC technology is utilized. Thus, they can offer ancillary services to the grid and enhance PSS.
- HVDC systems exhibit much higher reliability levels compared to HVAC systems
- HVDC technology enables also multi-terminal interconnections

2.3.2. MMC based HVDC power transmission overview

The advantages of the HVDC technology led to the evolution and the continuous development of the HVDC transmission. The heart of this type of interconnection links are the converter stations required to facilitate the power conversion from AC to DC and vice versa. Initially, HVDC links utilized line commutated thyristor based current source converters (CSCs) which are partially controllable and can handle large amount of power. However, the emergence of IGBTs and thus VSCs further enhanced the capabilities of the links increasing the

interest on their integration to power systems [69]. VSC-based HVDC systems can be met at various different configurations depending on the application [63] [67] [77]:

- **Monopolar configuration** (Figure 2.5a): In this type of configurations 2 converter stations are connected through a single DC line mainly in negative polarity due to the decreased corona losses and is mainly utilized in undersea cables. In this configuration, a ground, sea or metallic return path is considered depending on the location of installation.
- **Bipolar configuration** (Figure 2.5b): is the most common type of configuration in HVDC transmission. It interconnects the converter stations via 2 conductors of opposite polarity. Both conductors have the same rating and thus no return current is flown through the ground under normal conditions. The conductors can be independently operated allowing power transfer at half capacity if a fault in one of them occurs.
- **Homopolar configuration** (Figure 2.5c): consists of two converters connected with 2 DC poles of the same polarity (usually negative). It can also operate with a single conductor at the half power transfer capability. However, because of their high cost and ground return usually utilized, it is rarely used.
- **Multiterminal configuration** (Figure 2.5d): can interconnect more than 2 independently controlled converter stations connected either in parallel or series and thus interconnect multiple systems. It has been enabled by the constant DC voltage polarity of the VSCs.
- **Back-to-back configuration** (Figure 2.5e): In this configuration the converters are installed at the same location connected through a small DC link. It is mainly used to interconnect asynchronous systems or PV systems and ESS with the local grid.



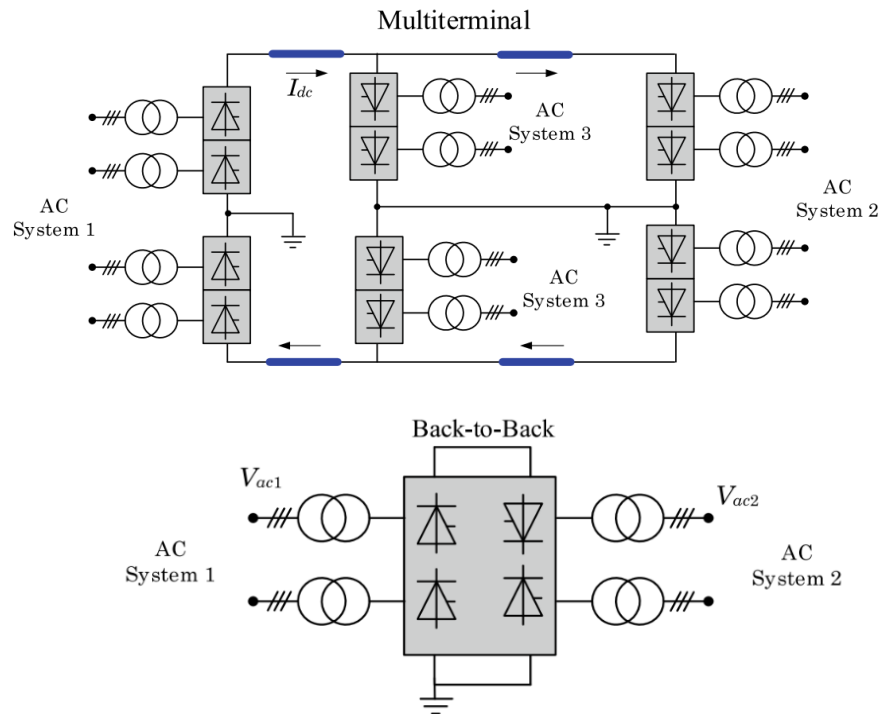


Figure 2.5: VSC-HVDC configurations: a) Monopolar b) Bipolar c) Homopolar d) Multiterminal e) Back to back [63].

A typical MMC-HVDC link consists of 2 MMC stations interconnected by DC cables, phase reactors and the transformers that interconnect them with the AC networks as observed in Figure 2.6 [78]. Since MMC are used, no filtering is required at the output as their waveform is almost perfectly sinusoidal [68].

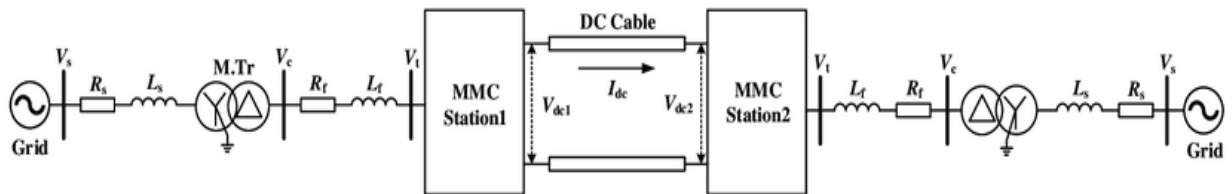


Figure 2.6: MMC-based HVDC interconnection link representation [78].

As far as the control of the power output of the converters of the HVDC link is concerned, it is performed independently in both converter stations without any means of communication as explained in section 2.2. Active power injection can be determined either based on an active power setpoint (P_{ref}), a DC voltage setpoint ($V_{dc_{ref}}$) or the frequency (f_n) compared to the corresponding measured values, whereas reactive power injection can be determined with respect to a reactive power setpoint (Q_{ref}) or an AC voltage setpoint ($V_{ac_{ref}}$) compared to the real operating values. Furthermore, for the control of active power one of the PECs (usually the one connected to the strongest network) must be set on Vdc mode to secure the balance on the DC link, whereas the other converter to be set in P mode. Considering the reactive power regulation both converters can be independently set in either control modes [79]. Apart from the basic control blocks utilized, supplementary controllers can be also used, able to modify the setpoints of the outer control loops, with respect to specific inputs to offer additional ancillary services when required [71]. A typical overview of the control loop of each of the converters based on [72] can be observed in Figure 2.7.

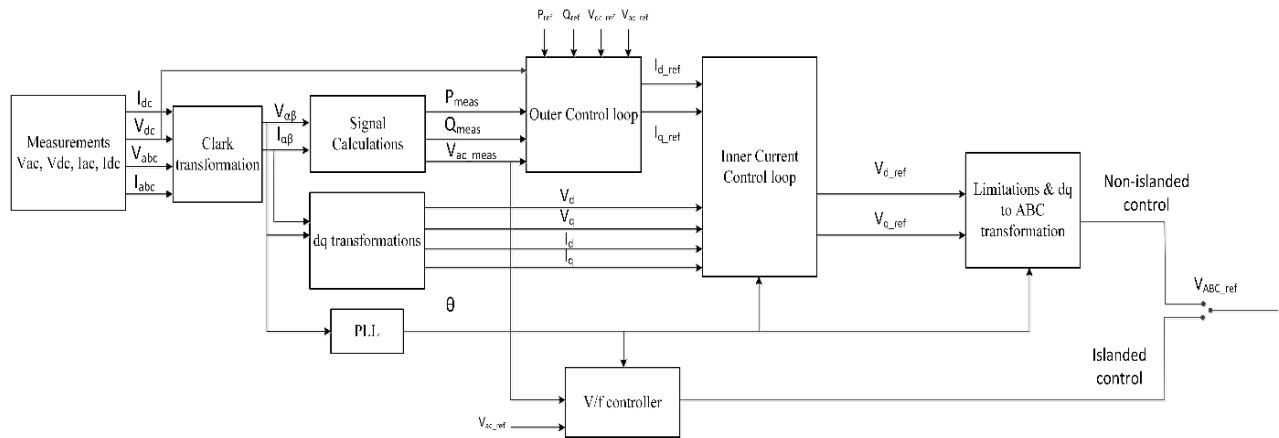


Figure 2.7: MMC station control loop based on current-vector control strategy [48].

2.4. PEM electrolyzers

2.4.1. Fundamentals of PEM electrolysis

Power-to-gas applications nowadays have gained great attention with respect to the energy transition and the goal to reduce CO₂ emissions. In fact, hydrogen is an efficient energy carrier able to be utilized in many applications in the industrial, transportation and electricity sectors [44]. According to [80], it is expected that by 2050 hydrogen-based facilities will overcome the 18% of the total energy consumption. Hydrogen can be produced by both renewable and non-renewable sources through various methods as observed in Figure 2.8. Among them water electrolysis based on the excess power coming from RES is one of the most sustainable, efficient and promising solutions as it utilizes the energy surplus to generate pure hydrogen (H₂) without producing any harmful byproducts [44] [81]. This energy transformation from electrons to hydrogen molecules takes place in electrolyzers and is characterized by a set of reactions, Equation 2.20 and Equation 2.21 [81].

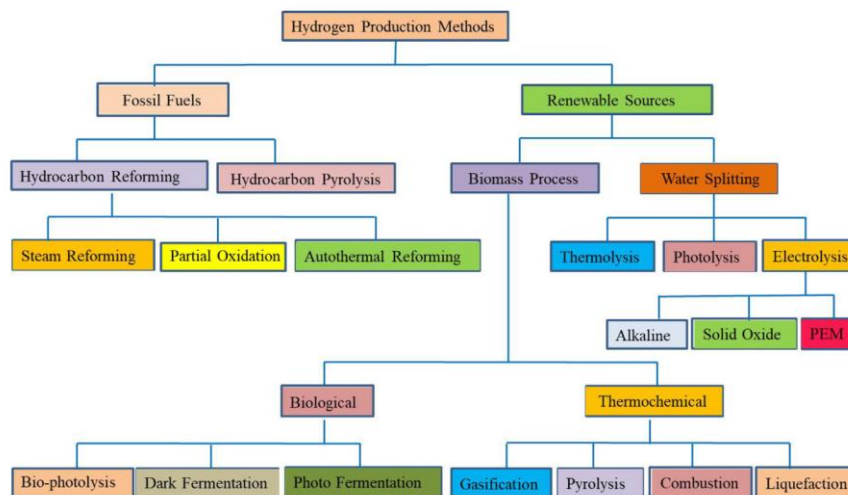


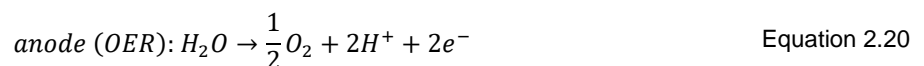
Figure 2.8: Main hydrogen production methods [81].

Water electrolysis methods can be further classified based on the type of electrolyte, the applied operating conditions and the ionic agents (OH⁻, H⁺, O₂) into five types [81] [82]:

- Alkaline water electrolysis (AWE)
- Solid oxide electrolysis (SOE)
- Microbial electrolysis cell (MEC)
- Anion exchange membrane (AEM) electrolysis
- Proton exchange membrane (PEM) electrolysis

Among them AWE is the most well established and commercially used method reaching efficiencies of 70%-80% in the conversion process. However, it is characterized by low current densities, low purity levels and low-pressure conditions, limiting its extensive application [81]. SOE can offer even higher efficiencies above 90% and operation under high pressure conditions, but still it is not commercially available, and it is characterized by large system design and limited lifetime. AEM and MEC electrolysis methods are still under development and have not been considered yet as commercialized solutions [81] [82]. On the contrary, PEM electrolysis is a solution of high potential as it is characterized by high current densities, fast dynamic response, high purity (99.99%) and efficiency levels (80%-90%) and compact design. The main drawbacks of this technology are its high cost and the acidic environment of operation it creates [44] [81] [82].

In more detail, PEM electrolyzers consist of 2 electrodes, the anode and cathode, separated by the electrolyte and catalyst layers and water electrolysis is performed in two stages the oxygen evolution reaction (OER) and the hydrogen evolution reaction (HER). Initially, water is pumped to the anode and power is used to split the water molecule into O₂, protons (H⁺) and electrons (e⁻) (OER). Protons then pass through a highly conducting membrane called proton exchange membrane to the cathode side. Electrons produced at the first stage are obtained from the cathode by an external electrical circuit which provide the driving force for the second stage of the electrolysis (HER) at the cathode, where the protons and the electrons recombine and produce the H₂ molecule [82]. A schematic diagram of a PEM electrolyzer can be observed in Figure 2.9 and the OER and HER reactions in Equation 2.20 and Equation 2.21 respectively [44] [82].



From the electrical point of view, the advantages of PEM electrolysis are encountered in its ability to produce H₂ of high purity in high efficiencies offering long term energy storage in the form of molecules, but also its capability to offer supportive interactions with the grid because of its very fast dynamic response [44]. In fact, PEM electrolyzers can offer ancillary services to the network such as active power support at fast rates. They can also mitigate fluctuations generated by the intermittent RES and can also be combined with fuel cells to formulate H₂ power plants and perform bidirectional energy transformation [44] [82]. Generally the main features considering the interaction of PEM electrolyzers with the grid are: very fast ramp up and ramp down of their consumption, capability to shut down very fast, operation for sustained periods of time in partial load conditions [44] [83]. For this reason, it is expected to be the main standard by 2030 [44] and its applicability

and scalability has been investigated in many projects in Germany [84], Austria [85] and the Netherlands [86], whereas the provision of ancillary services from PEM electrolyzers has been investigated in [20] [44] [83][87].

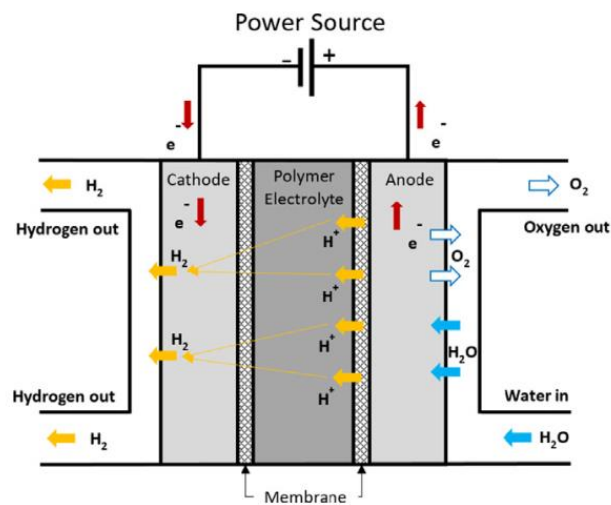


Figure 2.9: Schematic diagram of PEM electrolyzer [44].

2.4.2. Modelling and control of PEM electrolyzers for frequency stability studies

In recent years, important research has been performed to create accurate models for PEM electrolyzers. The models differ based on the variables and processes considered within the electrolyzer operation. Voltages, currents, temperature, pressure and entropy are some of the parameters that may be considered for electrical and thermal models. However, model simplifications are necessary to reduce the complexity and the computational needs [87]. Also, it is critical to be mentioned that the lack of models of large PEM electrolyzer units constitute their representation challenging. For this reason, most studies utilize the parallel connection of smaller, modular and compact units to formulate larger stacks [82] [83] [87].

From the electrical point of view, the complete representation of PEM electrolyzer consist of 3 parts as observed in Figure 2.10 [63].

- The electrolysis stack
- The supporting elements for the operation of the stack such as the circulation and feedwater pumped, also called Balance of Plant (BoP)
- The electrical conversion system consisting of PEC and transformer

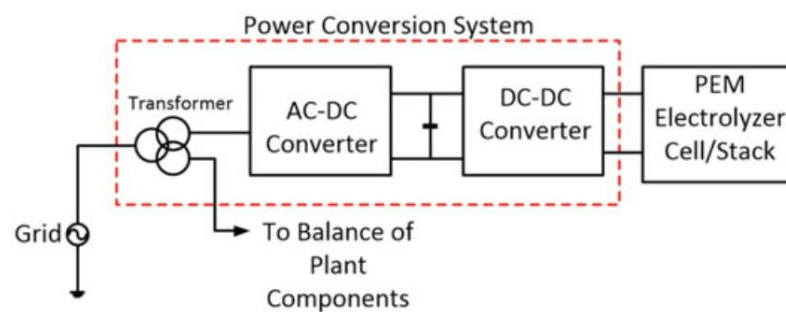


Figure 2.10: PEM electrolyzer representation [63].

Starting from the conversion system, as the electrolyzer operates at DC, an AC/DC inverter should be considered followed by a buck converter able to reduce the DC voltage at the required input levels. On the AC side of the inverter a transformer is used to offer connection to the CCP. The BoP can be considered as a constant load consumption as no significant variations in the demand of the supporting equipment are expected. Regarding the electrolysis stack, an equivalent circuit model can be utilized composed by a DC voltage source (open-circuit voltage) that needs to be overcome to enable the water electrolysis reaction, the various internal losses of the stack represented by the corresponding series resistances (activation resistance R_{act} , mass transfer resistance R_{mass} , ohmic losses R_{ohm}) and a capacitor that represents the double layer capacitance between the electrolyzer layers. A schematic diagram of the equivalent electrical circuit of the PEM electrolyzer can be observed in Figure 2.11 [82] [87].

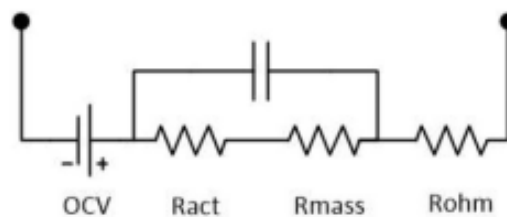


Figure 2.11: Equivalent electrical circuit of electrolysis stack [82].

For PSS studies, the most important feature of PEM electrolyzers is their fast interaction with the grid because of their rapid ramp-up and ramp-down rates of their consumption [44]. As a result, a simplified yet accurate representation can be considered consisting only of a general load consumption accompanied by its dynamic and control models connected to the local grid through a transformer [63] [83]. Dynamics of the PEM electrolyzers can be effectively modelled by a linear ramp rate limiter able to simulate the upward and downward ramping rates of the consumption of the PEM electrolyzer depending on their installed capacity. The dynamic model of the PEM electrolyzer can be enhanced also by a frequency controller so that the consumption of the stack is able to change automatically with respect to frequency deviations [83].

However, it is crucial to be mentioned that the lack of information regarding the dynamic response of large PEM electrolyzer to step changes constitutes the selection of accurate ramp rates more than challenging. As explained in [83] [87], validation of the model of a 1MW PEM electrolyzer pilot model installed in the Netherlands has been performed. Based on that pilot project, the 1 MW electrolyzers exhibits linear response to active power setpoint step changes at an average rate of 0.5MW/s and thus 0.5pu/s [87]. As a result, it is expected that larger units that constitute of parallel connection of multiple units may have the similar response. Furthermore, in [88], a 40kW PEM electrolyzer unit is studied regarding its dynamic response to power consumption step changes. This unit has shown a nonlinear dynamic response slightly influenced by the size of the setpoint change. When a step change equal to 50% of its consumption (20kW) is applied a ramp rate of 0.1MW/s or 2.5pu/s is achieved. Based on the latter findings and without neglecting the expected increase in the time response with respect to the installed capacity of a unit, it can be concluded that the ramp rates of PEM electrolyzers are expected to be within the range of 0.5pu/s – 2.5pu/s, providing an indication for the time frames of their expected dynamic response.

2.5. Wind energy systems

2.5.1. Operation overview of wind turbines

WTs are energy systems used for more than a century to utilize the kinetic energy of the wind and convert it to mechanical and then electrical power. Wind is atmospheric air in motion mainly created due to the pressure difference leading wind to blow from high to low pressure areas. This pressure difference depends on the temperature difference among different locations as solar irradiation falls unevenly in the earth surface and solar absorption is not performed at uniform rates. The pressure difference determines the velocity of the wind and thus the amount of kinetic energy stored in the moving air mass. Apart from the velocity, the kinetic energy of the wind depends on the volume and density (ρ) of air and can be expressed by Equation 2.22 [89].

$$KE = \frac{1}{2}mu^2 \quad \text{Equation 2.22}$$

Then, the wind power can be expressed as the time derivative of the kinetic energy of the wind as observed in Equation 2.23, where dm/dt represents the mass rate across a volume A .

$$P = \frac{dKE}{dt} = \frac{1}{2} \frac{dm}{dt} u^2 = \frac{1}{2} \rho A u^3 \quad \text{Equation 2.23}$$

Equation 2.23 gives the available power in the blowing air that can be utilized by various energy systems and has a highly non-linear cubic dependence on the ambient wind speed [89]. However, due to physical limitations originating from fluid mechanical nature of the wind and various other losses only a part of the available power may be utilized from WTs. The amount of mechanical power that can be obtained is calculated with the help of the power coefficient (C_p) (Equation 2.24), which is the ratio of the power extracted divided by the available wind power and has a maximum limit of $C_{pmax}=16/27$ or 59% of the available power. Finally, the amount of the power that can be extracted is calculated through Equation 2.25 [90].

$$C_p = \frac{P_{extracted}}{P_{wind_available}} = 4a(1 - a)^2 \quad \text{Equation 2.24}$$

$$P_m = \frac{1}{2} A \rho C_p U_w^3 = \frac{1}{2} \pi R^2 \rho 4a(1 - a)^2 U_w^3 \quad \text{Equation 2.25}$$

Where a is the induction factor, U_w is the ambient wind speed, A is the normal surface of the rotor, ρ is the air density and R is the rotor radius.

In practice, C_p is different for every WT and depends on the tip speed ratio (λ) and the pitch angle (β). The former one, is the fraction of the velocity of the blade's leading edge divided by the wind speed observed in Equation 2.26 and pitch angle (β) is the angle among the rotational plane and the chord line that connects the leading and the trailing edges of each airfoil of the blade.

$$\lambda = \frac{U_r}{U_w} = \frac{\omega R}{U_w} \quad \text{Equation 2.26}$$

Each WT is accompanied by a set of C_p - λ curves for different pitch angles provided by the manufacturer. It is a non-dimensional characteristic of the rotor with the help of which the mechanical power output of the rotor can be calculated with respect to any combination of rotor speeds (ω) and wind speeds (U_w). For the optimum operation of the WT and the maximum power extraction, λ has to be maintained at a value which maximizes the C_p so that the WT operates at the peak of the curve. However, if the blade is pitched, then the C_p - λ curve differs from the one at 0 pitch angle and has a different MPP smaller than the optimal one. A typical set of C_p - λ curves of a WT for various pitch angles can be observed in Figure 2.12. Furthermore, the operation of a WT depends on whether it has a variable or a constant speed. In case of constant rotor speed, a change in the wind speed away from the rated value will lead to sub-optimal operation and power output below its rated power. For this reason, variable speed WTs are more attractive since they are able to modify their rotational speed according to the ambient wind and achieve operation at the MPP of the C_p - λ curves [90].

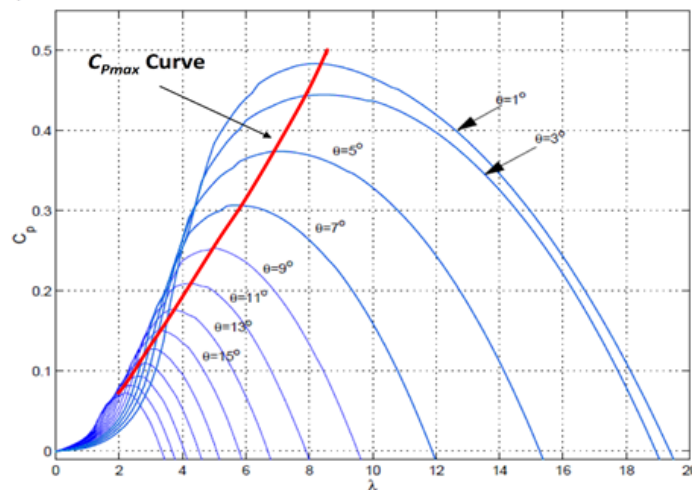


Figure 2.12: Typical set of C_p - λ curves of a WT [91].

Although it is expected that it is desirable to always obtain the maximum power from a WT, in reality the operation of a variable speed WT differs based on the ambient wind speeds and its power curve determine its operation as observed in Figure 2.13. Below the cut-in wind speed (U_{cut-in}) the WT is disconnected from the local grid and either rotates very slowly or it stands still being in idle mode. When the wind speed is equal to that speed, the WT switches on and until the rated wind speed, it operates in the partial load region. In this region the aim is to operate at the MPP of the C_p - λ curve. When the rated wind speed is reached, the WT turns to full load operation, meaning that it operates at its nominal power output and at the maximum load its generator is able to handle. In this region the goal is to maintain the mechanical power output constant to its rated value to avoid overloading of the electrical equipment. Finally, for wind above the cut-off speed, the operation of WT is under danger because of the very high wind speeds and thus it is disconnected again from the grid operating in idle mode [90].

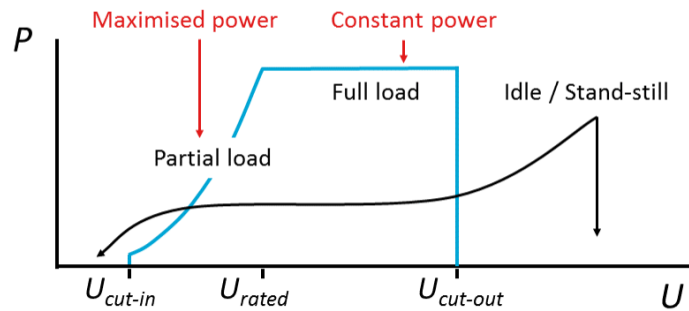


Figure 2.13: Typical power curve of a WT [90].

2.5.2. Wind energy system configurations

Depending on the generator utilized, the operational speed range and the way of interconnection with the grid, WTs can be split mainly into 4 types presented below [92] [93] [94]:

- **Type 1: Fixed speed WTs (Figure 2.14)**

This is the first WT configuration extensively utilized and is characterized by its constant speed. It consists of 3-blade WTs connected to a slow shaft interconnected through gearbox to the high-speed shaft of the generator. In this type, squirrel cage induction generators (SCIGs) are utilized due to their capability to operate at constant speeds and the generator is coupled to the grid via a transformer. Capacitor banks are necessary for reactive power compensation and to enable both the excitation and normal operation of the SCIGs. Also, soft starters are used to limit the magnitude of the large inrush currents during the start-up period. This type of configuration offers a simple, reliable, robust and affordable design without any sophisticated control systems. However, it is characterized inability to track the MPP, lack of power control and extensive reactive power needs. Also, due to its direct coupling to the grid, the variability of the wind speeds spreads to the mechanical and electrical parts of the system inducing mechanical fluctuations and thus stresses to the system and electrical power fluctuations to the grid setting in risk the PSS.

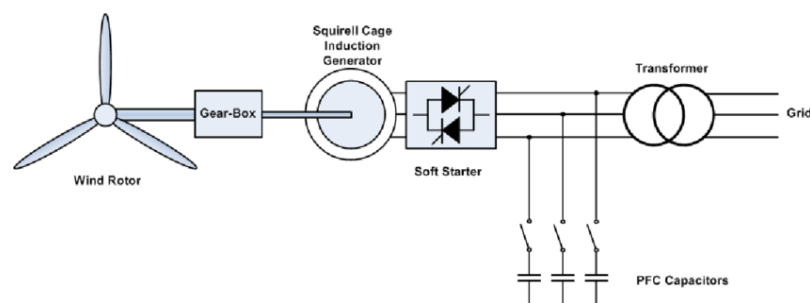


Figure 2.14: Type 1: fixed speed WT configuration [93].

- **Type 2: Partially variable speed WTs (Figure 2.15)**

This configuration is similar to type 1 apart from the fact that the SCIG is replaced by wound rotor induction generator (WRIG). Additionally, the stator of the WRIG is coupled with the grid, whereas the rotor is interconnected via a controlled variable resistance. The size of the resistance can control the energy extracted by the rotor and thus its speed. Thus, a partially variable speed up to 10% is obtained. It has a simple design without slip rings and sophisticated controllers and reduced mechanical stresses due to the improved operating speed range of its rotor. Although improved compared to type 1, its speed range is still limited and depends

on size of the resistance. Finally, it is characterized by poor levels of controllability of active and reactive power and by its extensive transient injections into the electromagnetically coupled grid.

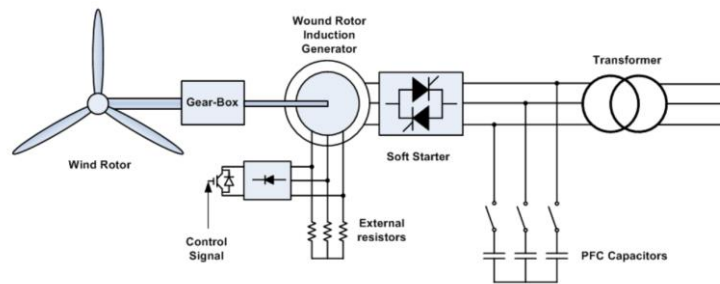


Figure 2.15: Type 2: Partially variable speed WT configuration [93].

- **Type 3: Variable speed – Partial scale power converter WTs (Figure 2.16)**

This type of configuration is a variable speed topology that utilizes doubly fed induction generators (DFIG) and a partial PEC. In fact, the stator of the generator is directly coupled with the system whereas the rotor uses a PEC of reduced capacity. Converter control actions effectively decouple the electrical and mechanical frequencies enabling operation of the rotor at variable speeds. The acceptable operational range varies within $\pm 30\%$ of the synchronous speed according to the size of the PEC. Furthermore, due to the utilization of the converter, smooth integration of the WT to the grid and reactive power compensation can be achieved and thus there is no need for soft starters or capacitor banks. In this type, the WT becomes an actively controllable element as the rotor side converter (RSC) can control the current flows in the rotor and thus the torque and the reactive power applied to the generator, whereas the grid side converter (GSC) can offer DC voltage control and AC side reactive power control. Finally, due to the variable speed, MMP tracking control strategies can be applied and pitch angle control can be used to preserve the output to nominal in case of strong ambient winds. The main disadvantage of this configuration is the utilization of sliprings and gearboxes, elements that are prone to failures and require regular maintenance.

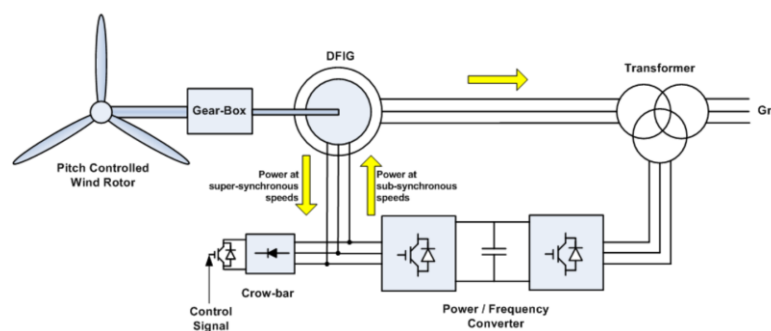


Figure 2.16: Type 3: Variable speed - Partial scale power converter WT configuration [93].

- **Type 4: Full-scale power converter – Variable speed WTs (Figure 2.17)**

In this type of configuration, a full-scale PEC to interconnect the generator with the local grid is utilized. This enables the operation at variable wind speeds and thus MMP tracking control strategy can be implemented. Furthermore, pitch control offers the necessary pitch to vane of the blades to avoid outputs above the rated of the generator. Typically, the generator in this configuration is a permanent magnet synchronous generator (PMSG) fully decoupled from the network due to the full-scale converter. Also, if a generator with increased number of poles and thus low rotational speed is selected, a direct drive train topology

without gearbox can be used, increasing the system's efficiency and reliability. Furthermore, the presence of the PEC enables the independent power control especially when VSCs are utilized enhanced with the control strategy explain in section 2.2. As a result, the WT can offer ancillary services to the grid and FLRT capabilities. Moreover, in this topology no slip rings are required and the PMSG does not need any additional equipment for soft start or compensation as excitation is achieved through a permanent magnet. The main disadvantage of this topology is the high cost of the converter. However, nowadays it is the most attractive option due to its efficiency, controllability and reliability.

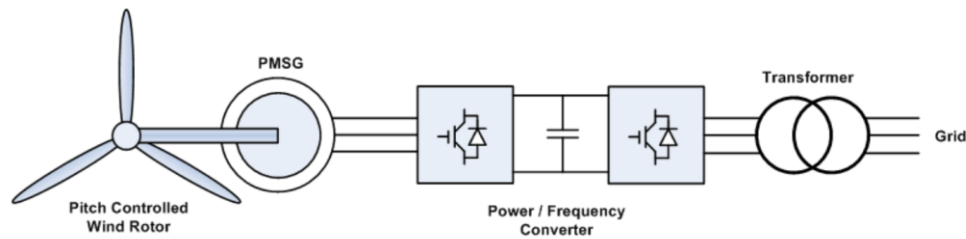


Figure 2.17: Type 4: Full scale power converter - Variable speed WT configuration [93].

2.5.3. WT type 4: advantages, modelling and control

Nowadays the main trend is utilizing WTs with variable speed connected to the grid with full scale fully controllable converter and HVDC transmission for remotely installed elements [95] [96] [97]. The main advantages of this configuration are listed below [95] [96] [97]:

- Maximum flexibility – fully controllable
- Independent active and reactive power control
- Controllable but limited contribution to faults (short-circuit current contribution)
- Electromagnetically decoupled WT and generator from grid-side faults and interactions
- Provision of ancillary services (low voltage ride through (LVRT) capability, reactive power-voltage support, active power-frequency support)
- Reactive power capability curve similar to SGUs
- Direct drive train topology enabled for multipole generators
- Easy maintenance and increased reliability (no gearbox, no sliprings)
- No capacitor banks or reactive power compensation devices and soft starters required

Modelling of a WT type 4 depends on the level of details required for a specific study. Generally, IEC has developed the IEC 61400-27 standard in which a generic model for a WT 4 has been proposed for dynamic stability studies [98] [99]. This model constitutes a simple and modular model of the WT and its controllers to accurately represent the system dynamics following commonly occurred disturbances. The time frame of interest is typically short-term and is valid for systems with at least minor SGUs and not 100% wind share. Also, all different parts of the WT should be considered starting from the aerodynamic block which calculates the mechanical power applied to the WT based on the wind availability and the rotor characteristics. Together with the mechanical block that contains either a single or two mass oscillator, a complete and simple representation of all the mechanically rotating elements (rotor and drive train with or without gearbox and the shafts) of the system is achieved. Then, the generator should be represented by its corresponding dynamic

model for grid stability studies, followed by a back-to-back converter and possibly a transformer allowing smooth interconnection to the grid. The proposed generic model structure of the WT according to the IEC 61400-27 standard can be observed in Figure 2.18 [98] [99].

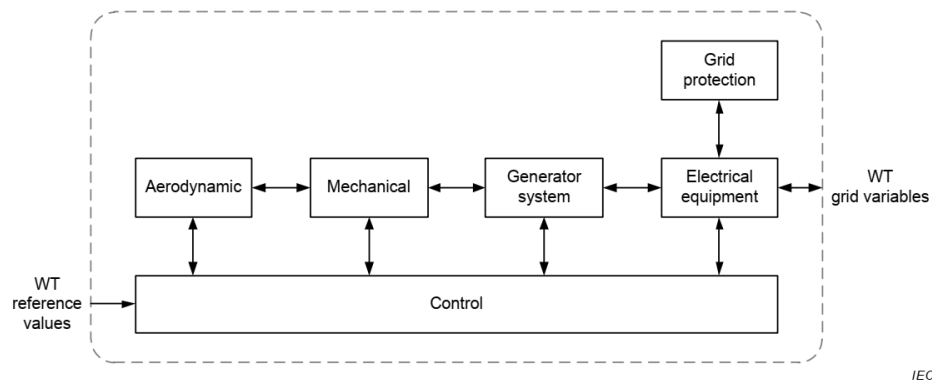


Figure 2.18 : Generic model structure of WT according to IEC 61400-27 [99].

What is also important to be mentioned is that the two converter stations in the WT type 4 configuration have an independent control strategy. In fact, the line side converter (LSC) deals with the interactions between the grid and the WT whereas the generator side or rotor side converter (RSC) deals with the control actions in the WT and its generator as observed in Figure 2.19. In more detail, the RSC is typically a bidirectional VSC controlled using the current vector control strategy and can independently control the power injection when the rotating stator and the d-axis are aligned. The latter is achieved through the control of the rotor speed of the WT with respect to the converter's predefined setpoints enabling operation at any point in the $C_p-\lambda$ curve. Also, reactive power exchange with the generator is handled by the RSC typically with respect to the voltage at the generator's terminal so that it is maintained within the acceptable limits. As far as the LSC is concerned, its control is also facilitated through current vector control. Normally in this converter station, the active power injection/absorption to/from the grid is controlled based on the voltage on the DC link which has to be maintained constant, whereas reactive power injection is either based on the AC voltage at the CCP, the power factor or a reactive power setpoints. Finally, supplementary controllers may be considered in both converter stations able to modify the power flows according to certain inputs so that ancillary services can be provided [89] [97].

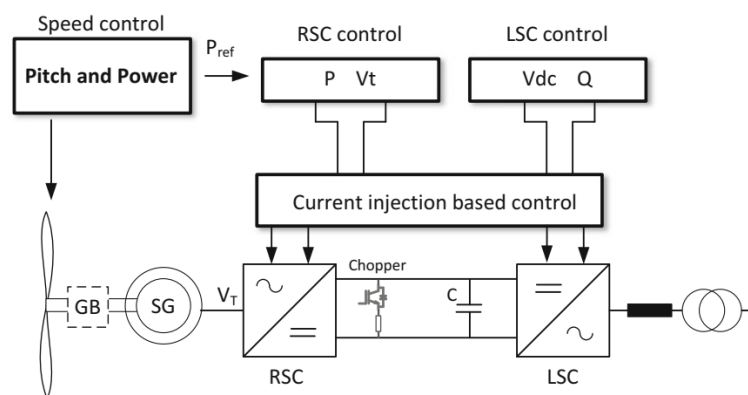


Figure 2.19: WT type 4 control strategy [97]

3

Study Case: FFS in Multi-area Multi-energy Power System

The goal of this chapter is to present in detail the developed case study of a multi-area, multi-energy power system with the provision of FFS from various elements in a coordinated manner. This case study will be used in Chapter 5 for extensive time domain (RMS) simulations to examine the effectiveness of the coordinated control actions against commonly occurred active power imbalances. For the modelling purposes DigSILENT PowerFactory 2020 has been utilized.

This study case has as a starting point the PST 16 benchmark system, a multi-area system developed for dynamic stability studies [100]. The original model has been modified to replace the AC interconnections among areas with the state-of-art MMC-based HVDC links, introduce RES by replacing existing SGUs with fully decoupled WTs type 4 and enhance the demand mix with controllable PEM electrolyzers. The modified system represents a power system of the future with volatile generation and demand mix, low inertia conditions and electromagnetically decoupled areas, suitable for frequency stability studies.

In these new conditions, the frequency stability of the system is expected to be in danger as explained in Chapter 1 if not any further control actions are taken. The high controllability levels of the converter-based elements introduced are accompanied by high potential of ancillary services if the control systems are enhanced to respond to the corresponding phenomena. In fact, MMC-HVDC links can share an imbalance among areas by controlling their power flows, electrolyzers can quickly adapt their consumption according to frequency deviations and fully decoupled WTs type 4 are able to provide support by altering their power output through control actions in their PEIs. To take advantage of these capabilities, the controllers of the introduced elements are modified to respond to active power imbalances-dynamic frequency excursions and provide FFS. The APG control strategy, that is easily applicable to the PEIs of these elements and has shown great potential in frequency regulation, is used to enable controlled in magnitude and rate support according to the system's frequency response. Finally, although these elements can be beneficial with their individual supporting capability, a coordinated tuning is required to avoid possible adverse control actions resulting in inadequate support or over regulation. Hence, the parameters of the participating controllers will be tuned according to the solution of an optimization problem in Python explained in Chapter 4.

The following sections provide an in-depth insight of the models utilized, the modifications applied, and the simulation platforms used to create the study case of interest.

3.1. Dynamic simulations in DigSILENT PowerFactory

This section provides an overview about the operating philosophy of DigSILENT PowerFactory (DPF), its main characteristics and functions used in this project. Detailed information about DPF can be found in [101]. DPF is a computer program created by DigSILENT to represent and analyze power networks in utility, industrial and commercial scale aiming at improved operation and successful planning. It has been extensively used by engineers and academia to perform various studies of phenomena in different time scales such as load flow calculations, short-circuit analysis, contingency analysis, harmonic analysis, modal analysis, power system dynamics and stability and many more. Simplicity of usage and accurate results are the main reasons behind the extensive usage of DPF by institutions, industry, organizations and universities. The main characteristics of DPF that make it friendly for the user are the fact that models developed can be used from different functions in the same project and program, whereas simulations and results can be executed and saved in a single file.

3.1.1. RMS & EMT Simulations

The examination of the dynamic response of a power system is strongly interconnected with the time frame the transient phenomena occur and the level of detail required in each study. For this reason, DPF offers different simulation methods: the RMS function and the electromagnetic transient (EMT) function. RMS function is mainly utilized for the analysis of transient phenomena occurring within millisecond to seconds time frame and the network representation is based on steady-state models. On the other hand, if the aim of the study is to focus on the time frame of microseconds to milliseconds, the EMT function can be utilized, in which detailed dynamic models of network elements should be considered [101]. For PSS studies of interest, the RMS function is adequate as it includes the dynamic response of electromechanical equipment and controllers applied to various elements and thus it is the main function utilized in this study. The main differences considering the RMS and EMT simulation methods in DPF are presented in Table 3.1.

Table 3.1: RMS and EMT simulation differences [72] [101].

DPF Function	Time Frame	Network Element Representation	Machine Equations
RMS	Mid-term to long-term (ms to s)	Algebraic Equations – RMS models $V = \left(R + j\omega L + \frac{1}{j\omega C} \right) I$	Slow dynamics considered (electromechanical, power/frequency control loops, turbine). Stator flux changes instantly.
EMT	Short-term to mid-term (μ s to ms)	Differential Equations – Dynamic models $u(t) = Ri(t) + L \frac{di(t)}{dt} + \frac{1}{C} \int i(t) dt$	Stator flux dynamics and harmonics considered. High-frequency ranges.

3.1.2. Simulation setup

Before any type of RMS simulation is executed, a series of actions needs to be performed to provide the necessary inputs for the simulation [101]. Initially, after the network model has been created, a load flow analysis needs to be performed to confirm that the system operates at normal operating conditions during

steady-state non-faulted conditions. Load flow function provides information about the voltage and phase angles in every system's node, the equipment' loading conditions and the power flows between every set of nodes. This information is necessary for the current system state, but also for system modifications, expansions and generally system planning. The latter ones are very critical for PSS studies, as the dynamic response of a system depends on the pre-disturbance state, the magnitude, the type and the location of the disturbance [24].

Following the load flow calculations, the initial conditions of the simulations need to be specified [101]. These includes the selection of the type of simulation (RMS or EMT), the operating conditions (balanced or unbalanced) and the step size. Furthermore, the initial parameters of the controllers attached to various elements such as gains and time constants and to the initial signals among the different control loops that constitute the complete control block are determined.

The next step in the simulation setup is to define the variables of interest during the time domain simulation and the possible set of events [101]. During a simulation, many variables such as currents, voltages, powers, control signals, bus signals, parameters and many more are calculated but only some of them are significant for a type of study. For this reason, the user should define beforehand the variables of interest. Then the user can execute the simulation without the creation of any event or define a set of events that will create a specific disturbance and observe the system response. DPF allows the utilization of different events such as dispatch event, load event, outage event, switching event, short-circuit event and many more and thus the type of event, the time and location of occurrence and the magnitude and the duration of the disturbance can be defined.

With the simulation setup ready, the RMS or EMT function can be executed for a specific simulation period [101]. During the simulation time, variables are calculated, events and disturbances are applied, results and plots are generated. The user is allowed at any time to stop the simulation and restart it if necessary. When the simulation is finished, the full set of results has been calculated and the various plots and result objects created by DPF can be exported to be externally used.

A flowchart of the simulation process in DPF can be observed in Figure 3.1 [101].

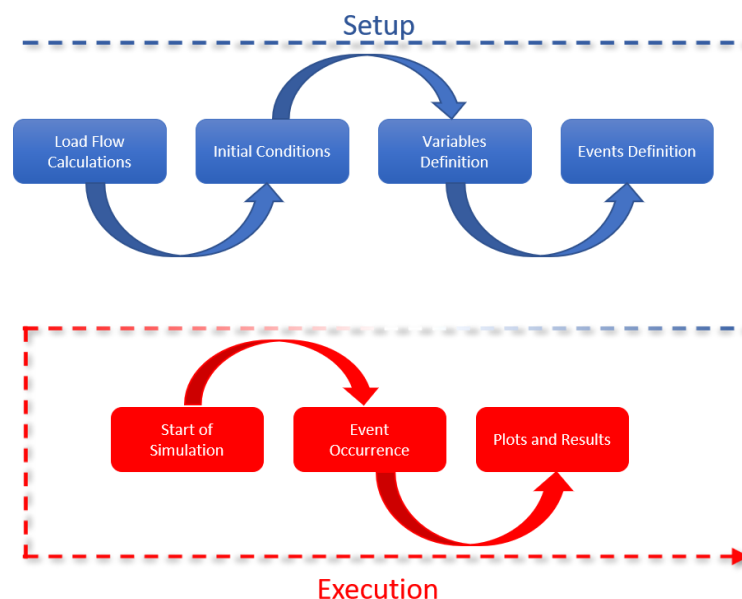


Figure 3.1: Simulation process in DPF - A flowchart.

3.1.3. Dynamic models and modelling approach – Use of templates

Before any dynamic simulation is executed in DPF, all different network elements need to be accurately modelled for the study of interest. The level of detail of the models and their complexity depends on the time frames of interest, the phenomena and responses evaluated. For dynamic simulations, DigSILENT has developed a library in DPF with models of the main mechanical and electrical equipment and its controllers found in a power system [101]. These models have been created based either on international standards developed by the International Electrical Commission (IEC), the Institute of Electrical and Electronics Engineers (IEEE) or the International Council for Large Electric Systems (French: CIGRE) or based on data provided by manufacturers and can be easily used. Apart from these models, DPF allows the development of new accurate models called “user-defined models” utilizing a special programming language, the DigSILENT Simulation Language (DSL). The latter feature is of great importance, as the user can create models of elements and controllers in cases that no standardized models exist, or when highly accurate models based on manufacturers’ data are required. In many cases accurate and validated models of complex network elements such as HVDC links, WTs, PV units, ESS or complete systems have already been developed by engineers, institutions, researchers or manufacturers. If these models are available, they can be easily introduced into new projects using templates. DigSILENT offers for example access to templates of systems or equipment to licensed users or to people participating in various seminars. In this project, templates of validated models of significant network elements have been utilized to form a multi-area, multi-energy power system for PSS studies. The utilization of templates in new projects has to be carefully done so that the newly introduced elements comply with the existing equipment in terms of frequency, voltage levels, power etc.

For the definition of an element model, DPF adheres to a specific hierarchical modelling that includes both graphical representation methods and scripting through DSL to effectively represent systems, elements, control loops and behaviours. The main components of this modelling approach are [101] [102]:

- **Build-in models:** Dynamic DPF models of standard network elements such as generators, motors, static generators, compensators etc.
- **Composite Frame:** A schematic diagram of all the external interconnection (inputs and outputs) signals among different building blocks that constitute a network element. These building blocks are called slots and its operation should be defined through their model or block definition.
- **Model or Block Definition:** Each of the slots in a composite frame, is correlated with a particular control loop, algorithm, behavior or part of mathematical equations used to represent a physical phenomenon or a control action. Hence, each of the slots needs to be associated with a model or block definition either through graphically created block diagrams or via scripting in DSL.
- **Common Model:** Network elements of the same type such as SGs, may have the same composite frames and model definitions. However, the parameters of the transfer functions or the differential equations within their model definitions may differ based on their location, their type and response. Hence, these parameters need to be externally provided by the user through common models, offering the user-model interface, created based on their corresponding model or block definition.
- **Composite Model:** Is used to associate all the different common models to the corresponding build-in network models. The composite model is based on the structure defined by each composite frame.

A schematic diagram of the components' interconnection in hierarchical modelling approach in DPF can be observed in Figure 3.2 [102].

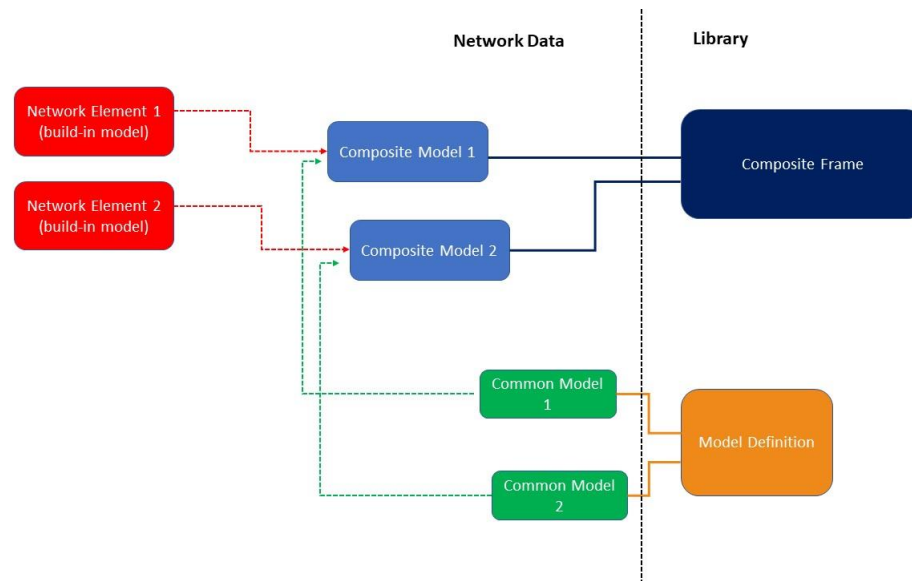


Figure 3.2: Single model definition-hierarchical modelling approach DPF [102].

3.2. The original PST 16 benchmark power system

As a starting point of this project, the PST 16 benchmark system, a single line diagram of which is shown in Figure 3.3, has been utilized. It is a 3-area strongly meshed power system widely used for PSS studies [100][103]. Initially, it was designed to perform dynamic simulations to improve its transient behavior and to mitigate the inter-area low frequency oscillations commonly occurred due to large power flows through long HVAC tie-lines [100] [103]. It consists of 16 SGUs widespread among highly meshed areas enabling large power flows through the areas' tie lines. Modelling of various equipment is based on build-in models provided by DPF and DSL has been used for the development of the controllers attached to various elements. The system parameters have been chosen according to real parameters of the European system aiming at realistic modelling scenarios.

Regarding the power generation, the largest amount of excess power is generated in area A and transferred through HVAC tie-lines to areas B and C. For this reason, area A is the mainly exporting area, whereas areas B, C have significant amount of load. Area C appears to be the weakest area due to its high loading levels and its meshed structure, whereas area B has a more balanced generation, demand mix and structure. Power flows also exist among areas B and C depending on the loading conditions of each area. Power transmission within the areas takes place at the three different voltage levels of 110kV, 220kV and 380kV whereas interconnection links among areas A and C and A and B operate at 380kV and between B and C at 220kV. Further details about the different elements confronting the original PST 16 benchmark system are provided below whereas Table 3.2 provides an overview of the element distribution:

- **Bus bars:** The original PST 16 benchmark system consists of 66 busbars operating at different voltage levels of 15.75kV, 110kV, 220kV and 380kV.

- **Transmission lines:** 51 transmission lines modelled by their Π (PI) lumped equivalent model are used in the system. They operate at voltage levels of 110kV, 220kV and 380kV and their length vary from 20 km to 290 km.

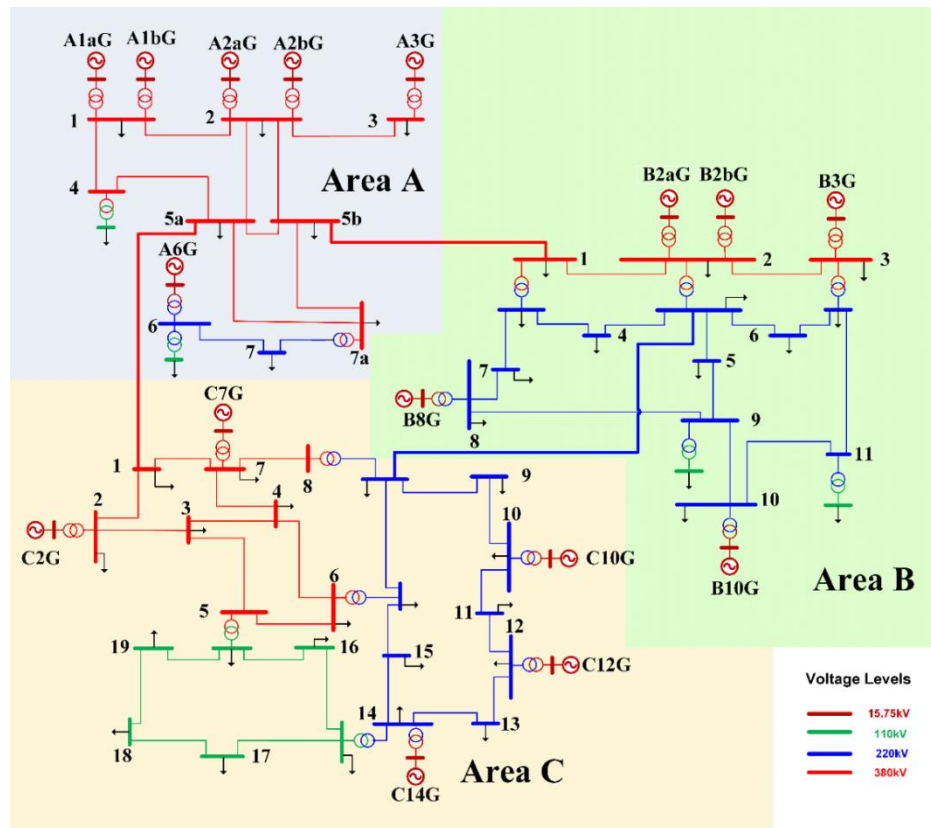


Figure 3.3: The original PST 16 benchmark power system [100].

- **SGUs:** The generation mix of the original system consists of 16 SGUs installed at different areas utilizing conventional sources of energy. In fact, 5 of the SGUs are hydro-based units with a power rating of 220 MVA, 7 of the SGUs are coal-based thermal units with a power rating of 247MVA and the last 4 are nuclear-based units with a power rating of 259MVA. Each of the 16 power plants operates at 15.75kV in a YN-D connection type and is represented by the parallel connection of multiple units of the same type and rating. All the SGUs are represented by their 5th order model suitable for PSS studies and are accompanied by their excitation and governor system and power system stabilizer based on the IEEE standards.
- **Power transformers:** 28 3-phase 2-winding and 3-winding power transformers of various power ratings have been utilized to step up and step down the voltage levels when required. Power transformers connecting SGUs to the grid have a YN-D vector group connection, whereas those installed for transmission purposes have a YN-YN vector group connection.
- **Load demand centers:** 44 loads of active and reactive power demand have been installed in various locations of the system, with area C being the most loaded area.

Table 3.2: Element distribution in the original PST 16 benchmark system.

	Buses	Transmission Lines	Power Transformers	SGUs	Hydro	Thermal	Nuclear
Area A	17	12	9	6	5	1	0
Area B	21	15	10	5	0	1	4
Area C	28	24	9	5	0	5	0
Total	66	51	28	16	5	7	4

Considering the generation and load conditions, the PST16 benchmark system has been designed to operate in multiple scenarios as it is expected that load demand and thus the generation profile changes throughout the year [100]. The selected scenario specifies the amount of generated power and the amount of the load in each area and thus the power flows through the tie-lines. Also, different structural conditions can be considered by modifying the number of parallel operating tie-lines among areas. In the worst-case scenario, the load and generation mixes reach 15.6GW and 15.9GW respectively representing very high loading conditions during wintertime and equipment operating close to its operating limits [100].

3.3. The modified PST 16 benchmark system

The original system has been modified in this study case to facilitate the instalment of HDVC links, PEM electrolyzers and WTs to form a generic multi-area multi-energy hybrid HVAC/HVDC power system. The models of all the elements have been designed to offer the necessary accuracy for dynamic stability studies of interest. The modified PST 16 benchmark power system can be observed in Figure 3.4. In comparison to the original PST 16 system an overview of the elements of the modified PST 16 benchmark system is listed below, whereas detailed information about the applied changes can be found in section 3.4.

- **11 Conventional SGUs** remain in operation in the modified system installed at buses A1a, A1b, A2a, A2b, A3, A6, B2b, B3, C2, C7 and C14 operating at 15.75kV and connected through transformers to the grid. Area A has a generation mix coming completely from SGs, whereas the share by SGUs in areas B and C is equal to 40% and 60% respectively. Three different types of SGUs have been considered similar to the original system with power ratings of 220MVA, 247MVA and 259MVA. The system operates at medium load conditions and the total generation is 10280MW.
- **88 AC and 12 DC bus terminals** are used to interconnect various elements. Among the AC terminals 20 of them are in area A, 24 in area B and 32 in area C, while 12 AC buses and 12 DC buses are utilized in the HVDC links. The bus voltages differ depending on the transmission level or the operating voltage of various elements and thus 8 different voltages can be observed: 380kV AC, 220kV AC and 110kV AC for transmission purposes, 20kV AC at the electrolyzers buses, 0.4kV AC at the WT terminals, 15.75 kV AC at the SGUs terminals, 350kV AC on the AC side and 380kV DC on the DC side of the HVDC links.
- **43 2-winding transformers** are used to interconnect different elements such as SGUs, WTs and electrolyzers operating at different voltages to the local grid and for transmission purposes to regulate the voltage at the required levels. Among them, 11 are installed in area A, 13 in area B, 13 in area C and 6 are utilized at the CCPs of the HVDC links. The rating and the characteristics of the transformers varies

depending on the type of the transformer, the required power transfer, the number of parallel units and the element they interconnect. No modifications have been applied to the originally existing transformers while the parameters of the transformers newly installed are based on their templates.

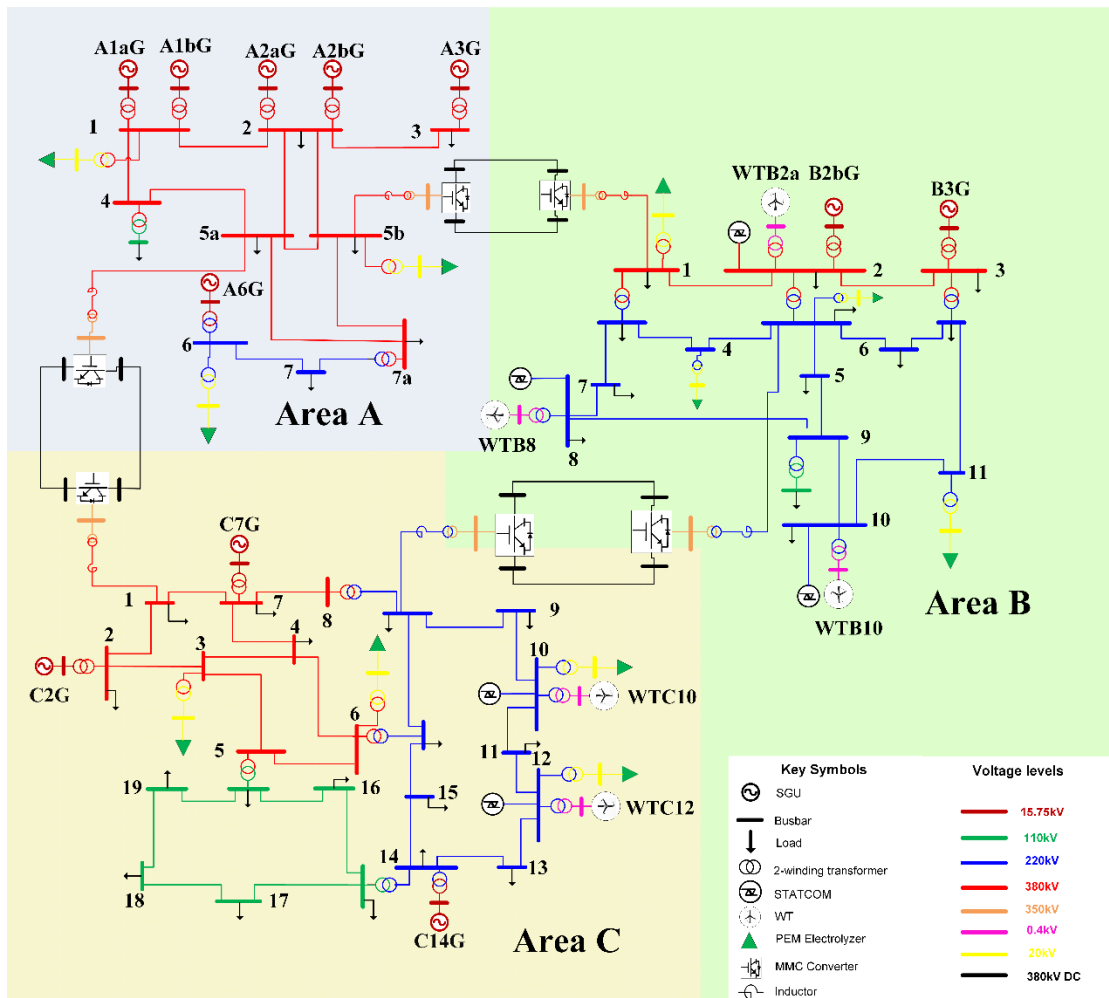


Figure 3.4: The modified PST 16 benchmark system.

- 47 demand units** from which 11 are installed in area A, 15 in area B and 21 in area C. The total load demand is equal to 10145MW operating the system in a medium loading condition. Among the different demand units 11 of them are PEM electrolyzers shown in green triangle in Figure 3.4, constituting in total 21% of the total load demand equally spread in the 3 areas. These units are electromagnetically decoupled from the grid and are not able to offer natural load frequency regulation but have the provision of FFS based on their control blocks. Electrolyzers have been installed at specific buses considered to be significant system points: A1a (close to largest SGU), A5b (at the CCP of the HVDC link), A6b (remote point), B1 (CCP of the HVDC link), B3 (point close to WTs and at the CCP of the HVDC link), B4 (randomly selected point), B11 (next to largest WT), C3 (close to SGUs and HVDC link CCP), C6 (significant system point), C10 (WT CCP), C12 (WT CCP). The relationship between the electrolyzers' location and their response to imbalances will be evaluated through RMS simulations in Chapter 5. Finally, the units installed operate at 20kV and are coupled with the grid utilizing power transformers.

- **5 WT power plants:** have been installed to replace the SGUs at buses B2a, B8, B10, C10 and C12 and can be observed in Figure 3.4 with the characteristic symbol of the WT. The WTs have the power rating required to offer the active power that the replaced SGUs used to provide during steady state conditions. They are modelled as a single unit consisting of multiple WTs of smaller rating (2.35MW) in parallel operating at 0.4kV and are connected to the grid through step-up transformers. The selection of the units replaced is based on the scenario that the 3 decoupled areas are characterized by different generation mixes: area A being a conventional strong area with only SGUs, area B being an area of significant non-synchronous energy share (60% coming from converter-based units) and area C being a strongly meshed area with 60% of generation coming from SGUs and 40% from converter-based units.
- **5 Static compensator (STATCOM) devices:** have been installed at the CCPs of the WT units to offer the required reactive power during steady state and voltage support when necessary. They are modelled by static generator build in models provided by DPF as can be observed in Figure 3.4 and are dynamically controlled through DSL.
- **3 MMC-based HVDC links:** are utilized to replace the weak AC tie-lines and to offer electromagnetically decoupled areas. Each HVDC link consists of 2 MMC converter stations one operating as a rectifier installed at the sending end and one operating as an inverter located at the receiving end. The MMCs operate at 350kV AC and thus a transformer is utilized to enable the grid interconnection followed by an inductor. In case of the links A-C and A-B voltage is increased at 380kV whereas in case of link B-C the CCP operates at 220kV. On the DC side of the MMC, a bipolar configuration is used facilitated by 4 buses operating at 380kV DC followed by 2 HVDC cables operating at opposite polarities.
- **49 AC transmission lines:** enabling the power flow between each areas' nodes operating at different transmission voltages (380kV, 220kV and 110kV) and with no modifications applied in their parameters

The modified PST 16 benchmark system operates at medium loading conditions during steady state with the total load demand being equal to 10145MW spread in the 3 areas. In fact, area A has a total load of 1770MW, area B a load of 4670MW and area C a load of 3705MW. To sufficiently cover the demand, power transfers mainly from area A to the other areas through the HVDC links have to be enabled. For this reason and according to the normal power flows through the AC tie-lines, the setpoints of the HVDC links have been set leading to a power transfer of 700MW from area A to C, 600MW from area A to B and 100MW from area C to B during steady state conditions. In this way, the load flow effectively converges within 4 iterations of Newton-Raphson algorithm and all the equipment and the bus voltages remain within their capability limits as it can be observed in Figure 3.8 with the corresponding power flows. Now that the 3 areas are decoupled, 3 different SGUs act as reference machines in each area: A1aG, B2aG and C7G, respectively and the system is characterized by 3 frequencies one for each area. During steady state conditions the frequency in all 3 areas remain constant at 50Hz as observed in Figure 3.5, meaning that the generation and demand equilibrium is successfully preserved. Then, the initial conditions for RMS simulations are successfully executed for a balanced positive sequence network and for a step size equal to 0.001. Also, the frequency response of the 3 areas has been validated with respect to possible loss of SGUs in each of the areas. The corresponding responses can be observed in Figure 3.6 for a loss of SGUs A2bG, B2aG and C14G taking place at the 1st second of simulation. The frequency response in each of the cases is the expected one considering the inertia

levels of each area, the synchronous power reserves of each area, the percentage of the non-synchronous generation and imports with respect to the total demand and finally the magnitude and the location of the disturbance. In fact, area A, during the transient period has the smallest RoCof compared to other areas and effectively preserves the minimum maximum instantaneous frequency deviation before stabilizing at a new equilibrium point as expected due to the lack of SFC schemes [24][26]. Area B, experiences higher RoCofs and deviations compared to other areas and larger stabilization time due to the low inertia conditions, the large share of non-synchronous generation and the limited local synchronous reserves before stabilizing at a much lower level compared to other areas due to the lack of synchronous reserves [24] [26] [104]. Also, as explained in [104], in case the percentage of wind power and non-synchronous imports is large compared to the local coupled demand and exports during medium or large loading conditions, the frequency of the system may experience an initial drop followed by a period the frequency tries to restore before starting dropping again having an extended stabilization period before reaching the equilibrium due to the limited support capability by the local units and the WTs' response. Finally, area C as expected has a lower inertia compared to area A but larger compared to B leading to a response of RoCof between the other areas and a stabilization at a lower level compared to area A.

The modified PST 16 system created acts in this study as a basic system representing 3 different areas electromagnetically decoupled and with different generation and demand characteristics. Modelling of all the different elements is detailed enough for RMS simulations and is based either on DPF proposed models, on templates created based on international standards or on guidelines provided by international standards. Furthermore, all the different elements such as SGUs, MMC converters of the HVDC links, WTs and PEM electrolyzers have various controllers attached offering the provision of FFS to active power imbalances. As a result, this system can effectively act as a benchmark system for extensive frequency stability studies and RMS simulations of interest.

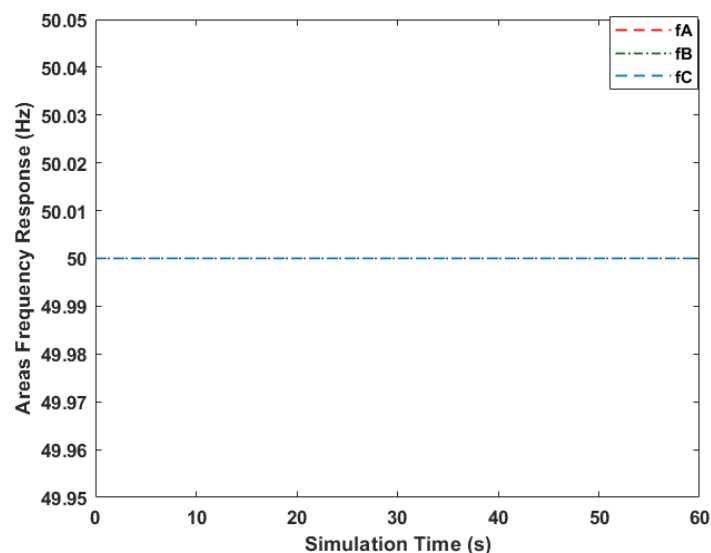


Figure 3.5: Areas' frequency response during steady state conditions.

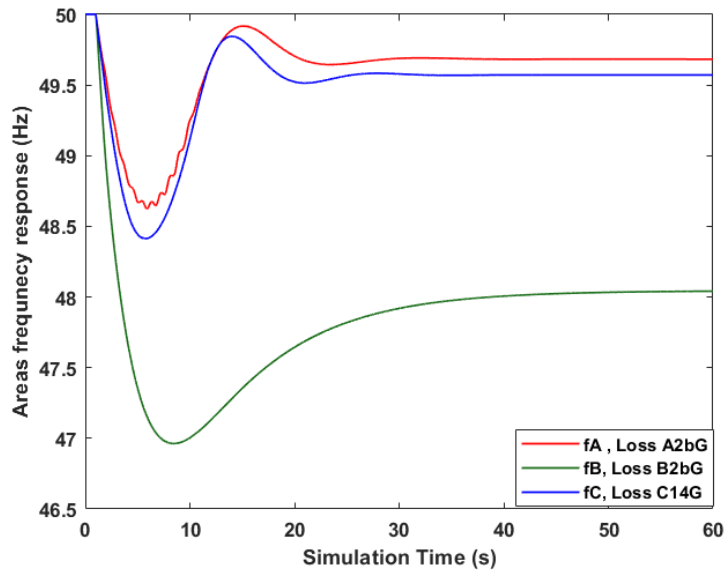


Figure 3.6: Areas' frequency response under commonly occurred imbalances.

3.4. Modifications on the original PST 16 benchmark power system

In this section, all the modifications applied to the original PST 16 benchmark system will be analyzed. These modifications refer to the introduction of new element models and modifications in their control structures to enable the provision of FFS against active power imbalances through APG control scheme.

3.4.1. Synchronous generators modelling and control

For the modelling of SGUs the build in model ElmSym of DPF has been utilized based in the 5th order model which is suitable for PSS studies of interest [105]. Further information is provided in the manual of DPF for SMs [106]. The SGUs are installed at the same locations with the original system and have different ratings (220MVA, 247MVA and 259MVA) depending on their type. They operate at 15.75kV and are connected through step-up transformers in a YN-D connection to the grid. Each power plant consists of multiple SGUs of the same type connected in parallel. The parameters used for the SGUs and the power transformers is based on their type and rating and has not been modified.

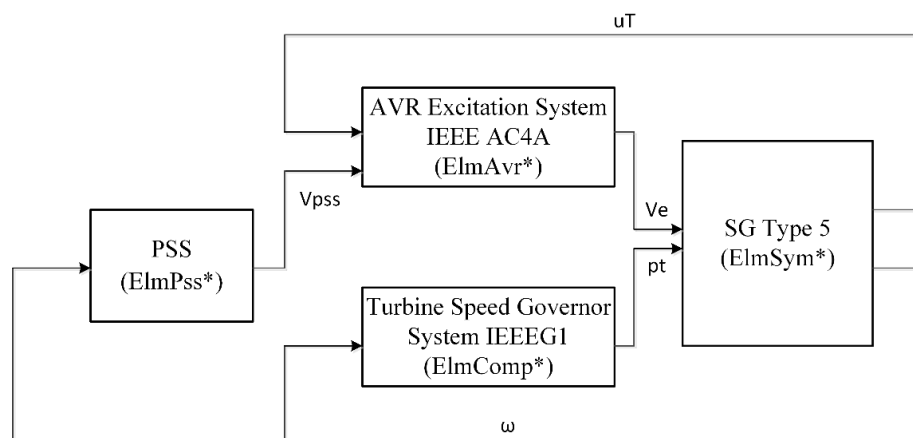


Figure 3.7: SGU Composite Frame.



Figure 3.8: Heatmap of the modified PST 16 benchmark system - Load flow & Elements Loading.

Considering the control loops of the SGUs, all the units have the same control structure that consists of an excitation system, a speed-governor and a power system stabilizer. The schematic diagram of the control loops of each SGU applied can be observed in the composite frame in Figure 3.7. The role of the excitation system is to perform voltage-reactive power control to preserve the terminal voltage at acceptable limits and to support the grid within the acceptable excitation and thermal limits of each unit [24]. In this study, one of the most used systems, the IEEE AC4A excitation system has been utilized and its model definition can be observed in Figure B.2 [107]. Power system stabilizer is a supplementary control loop in the excitation system, acting as feedback controller aiming at effectively reduced rotor angle swings and thus improved dynamic performance. Various input signals such as rotor speed, frequency, active power, or mechanical torque may be used depending on the controller's design [24] [107]. In this study, a simple PSS with rotor speed difference as input is used as presented in [103]. The model definition of the PSS can be observed in Figure B.5. Parameter selection for the PSS block has been done based on typical values provided by [103] as their optimal tuning is out of scope of this study. Finally, the last slot in the SGUs composite frame is the speed governor system. With the aid of this system the transient rotor angle stability can be maintained, and the frequency stability of the system is enhanced as it is able to adjust the active power output of the SGUs by modifying the gate or valve position of the turbine enabling additional or less fuel flow [24]. In this study case all units are enhanced with the same turbine and governor models according to the IEEEG1 model widely used [108]. The turbine and governor model definitions comprising the speed-governing system are presented in Figure B.3 and in Figure B.4 respectively. Parameter selection for the controllers has been facilitated according to the international standards [108] [109] and the SGUs' type.

3.4.2. Areas' tie-lines, MMC-HVDC interconnection links modelling and control

3.4.2.1. MMC- HVDC interconnection links representation

With respect to the research questions presented in Chapter 1, one of the goals of this study is to introduce MMC-based HVDC links among the areas in the original PST 16 benchmark system. Based on that, 3 MMC-HVDC interconnection links have been installed to replace the weak HVAC tie-lines at the same locations and effectively decouple the 3 areas. A schematic diagram of the MMC-HVDC interconnection link in DPF can be observed in Figure 3.9.

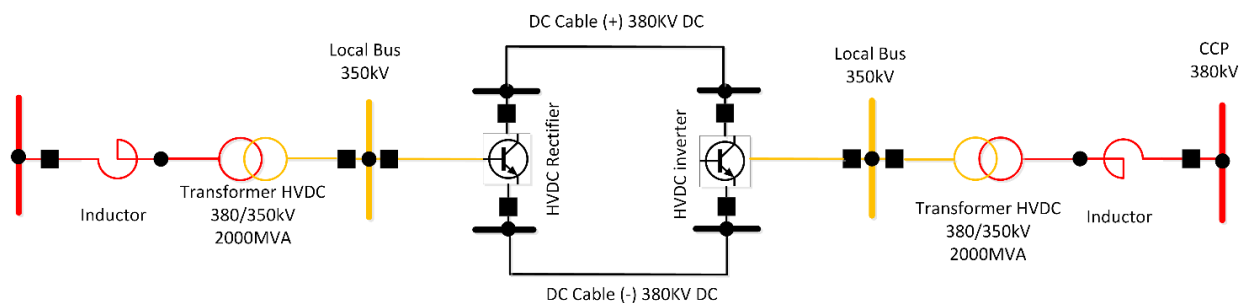


Figure 3.9: HVDC interconnection link schematic diagram.

For the modelling purposes of the MMC HVDC interconnection link, a template provided by DIgSILENT GmbH has been utilized [71]. This model has been created according to the proposals of CIGRE in [72] and

works as an AVM type 6 suitable for RMS simulations and PSS studies of interest. It consists of 2 half-bridge MMC type converter stations operating at 350kV and at 760kV on the AC and DC sides respectively able to handle 2000MVA of power bidirectionally. Each of the MMC converter stations consists of 200 SMs to create an almost perfectly sinusoidal output waveform. On the DC side a bipolar configuration has been considered as the most preferable configuration for interconnection links and thus the two poles operate at opposite polarities. As this study refers to a symmetrical bipolar topology, the build in ElmVsc model of DPF has been used for the converter stations. Further information on the ElmVsc model utilized can be found in the corresponding technical reference of DPF [110]. Apart from its grid interface, each converter station is accompanied by its dynamic control system that enables the control of its power output and its composite frame can be observed in Figure C.1. Further details about the control blocks of the MMC converter are provided in section 3.4.2.2.

Apart from the MMCs various other elements have been modelled on both sides of the converters. On the AC side, a power transformer has been used to allow voltage regulation with respect to the local grid enabling interconnection of the A-B and A-C HVDC links at 380kV and the B-C link at 220kV of the CCPs. Moreover, next to the transformer, an inductor has also been installed on both AC sides acting as an additional AC filter when the same model is used for VSC applications. On the DC side, the 2 DC cables of the bipolar configuration have been modelled with their equivalent Π (PI) model operating at ± 380 kV at opposite polarities

3.4.2.2. MMC-HVDC interconnection link operational behaviour and control

The HVDC interconnection link has 2 MMC stations each of which can operate at 4 quadrants in a bidirectional philosophy [71]. One of the converter stations acts as a rectifier, in the sending end of the link, whereas the second one as an inverter installed at the receiving end. Each of the MMCs can independently control the active and reactive power outputs through the current vector control applied. Considering the active power output, all rectifier stations operate at Vdc mode, whereas all inverter stations adjust their output according to the P mode to effectively maintain the balance on the DC link. As far as the reactive power is concerned, all the converter stations have been set in Q mode providing the corresponding setpoints with respect to the steady state power flows.

In parallel, the control strategy of the MMCs has been created by DIgSILENT according to the guidelines of CIGRE in [72] in DSL and is provided within the HVDC link template [71]. The complete composite frame of the control system of the MMC converter can be observed in Figure C.1 and further details can be found in [71]. The design of the control system is based on the 3 levels of hierarchical control presented in [72] and as the AVM type 6 sets, only the upper-level controllers need to be modelled. Hence, the required setpoints are provided either by load flow solution or the user to the outer controllers of the system that generate the reference currents for the inner current control loop responsible to provide the references for the lower-level controllers. However, to effectively control the build in converter model (ElmVsc) of DPF the real and imaginary part of the pulse width modulation index should be generated according to the voltage references provided by the inner control loop [110].

An overview of the slots of the composite frame of the MMC of the HVDC link is provided below [71]:

Measurement and signal processing:

This block contains all the different elements utilized to measure the voltage (StaVmea) and the current (Stalmea) on both sides of the converters. Measurement of the AC voltages and currents can either be implemented locally at the bus terminal next to the converter or at the CCP with the grid. Apart from the measuring devices, a phase lock loop (PLL) is used for synchronization with the voltage vector at the CCP through the generation of angle θ utilized for the transformation from the ABC to the dq frame and vice versa. PLL is also responsible to provide the frequency measurement to control blocks operating with respect to a frequency input. For the utilization of the PLL the build in model of DPF ElmPhi_pll has been used. Finally, the signal processing slot obtains the measurements from the different devices and performs all the required calculations to provide AC and DC voltages and currents, power and frequency as inputs to the following control blocks and to perform transformations from the ABC to the dq frame.

Outer control loops:

The role of the outer control loops is to generate the reference signals i_{d_ref} and i_{q_ref} for the inner current control loops to effectively control the active and reactive power outputs of the MMCs. According to their response they can be split into fast and slow dynamic controllers. Among them, P/Vdc controller and Q/Vac controller are the main blocks responsible to generate the current reference, whereas the other blocks constitute supplementary control blocks enabling modifications according to specific phenomena. The role of the outer control loops in the composite frame of the MMC are summarized below:

- Active Power Controller (P/Vdc controller):** The complete block diagram of the active power controller can be observed in Figure C.2. This controller is responsible to generate the active power current reference (i_{d_ref}) to control the active power output. According to the operational behavior of the MMC, it can work either in P mode or Vdc mode and thus the corresponding setpoints should be provided. Additional signals from supplementary controllers can adjust the reference points (P_{ac_ref} or V_{dc_ref}) to respond to various phenomena of interest. Also, the setpoints may be adapted by droop controllers taking into consideration the DC voltage magnitude in case of the P control mode and the active power in the DC voltage control mode. Furthermore, rate limiters are installed to control the rate the setpoints change on time. The final setpoints are compared to the measured values and the error signal is applied to PI controllers to generate the I_{d_ref} within the current capabilities of the MMC. In this study, no supplementary signals from the existing controllers have been considered. Further details can be found in [71].
- Reactive Power Controller (Q/Vac controller):** The complete block diagram of the reactive power controller can be observed in Figure C.3. This controller is responsible to generate the reactive power current reference (i_{q_ref}) to control the reactive power output. Each station can work in 3 modes Q mode, Vac mode or PF mode performing control actions with respect to different setpoints. Measured values of the corresponding variables are provided by the signal calculator based either on local or remote points to enable the error signal calculation. The latter one can be modified by supplementary control signals, droop controllers and the rate limiters before applied to a PI controller. In this study, all converters operate at Q mode according to steady state load flow settings and no further supplementary signals have been considered. Further details can be found in [71].

- **Emergency Power Controller (EPC):** is a supplementary control loop used in case of emergency so that the TSOs can rapidly control the power output of the converter station and is implemented through scripting in DSL. This control block is not considered in this study and thus it has been deactivated.
- **Synthetic Inertia Controller (SI):** is a supplementary control loop acting on the setpoint of the P/Vdc controller to sustain extensive frequency deviations at the local grid based on the calculation of frequency derivative. This control block is not considered in this study and has been deactivated.
- **Frequency Sensitive Mode (FSM):** is a supplementary controller acting on setpoint of the P/Vdc controller aiming at regulation of the power output of the MMC with respect to sensed frequency deviations. This control loop is not considered in this study and has been deactivated.
- **Power Oscillating Damping (POD):** is a supplementary control loop acting both on the P/Vdc and the Q/Vac controller to adjust the power output with the goal of effective damping of oscillations in the interconnected AC network. This control block is not considered in this study and it has been deactivated.
- **Fault-Ride-Through (FRT):** is a fast control loop able to modify the reference currents i_{d_ref} and i_{q_ref} created by the active and reactive power controllers to facilitate very fast dynamic voltage-reactive power support during faults. In this way, the HVDC link can rapidly react and support the network in case of very low voltage conditions and faults.
- **Voltage-Frequency controller (V/F controller):** This controller can be used when the converter station is connected to a weak or islanded network. In this case, the converter is responsible to set the voltage and the frequency in the AC network being able to form the AC network characteristics. Since in this study a grid-following control strategy has been considered, this control block has been deactivated.

Inner control loop:

The inner control loop has as inputs the reference currents i_{d_ref} and i_{q_ref} and the currents measured at the AC side of the MMC transformed to the dq frame. Before applied to the current control loop responsible to create the reference signals for the low-level controllers, a current limiter block is required to maintain the current reference within the capability limits of the converter. Various strategies can be utilized in the current limitation as explained in [72], giving priority either to active or to the reactive current. In this study, it has been selected that the maximum current on the converter would not exceed the 1.1pu and that priority is provided to the active power current under normal operation and priority to reactive current when FRT is activated due to low voltage conditions encountered.

Modulation factor limitation and transformation:

This block is responsible to obtain the voltage reference signals calculated in the upper-level control blocks (V_d , V_q) and transform them back to the ABC frame. For this reason, the angle θ has to be provided by the PLL device. Then these signals with the help of the measured AC voltage are used to calculate the modulation indices required for the control of the converter build in model (ElmVsc). In RMS simulations, the real and the imaginary part of the PWM modulation index is utilized as explained in [71].

3.4.2.3. Introducing APG control strategy in the converter control loop

Having modelled the HVDC link in a suitable manner for RMS simulations and defined the basic control loops, the next step is to introduce the APG control strategy to the control loop of the MMC and enable the rapid response of the link to frequency excursions.

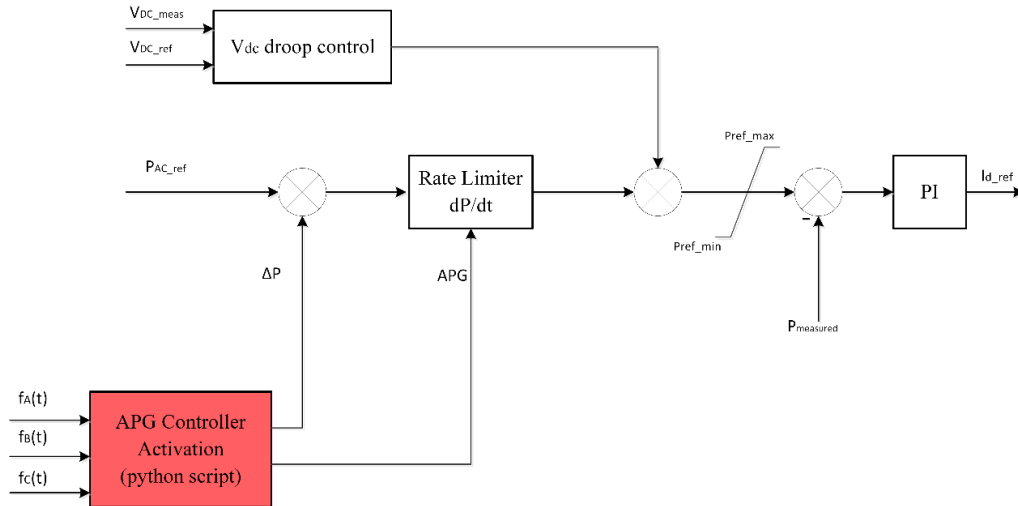


Figure 3.10: Modified P/Vdc controller HVDC link with APG control strategy.

The APG control strategy as explained in [48], is based on the modification of the active power reference (P_{ac_ref}) of the P/Vdc controller of the converter terminal operating at P control mode by a value ΔP . Additionally, APG aims at the control of the rate this change in the active power reference (dP_{ref}/dt) is performed. The values of the parameters ΔP and dP_{ref}/dt of the APG controller can be either selected by the user or externally defined by optimization algorithms. In this study, the optimal values for the additional active power and its rate of change have been calculated via an external python script which facilitates an optimization algorithm able to perform a series of a predefined number of RMS simulations to find the solution vector that achieves the best frequency response in all system areas. Further details on the optimization algorithm will be provided in Chapter 4. The inputs of APG controller in this case are the frequency profiles of the 3 interconnected areas when the candidate variables ΔP and dP_{ref}/dt are applied. In this way, the HVDC link can react to frequency-active power events occurring in the interconnected AC networks by changing its power flow once per simulation with respect to the selected variables and offer FFS. The modified block diagram of the P/Vdc controller with the APG control scheme can be observed in Figure 3.10 and a corresponding flowchart of the actions of the APG controller can be observed in Figure 3.11.

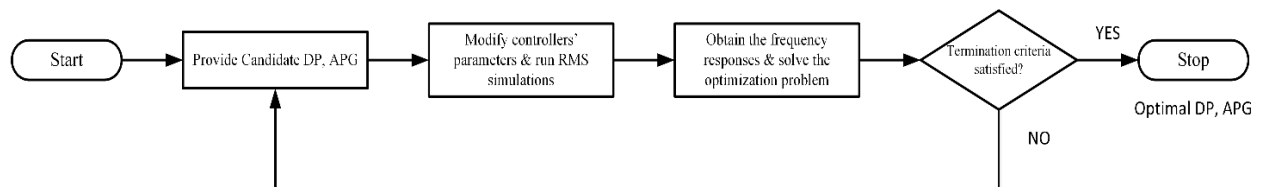


Figure 3.11: APG Controller HVDC link flowchart.

The implementation of the parameters modification in DPF observed in Figure 3.11 has been facilitated by the creation of a parameter event able to modify the active power reference setpoint by a predefined value (ΔP), as observed in Figure 3.12. The parameter event is activated 0.3s following an active power imbalance

so that various delays in the controller actions are considered [20][50]. The value of the new active power reference ($P_{ac_ref_new} = P_{ac_ref} + \Delta P$) introduced in the parameter event is externally controlled through a python script able to modify its value according to the optimal value provided by the solution of the optimization problem. It is also important that the new setpoint should be bounded within the power transfer capability of the link which in this case is 2000MW.

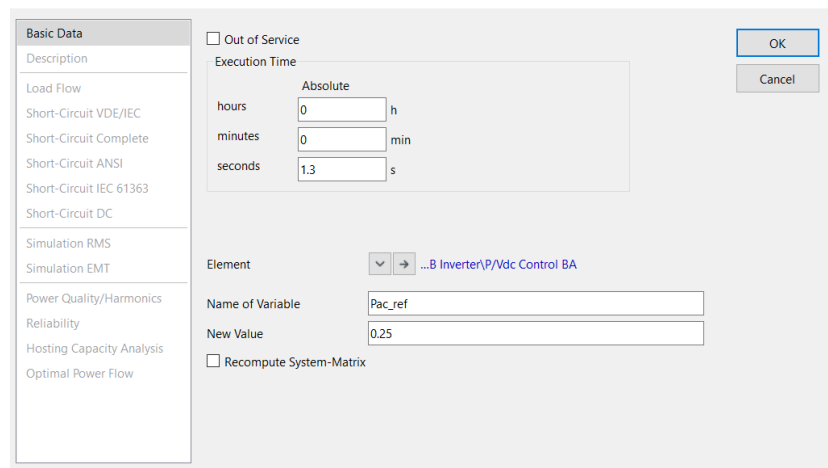


Figure 3.12: Active power event in the MMC link.

As far as the rate of change of the active power reference is concerned, this can be also externally controlled through a python script by modifying the corresponding parameter of the rate limiter in the common model of the P/Vdc control loop of the converter station of interest that can be observed in Figure 3.13. The optimal value of the dP_{ref}/dt is again obtained from the optimization problem solution. The rate of change of active power reference should also remain bounded within the acceptable rate of change of power the link can handle. Based on [50] the maximum acceptable rate of change is equal to 60GW/min which corresponds to 1000MW/s and thus to maximum a change in the active power reference value by 50% pu/s of the power transfer capability of the link utilized which is equal to 2000MW.

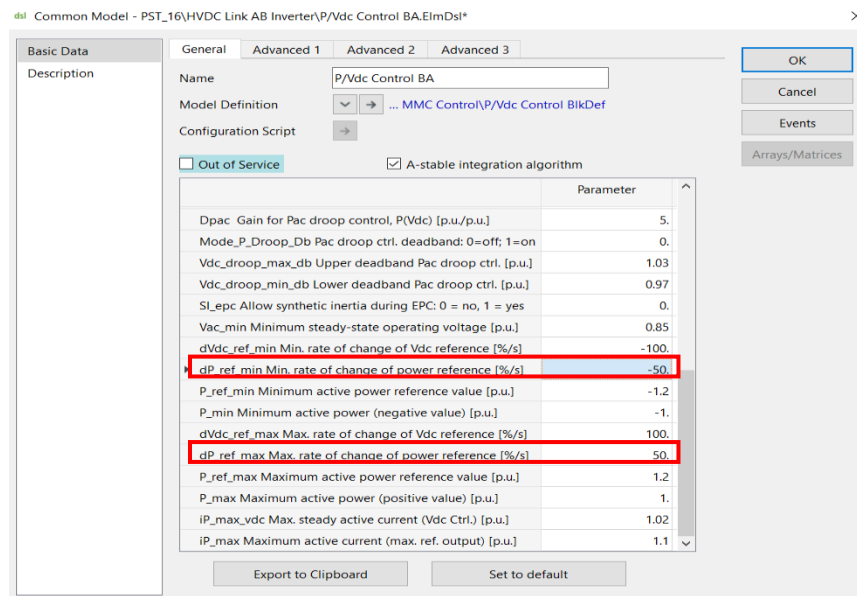


Figure 3.13: APG modification in the P/Vdc controller's common model.

3.4.3. Modelling and control of PEM electrolyzers

As explained in Chapter 1 another goal of this thesis project is to introduce responsive demand units to the original PST 16 benchmark power system able to provide FFS. PEM electrolyzers have been selected as a state-of-art solution due to the advantages of hydrogen technology, their fast-dynamic response capability to active power changes and the provision that they will constitute a significant amount of demand (up to 20%) by 2050 [63] [80] [83]. Based on the latter one, the system has been modified and 20% of the loads of each area has been replaced by PEM electrolyzers. The location of installation of the PEM electrolyzers can vary across the region. In this study, the location of the electrolyzers has been assumed to be constant at significant points such as WT terminals, weak connection points, close to large SGUs and at the CCP of the HVDC links to evaluate their response with respect to their location. In more detail, in area A, PEM electrolyzers have been installed at buses A1 (next to the largest generator), A5b (CCP with HVDC link), A6b (remote grid point) in area B at buses B1 (CCP with HVDC link), B2c (point close to WT and HVDC link connection), B11 (bus next to WT) and B4 (randomly selected point) and finally in area C, at buses C3 (close to large generators and HVDC link CCP), C6 (bus next to the largest generator), C10 (WT connection point) and C12 (WT connection point) representing around 20% of the total load demand.

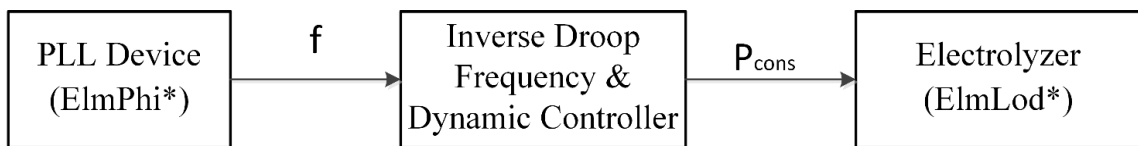


Figure 3.14: PEM electrolyzers composite frame.

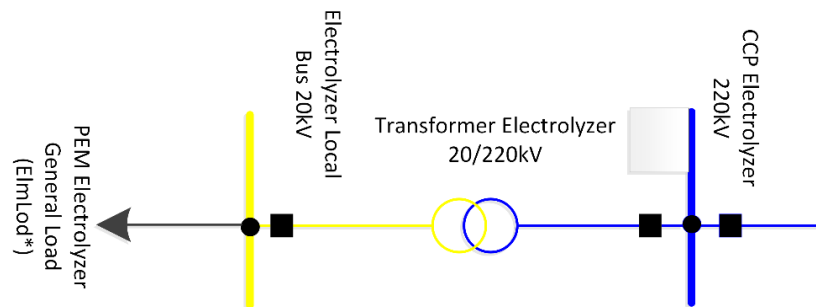


Figure 3.15: PEM electrolyzer model in DPF.

Modelling of PEM electrolyzers depends on the level of accuracy required and the phenomena and time frames of interest as explained in Chapter 2. In this study, which mainly focuses on the dynamic response of the electrolyzers to active power-frequency imbalances, the PEM electrolyzer can be represented in DPF as a dynamically controllable general load (ElmLod) with constant demand plus its dynamic model and control loops developed graphically. The composite frame of the PEM electrolyzer can be observed in Figure 3.14. Considering its interface with the grid, the electrolyzer utilizes power transformer to step up its operating voltage of 20kV to the local CCP voltage level. Also what is important to be highlighted is that the general load has been selected not to be adjustable though the load scaling option provided by the DPF build in model ElmLod as PEM electrolyzers are expected to be electromagnetically decoupled from the grid and thus there is no natural response of the electrolyzer to frequency changes (self load regulation) [63] [111]. Furthermore, since no large electrolyzer models are yet available it has been assumed that large units constitute of the

parallel interconnection of multiple smaller in size units [83]. The general template model of PEM electrolyzer utilized can be observed in Figure 3.15 and has been developed according to [63] [83].

In parallel to the grid model, the common model of the electrolyzers dynamic and frequency controller has to be defined. Initially, the dynamic response of the electrolyzer to active power imbalances is modelled by a rate limiter leading to a linear response bounded by the maximum ramp rate the electrolyzer can handle. In this study, as explained in Chapter 2, a maximum rate of 50% of the rated capacity of each electrolyzer has been utilized [63] [83]. Apart from the modelling of the linear dynamic response of the electrolyser's consumption, a frequency controller is introduced able to modify the active power setpoint according to frequency deviations. Finally, an additional block representing the APG control strategy has been introduced able to modify externally through python the frequency controller parameters and the ramp rate of the electrolyzer with respect to the frequency profiles of the interconnected areas. The block diagram of the PEM electrolyzer dynamic control can be observed in Figure 3.16 inspired by [20] [63] whereas Figure 3.17 provides a flowchart of the process followed within the APG Controller.

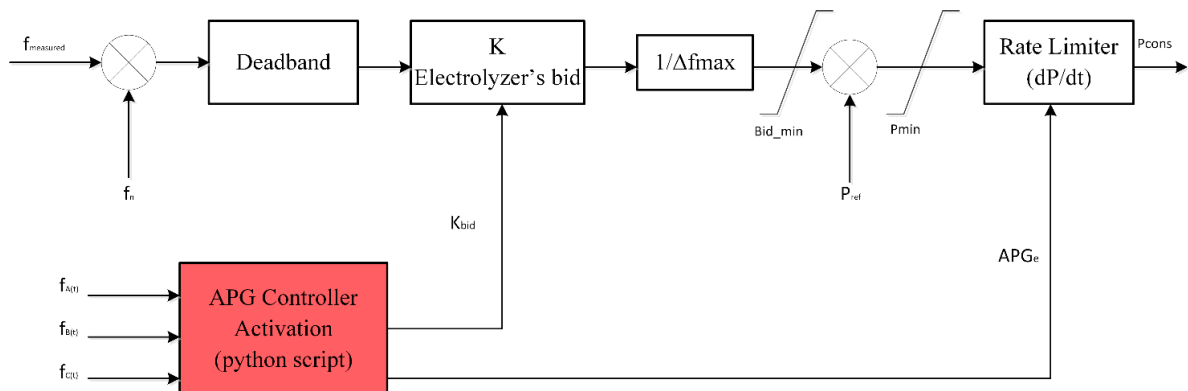


Figure 3.16: PEM electrolyzer dynamic control block diagram.

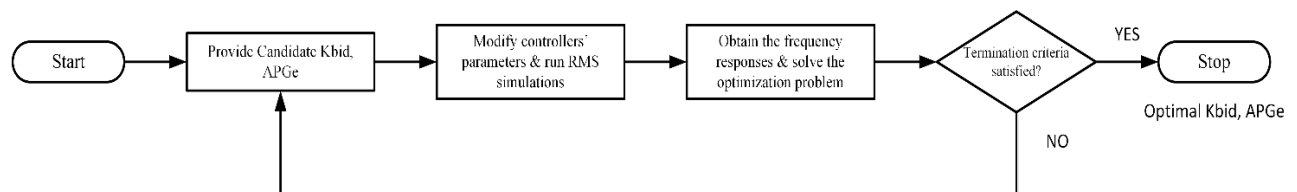


Figure 3.17: APG Controller Electrolyzer – flowchart.

This frequency controller is an opposite droop controller. The frequency is measured at the terminal bus through the utilization of the build in model of PLL (ElmPhi_pll) and is compared to the nominal frequency. Then a deadband is considered so that the electrolyzer does not respond to minor deviations, smaller than 10mHz. Then the error is introduced to a proportional controller that consists of the bid size provided by each unit and the maximum acceptable frequency deviation which is set to 200mHz. These settings have been chosen according to the FCR rules analyzed in Chapter 2 [58]. The bid size of the electrolyzers is externally controlled through a python script with respect to the frequency responses of the interconnected areas and can be observed in Figure 3.18. In addition, it has been assumed that the bid size for FFS is limited to 70% of the rated capacity of the electrolyzer so that its consumption never drops below 0.3pu. The generated ΔP signal is then added then to active power reference of the electrolyzer, limited by its maximum allowed consumption which is equal to its rated active power. Finally, the rate limiter controls the ramp rate of the

changes applied in the active power setpoint and thus in the corresponding consumption. The latter rate can be externally controlled by a python script as shown in Figure 3.18. The value of the APG of the electrolyzer (APGe) is bounded by the maximum acceptable rate the electrolyzer can handle [20] [63] [83].

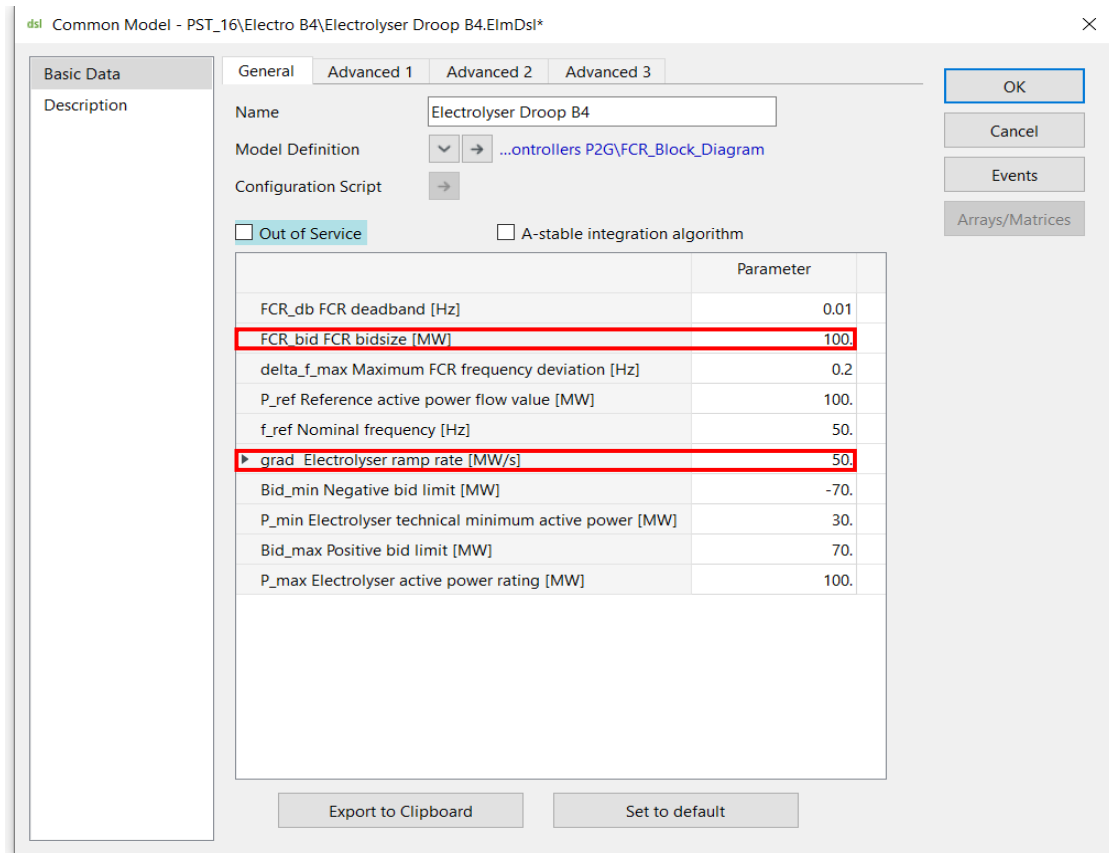


Figure 3.18: Parameter modification in the electrolyzer's common model.

3.4.4. Introducing, modelling and control of WTs

Another goal of this study as defined in Chapter 1 is the introduction of WTs type 4 in the original PST 16 benchmark system. The latter one has been facilitated through the decommissioning of some of the existing SGUs leading to lower inertia levels. With respect to the decoupling of the areas achieved through the replacement of the AC tie-lines by MMC HVDC links, in this study the 3 areas have been modified aiming at a representation of regions with different generation characteristics. For this reason, area A represents a conventional strong and mainly exporting area with a generation mix coming only from SGUs and thus no WTs are installed in this area. Area B represents an area of significant wind generation and thus 3 out of 5 SGUs have been replaced by WTs connected at buses B2a, B8 and B10. As a result, the local generation in area B comes almost by 50% from WT and over 60% from converter-based units (WTs and imports from HVDC links). Finally, area C represents a meshed area with large number of loads distributed at various voltage levels (110kV, 220kV, 380kV) and a generation mix coming from local SGUs by 60%, 22% from WTs installed at buses C10 and C12 and 18% through imports from the HVDC links. The rating of the WTs installed is equal

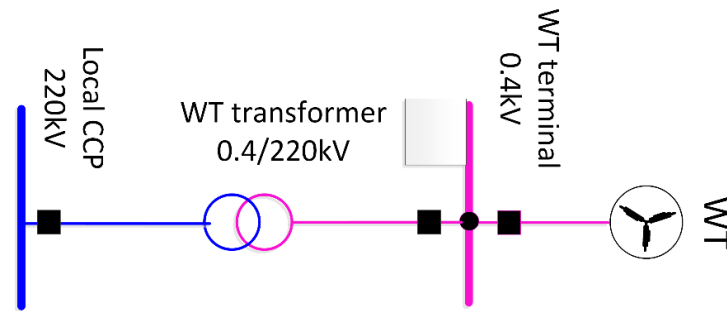


Figure 3.20: WT model in DPF.

An overview of the role of the different controllers included in the WT's composite frame is provided below. Further details can be found in [112].

Measurements: This block contains the different devices utilized to measure the frequency, the power and the voltage at the local bus of the WT. The latter ones will be used to initialize the model and to provide the necessary inputs to the following control blocks.

Wind Speed and Power input: In this block the user should provide an external file with either the available wind speeds at the location of interest or directly the available power in the ambient wind speed. In this study, all the WT models operate at a constant wind speed provided by an external file. Output of this block is the wind speed that is provided to the aerodynamic model and for the calculation of the available power.

Aerodynamic and Mechanical model: This block is utilized to calculate the aerodynamic power which is the power that can be utilized by the rotor of the WT with respect to the available power on the ambient wind speed, the rotor characteristics and the C_p - λ curves. It also takes into consideration the current rotor speed and the blade pitch angle. The user can select among different aerodynamic models developed either by GE, Mathworks or Heier. In this study, the aerodynamic model of GE has been utilized. The outputs of the aerodynamic block are provided to the mechanical model which describes the different mechanical parts of the WT as a single or a two-mass oscillator. According to Energynautics [112] for WTs type 4, the representation of the turbine-generator system should be facilitated by a single mass model.

Pitch angle controller: This controller can adjust the pitch angle of the blades of the WT provided to the aerodynamic model according to the power and rotor speed reference values of the turbine. This is achieved through PI controllers. Also, it is responsible to compensate possible power changes enforced by the supplementary frequency controller, so that this loop cannot alter the pitch angle of the blades.

P controller: Active power controller is one of the main control blocks responsible to generate the current reference (i_{pcmd}) for the generator block to control the active power output. This is achieved through the generation of a power signal based on local measurements, the generator speed and other supplementary controllers. Also, it provides as output signals the rotor speed reference value and the active power reference to the pitch controller loop to control the blade pitching.

Q controller: This block contains a PI controller responsible to provide the input current (i_{qcmd}) to the generator block to regulate the reactive power output. This can be achieved with respect to a reactive power or to a power factor setpoint. Also, in this block possible low voltage conditions are detected, and a corresponding signal is sent to the current limiter aiming at enhanced voltage support from the WT.

P choice and reduction: This block provides the reference to the pitch angle controller to regulate the blade position and thus the power output. This signal is provided either based on the available power in the ambient wind or based on externally provided active power setpoints. Also, this block can reduce the active power output when over frequency events occur.

Current Limiter: This block is responsible to regulate the reference currents i_{pcmd} and i_{qcmd} provided by the active and reactive power controllers before sent to the generator block to avoid overloading of the equipment and to provide priority to voltage-reactive power control in case of low voltage conditions.

Generator: This block consists of 2 slots one representing the type 4 generator system and its characteristics and the second one being the build in static generator build in model (ElmGenstat) provided by DPF. The latter one is a fully controllable current source controlled by the active and reactive currents in dq.

Frequency controller: The frequency control block is a supplementary control loop acting on the active power controller with respect to frequency excursions during under frequency events. It is a droop controller inspired by [113] enhanced with the APG control strategy. Initially the frequency is measured and is provided as input to the block. Then it is compared to a threshold ($f_{trigger}$) above which the controller is activated and starts acting upon the active power output of the WT. It performs as a linear controller able to inject the maximum acceptable additional active power when a maximum frequency deviation threshold (f_{pinmax}) is reached. The available additional power provided by the WT is not unlimited, but it's bounded by the overloading capabilities of the WT. In this study it has been assumed according to [113] that this parameter, $P_{emuinmax}$, does not overcome 0.3pu. Furthermore, the additional power injection should be also bounded timewise. Hence, after the activation of the frequency support, a timer is turned on allowing the modification of the output for a maximum period of 15s. Finally, at the end of the controller a rate limiter has been installed to control the rate the changes in the setpoint take place. The selection of the values of the constant parameters of the controller is based on sensitivity analysis performed in [113]. Among the different parameters, the droop constant ($P_{emuinmax}$) and the ramp rate are externally controlled through python code based on the response of the interconnected areas according to the flowchart provided in Figure 3.21. The modifications of the corresponding control parameters ($p_{emuinmax}$ and $gradW$) are performed in the common models of each of the WTs as observed in Figure 3.22. Finally, the complete block diagram of the frequency controller can be observed in Figure 3.23.

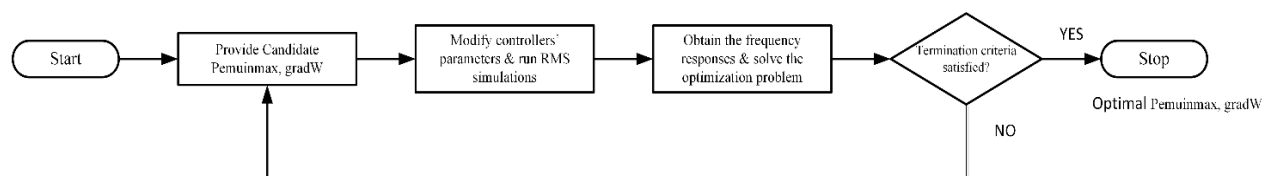


Figure 3.21: APG Controller WT – flowchart.

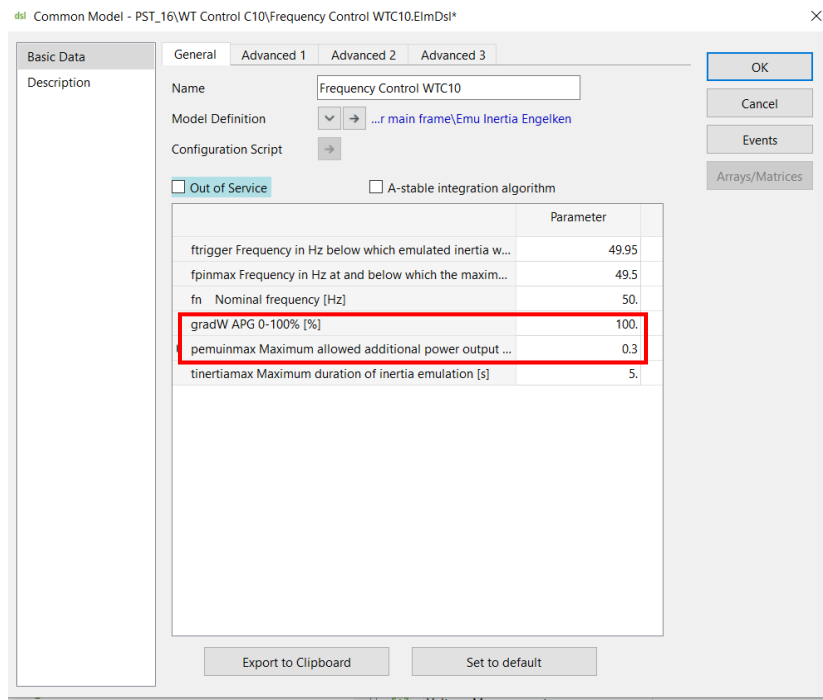


Figure 3.22: WT Common model parameter modification through python.

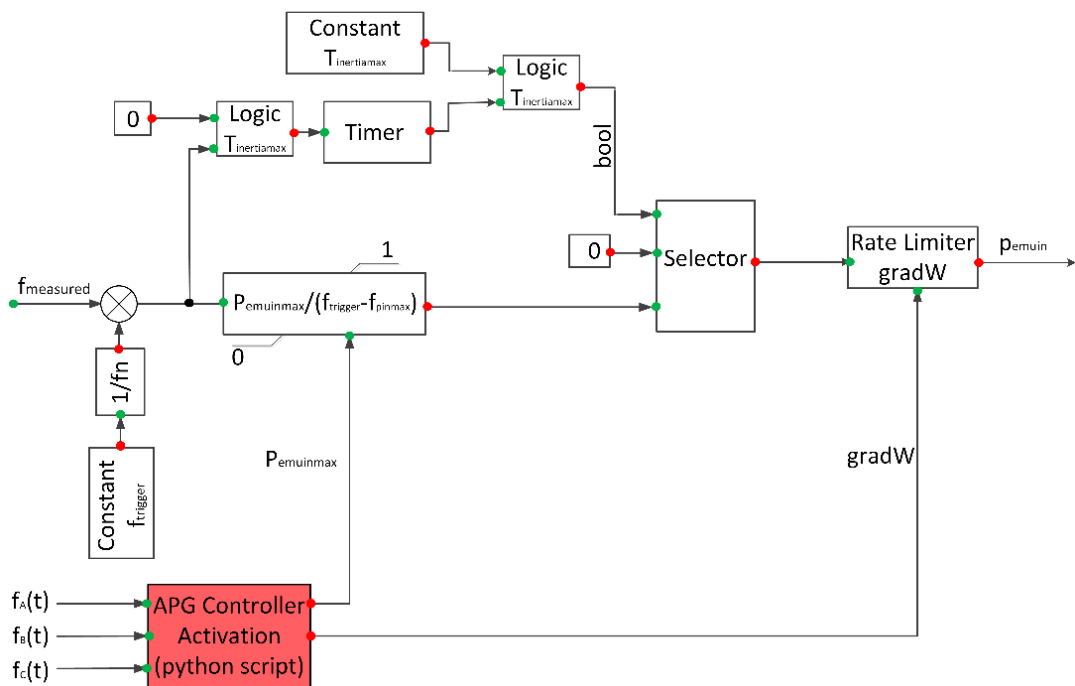


Figure 3.23: WT frequency controller block diagram.

3.4.5. Modelling and control of static compensators

Due to the replacement of SGUs in areas B and C in the original PST 16 system by WTs injecting active power to the grid and the decoupling of the areas through HVDC links, reactive power compensation has been observed to be necessary to maintain the bus voltages within the acceptable limits during steady state conditions. Furthermore, during severe active power imbalances such as loss of generating units the remaining units were unable to cope with the low voltage conditions and additional reactive power support was required. For the reasons above, dynamically controlled STATCOM devices have been installed at the buses where WT units were introduced (B2, B8, B10, C10, C12). These devices are designed to offer the required reactive power during steady state conditions operating at a constant Q mode and are also dynamically controlled to offer voltage support during RMS simulations.

For the modelling of the static compensator devices, the build in model static generator (ElmGenstat) of DPF has been considered operating as a STATCOM device at constant Q mode. The load flow values have been determined with respect to the reactive power injection of the replaced SGUs during steady state conditions. The static generator element acts a controllable source its composite frame can be observed in Figure 3.24. It consists of a measuring device able to measure the voltage magnitude (V_{mea}) at the local bus to provide it as input to the other control blocks. The POD slot is a power oscillation damper responsible to modify the voltage signal of the STATCOM controller aiming at reduced voltage oscillations. Finally, STATCOM controller obtains the measured voltage magnitude and compares it to the voltage reference value obtained from load flow conditions modified by the voltage provided from the POD controller to generate the reference currents able to control accordingly the power output. Further details about the control and the parameter tuning of the dynamically controlled static compensator units can be found in [103].

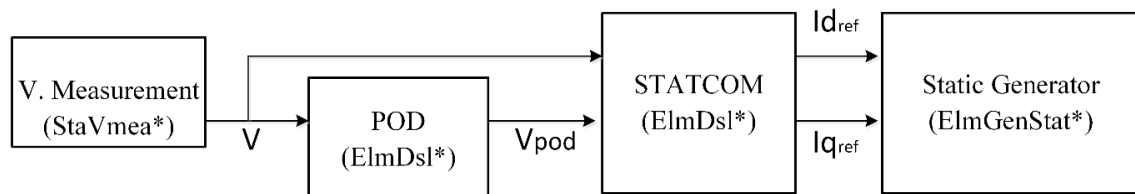


Figure 3.24: STATCOM composite frame.

4

Optimizing the APG control for FFS

4.1. Introduction

The modified PST 16 system designed in Chapter 3 will be utilized in Chapter 5 as a benchmark system for frequency stability studies. The various elements introduced, such as MMC HVDC links, PEM electrolyzers and WTs type 4 are fully decoupled elements through PEIs able to offer FFS during active power events due to their modified control systems. The tuning of these controllers is a challenging task as random tuning may lead to adverse control actions, poor performance and poor coordination among the different sources providing simultaneous support. To achieve an optimal coordination among the various elements participating in the FFS without the introduction of communication means, APG control strategy can be utilized. This strategy is able to modify the active power setpoint or the droop constants applied to supplementary frequency controllers and the rate these changes are performed in a coordinated manner. It is also able to externally control through python the parameters' values based on the magnitude and the location of the disturbance, the availability of the FCRs and their technical limitations. The values of the controllers' parameters are chosen after an optimization algorithm performs a series of RMS simulations, enabled through co-simulation between python and DPF and selects the values that succeed in the optimal utilization of the available FFS sources within their technical limitations and achieved the best frequency response.

To achieve the best frequency response in the system and effectively utilize all the available sources of SI, two different problem formulations have been proposed in this study, presented in sections 4.2 and 4.3, approaching the same problem from different perspective. The former one is based on the minimization of the frequency excursions in all areas from their nominal value following an active power imbalance, whereas the latter one aims at the minimization of the rate of change of the dynamic displacements of the areas' speeds following the imbalance.

To solve the optimization problems and effectively tune the controllers, the mean variance mapping algorithm (MVMO) has been utilized in this study. It has been selected as an algorithm that has shown high potential in solving optimization problems in power system applications, achieving great results and high efficiency and is presented in section 4.4 [114].

4.2. Problem formulation 1

When an active power event takes place, the balance between the generation and demand is perturbed. If the generated power is larger than the load, the frequency tends to deviate upwards from its nominal value, whereas when the load is larger than the generated power, a frequency drop is expected. The first seconds following the disturbance, the RoCof depends on the natural response of the system and thus to the rate at

which the kinetic energy of the rotating masses changes with respect to the system's inertia. Afterwards, based on the speed governor systems attached to the SGUs the frequency deviation is contained by changing the active power output of the SGUs. The latter phenomena determine the response of the system when no sources of SI are utilized. The goal of the latter sources is to tune their supplementary controllers in a suitable manner to sustain the deviations, by providing the essential amount of active power at the required rate to reduce the initial RoCof, arrest the maximum instantaneous frequency deviation and achieve the minimum steady state deviation. These all phenomena are reflected to the frequency of each of the decoupled areas that can be measured at any point being a global variable in each area. According to the latter responses the first problem formulation aims at the minimization of the frequency deviations in each of the areas over the whole simulation period from its nominal value and is presented below (Equation 4.1 to Equation 4.2):

Minimize

$$OF_1(\mathbf{x}) = \int_0^{\tau} [w_A(f_A(\mathbf{x}, t) - f_{nA})^2 + w_B(f_B(\mathbf{x}, t) - f_{nB})^2 + \dots + w_k(f_k(\mathbf{x}, t) - f_{nk})^2] dt \quad \text{Equation 4.1}$$

Subjected to

$$\mathbf{x}_{min} \leq \mathbf{x} \leq \mathbf{x}_{max} \quad \text{Equation 4.2}$$

Where $f_k(\mathbf{x}, t)$ is the measured instantaneous frequency at the k-th interconnected area when the candidate variables of vector \mathbf{x} are applied, f_{nk} is the nominal frequency of the k-th area and in this study is equal to 50Hz, and w_k are weight factors which are considered to be equal to 1 in order not to prioritize an area over another. The optimization vector \mathbf{x} contains D variables which are the parameters of the frequency controllers attached to the introduced elements as explained in Chapter 3. The size of the optimization vector depends on the number of available FFS sources. Hence, its size varies depending on the scenario to reduce the computational needs. At its full extend, it contains 38 optimization variables: 2 for each of the 3 MMC-based HVDC links, 2 for each of the 11 installed PEM electrolyzers and 2 for each of the 5 installed WTs. The complete optimization vector \mathbf{x} can be observed in equation 4.3.

$$\mathbf{x} = [\Delta P_{AB}, APG_{AB}, \Delta P_{AC}, APG_{AC}, \Delta P_{BC}, APG_{BC}, Be_{A1}, APGe_{A1}, Be_{A5b}, APGe_{A5b}, Be_{A6}, APGe_{A6}, Be_{B1}, APGe_{B1}, Be_{B11}, APGe_{B11}, Be_{B2}, APGe_{B2}, Be_{B4}, APGe_{B4}, Be_{C10}, APGe_{C10}, Be_{C12}, APGe_{C12}, Be_{C3}, APGe_{C3}, Be_{C6}, APGe_{C6}, APGWT_{C10}, PmWT_{C10}, APGWT_{C12}, PmWT_{C12}, APGWT_{B2}, PmWT_{B2}, APGWT_{B8}, PmWT_{B8}, APGWT_{B10}, PmWT_{B10}] \quad \text{Equation 4.3}$$

Where:

ΔP_i , $i=AB, BC, AC$: is the amount of active power added to the active power setpoint of each of the P controllers operating in P-mode of the i-th HVDC link and can be applied in the i-th parameter event.

APG_i : is the rate of change of the active power setpoint in each of the P controllers operating in P-mode of the i-th HVDC link that can be applied in the common model of the i-th HVDC link.

Be_j : is the bid size offered by each of the j electrolyzers and acts as a proportional gain in the frequency controller and can be modified in the common model of the j-th electrolyzer. $j=A1, A5b, A6, B1, B11, B2, B4, C10, C12, C3, C6$.

APGe_j: is the rate of change of the active power consumption of each of the j-th electrolyzer, met in the rate limiter of the frequency controller and can be modified in the corresponding common model.

PmWT_ω: is the maximum additional active power in pu that can be provided by the WT and acts as a proportional gain in the frequency controller and can be modified in the corresponding common model. Where $\omega=C10,C12,B2,B8,B10$.

APGWT_ω: is the rate at which the additional active power signal from the frequency controller is applied to the active power reference of the WT met on the rate limiter of the frequency controller and can be modified in the common model of the frequency controller of the ω WT.

Each of the optimization variables in the optimization vector \mathbf{x} is limited within its minimum and maximum boundaries due to the technical limitations of each element as explained in Chapter 3. The following boundaries have been considered for the different optimization variables of each element.

For the HVDC interconnection links according to [20]:

$$0 \leq P_{ref_i} + \Delta P_i \leq P_{rated_i} = 2000MW \quad \text{Equation 4.4}$$

$$0 \leq APG_i \leq 60 \frac{GW}{min} = 1000 \frac{MW}{s} = 50\% \frac{pu}{s} \quad \text{Equation 4.5}$$

$(P_{base} = P_{rated_i} = 2000MW)$

Where $\mathbf{i=AB, AC, BC}$ denoting the corresponding HVDC link

P_{ref_i} is the active power setpoint in the P controller of the i-th HVDC link

ΔP_i is the optimization variable of the i-th HVDC link

P_{rated_i} is the maximum power transfer capability of the i-th HVDC link which in this study is equal to 2000MW

APG_i is the corresponding optimization variable of the i-th HVDC link.

For the PEM electrolyzers according to [83]:

$$0 \leq Be_j \leq 0.7 P_{rated_j} MW \quad \text{Equation 4.6}$$

$$0 \leq APGe_j \leq 0.5 P_{rated_j} \frac{MW}{s} \quad \text{Equation 4.7}$$

Where: Be_j : is the bid size of the j-th electrolyzer

$APGe_j$: is the ramp rate of the j-th electrolyzer

For the WTs according to [113]:

$$0 \leq PmWT_{\omega} \leq 0.3 pu \quad \text{Equation 4.8}$$

$$0 \leq \mathbf{APGWT}_{\omega} \leq 100\% \frac{pu}{s}$$

Equation 4.9

Where: \mathbf{PmWT}_{ω} and \mathbf{APGWT}_{ω} are the maximum additional active power that can be offered by the ω -th WT and the ramp rate the changes in the setpoint are performed respectively.

The problem formulation 1 has been implemented in python script to be solved within the main python file of the MVMO algorithm. The corresponding script containing \mathbf{x} at its full size can be found in appendix E.

4.3. Problem formulation 2

In the second problem formulation proposed, the frequency stability of the system is evaluated according to the shift of dynamic trajectories of the speed of each of the interconnected areas when a commonly occurred active power imbalance takes place. The developed problem formulation is an expansion of the objective function proposed in [20] to a multi-area system of a larger size and complexity.

During steady state conditions the frequency of a system can be represented by a vector with constant length equal to 1 pu. When an imbalance occurs, the size of this vector changes on time with respect to the frequency deviations at a rate based on the system's inertia and the control actions performed. The size of the vector becomes again constant when an equilibrium point is reached. According to this representation, the vector length is smaller than the initial one in case of under frequencies and larger than the initial one in case of over frequency events. When FFS is provided, the tuning of the corresponding controllers aims at the minimization of the displacement both in size and rate of the frequency vector. In that way, smaller RoCofs and limited maximum frequency deviations are achieved and thus the stability margin is enhanced. Minimizing the rate the displacements occur, effectively reduces the size of the deviation.

If the latter case is now expanded to an electromagnetically decoupled multi-area system, with areas interconnected with HVDC links, the frequency response of the system can be represented by a set of n vectors one for each of the n areas. Each of these vectors evolves at a different dimension and can be considered in pu if the areas have different nominal frequencies. In case of a three-area system, 3 vectors ω_1 , ω_2 and ω_3 represent the instantaneous frequency of each of the 3 interconnected areas. The size of the vectors is changing on time and during steady state conditions is aligned to x,y,z axes respectively forming a cube with side equal to 1 pu and a volume of 1 pu as observed in Figure 4.1 in light blue. When an active power disturbance occurs, the geometrical properties of the cube change with respect to the changes each of the 3 vectors impose. As a result, the frequency changes in each area can be interpret as volumetric changes in the frequency cube both in size and rate. In the ideal case the frequency response leads to the same equilibrium point in all 3 areas following a disturbance then the cube changes only in size being equally larger in all dimensions following an over frequency event as shown in pink in Figure 4.1 or being equally smaller in all directions following an under frequency event as shown in blue in Figure 4.1.

To improve the frequency profile at each area and optimally share the disturbance among them, the goal of the optimization problem is to find a solution vector \mathbf{x} able to minimize the volumetric changes with respect to the steady state volume and to achieve minimal and equal rates at the shape changes. To mathematically describe the instantaneous volume of the "frequency cube" Equation 4.10 can be utilized.

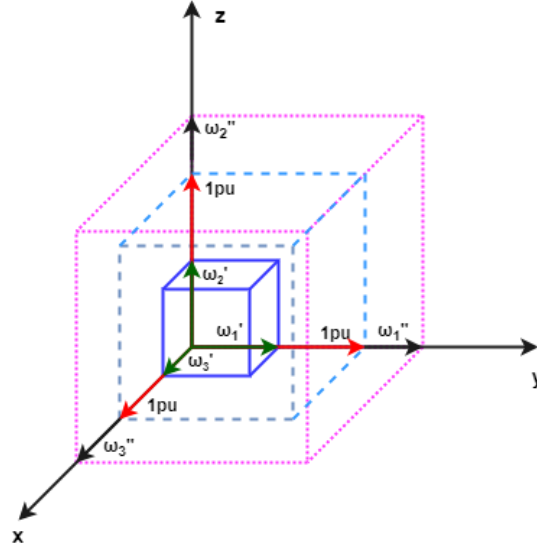


Figure 4.1: Schematic interpretation of OF2.

$$V(t) = \omega_1(t)\omega_2(t)\omega_3(t) \quad \text{Equation 4.10}$$

Where ω_i is the instantaneous frequency of each of the i -th area. For the determination of the ω_i of each area consisting of a multiple SGUs, this frequency can be either considered as the average frequency of the SGUs of that area as in [20] or for increased accuracy it can be considered as the frequency of an equivalent SGU known as center of inertia (COI). In this case, the frequency depends on the inertia of each of the SGUs and can be calculated through Equation 4.11 [115].

$$\omega_{COI}(t) = \frac{\sum_{i=1}^n H_i S_{Bi} \omega_i(t)}{\sum_{i=1}^n H_i S_{Bi}} \quad \text{Equation 4.11}$$

Where $\omega_i(t)$ is the time frequency response of the i -th SGU in each area in Hz, H_i is the inertia constant of the i -th SGU in s and S_{Bi} is the nominal apparent power of the i -th SGU in MVA.

As previously explained, to achieve improved frequency stability in the whole system, the changes in the dynamic displacements of each of the participating vectors should be minimized and equalized in rate of change leading to the minimum volumetric changes of the “frequency cube” in size and shape. The latter is mathematically expressed as the derivative of the volume V as observed in Equation 4.12.

$$\frac{dV(t)}{dt} = \frac{d\omega_1(t)}{dt} \omega_2(t)\omega_3(t) + \frac{d\omega_2(t)}{dt} \omega_1(t)\omega_3(t) + \frac{d\omega_3(t)}{dt} \omega_1(t)\omega_2(t) \quad \text{Equation 4.12}$$

Taking the aforementioned into consideration objective function 2 (OF₂) can be formulated (Equation 4.13 to Equation 4.15):

$$\text{Minimize: } OF_2(\mathbf{x}) = \frac{dV(\mathbf{x}, t)}{dt} \quad \text{Equation 4.13}$$

Subjected to

$$\frac{d\omega_1(t)}{dt} = \frac{d\omega_2(t)}{dt} = \frac{d\omega_3(t)}{dt} \quad \text{Equation 4.14}$$

$$\mathbf{x}_{min} \leq \mathbf{x} \leq \mathbf{x}_{max} \quad \text{Equation 4.15}$$

In this formulation the optimization vector \mathbf{x} comprises of the same variables as in OF1 and can be observed in its full extend in equation 4.3. The bounds of the corresponding optimization variables are determined in equations Equation 4.4 to Equation 4.9 as explained in section 4.2. The problem formulation 2 has been implemented in python script to be solved in the main python file of the MVMO algorithm. The corresponding script containing \mathbf{x} and its boundaries at its full size can be found in appendix E.

4.4. The MVMO algorithm

The MVMO algorithm is one of the representative algorithms in the family of metaheuristic evolutionary algorithms developed to deal with computationally expensive optimization problems [114]. Being utilized in various highly expensive and complex problems it has shown great results considering the convergence rate and the solutions' quality in a short number of fitness evaluations [20] [50] [114]. Hence, it has been utilized in this study to tune the frequency controllers and solve the optimization problems presented in sections 4.2 and 4.3 when active power–frequency events occur. To achieve this the MVMO algorithm has been programmed in Python 3.8 and operates in a co-simulation environment with DPF 2020.

The MVMO as an evolutionary algorithm can generate a single solution with respect to the best parent solution achieved so far within the iteration process. The latter one evolves throughout the process until the termination criteria has not been fulfilled with the aid of a mapping function providing the direction of evolution. The overall process of the MVMO algorithm is presented in Figure 4.2 and is analyzed below [114]:

Initially, the user should provide all the necessary parameters required for the algorithm's initialization. The most significant of them are: the size of the optimization vector D , the termination criteria, the number of fitness evaluations, the mutated variables m , the size of the archive n , the objective function to be optimized, the boundaries of each of the optimization variables and the constraints. Furthermore, an initial solution vector \mathbf{x}_0 can be provided to set a starting point in the research space. If the latter one is not provided, the algorithm can randomly generate \mathbf{x}_0 within the acceptable bounds. The vector is then normalized from $[\min, \max]$ to $[0, 1]$ range as the evolution of the offspring solution is performed within the normalized range. In this way, the generated solutions remain within the acceptable boundaries and no penalties or modifications are required leading to improved efficiency. Then an iterative loop starts with the candidate vector, being either \mathbf{x}_0 or a child solution generated in the last iteration, being denormalized to perform the fitness evaluation. This loop performs until the termination criteria is reached leading to the exit of the algorithm. The termination criteria

can either be a predefined number of fitness evaluations or a condition that denotes infinitesimal improvement in the fitness evaluations. Then an offspring solution is produced based on the best parent solution achieved so far with the aid of a mapping function. To do this, an archive of a predefined size n is used able to store the n best solution vectors, their calculated fitness evaluations and statistical data of each of the optimization variables such as the mean and the variance. The archive is updated whenever a child solution achieves better fitness evaluation replacing the last in sort vector stored. The offspring solution is generated within the normalized range using a mapping function which has as inputs statical data of the optimization variables to provide guidance for the solution evolution. Throughout the process, a predefined number of mutated optimization variables $m \leq D$ can be set to reduce the number of optimization variables to be changed and thus reduce the computational needs. Further details about the MVMO can be found in [114].

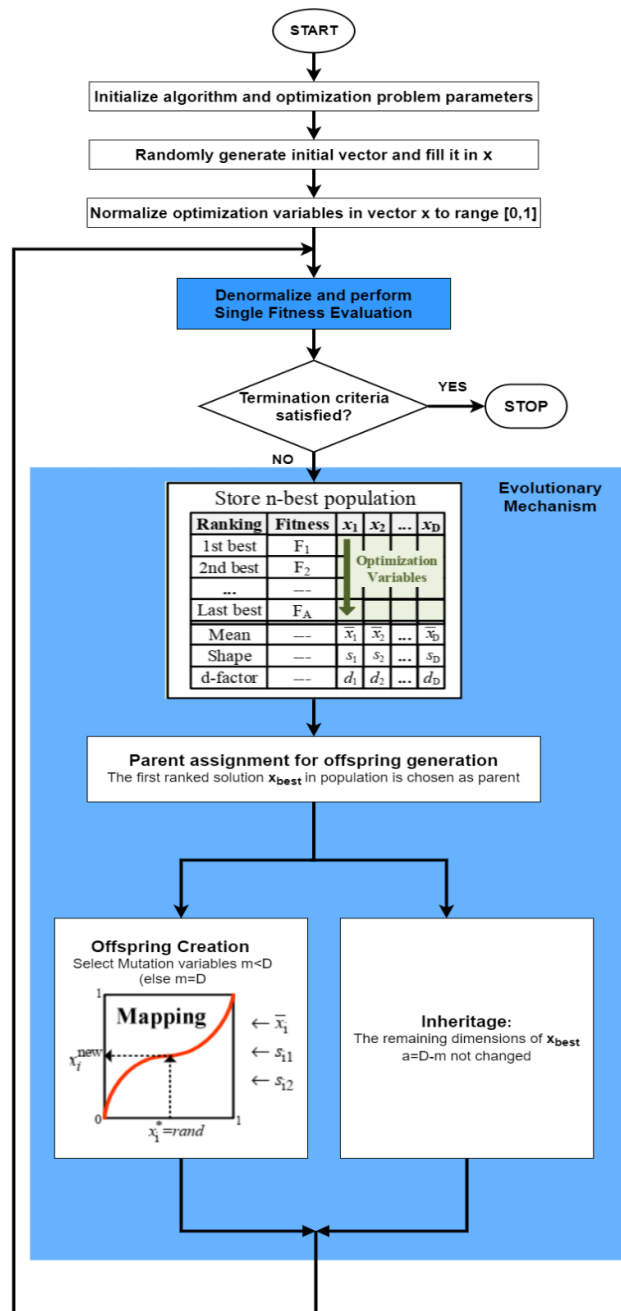


Figure 4.2: MVMO algorithm algorithmic process. Fitness evaluation counter denoted by i [114].

4.5. MVMO algorithm implementation in Python and co-simulation with DPF

The execution of the MVMO algorithm in a python-DPF co-simulation environment for solving the optimization problem of interest requires various steps analyzed below:

- Definition of the MVMO algorithm in Python
- Definition of the problem formulation (Objective function, boundaries, constraints, optimization vector and variables, initial solution vector) and scripting in Python
- Creation of a co-simulation environment between Python and DPF
- Gain access to the DPF objects of through Python
- Definition of import/export files
- Calculation of the load flow and initial conditions-system initialization
- MVMO algorithm initialization and execution through python
- Result collection and export

A short description of each of the steps is provided below:

Definition of MVMO algorithm in Python: In this study the MVMO algorithm has been programmed in Python 3.8. The python file contains the mvmo class with its functions and is callable by any python script if the corresponding module is imported. The mvmo class contains various functions for the algorithm initialization, the constraints fulfillment, the main function that contains the body of the algorithm and the function that optimizes the value of the input objective function. In the utilized version of MVMO a single offspring solution is generated based on the based achieved fitness evaluation so far. To use the mvmo class the user should provide the necessary inputs: the termination criteria (number of iterations), the number of mutated variables, the size of the archive and the platform of execution (in this case DPF). Furthermore, each of the functions requires a set of inputs such as the objective function considered, the boundaries, the constraints and an initial vector that should be provided to enable its execution. The complete MVMO algorithm class with its functions implemented in Python 3.8 based on [114] can be found in Appendix E.

Definition of problem formulation: To initialize the algorithm, the user should develop a script containing the complete problem formulation. This can be either done in the main python file or in a separate file callable by the main script. In this study the different problem formulations considered have been included in the main python script as separate functions. The latter ones although they approach the optimization problem from different perspective, they share the same structural philosophy. Initially, a candidate optimization vector is provided as input to the function so that its variables represent a parameter of an element in the modified system that needs to be optimized to offer improved frequency response. Based on that, the function modifies the corresponding parameter with respect to the candidate solution vector as explained in Chapter 3. Then, load flow and initial conditions are calculated followed by the execution of the RMS time domain simulation. The variables of interest in the RMS simulation have already been defined in DPF and a result object is created in DPF. The latter one is accessed by python and is stored in a csv file in a predefined form that can be later read by the python script to perform the fitness evaluation. Finally, at the output of the objective function in python the candidate solution vector is provided with the fitness evaluation result.

Creation of a co-simulation environment between python and DPF: To enable the execution of python scripts in DPF an interface between python and DPF has to be created. To do so, a python object (ComPython)

should be created in DPF library under the folder scripts. Then, the script developed has to be loaded in the object created. Further details about the functionalities of the python object can be found in [116]. It is also important to utilize the same version of python in both platforms to enable the co-simulation process. For this reason, in DPF the python version should be set accordingly and the system path in the python script should be set to the corresponding DPF python folder. After that, the powerfactory module should be imported in the python script and the `powerfactory.GetApplication()` function has to be used to enable modifications in DPF elements. Finally, to execute the MVMO algorithm, the `mvmo` class should be imported to the main script.

Access to DPF objects: During the iterations of the MVMO algorithm, various parameters of the controllers of the HVDC links, electrolyzers and WTs have to be modified with respect to candidate vectors. To enable this modification, access should be enabled to the corresponding DPF objects. Hence, special functions of powerfactory module can be used to define and access the DPF objects and parameters of interest. Having defined these variables in python, the parameters of the corresponding elements can be modified. Further information about the different functions of the powerfactory module can be found in [116].

Definition of import/export files: As explained in step 2 to gain access to the results of the RMS simulations and use them for the calculation of the fitness evaluation, the results should be exported from DPF in a form readable from python. The best method to tackle this problem is to export the results from DPF in a csv file in the required form and then to read and load them from the csv file to python. To achieve this, in the python script an export csv file and the required form of the data stored should be clearly defined. Finally, the location in the system path at which the csv file will be saved should also be defined to be reachable.

MVMO algorithm initialization and execution: At this stage the `mvmo` algorithm should be initialized before it can be executed. For this reason, the user should provide the necessary class and function inputs for the `mvmo` algorithm such as the objective function developed at step 2, the variables' boundaries, the termination criteria, the number of mutated variables, constraints, the size of the archive and possibly an initial vector. With all the necessary inputs the `mvmo` algorithm can be executed to solve the optimization problem.

Initial conditions calculation: Having set up the scene for the interface between python and DPF, the main and the supplementary python scripts and clearly defined accessible DPF objects and input-output files, the series of the RMS time domain simulations can start. To achieve this, the initial conditions of the power system should be calculated utilizing the corresponding functions included in the powerfactory module.

Result collection and export: The last commands in the main python script have to do with the access to the results of the optimization algorithm that can be accessed from the corresponding class. These results can be later either plotted in python, stored in an external file or printed in the output window of DPF. Depending on the user preferences, the corresponding set of functions can be utilized.

The various steps analyzed in this section have been carefully followed throughout the whole scripting process and can be observed at the corresponding scripts in the appendix E. The complete flow of the simulation process highlighting the various steps in DPF and python can be observed in Figure 4.3.

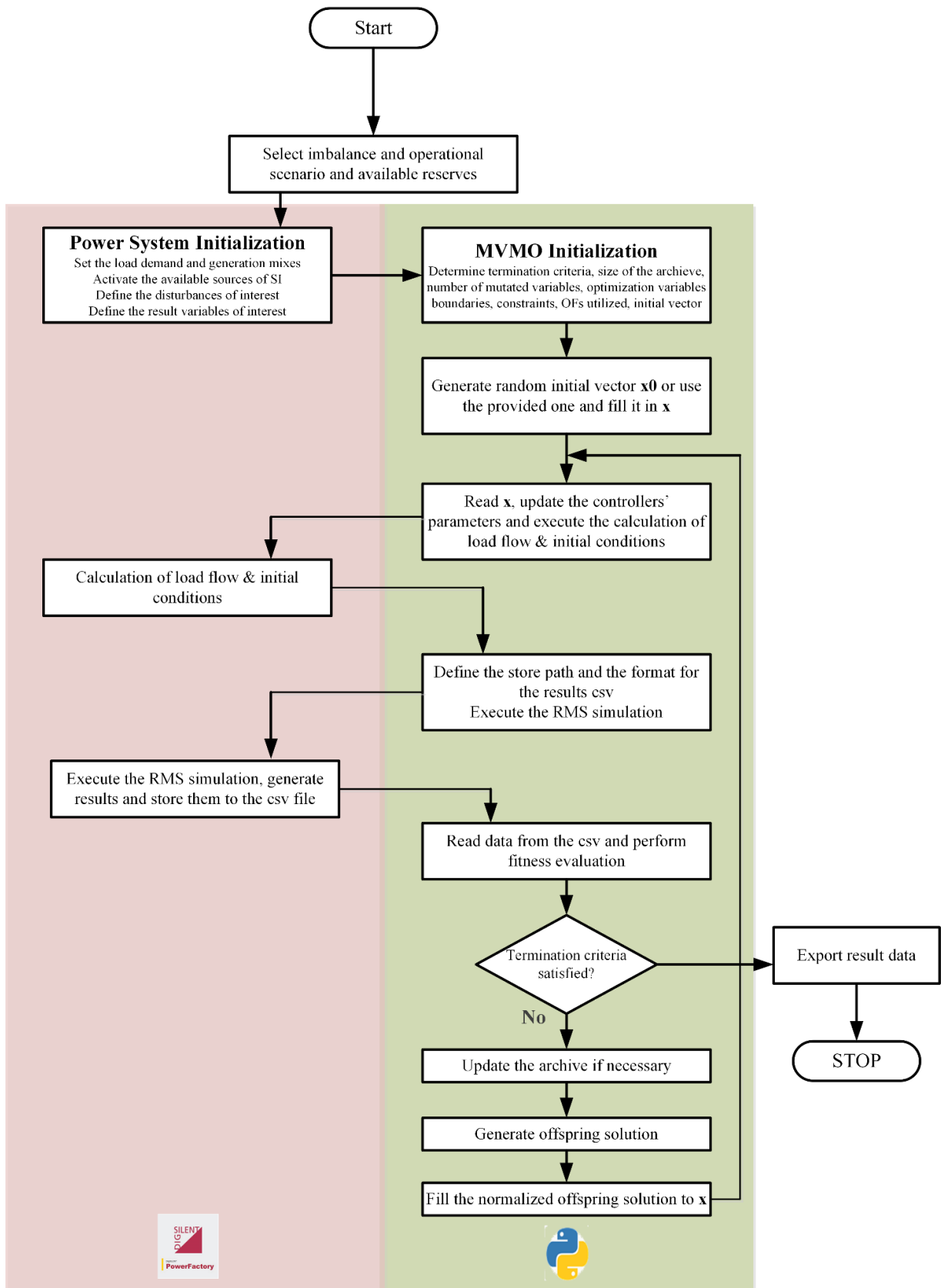


Figure 4.3: Simulation process flow.

5 Results and performance evaluation

5.1. Introduction

The objective of this chapter is to provide further insight on the effectiveness of the FFS strategy utilized in this study. Initially, a set of significantly commonly occurred active power imbalances is defined and applied to the modified PST 16 benchmark system. Then, different groups of FCRs are activated to provide FFS to the participating areas. The parameters of the frequency controllers of the activated FCRs are tuned with the aid of the MVMO algorithm under both proposed problem formulations per event and scenario aiming at optimal coordination among the elements and improved frequency responses in the interconnected areas. For the simulation process Python 3.8 and DPF 2020 have been used and the simulations are performed in Intel Core i5 2.50 GHz processor, 8GB RAM 64-bit operating system. In this way the following points can be evaluated:

- Is the coordinated APG – MVMO control scheme applied to various SI sources able to provide sufficient FFS in the system under different commonly occurred active power imbalances?
- Depending on the type and the location of the disturbance which group of FCRs achieves the best frequency results in the affected area and what is the expense in the supporting areas?
- Which of the FCRs achieve improved performance in terms of maximum instantaneous frequency deviation, RoCof and steady state frequency deviation?
- What is the influence of the location of the FFS elements with respect to the location of the disturbance?
- Which of the problem formulations utilized achieves the best coordinated tuning of the participating elements and thus the best frequency responses in the system?

To examine the efficiency of the control strategy proposed, a set of scenarios has to be defined. Since the modified system consists of 3 electromagnetically decoupled areas, 3 different frequency responses, one for each area, are obtained from each simulation. Hence, active power events should be considered for each one of them. Among the different events the most critical ones are expected to be the loss of significant generating units, frequency-load events due to abrupt demand changes and loss of significant transmission elements. The loss of the largest generating unit is expected to cause significant frequency deviations since the areas are isolated, the inertia levels are much lower compared to the interconnected and synchronously operating system and the FCRs are limited. Load events are also examined as the system should be able to respond fast to common demand variations of a size 6-10% of the total demand of each area taking place at neighboring system nodes. The active power frequency events considered in this study are enumerated below:

1. Loss of largest generating unit in area C (SGU C7G) – Active power imbalance of 960 MW
2. Loss of largest generating unit in area A (SGU A1aG) – Active power imbalance of 750 MW
3. Loss of largest generating unit in area B (WTB10) – Active power imbalance of 1200 MW

4. 10% increase in the load demand of area A (load at bus A5a) – Active power imbalance of 180MW
5. 10% increase in the load demand of area B (loads at buses B8,B10) –Active power imbalance of 500MW
6. 10% increase in the load demand in area C (loads at buses C4,C7) – Active power imbalance of 370MW

For each of these events, different simulations have been performed using different groups of FFS sources. According to their availability, the size of the optimization vector changes as explained in Chapter 4. The groups of available FFS sources considered are: FFS from local WTs, FFS from local electrolyzers, FFS from local means (electrolyzers and WTs), FFS utilizing HVDC links (no local means), FFS utilizing HVDC links and WTs in all areas, FFS utilizing HVDC links and electrolyzers in all areas, FFS utilizing all available means of SI (WTs, electrolyzers, HVDC links). Finally, all the different events and groups of FCRs are examined under the 2 different problem formulations proposed in sections 4.2 and 4.3 to highlight the most promising strategy.

5.2. Results under problem formulation 1

In this section all the different active power frequency events will be applied to the modified system and the parameters of the frequency controllers will be tuned based on problem formulation 1 explained in section 4.2 for the different groups of available sources of FFS. Hence, the goal of the optimization problem is to preserve the frequency in all the participating areas close to its nominal value of 50Hz throughout the whole simulation period. Then, the best achieved responses are compared and analyzed considering the elements participation and the impact on the neighboring areas.

5.2.1. Loss of largest generating unit in area C (C7G)

In this scenario, the largest generating unit in area C is set out of operation on the 1st s of simulation. This loss leads to an active power imbalance of 960MW that needs to be covered by the available sources either synchronous or PEI ones if their frequency controllers are activated. Then the frequency response of the system is obtained for all the different groups of SI sources having their parameters tuned under problem formulation 1. The execution of the MVMO algorithm is characterized by a predefined number of fitness evaluations equal to 100 and a simulation time equal to 60s. Also, depending on the event, different boundaries and initial vectors can be utilized to minimize the research space.

In case no frequency support is provided by SI means such as WTs, HVDC links and electrolyzers, only the remaining SGUs installed at buses C2 and C14 can help with the frequency regulation with respect to their speed-governing systems. In this case, the frequency response of the system can be observed in Figure 5.1. As it can be observed, the frequency in the affected area drops to a nadir of 42.90Hz. Although that during the simulation the frequency response in the affected area restores to a new equilibrium point of 49.15Hz, in real practice the initial deviation is expected to trigger protection and UFLS schemes that would disconnect critical system elements and thus the active power balance will be further perturbed and maybe the system is led to collapse. Hence, it is obvious that frequency support from SI means is more than necessary. In areas A and B, frequency remains at its nominal level of 50Hz since the 3 areas are electromagnetically decoupled by the HVDC links and no supplementary frequency controllers have been activated.

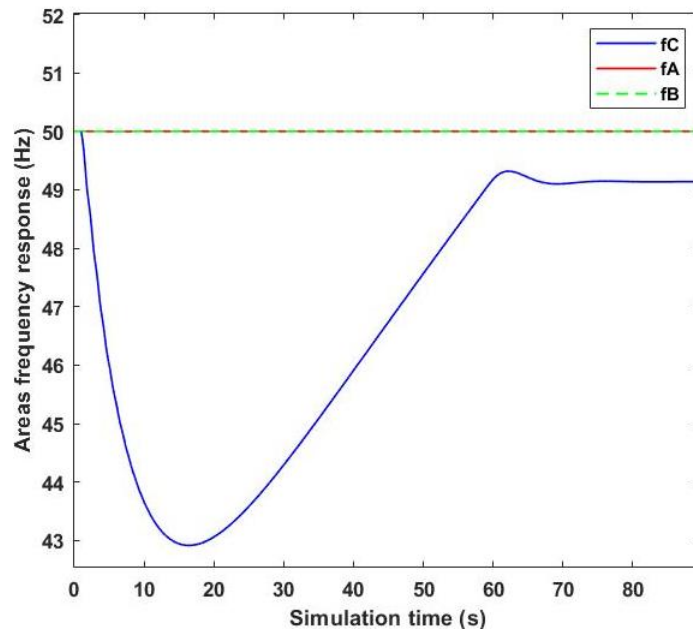


Figure 5.1: Areas' frequency response - Loss of SGU C7G - No FFS.

Following that initial case, supplementary frequency controllers have been activated in the local means of SI to provide FFS and arrest the frequency deviations. The latter means can be considered separately or combined responding to the event at their maximum capability. In that way, it can be examined if the local means can effectively handle the imbalance in a local perspective, a significant result for the effect on the interconnected areas which in this case nullifies. The corresponding frequency responses of the affected area considering the latter FCRs can be observed in Figure 5.2. As it can be observed the best frequency response is achieved when all the local means provide their combined maximal support. In this case, the frequency nadir is at the level of 49.45Hz and stabilizes to 49.73Hz. Also, a second dip occurs after 16s as the support from WTs is interrupted. That is faced by the grid as a second -smaller in size- active power disturbance that needs to be handled. From the rest of the results, it can be concluded that FFS only from the local WTs is not sufficient for the magnitude of the disturbance due to WTs' limitations in capacity and time, whereas support from electrolyzers can lead to significantly improved results due to the larger bid size and their unlimited in time supporting capability. Apart from the affected area, the frequency in areas A and B remains intact at 50Hz as expected. Hence, in these scenarios the fitness evaluation of the OF1 depends only on the frequency response in the affected area. The corresponding results can be observed in Table 5.1. As it can be concluded, even in the best-case local scenario at which all the local means are combined, the frequency response of the affected area does not fulfil the TSO's requirements of maximum instantaneous frequency deviation smaller than 800mHz and maximum steady state frequency deviation smaller than 200mHz.

Table 5.1: Frequency response results – Loss of SGU C7G - FFS local means.

MEANS OF FFS	Local WTs	Local Electrolyzers	Local WTs + Electrolyzers
OF1: Best Fitness Evaluation Value (60s)	101.11	9.4687	4.2732
F_c nadir (Hz)	47.18	48.77	49.45
F_c steady state (Hz)	49.14	49.73	49.73

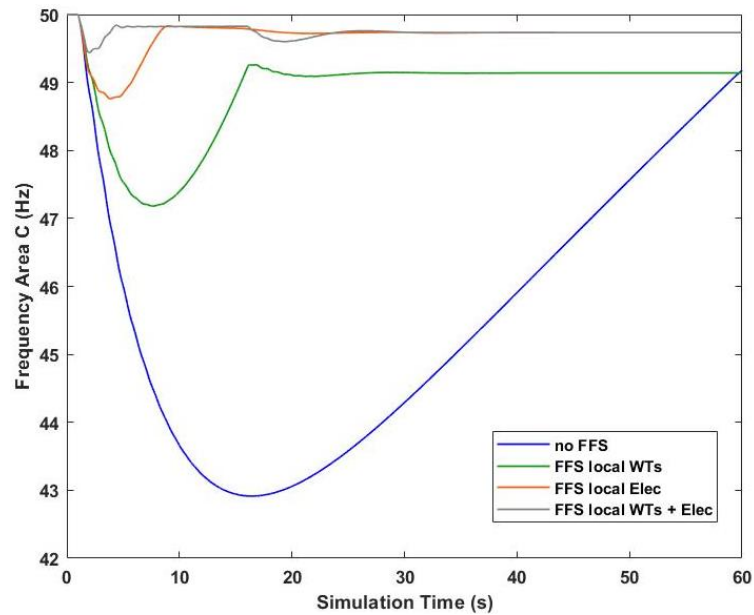


Figure 5.2: Frequency response area C – Loss of SGU C7G - FFS by local means.

Another option to mitigate the imbalance is to alter the power flows in the HVDC links among the interconnected areas. In this way, the imbalance can be shared among the 3 areas and the MVMO algorithm can search for a local optimum result to minimize the effect not only in the affected area but also in the neighbouring areas that now participate in the regulation. The corresponding response of the affected area can be observed in Figure 5.3 in red. In this case, the frequency nadir in the affected area drops to a level of 49.32Hz and stabilizes close to 50Hz. Although this result achieves an acceptable response in terms of limits, it is also clear that during the recovery period a temporary over frequency at 50.2Hz cannot be avoided as the regulation of the HVDC links takes place once per simulation and does not vary according to the instantaneous frequency deviation. Also, since in this case the frequency in the other areas is also affected, the best achieved fitness evaluation is equal to 5.078, a value larger than the one achieved from the local means. This means that the total deviation in the 3 interconnected areas when the imbalance is shared, leads to a worse value of the OF1. However, the combination of the local means and the HVDC links against the imbalance in all the participating areas is expected to lead to improved responses and has been examined.

As it can be observed in Figure 5.3, the frequency response in the affected area can be further improved by combining the local means with the power flows through the HVDC links. 3 different combinations can be considered: FFS from the HVDC links and WTs shown in light blue, FFS from HVDC links and electrolyzers shown in pink and finally FFS from all the installed means of SI in the interconnected areas shown in black. As it is clear, when all the different means are utilized, and the controllers' parameters are optimally tuned by the MVMO algorithm the best frequency response is obtained. In this case, the frequency nadir in the affected area significantly improves to a level of 49.61Hz and stabilizes to 49.97Hz. This result shows the best performance in terms of RoCof, frequency nadir and steady state deviation among the different options for the affected area as it combines the advantages of each of the available sources and can mitigate the possible flaws. Also, since the frequency regulation of the WTs and electrolyzers is based on the instantaneous frequency deviation, no over-frequency event takes place during the recovery period. As far as the other combinations of sources are concerned, it can be concluded that when HVDC links are combined with

electrolyzers, great results can be also achieved due to the supporting capability of these means. However, compared to the best case, a worse frequency nadir is obtained, since when WTs are considered, their fast activation and response can lead to improved inertial response. Finally, considering the combination of WTs and HVDC links, it is obvious that this combination lacks in terms of regulation after the frequency support from the WTs stops leading to a second frequency dip that combined with the time invariant regulation of the HVDC links power flow, leads to worse responses compared to other options.

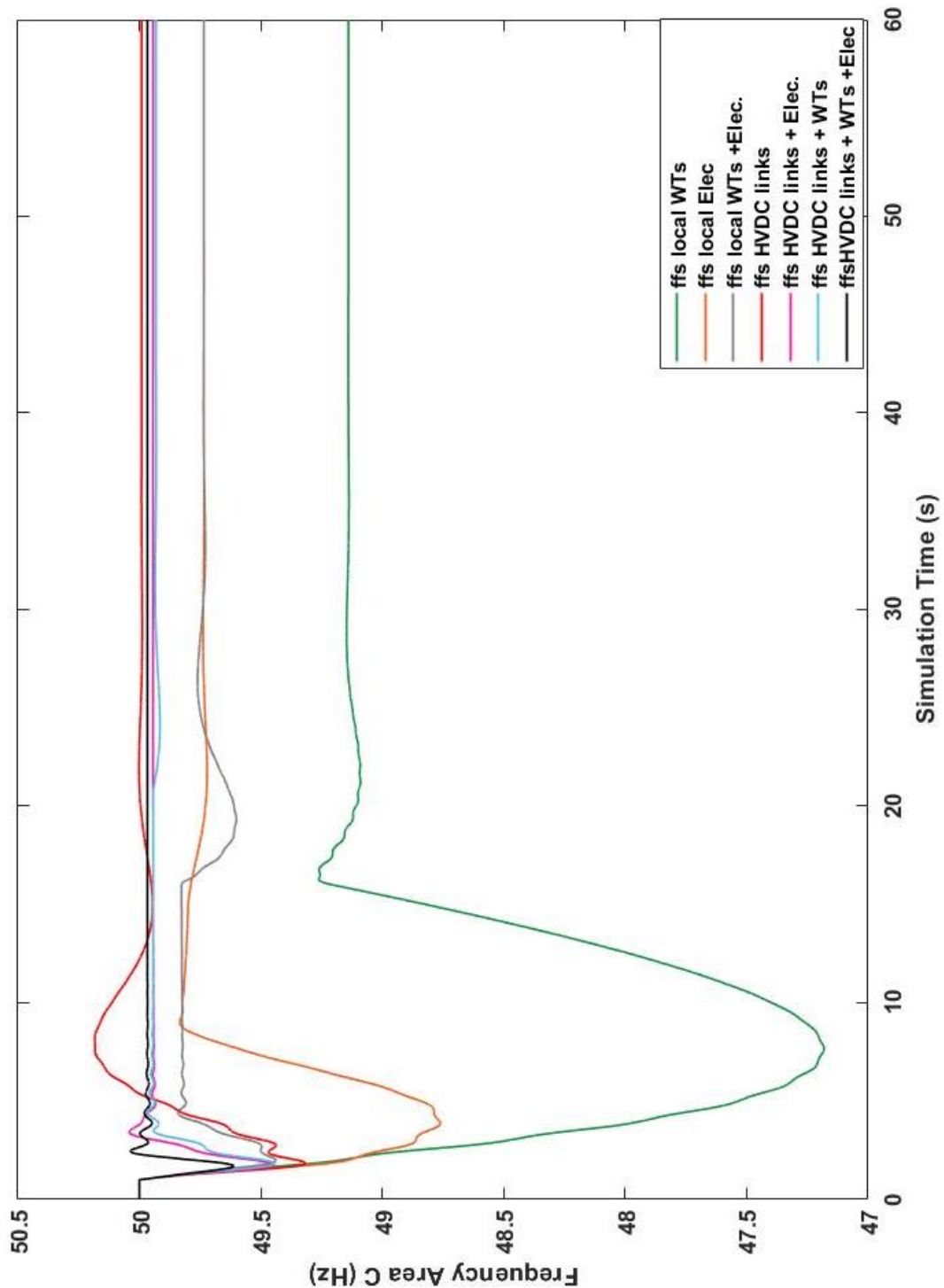


Figure 5.3: Frequency response area C - Loss of SGU C7G - FFS by local and inter-area means.

Apart from the frequency response in the affected area, the impact on the neighbouring areas is also important to be examined. That can be achieved by comparing the value of the best achieved fitness evaluation of the OF1 which depends on the squared difference of the frequency from its nominal value in all the participating areas. The corresponding results can be observed in Table 5.2 for all the different combinations. As it is clear, the best fitness evaluation is achieved when all the different sources are activated. In the affected area, the local means are rapidly activated to arrest the frequency deviation, then in a short amount of time the HVDC links change rapidly their power flows against the imbalance. Due to the fast actions of the controllers of the HVDC links, the change in their power flows is perceived as an active power event in the neighbouring areas, in which the various local means of SI can properly counteract to arrest the deviation, as they are optimally tuned from the MVMO algorithm.

Table 5.2: Frequency response results - Loss of SGU C7G - FFS by local and inter-area means.

MEANS OF FFS	HVDC links	HVDC links + WTs	HVDC links + Electrolyzers	HVDC links + Electr. + WTs
OF1: Best Fitness Evaluation Value (60s)	5.078	3.7094	1.4681	1.3197
Fc nadir (Hz)	49.32	49.45	49.45	49.61
Fc steady state (Hz)	49.99	49.93	49.94	49.97

In case of the best achieved result, with all the installed sources of FFS utilized the frequency response of the interconnected areas can be observed in Figure 5.4. In this scenario, frequency in the affected area has a nadir of 49.61Hz and stabilizes to 49.97Hz. In the supporting areas, in area A the frequency response has a maximum deviation of 49.87Hz that stabilizes to 49.94Hz in a short time, whereas in area B the initial rapid drop due to the low inertia conditions this area exhibits is arrested followed by a time period at which the frequency continues to drop at a short rate. After 15s, a second dip in the frequency in area B is observed due to the interruption of support from WTs. However, the frequency finally stabilizes at 49.86Hz. All the aforementioned responses fulfil the requirements set by TSOs of maximum instantaneous frequency deviation smaller than 800mHz and steady state deviation smaller than 200mHz and also achieve the minimum fitness evaluation under problem formulation 1. This means that it constitutes an acceptable result that achieves an optimal coordination among the elements with the minimum effect in the neighbouring areas.

Apart from the frequency response itself, the behaviour and the tuning of the different elements with respect to their characteristics, location and size and the disturbance itself is of great importance. As it can be observed in Figure 5.5 to Figure 5.7 when the disturbance in area C occurs, the frequency starts to drop rapidly and has not been perceived by the local reserves. When the drop reaches the threshold of the frequency controllers of the WTs and the electrolyzers, these elements change their outputs rapidly according to the measured deviation and their tuned parameters to support the grid. Electrolyzers installed closer to the disturbance such as C3 and C6 exhibit significant changes in their active power consumption and at higher rates compared to the ones installed in electrically remote points in the same area. Consequently, the units closer to the disturbance have more significant changes in their outputs and electrolyzers of larger bid size installed close to the disturbance shoulder the imbalance due to their size and their faster power injection capability.

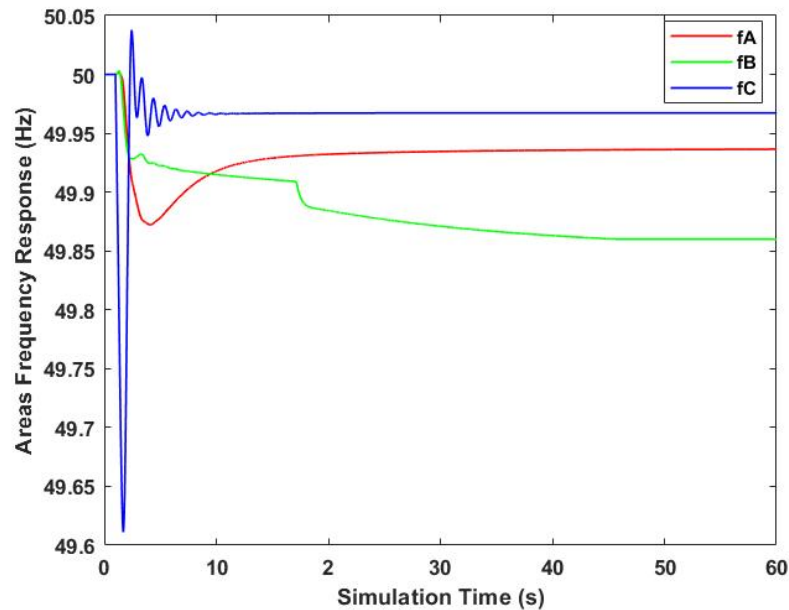


Figure 5.4: Areas' frequency response - Loss of SGU C7G - FFS by all SI means.

Following this initial period of local support, HVDC links are also activated. That happens 0.3s following the disturbance, as a measurement – activation time delay has been assumed as explained in Chapter 3. Until that point, frequency in the other areas and the power output of their FCRs are unaffected. Then according to the solution of the optimization algorithm, the power flows in the links change linearly as observed in Figure 5.7. The power flow between areas A and C increases by 350MW at a rate of 780MW/s, in B-C link changes its direction and now area B offers to area C 257MW of active power at a rate of 700MW/s and finally the power flow between areas A and B is adjusted by 140 MW to mitigate the frequency deviations in the supporting areas. The rapid power injection to area C, leads the frequency in the affected area to restore faster and thus the consumption of the local electrolyzers increases again and stabilizes close to its nominal value, whereas the frequency support from the WTs stops and their output returns to its nominal value. In the supporting areas A and B, the electrolyzers and the WTs installed, perceive the disturbance as an active power imbalance caused by the change in the tie-lines power flows and thus they are activated to arrest the local frequency deviations after a short period. This helps to the minimization of the effect of the original imbalance in the supporting areas. Electrolyzers in area A exhibit a similar pattern in the change of their active power output in terms of bid and rate as in Figure 5.6. Their consumption finally stabilizes at a new equilibrium point below their nominal value as the steady state deviation of the frequency is out of the deadband zone of the electrolyzers and these units exhibit unlimited in time supporting capability. In area B the larger WT, WT B10, is the most significantly affected one as observed in Figure 5.5 due to its large supporting capacity followed by WTB2 and WTB8. After 15s, their outputs return to their nominal values and thus a dip in frequency in area B occurs. The latter one, affects the power consumption of the local electrolyzers according to the deviation after a short period as it is clear in Figure 5.6. Finally, with the aid of the local SGUs and the regulation of the local electrolyzers consumptions, the frequency reaches a new equilibrium point. For the restoration of the areas' frequency back to 50Hz, SFC schemes need to be activated, which is out of the scope of this study.

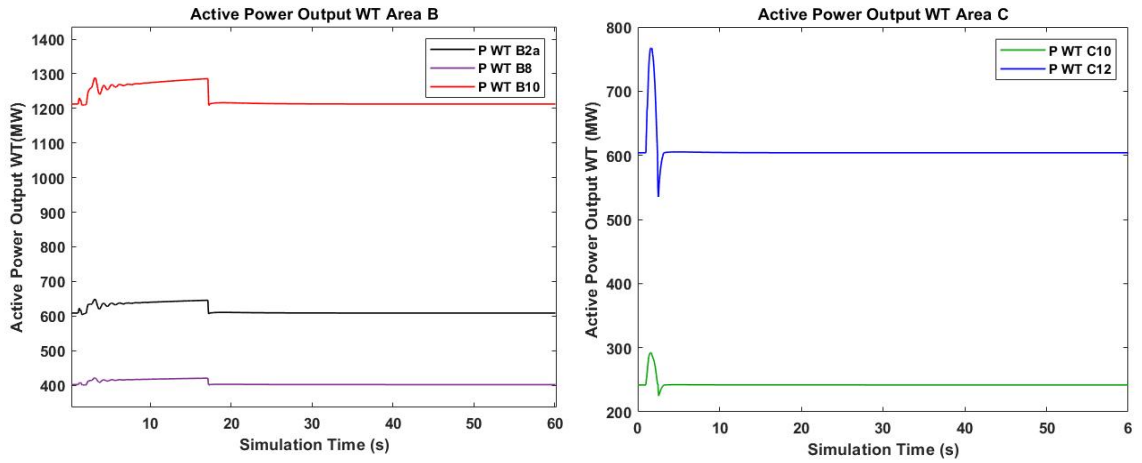


Figure 5.5 WTs' active power output - Loss of SGU C7G – FFS by all SI means.

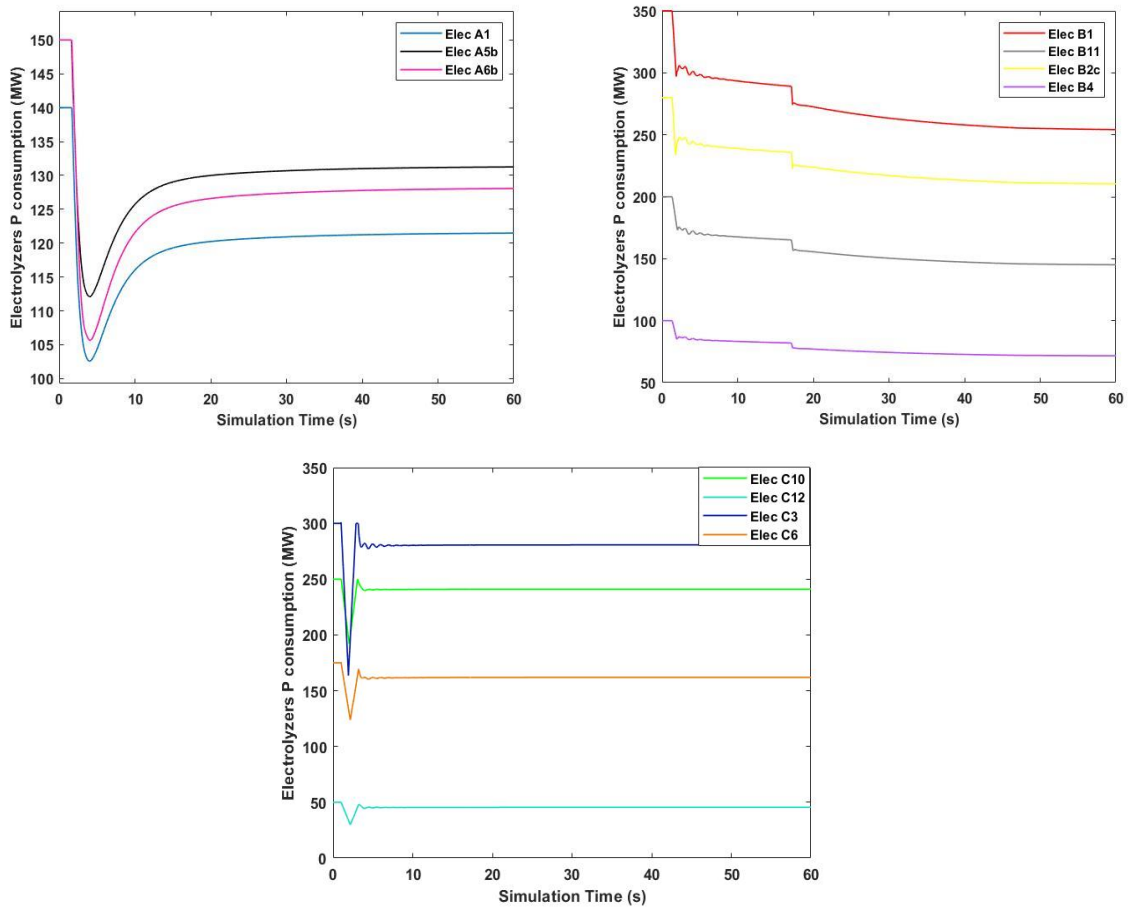


Figure 5.6: PEM Electrolyzers' power consumption - Loss of SGU C7G -FFS by all SI means.

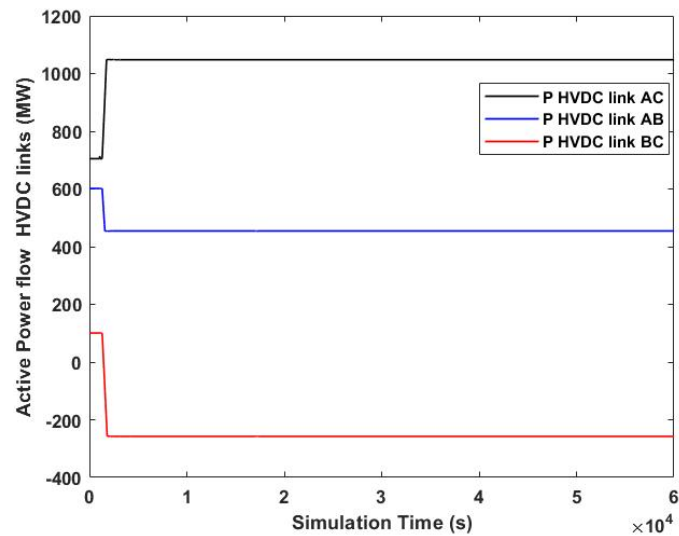


Figure 5.7: Active Power Flows HVDC links – Loss of SGU C7G – FFS by all SI means.

5.2.2. Loss of largest generating unit in area A (A1aG)

In this scenario the largest generating unit in area A, SGU A1aG, is set out of operation at the 1st s of the simulation. This constitutes an active power imbalance of 750MW in area A and a loss of the local reference machine. The effect of this imbalance in the system's frequency has been evaluated under different scenarios: when no SI is provided and when FFS is provided by different groups of FCRs with optimally tuned parameters under the problem formulation 1 considering a number of 100 iterations and simulation time of 60s.

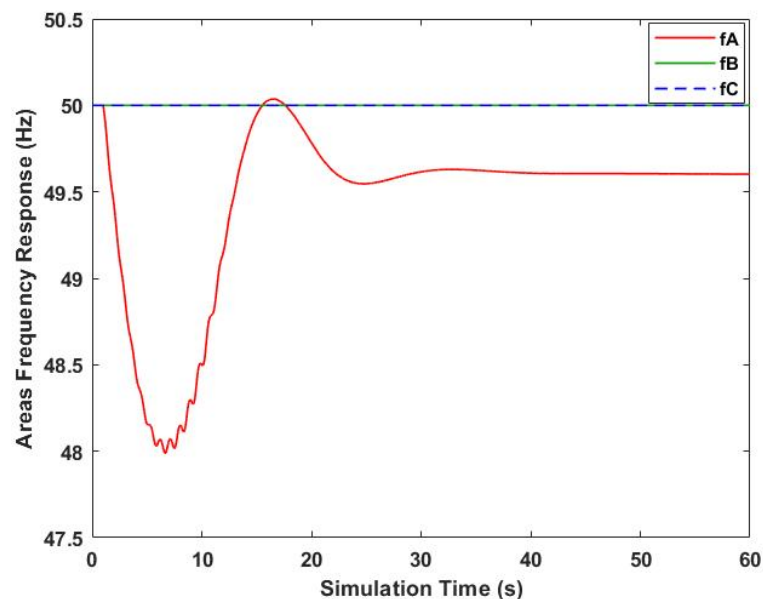


Figure 5.8: Areas' frequency response - Loss of SGU A1aG - No FFS.

In case no frequency support is provided by any means of SI, the SGUs installed in area A adjust their power outputs with respect to their speed-governing systems to arrest the deviation. Since area A has no local RES but a larger number of SGUs compared to other areas, it is expected to have an improved response compared to the other areas for a disturbance of the same magnitude. Still, the inertia of area A is decreased compared to the original system as the areas are electromagnetically decoupled and 20% of the local demand

has been replaced by non-synchronous demand units. Under this scenario, the areas' frequency response can be observed in Figure 5.8. When the imbalance occurs, the frequency in area A drops at high rate and arrives to a frequency nadir of 48Hz. This frequency drop is expected to put the system in danger and lead to the activation of protection schemes. Even if no load demand is disconnected, the SGUs can restore the frequency to a level of 49.6Hz. However, this frequency response in real practice forces the system out of the normal operating state and is not considered as acceptable for commonly occurred disturbances. Another important observation is that the frequency in areas B and C remains intact at 50Hz, due to the effective decoupling of the areas achieved by the HVDC links. For the reasons above, FFS by means of SI installed such as HVDC links and PEM electrolyzers is considered important and has been examined.

In a first sub-scenario, all the local sources of FFS are activated to offer ancillary services to area A. Since no WTs are installed locally, only electrolyzers may offer support by rapidly changing their active power consumption. Operating at their maximum capability in terms of magnitude and rate, the frequency response of the 3 areas can be observed in Figure 5.9, where frequency in the affected area is shown in red in solid style considering the initial case of no FFS and in dashed style when electrolyzers are activated. As it is expected, the frequency in area A improves in terms of RoCof, nadir and steady state deviation as the local demand of the electrolyzers reduces rapidly. In this case, the maximum deviation is 49Hz and restores to 49.77Hz reaching a new equilibrium point. However, the latter support from the electrolyzers is insufficient to lead to a response within the normal operating bounds due to the technical limitations in capacity and rate of the electrolyzers. Also, from Figure 5.9 it is clear that the frequency in the interconnected areas remain constant at 50Hz and thus the calculation of OF1 in this case is based only on area A and is equal to 6.8412.

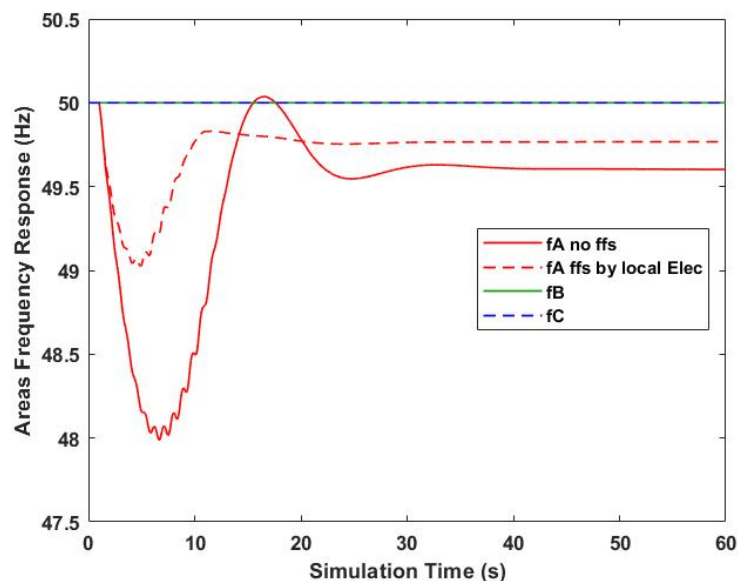


Figure 5.9: Areas' frequency response - Loss of SGU A1aG - FFS by local electrolyzers.

Having examined the scenario of FFS from the local means, the next set of simulations evaluates the coordination of available sources in all the interconnected areas. In this case, the power flows of the HVDC links are adjusted based on the solution of the optimization problem. The local sources of FFS may be considered or not formulating 3 different scenarios: FFS only from HVDC links, FFS from HVDC links and electrolyzers and FFS from all the installed SI means. The scenario of support from HVDC links and local WTs

will not be considered as no WTs are installed in the affected area. In case of frequency support from the HVDC links, the new setpoints and the rates applied are determined by the MVMO algorithm. The best achieved result leads to a frequency nadir of 49.6Hz that stabilizes at 49.93Hz in the affected area. However, the supporting areas are also affected leading to a value of the best achieved fitness evaluation equal to 3.7374. The impact on the supporting areas can be minimized with the optimal utilization of the electrolyzers and the WTs installed in areas B and C. Also, electrolyzers installed in area A can be used to further minimize the frequency excursions. The responses from all the aforementioned scenarios can be observed in Figure 5.10, whereas the corresponding detailed results with the best achieved fitness evaluations in Table 5.3.

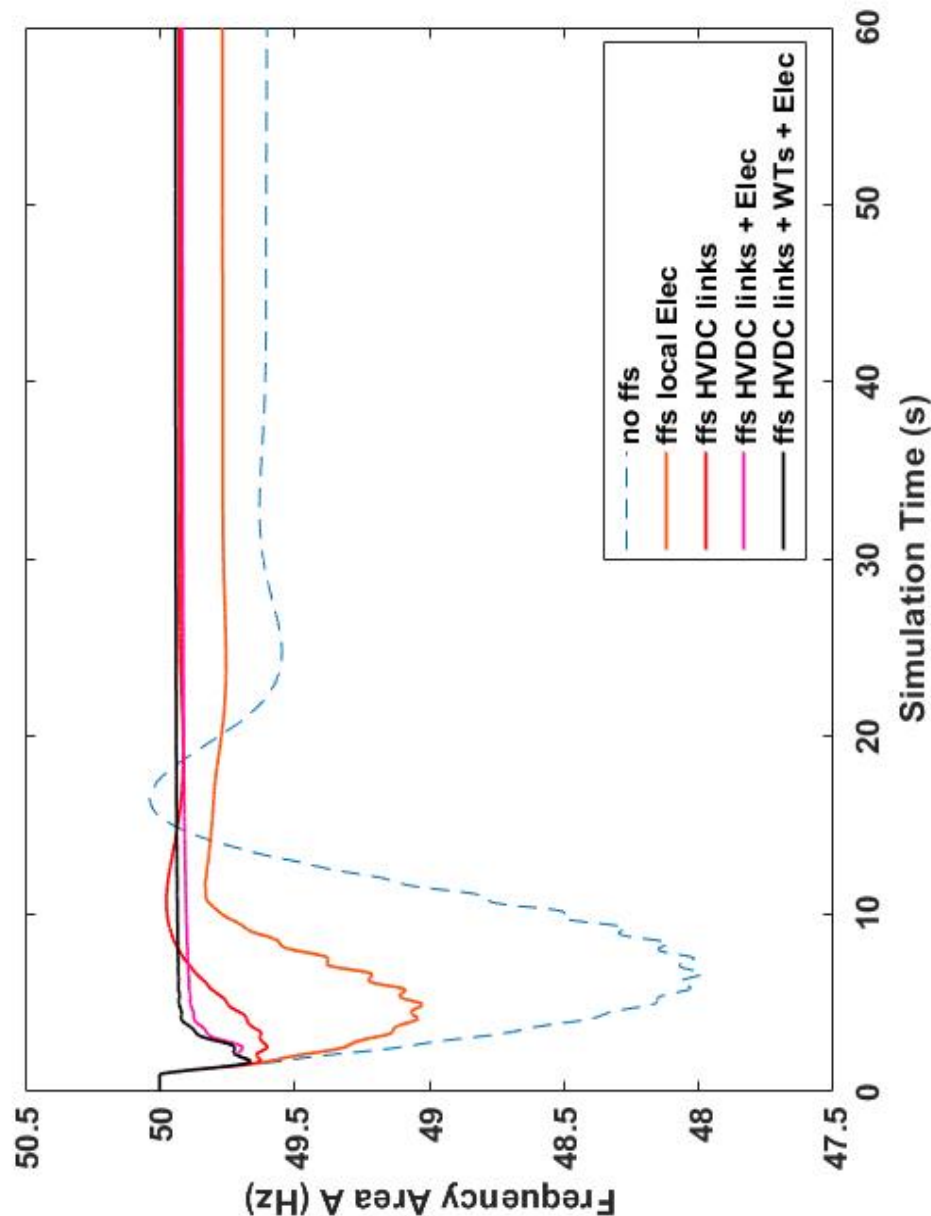


Figure 5.10: Frequency response area A - Loss of SGU A1aG - FFS by local and inter-area means.

As it can be observed the best frequency response in the affected area and best fitness evaluation value are obtained when all the available means of FFS in the interconnected areas are utilized. However, minor differences are encountered with the scenario at which WTs are not providing FFS. This can be explained

considering that the disturbance takes place in an area with no WTs and the impact on the other areas is not large to lead to changes in the WTs output. Additionally, the WTs can only support the grid for 15s and thus for small in magnitude active power disturbances no significant differences are encountered.

Table 5.3: Frequency response results -Loss SGU A1aG- FFS by local and inter-area means.

MEANS OF FFS	Local Electrolyzers	HVDC links	HVDC links + Electrolyzers	HVDC links + Electr. + WTs
OF1: Best Fitness Evaluation Value (60s)	6.8412	3.7374	1.0433	0.9436
F _A nadir (Hz)	49	49.6	49.67	49.67
F _A steady state (Hz)	49.77	49.93	49.92	49.94

Analysing the best achieved frequency response considering the optimal coordination of all the installed sources of FFS, the areas' frequency response can be observed in solid lines in Figure 5.11, in comparison to the original case shown in dashed line. As it can be observed, the frequency of the affected area improves significantly in terms of RoCof, nadir and steady state deviation whereas the effect of the imbalance on the supporting areas is limited by the optimal coordination and rapid response of the local elements such as electrolyzers and WTs. In fact, area A experiences a nadir of 49.67Hz that stabilizes very fast at 49.94Hz. Area B experiences an initial drop arrested by the rapid response of the FFS means which is followed by a second dip due to the limited in time support from the WTs. Finally, the frequency in area B stabilizes at 49.9Hz. In area C, a frequency nadir is met at 49.93Hz which restores in a short period at 49.95Hz. Consequently, the frequency in all areas remains within the normal operating limits throughout the simulation.

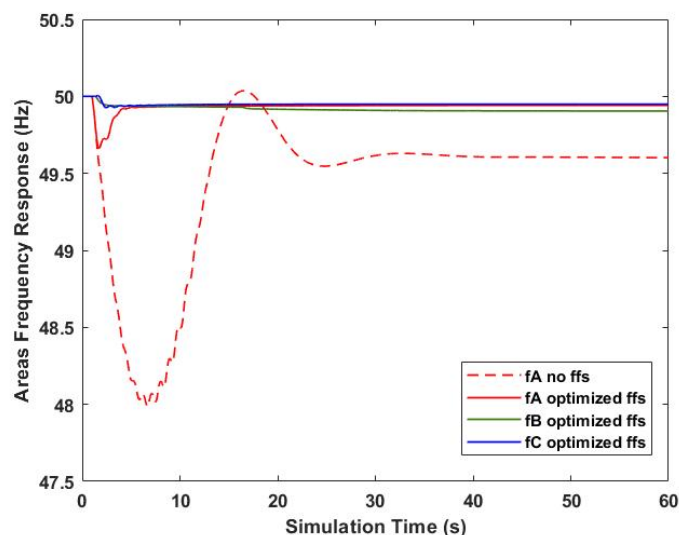


Figure 5.11: Areas' frequency response - Loss of SGU A1a - FFS by all SI means.

As far as the other supporting elements is concerned, when the imbalance occurs, the frequency drop in area A triggers almost instantaneously the activation of the local electrolyzers, which change their demand according to the instantaneous deviation. In this period, support from other areas has not been activated yet due to the assumed time delay of 0.3s for the actuation of the HVDC links. As it can be observed in Figure 5.12, the electrolyzers installed closer to the disturbance, such as A1, experience the most significant changes

in their demand. The frequency in the affected area is then arrested and starts to restore leading the consumption of the electrolyzers to increase again and to stabilize at a new point, lower than the nominal one as these units offer unlimited in time support, whereas the steady state frequency deviation of the frequency is out of the deadband zone of the electrolyzers. Additionally, it can be mentioned that the closest to the disturbance unit experiences not only the most significant change in its consumption during the transient period but also in steady state. For example, as it can be observed in Figure 5.12, electrolyzer A1 has the most significant shift from its nominal demand equal to 30MW. The latter shows the tendency of the optimization algorithm to make the FCRs installed close to the disturbance accountable for its treatment.

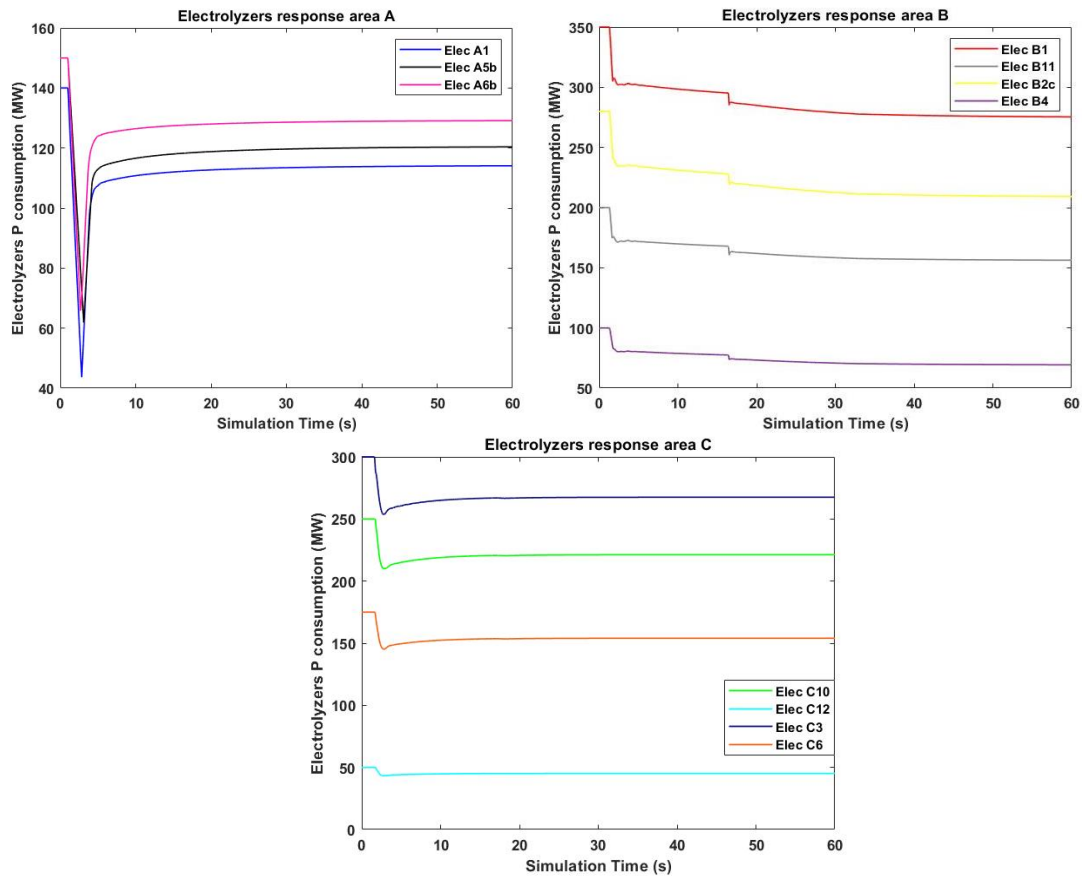


Figure 5.12: PEM Electrolyzers' power consumption - Loss of SGU A1a -FFS by all SI means.

When now the HVDC links are activated to support, power flows from area A to neighboring areas decrease to regulate the local imbalance. As it can be observed in Figure 5.13, HVDC link AC changes its active power setpoint by 350MW at a rate of 760MW/s to decrease the exporting flows to area C. Similarly, HVDC link AB adjusts its power flow to a reduced level of 400MW, a change performed at 720MW/s. Finally, power flow between areas B and C also changes and the direction of it reserves. Now area B provides 100MW of power to area C. That result aims to mitigate the impact on area C which experiences the largest change. Due to the changes in the HVDC links, the active power balance in the neighboring areas is also perturbed leading to frequency deviations. Hence, WTs and electrolyzers are activated to sustain and restore the local frequency. In area B as its clear in Figure 5.12, the electrolyzers whose demand is affected the most are those installed closer to the origin of the disturbance, which for the supporting areas is the HVDC links' CCPs and thus electrolyzer B2c experiences a large change. Also, the bid size and the ramp rate capability of each one of

them plays a significant role on their accountability. The electrolyzers' demand in area B is also affected at a later stage by the abrupt change in output of the WTs due to their limited in time supporting capability. The WTs in area B are also supporting to handle the local disturbance. In fact, as observed in Figure 5.14, the size and the technical limitations of the WTs installed determine the magnitude of their support. However, their limited support is not sufficient to restore the frequency to a value within their deadband zone. In area C, electrolyzers adjust their consumption following the changes in HVDC links that lead to the local perturbations. Again, in this case the units installed close to the origin of the imbalance, buses C1 and C8, shoulder the disturbance. Hence, as observed in Figure 5.12, electrolyzers C3 and C10 have the most significant adjustment, whereas electrolyzer C12 being remotely installed has almost a constant consumption. Finally, their consumption stabilizes at a new equilibrium point lower than their nominal consumption as expected. For the WTs in area C, Figure 5.14 shows that they are triggered to offer FFS after the disturbance is shared through the HVDC links. However, the imbalance is already handled by the local electrolyzers and thus no significant changes are encountered in the outputs of the WTs which quickly restore to their nominal outputs.

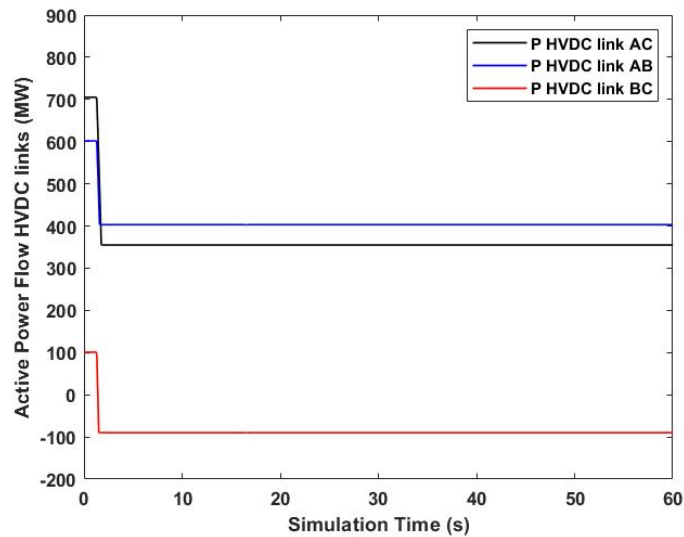


Figure 5.13: Active Power Flows HVDC links – Loss of SGU A1aG - FFS by all SI means.

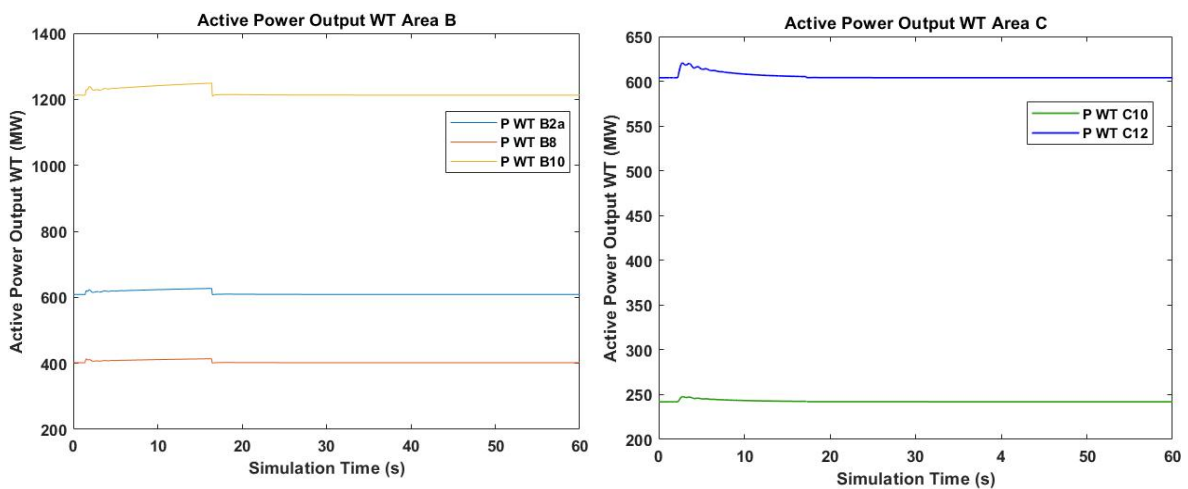


Figure 5.14: WTs' active power output - Loss of SGU A1aG - FFS by all SI means.

5.2.3. Loss of largest generating unit in area B (WTB10)

In this scenario the largest generating unit in area B, WTB10, is set out of operation on the 1st s of simulation, which corresponds to an active power imbalance equal to 1200MW. The effect of the imbalance has been evaluated under all the scenarios utilizing all the different groups of available FFS sources. Tuning of the frequency controllers is based on the MVMO algorithm under problem formulation 1 and the calculation of OF1 value refers to a simulation time of 60s.

If no FFS is provided by any means of SI, only the local SGUs installed at buses B2b and B3 can handle the imbalance. Hence, the frequency response shown in Figure 5.15 depends on the inertia constants of the local SGUs and the characteristics of their speed-governing systems. As it is clear, the frequency in the affected area initially drops to 49.22Hz and tries to restore. However, the active power regulation provided by the SGUs is not sufficient and the frequency tends to drop again before stabilizing at a level of 49.36Hz. Moreover, the frequency in the interconnected areas A and C remains constant at 50Hz being decoupled by the HVDC links. The frequency response in this case shows the inability of the local SGUs to handle the imbalance and restore the frequency at an acceptable point as this area is characterized by a large share of non-synchronous generation and imports that significantly limit its conventional frequency regulation capabilities. As a result, FFS by local means of SI and increased imports are more than necessary.

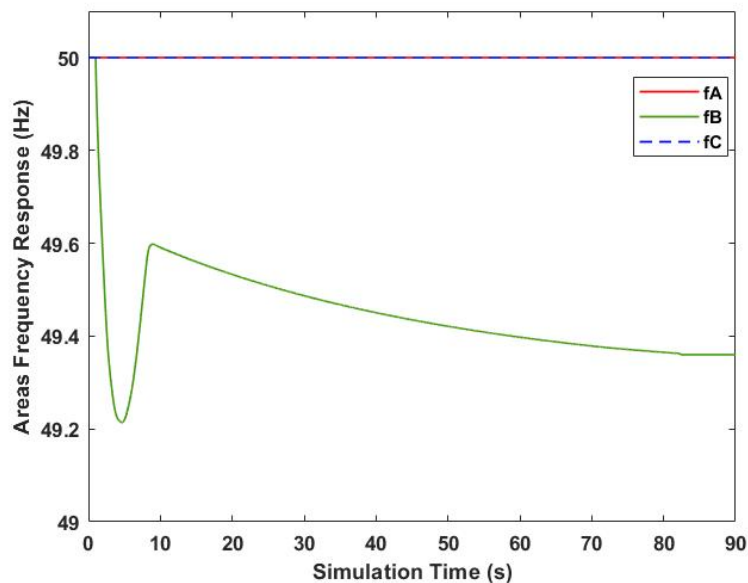


Figure 5.15: Areas' frequency response - Loss of WTB10 - No FFS.

To mitigate the active power imbalance in area B, the locally installed means of SI may be utilized. For this reason, 3 set of simulations can be performed: FFS by local electrolyzers, FFS by local WTs and finally FFS by all the local means. Due to the magnitude of the disturbance all the local means are set to operate at their maximum supporting capability. The frequency response of the affected area in the latter set of simulations can be observed in Figure 5.16, whereas the simulation results are presented in Table 5.4. As it is expected the best frequency response for the affected area is achieved utilizing all the available local means. The latter ones can offer improved frequency performance in terms of initial frequency drop, RoCof and steady state deviation. In the cases at which the local electrolyzers provide their support to the imbalance, the frequency seems to reach a stable point faster, whereas when support from WTs is provided, a second dip in the

frequency is observed due to their limited in time supporting capability. In the best achieved response by the local units the frequency in area B stabilizes at 49.69Hz, a level which is still out of the acceptable bounds set by the regulations. Also, it can be observed that in some scenarios the steady state deviation may be larger than the initial drop as the supporting capability of the local elements and the SGUs remaining is quickly released. That is an expected response as the area is characterized by a large non-synchronous share of imports and generation [104].

Table 5.4: Frequency response results - loss WTB10 - FFS local means.

MEANS OF FFS	Local WTs	Local Electrolyzers	Local WTs + Electrolyzers
OF1: Best Fitness Evaluation Value (60s)	6.8003	1.7993	1.5302
F_B Initial drop (Hz)	49.44	49.72	49.81
F_B steady state (Hz)	49.37	49.69	49.69

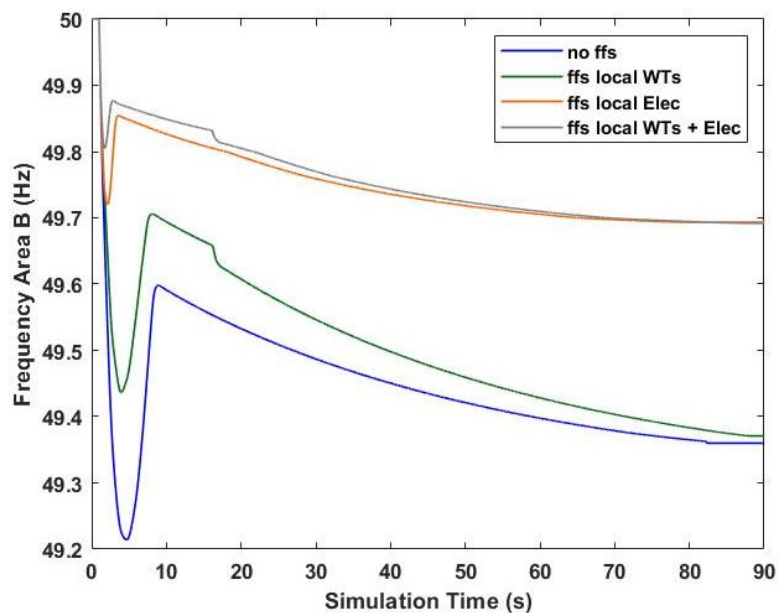


Figure 5.16: Frequency response area C – Loss WTB10 - FFS by local means.

Another possible scenario to deal with the imbalance in area B is to optimally modify the power flows of the HVDC links. In this case, the electrolyzers and WTs installed may also provide FFS or may have constant outputs. This leads to 4 possible combinations of the available sources: FFS only from HVDC links, FFS from HVDC links and WTs, FFS from HVDC links and electrolyzers and FFS from all the installed means of each area. The frequency response of area B considering all the different groups of FFS sources may be observed in Figure 5.17. As it is clear, the best results in terms of RoCof, initial frequency drop and steady state deviation in area B can be achieved when all the installed SI means are cooperatively supporting the grid. Also, it can be concluded that when the WTs are acting against the imbalance improved RoCof and initial drop can be achieved as the share of the WTs in this area is significant and faster activated than the HVDC links. Furthermore, when support from electrolyzers is also considered, the frequency reaches a stable point much faster compared to other cases. Also, it is clear that for such a large in magnitude disturbance, the only cases that satisfy the requirements of the maximum allowed instantaneous and steady state frequency deviation are those who either utilize all the installed means of SI or at least the HVDC links and the areas' electrolyzers.

Detailed results of the latter set of simulations and the best achieved fitness evaluations can be observed in Table 5.5. Examining the impact on the neighboring areas when HVDC links modifications are applied, the values of the best achieved fitness evaluations highlight the role of electrolyzers and WTs in the supporting scheme. When not considered, the modifications on the HVDC links can significantly affect the neighboring areas leading the value of the OF1 to 4.8103, whereas when local means provide their support this value drops close to 1. Still the best achieved scenario is the one that utilizes all the available means with a value of 1.1775.

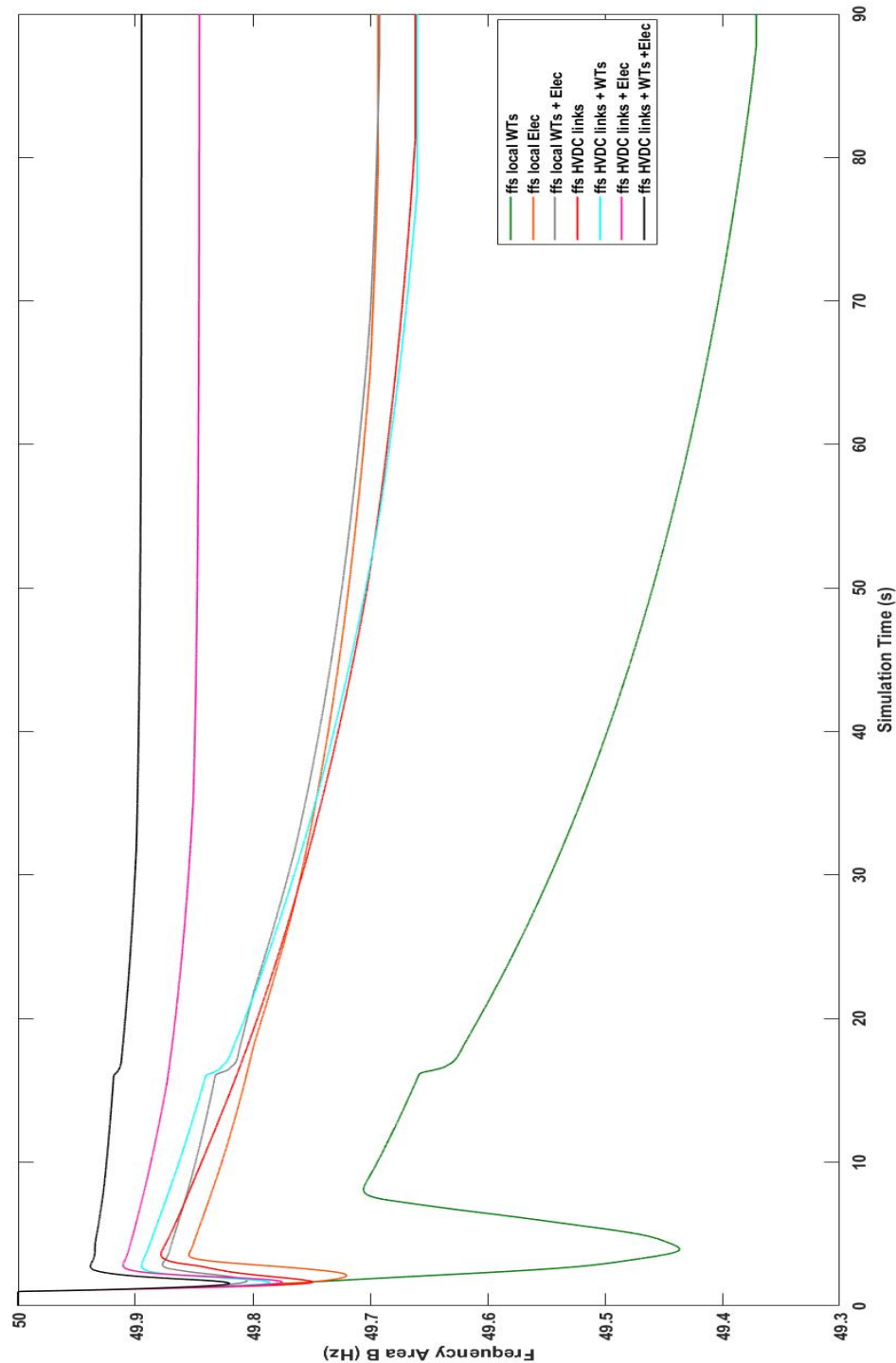


Figure 5.17: Frequency response area B - Loss of WTB10 - FFS by local and inter-area means.

Table 5.5: Frequency response results - Loss of WTB10 - FFS local and inter-area means .

MEANS OF FFS	HVDC links	HVDC links + WTs	HVDC links + Electrolyzers	HVDC links + Electr. + WTs
OF1: Best Fitness Evaluation Value (60s)	4.8103	4.11	1.2963	1.1775
Fc nadir (Hz)	49.75	49.79	49.78	49.82
Fc steady state (Hz)	49.66	49.66	49.85	49.89

In the best scenario the areas' frequency response can be observed in Figure 5.18. In this case, it is clear that area C is the one that is forced by the optimization results to shoulder the imbalance. Frequency in area C drops to a nadir of 49.77Hz followed by a restoration period characterized by a second dip due to the expected interruption of support from WTs before stabilizing at 49.83Hz. In area B, frequency drops at 49.82Hz and restores due to the provided FFS close to 49.9Hz. Finally, area A being a synchronous area experiences a drop to 49.87Hz which restores to 49.94Hz with the aid of the synchronous and non-synchronous means. Although in all areas the bounds of the normal operating state considering the frequency of the system are satisfied, the frequency responses do not effectively converge during steady state under OF1.

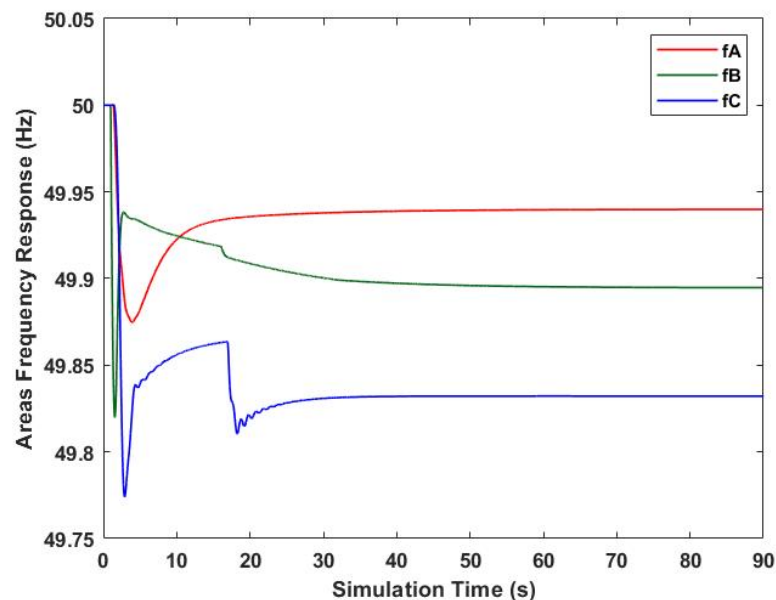


Figure 5.18: Areas' frequency response - Loss of W B10 - FFS by all SI means.

Considering the response of the various elements of SI, the first seconds following the disturbance and before the activation of the HVDC links, the electrolyzers and WTs in area B alter their power output to sustain the initial frequency drop. As observed in Figure 5.21, all the electrolyzers installed close to bus B10, the point the imbalance occurs, are forced to rapidly change their consumption utilizing the maximum of their bid size. Electrolyzer B1 which is remotely installed is also affected having the largest supporting capability among the units. Furthermore, WTs in area B are also forced to their maximum supporting capability due to the magnitude of the disturbance as observed in Figure 5.19. The power output of the WTs and the local electrolyzers is regulated with respect to the instantaneous deviations, which later shrink with the injections from the HVDC links by the supporting areas that can be observed in Figure 5.20. The most significant change in the power flows of the HVDC links happens in link BC at which an increase of 650MW is encountered taking place at a

rate of 665MW/s which is also observed in the frequency response of area C in Figure 5.18. Area A also supports area B by an increased export of 65MW but mainly increases the export to area C by 120MW at a rate of 600MW/s as area C is highly impacted. When the shared imbalance is encountered by the local means of SI in other areas, they modify their outputs with respect to the frequency deviations. In area A electrolyzers installed closer to the CCPs of the HVDC links are more critically affected than electrolyzer A1 which is installed at a remote point. When the frequency reaches a new equilibrium point their consumption also stabilizes at a point below their nominal consumption due to their unlimited in time supporting capability. Similar is the case with the electrolyzers in area C which are also differently affected based on their capacity and their location. In parallel, electrolyzers in areas B and C face a second change in their consumption after 16s of simulation due to the WTs limited in time support. Finally, WTs in area C, which experiences the main impact as supporting area, provide their support at the maximum capability for 15s before returning to their nominal output.

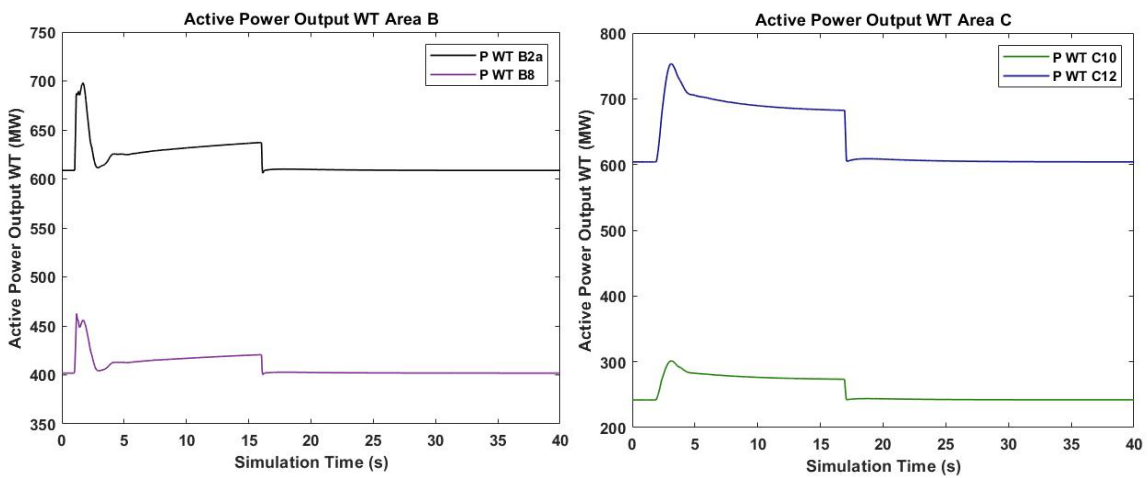


Figure 5.19: WTs' active power output - Loss of WTB10 – FFS by all SI means.

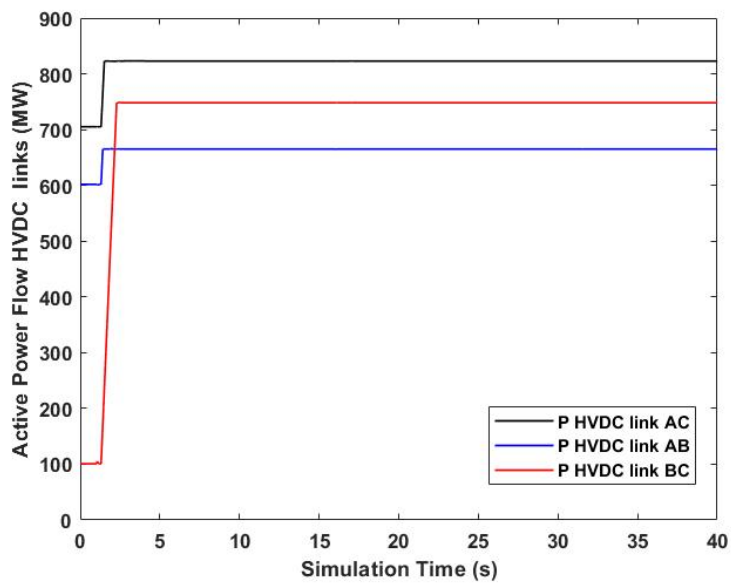


Figure 5.20: Active Power Flows HVDC links – Loss of WTB10 – FFS by all SI means.

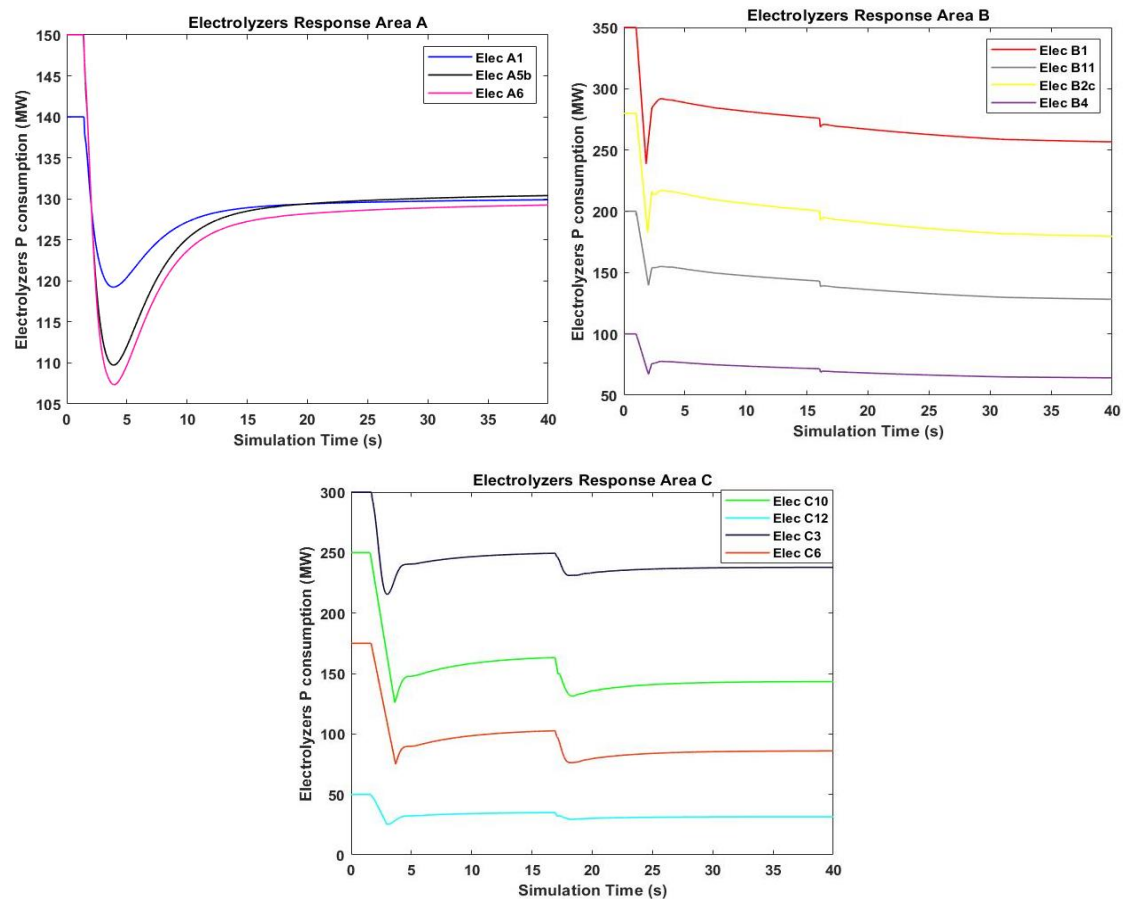


Figure 5.21:PEM Electrolyzers' power consumption - Loss of WTB10 -FFS by all SI means.

5.2.4. Load event area B

One of the most common active power imbalances in a power system that can perturb its balance is an abrupt change in the load demand. Hence, the effectiveness of the frequency supporting scheme designed has been evaluated for a 10% increase in the active power consumption of each area. In area B the total load demand under steady state conditions is equal to 4670MW, 15% of which is fed by imports, 50% from local WTs and 35% from SGUs. An increase by 10% in the load demand leads to an increase of 500MW that may occur either in a single point or in multiple system nodes. In most cases, the most severe effect is encountered when it occurs at neighbouring system nodes. Thus, a load event leading to an increase of 500MW has been considered at the 1st s of the simulation at the loads installed at buses B8 and B10 in area B.

In case no frequency support is provided by any means of SI but only from the local SGUs, the frequency response of the system can be observed in Figure 5.22. At the first ms following the disturbance and before the activation of SGUs, the response is characterized by a stiff RoCof followed by a period that local SGUs try to regulate the deviation before starting to stabilize at a level of 49.72Hz. The frequency in areas A and C remains as expected unaffected at 50Hz as the 3 areas are electromagnetically decoupled by the HVDC links. As it is clear, due to the large non-synchronous share in area B and the areas decoupling, support from means of SI is necessary.

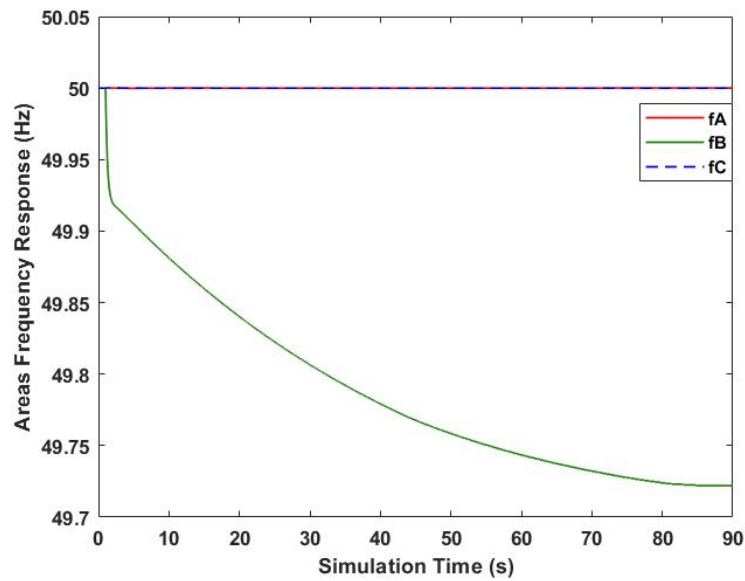


Figure 5.22: Areas' frequency response - Load event area B - No FFS.

Considering the available means of local support, 3 different scenarios have been formulated: FFS by local WTs, FFS by local electrolyzers and finally FFs by local FCRs. The frequency response of the affected area in the latter scenarios may be observed in Figure 5.23. As it can be observed, the best achieved response is obtained when both local WTs and electrolyzers are utilized. The initial RoCof in area B improves and the area's frequency reaches a stable point at 49.9Hz. Similar result is obtained when only the local electrolyzers are used at their maximum capability, with the main difference tracked the first 16s of simulation before the deactivation of the WTs' support leading to a second dip in the frequency. When only local WTs are used, the response of the affected area does not significantly improve due to the limited in capacity and time supporting capability of the WTs. Areas A and C remain unaffected in these scenarios as no modifications are applied to the power flows of the HVDC links and thus the disturbance is not spread to other areas. The complete results of this set of simulations can be found in Table 5.6.

Table 5.6: Frequency response results - Load event area B - FFS local means.

MEANS OF FFS	Local WTs	Local Electrolyzers	Local WTs + Electrolyzers
OF1: Best Fitness Evaluation Value (60s)	0.8611	0.3083	0.2967
F_B Initial drop (Hz)	49.93	49.94	49.94
F_B steady state (Hz)	49.72	49.9	49.9

As in the previous sections, in the next set of simulations the provision of FFS utilizing different groups of available FCRs installed in the 3 interconnected areas by modifying the power flows on the HVDC links has been evaluated. The frequency response of area B in each of these scenarios can be observed in Figure 5.24. As it is clear, the best achieved response is obtained when either all the installed means of SI provide cooperatively their support tuned by the MVMO or at least when HVDC link modifications are applied in coordination with the electrolyzers of each area. In these scenarios, the frequency in the affected area remains above 49.9Hz throughout the whole simulation period and effectively stabilizes at 49.94Hz. Minor impact is

encountered on the neighboring areas as it can be concluded from the fitness evaluation values of OF1 which are equal to 0.287 and 0.282 respectively. Detailed results of this set can be found in Table 5.7.

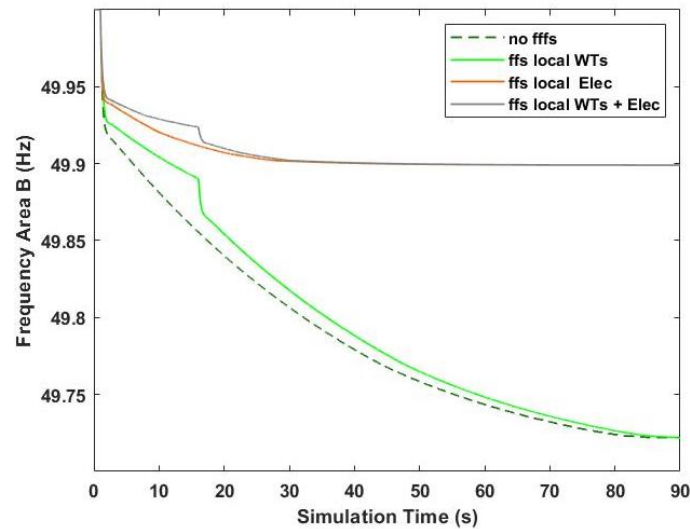


Figure 5.23: Frequency response area B - Load event area B - FFS by local means.

Table 5.7: Frequency response results - Load event area B - FFS local and inter-area means .

MEANS OF FFS	HVDC links	HVDC links + WTs	HVDC links + Electrolyzers	HVDC links + Electr. + WTs
OF1: Best Fitness Evaluation Value (60s)	0.8944	0.8924	0.2873	0.287
Fc nadir (Hz)	49.94	49.93	49.94	49.95
Fc steady state (Hz)	49.82	49.86	49.94	49.94

As far as the frequency response in the affected area is concerned, as it is clear in Figure 5.24, the utilization of local means in the area B leads to a better response compared to the case support is provided only through HVDC links. Moreover, as it can be observed in Table 5.6 and Table 5.7 the same result arises in the value of the best achieved fitness evaluations. In fact, the 3rd best fitness evaluation value is achieved by the local FCRs in area B as these units have the capacity to handle such an event without applying any modifications in the HVDC links, nullifying the impact on other areas. On the other hand, when HVDC links act alone or in cooperation with the WTs, their support is not sufficient to achieve responses of similar quality without a significant impact on the neighboring areas.

In case now all the sources of SI are cooperatively tuned against the imbalance the areas' frequency response can be observed in Figure 5.25. As it is clear, area A mainly supports the affected area B, but its frequency quickly stabilizes due to the local SGUs and electrolyzers. Area B following the initial stiff drop, experiences a second dip due to the interruption of WTs' support before stabilizing at 49.94Hz. Finally, the frequency in all areas remains within the normal operating state bounds during the simulation period and converge to a close point.

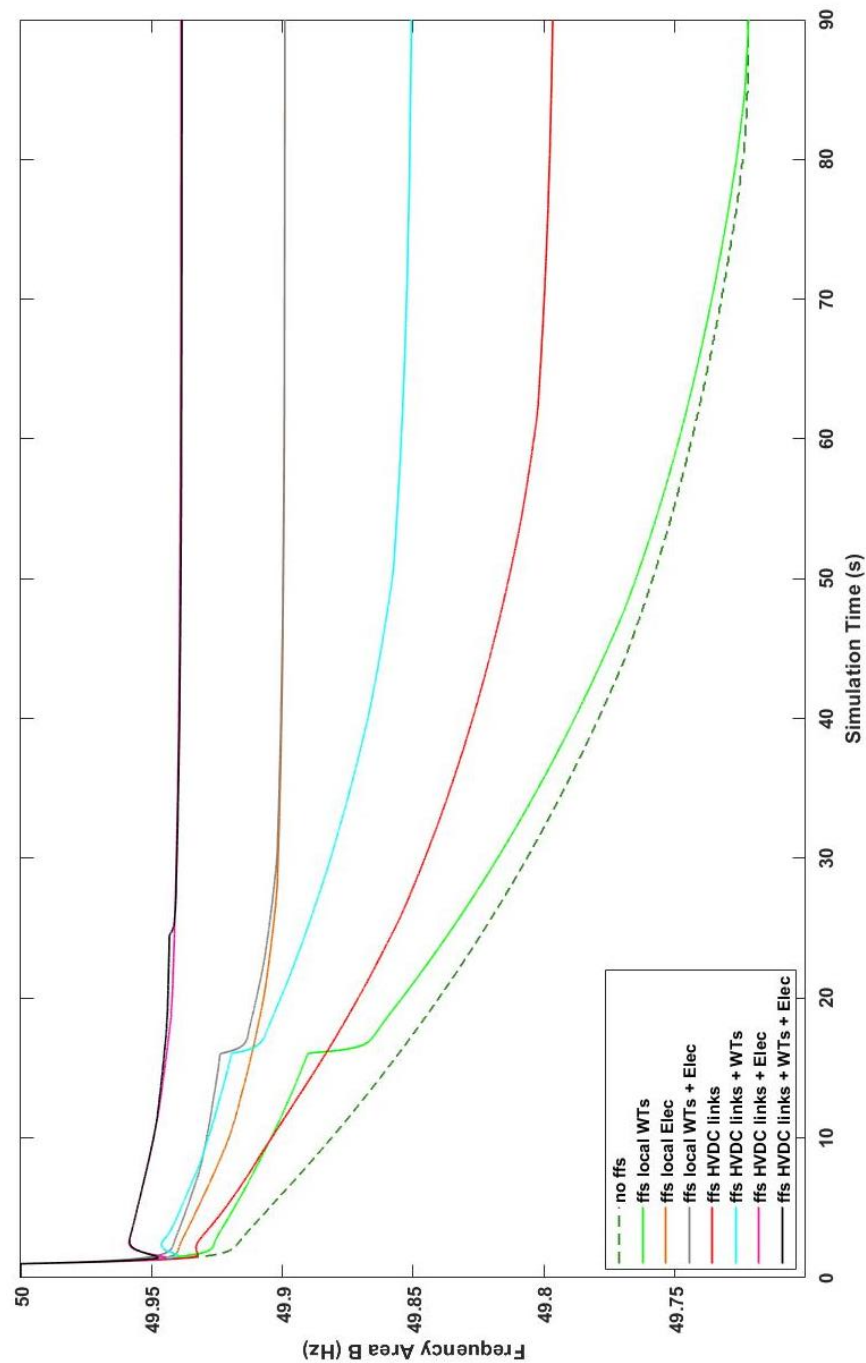


Figure 5.24: Frequency response area B - Load event area B - FFS by local and inter-area means.

Analyzing the best achieved result, the response of the various elements such as HVDC links, electrolyzers and WTs can be observed in Figure 5.26 to Figure 5.27. When the imbalance occurs, the local electrolyzers are initially activated to support the grid. Electrolyzer B1, the largest unit in the affected area, is the mainly affected one considering its power consumption. This unit is close to the location of the event and to the CCP of the HVDC link AB. After some ms local WTs are activated to support, but due to the regulation of the activated electrolyzers, frequency remains close to the threshold level of the frequency controller of the WTs and thus no significant changes are encountered in their output.

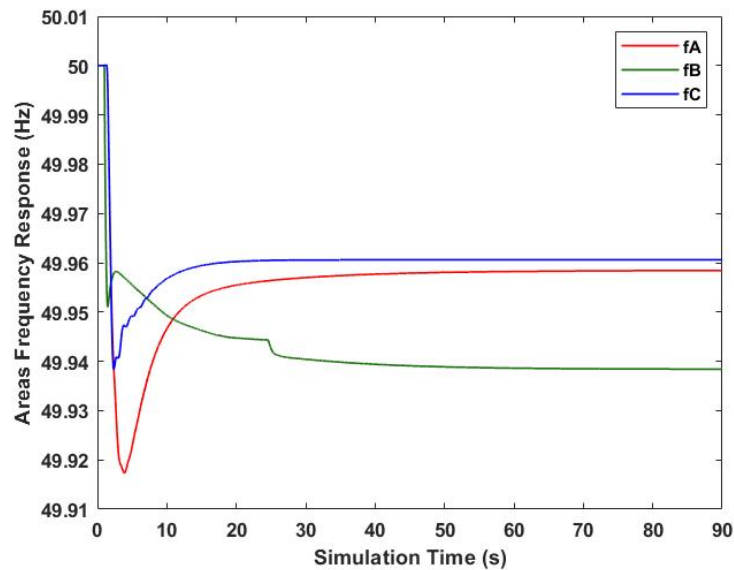


Figure 5.25: Areas' frequency response - Load event area B - FFS by all SI means.

After 0.3s, the power flows in the HVDC links are modified with respect to the optimization problem results to inject power to area B. As observed in Figure 5.26, links AB and BC increase their injection to area B by 100MW and 160MW respectively at rapid rates of 620MW/s and 800MW/s respectively to sustain the frequency deviations. Small modifications are also encountered in the AC link which tends to increase the export from area A to area C by 30MW to mitigate the impact on area C from the abrupt change in the power flow in the BC link. When now the imbalance is shared the frequency in these areas tends to drop and thus the local units are triggered. In area A, electrolyzer A1, the largest unit installed, and electrolyzer A5b, installed at the CCP with HVDC link AB, face the most significant changes in their consumption. In area C, electrolyzers are again those who mainly shoulder the shared disturbance, with PEM C10 being the most affected one. In the meantime, no significant changes in the output of the WTs occur, as the frequency in area C restores gradually within their deadband zone.

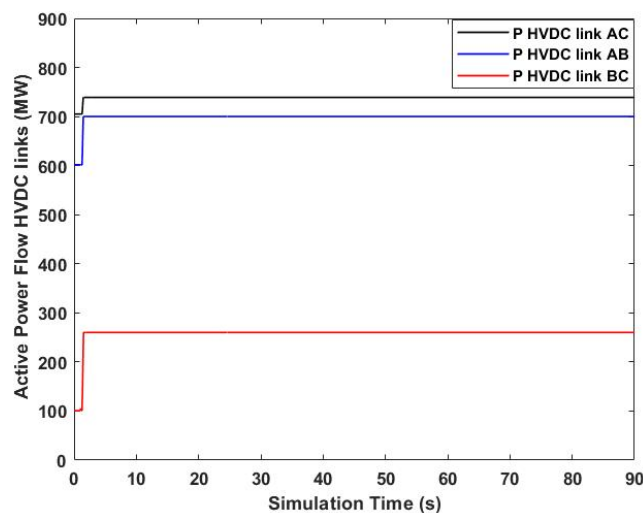


Figure 5.26: Active Power Flows HVDC links – Load event area B - FFS by all SI means.

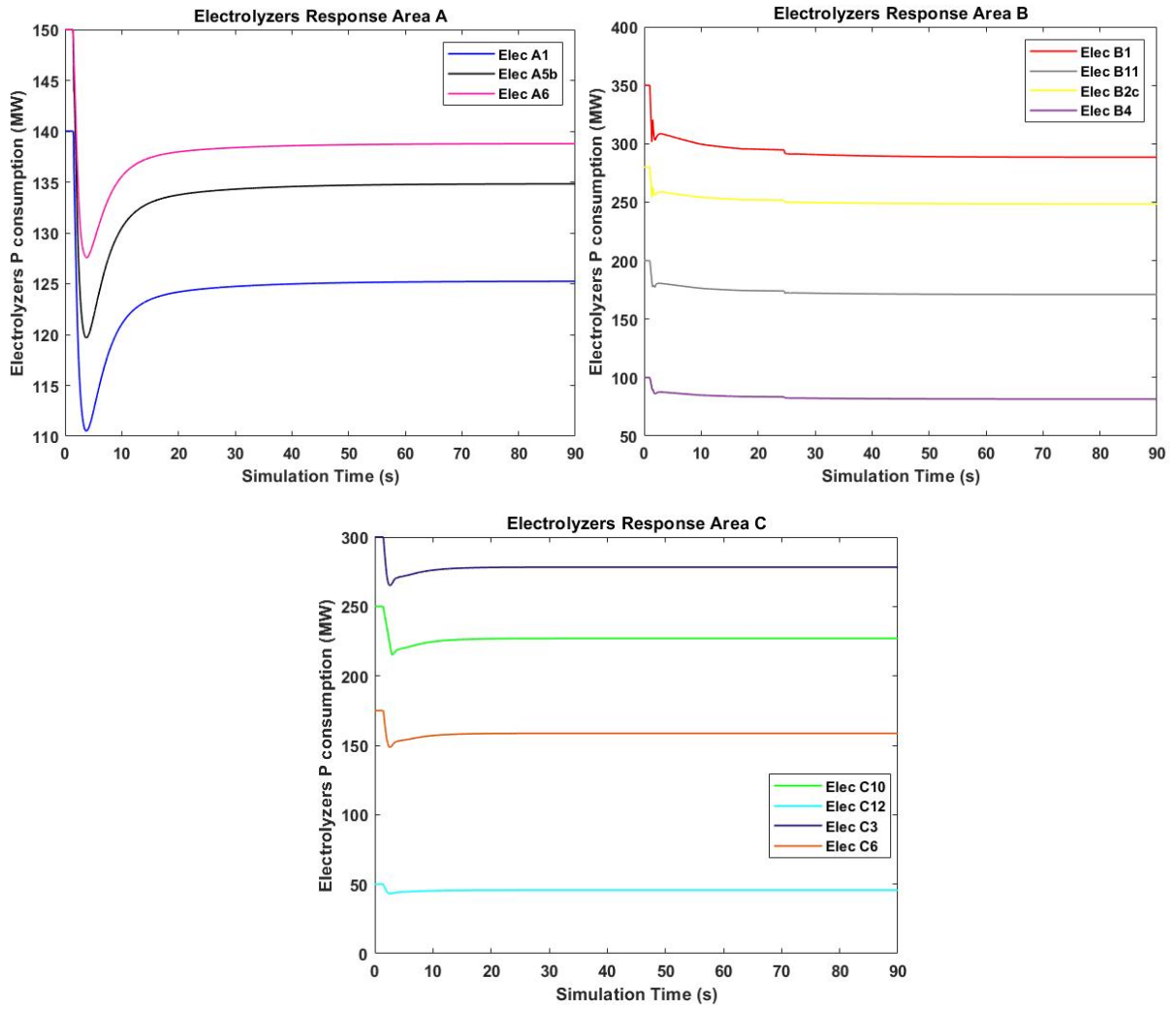


Figure 5.27: PEM Electrolyzers' power consumption - Load event area B -FFS by all SI means.

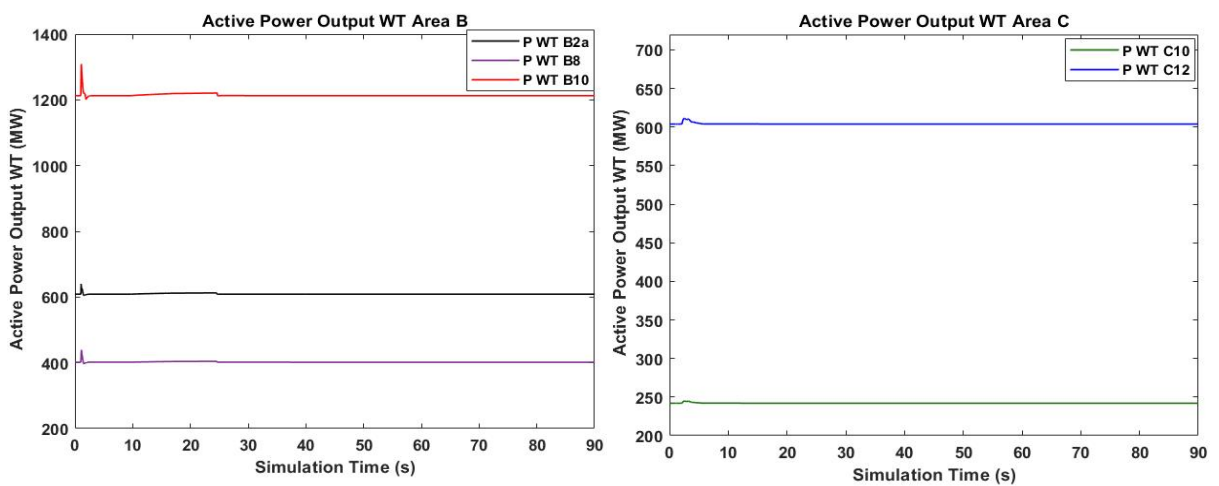


Figure 5.28: WTs' active power output - Load event area B – FFS by all SI means.

5.2.5. Load event area A

In the next set of simulations, the effectiveness of the proposed strategy of FFS is evaluated in case of a load event in area A. The total load demand under normal operating conditions in area A is equal to 1770MW. If the local load is increased by 10% an active power imbalance of 177MW is encountered. The latter imbalance is applied through a step increase in the load at bus A5a on the 1st s of the simulation. The system response under this event has been evaluated when various groups of available FCRs are activated.

In case the frequency response of area A is based only on the local SGUs, a nadir of 49.77Hz in the affected area is encountered, followed by a restoration period before stabilizing at 49.93Hz as observed in Figure 5.29. Consequently, it is clear that such a disturbance can be effectively handled by the local SMs preserving the frequency within the normal operating state bounds. In this case, it is interesting to examine whether an improved frequency response can be obtained utilizing the various means of SI and if the optimization algorithm can optimally coordinate the different elements to face such an event.

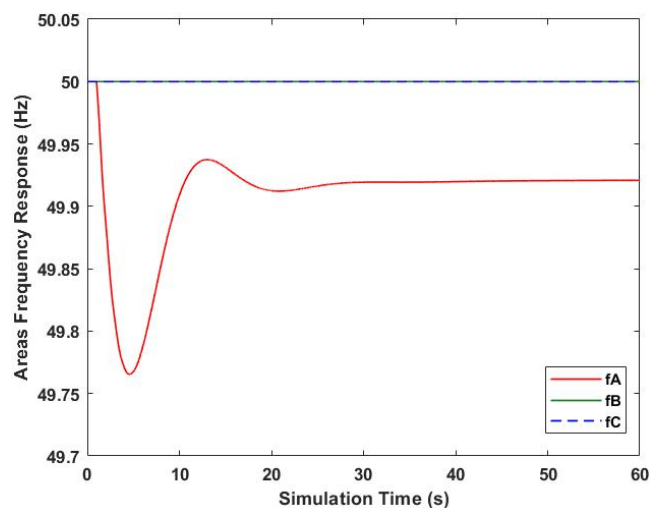


Figure 5.29: Areas' frequency response- Load event area A - no FFS.

In area A, the only local means of FFS installed are the electrolyzers. The frequency response of the affected area when the PEM units provide their support additionally to the local SMs can be observed in Figure 5.30 compared to the case no FFS is provided shown in dashed red line. As expected, the frequency in area A has a slightly improved RoCof and its maximum deviation is encountered at a level equal to 49.92Hz before stabilizing at 49.94Hz faster compared to the case only SGUs considered. The frequency does not restore to its nominal value since the support from electrolyzers depends on the instantaneous frequency deviation and the deadband zone at which no changes in the consumption are applied.

The frequency response in the affected area can be further improved if the other areas are actively providing their support. As it can be observed in Figure 5.31 when support is provided by the HVDC links without considering any modifications in the electrolyzers and WTs in the 3 areas, the frequency in the affected area can reach a significantly improved nadir and stabilize close to its nominal value. However, as it is clear from the best achieved fitness evaluation value of this case shown in Table 5.8 the latter result has a significant impact on areas B and C. To mitigate this problem, electrolyzers and WTs may also change their outputs with respect to frequency deviations and achieve an even improved response for area A with the minimal impact on the other areas.

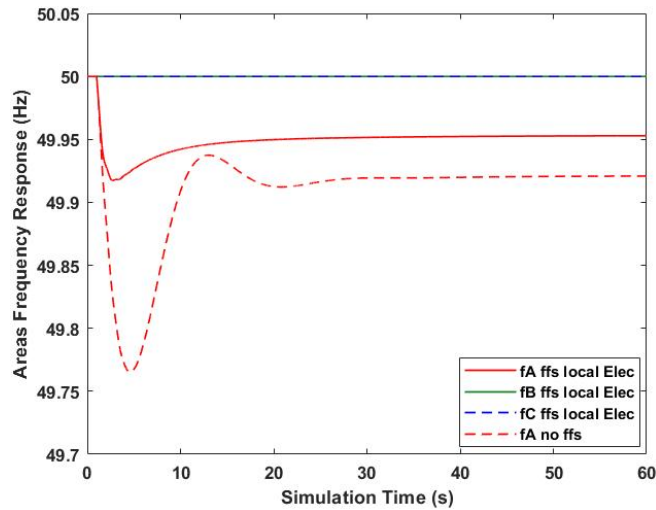


Figure 5.30: Areas' frequency response- Load event area A - FFS by local electrolyzers.

Table 5.8: Frequency response results - Load event area A - FFS local and inter-area means .

MEANS OF FFS	Local Electrolyzers	HVDC links	HVDC links + Electrolyzers	HVDC links + Electr. + WTs
OF1: Best Fitness Evaluation Value (40s)	0.1172	0.1453	0.0512	0.0395
F _A nadir (Hz)	49.92	49.91	49.95	49.955
F _A steady state (Hz)	49.94	49.98	49.98	49.99

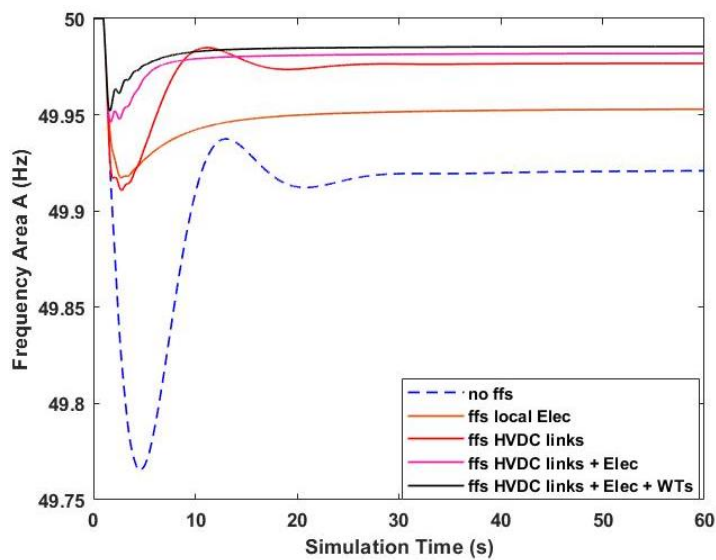


Figure 5.31: Frequency response area A - Load event area A - FFS by local and inter-area means.

In the best achieved response shown in Figure 5.32 and in Table 5.8 the frequency in area A has a maximum deviation at 49.95Hz and stabilizes very fast at 50Hz, whereas the fitness evaluation value achieved leads to the conclusion that the other areas remain almost unaffected as it is close to the optimal zero value.

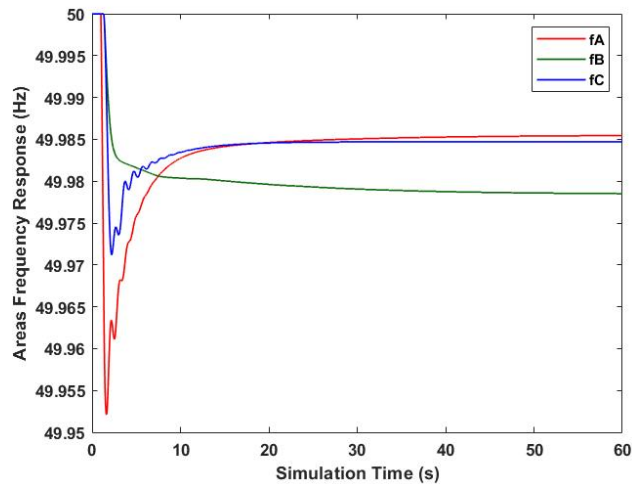


Figure 5.32: Areas' frequency response - Load event area A - FFS by all SI means.

In the latter case, it is not only the frequency in area A that has been improved. In fact, the 3 areas share the imbalance by changing the power flows in the HVDC links as observed in Figure 5.33 and the local electrolyzers are acting rapidly to deal with the imbalance as observed in Figure 5.34. As a result, the frequency in each of the 3 areas remains within the deadband zone of the WTs' controller and thus their outputs remain constant. Regarding the HVDC links, the active power injected to area C from area A reduces at 650MW and the power injection to area B from area A reduces at 520MW. As a result, the exports from area A are limited to maintain the frequency in area A within the acceptable limits. Due to the limited impact on the neighboring areas no changes are necessary in the HVDC link BC. When the imbalance in area A occurs, the local electrolyzers are activated to change their consumption according to the deviations and their supporting capability. Electrolyzers A5b and A6b located closer to the imbalance, experience the most significant change in their outputs as observed in Figure 5.34. As the frequency in area A restores, the demand of the electrolyzers reaches a new equilibrium point due to their unlimited in time supporting capability. Finally, in areas B and C which experience the effect of the shared imbalance, local electrolyzers are activated some ms following the modifications in the HVDC links. Units installed closer to the CCPs of the HVDC links experience the most significant change in their consumption. Finally, the frequency in all 3 areas restores to a point close to 49.98Hz.

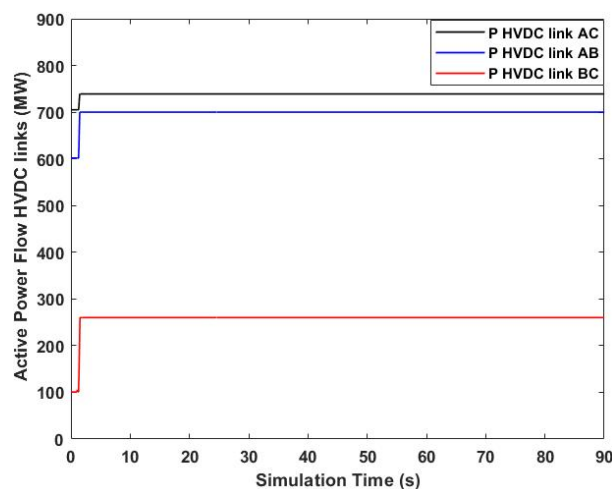


Figure 5.33: Active Power Flows HVDC links – Load event area A - FFS by all SI means.

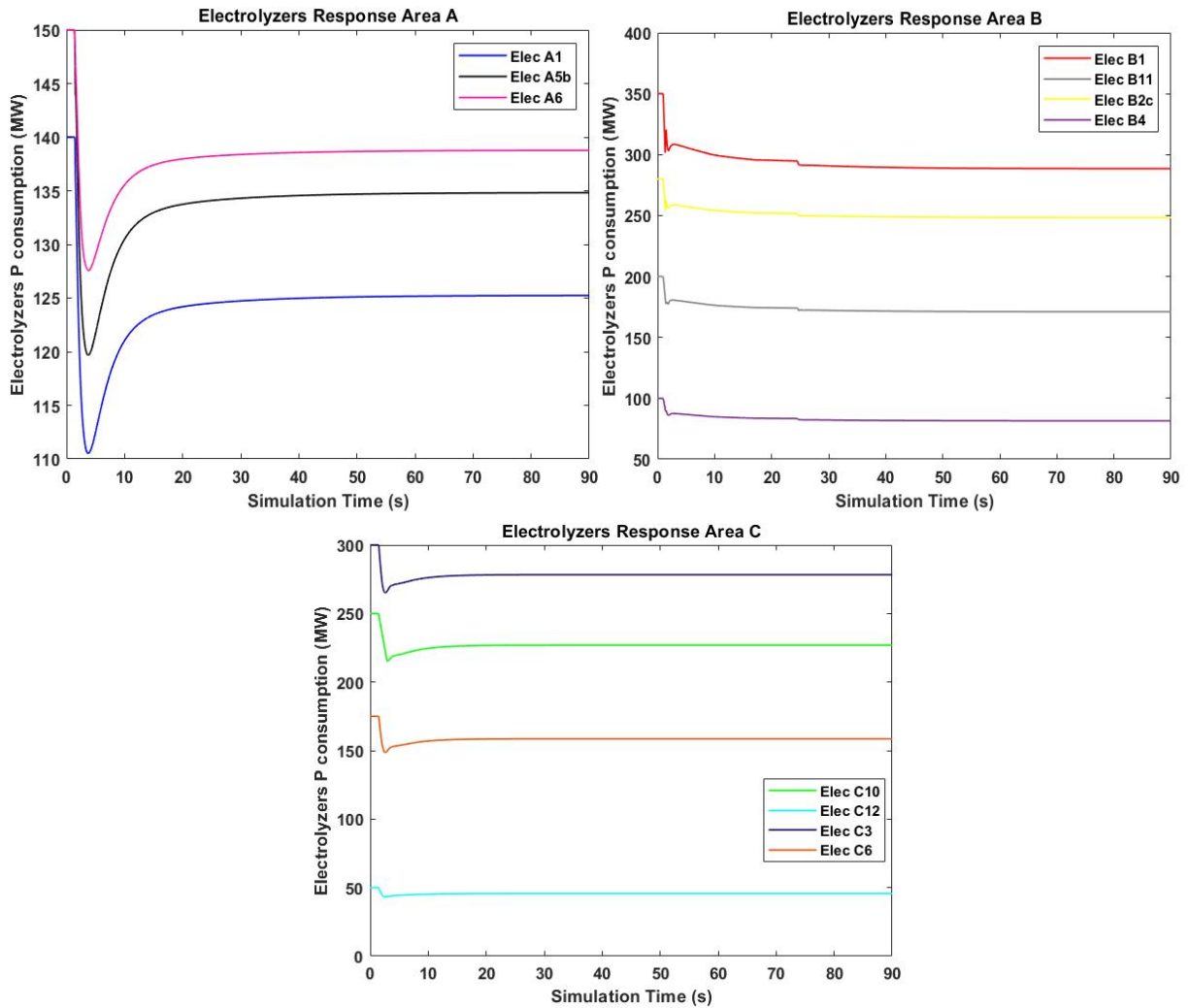


Figure 5.34: PEM Electrolyzers' power consumption - Load event area A -FFS by all SI means.

5.2.6. Load event area C

Concluding the section of load events, an active power event in area C is considered. The total load demand in area C under steady state conditions is equal to 3705MW and thus a 10% increase corresponds to a 370MW imbalance. The latter one has been applied by a step increase in the loads installed at the neighboring buses C4 and C7 of area C on the 1st s of simulation. Then the system's response has been examined when different groups of FCRs are activated. Similarly, to the previous cases, the parameters of the frequency controllers are selected based on the solution of the MVMO algorithm under problem formulation 1.

Initially, in case no FFS is provided by any means of SI in area C the frequency response of the system under the applied event can be observed in Figure 5.35. In the affected area, the frequency drops at 49.35Hz and restores at a new equilibrium point of 49.75Hz. In areas A and B, the frequency is not affected due to their isolation from area C through the HVDC links and the converters' technology.

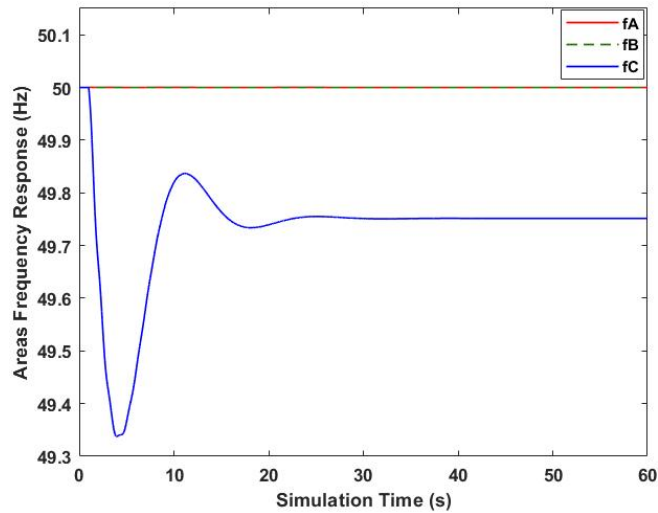


Figure 5.35: Areas' frequency response- Load event area C - no FFS.

An initial solution to further reduce the imbalance in area C is to take advantage of the local units of FFS such as WTs and electrolyzers. Considering all the different possible combinations and operating the elements at their maximum capability, the frequency response of area C in each of the scenarios can be observed in Figure 5.36 compared to the original response shown in dashed style. When the local WTs installed at buses C10 and C12 are activated to support the grid, the frequency drops to an improved nadir. However, following the supporting period of 15s from the WTs, a second drop in the frequency is observed due to the abrupt change in their output. After that period, the area operates again only with the support from the local SGUs and thus the frequency restores at the same level with the original case. On the other hand, when electrolyzers or the combination of all local elements offer their support, the frequency response is significantly improved. In this case in area C the maximum frequency deviation is encountered at 49.83Hz and restores close to 49.91Hz. Furthermore, great results are obtained considering the calculation of OF1 as the other areas remain unaffected. The complete set of results can be observed in Table 5.9.

Table 5.9: Frequency response results - Load event area C - FFS local means.

MEANS OF FFS	Local WTs	Local Electrolyzers	Local WTs + Electrolyzers
OF1: Best Fitness Evaluation Value (40s)	2.2995	0.337	0.301
F_C Initial nadir (Hz)	49.61	49.83	49.86
F_C steady state (Hz)	49.75	49.91	49.91

Another possible choice to provide FFS to the affected area, is to modify the power flows on the HVDC links and thus to increase the power injection in area C. The latter case, observed in Figure 5.37 in red solid line, leads to a nadir of 49.77 Hz before stabilizing at 49.93Hz. However, in this case the interconnected areas A and B are also affected as the imbalance is shared on them through the HVDC links. As it is clear from Table 5.9 and Table 5.10 when the values of OF1 for the last 2 cases are compared, it is preferable to face the imbalance by the local means and limit the imbalance on the other areas.

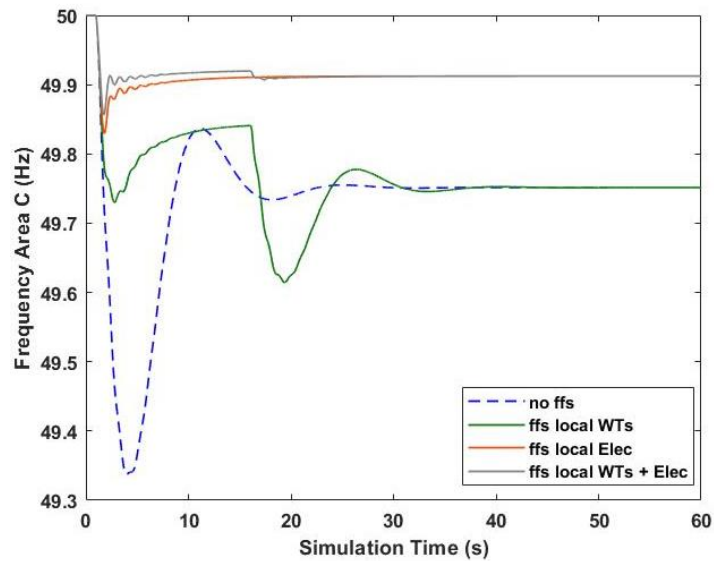


Figure 5.36: Frequency response area C – Load event area C - FFS by local means.

To improve even further the frequency in area C and minimize the impact on the supporting areas, the local units of FFS may be used in a coordinated manner with the HVDC links. As it is clear in Figure 5.37, the best achieved response is obtained when all the available means of SI cooperate to sustain the deviation. In this way, the maximum frequency deviation in area C is equal to 49.86Hz and stabilizes rapidly at 49.97Hz. As it is also clear from the value of the best achieved fitness evaluation in this case and Figure 5.38, the effect on the neighboring areas is effectively minimized. The 3 areas can optimally share the active power imbalance occurred in area C as the frequency in all of them remains within the acceptable limits of normal operating state and stabilizes at a very close point of around 49.97Hz.

Table 5.10: Frequency response results - Load event area C - FFS local and inter-area means.

MEANS OF FFS	HVDC links	HVDC links + WTs	HVDC links + Electrolyzers	HVDC links + Electr. + WTs
OF1: Best Fitness Evaluation Value (40s)	0.7	0.602	0.1856	0.1558
Fc nadir (Hz)	49.77	49.83	49.85	49.86
Fc steady state (Hz)	49.93	49.93	49.96	49.97

Considering the response of the local elements of FFS installed at various system points when the optimal coordination among all the available means is achieved under problem formulation 1, the graphs Figure 5.39 to Figure 5.41 are obtained. The first ms following the disturbance, the electrolyzers of area C are activated when the frequency drops below 49.99Hz and alter their consumption based on the measured Δf . In this case, units installed at buses C6 and C10 are critically affected and change their consumption rapidly. In addition, electrolyzer C3 which is close to large SGUs is not significantly affected although close to the disturbance, compared to electrolyzer C10 which is installed at a weak system point close to the WT terminal and the CCP of the HVDC link BC. In the same period, WTs are activated to modify their outputs with respect to the frequency deviations. Their support depends on the capability of each unit and lasts for a small period as the frequency restores very fast within their deadband zone.

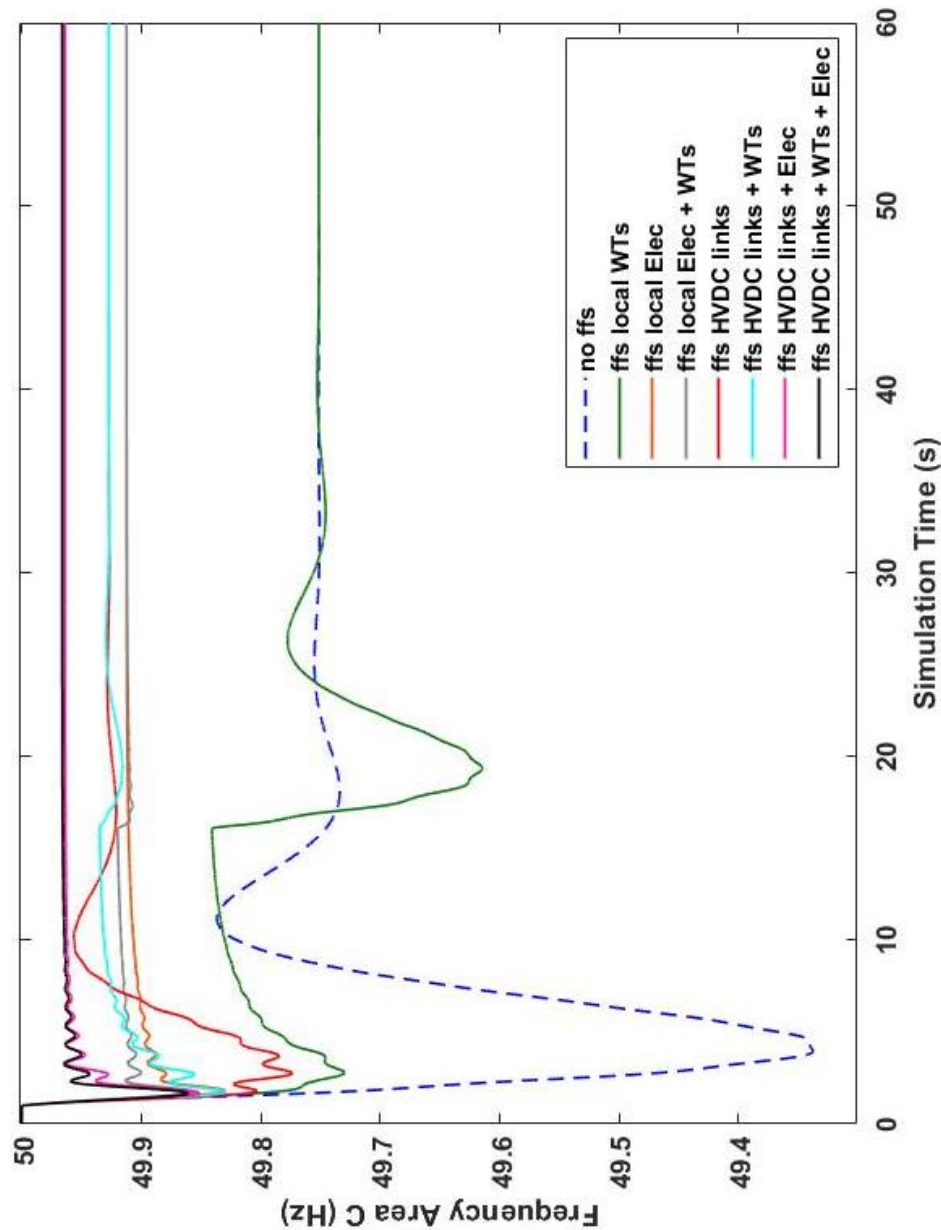


Figure 5.37: Frequency response area C - Load event area C - FFS by local and inter-area means.

After 1.3 s of simulation, new power flows are applied to the HVDC links. In fact, HVDC link AC increases its initial injection to area C to 800MW at a rate of 389MW/s and link BC changes the direction of the power flow across the link so that 80 MW are provided from area B to area C. A minor change in the power flow of the HVDC link AB is also observed as area A tries to minimize the effect on area B. The modified power flows on the HVDC links lead the frequency in areas A and B to drop and thus the local electrolyzers are activated to sustain the deviation. In area A, electrolyzers A1 and A6b are those mainly affected whereas units in area B close to the HVDC links such as electrolyzers B1 and B2c experience the most significant change. WTs in area B preserve their power output to its nominal value as the frequency remains above the activation threshold of the corresponding frequency controllers.

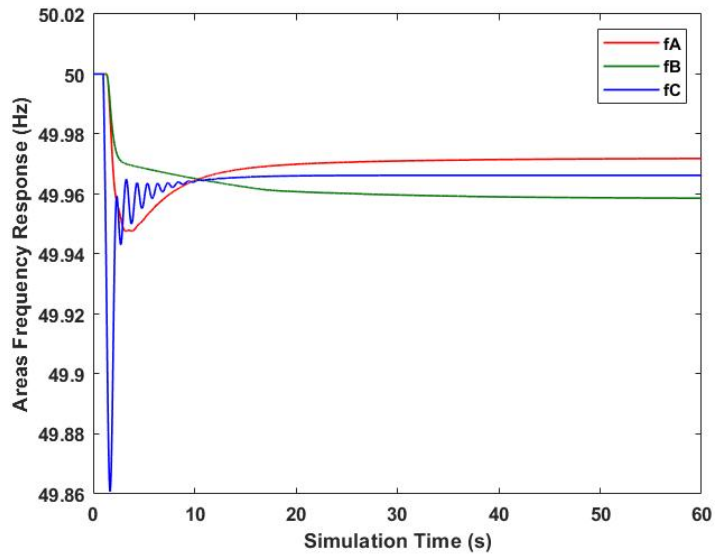


Figure 5.38: Areas' frequency response - Load event area C - FFS by all SI means.

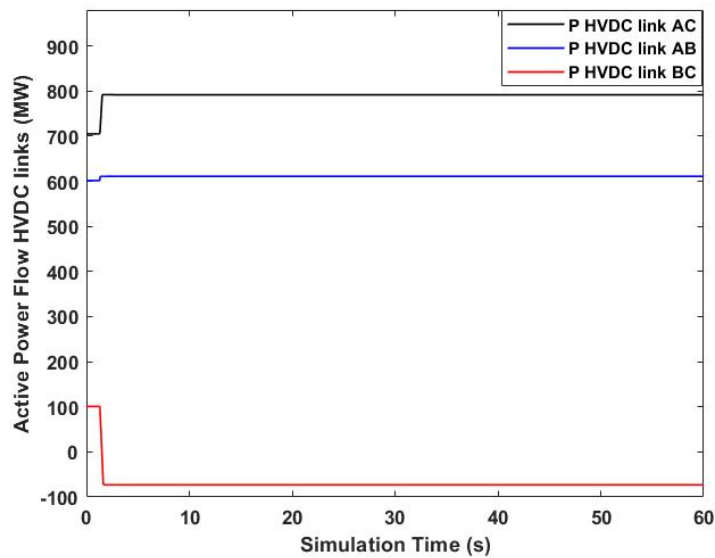


Figure 5.39: Active Power Flows HVDC links – Load event area C - FFS by all SI means.

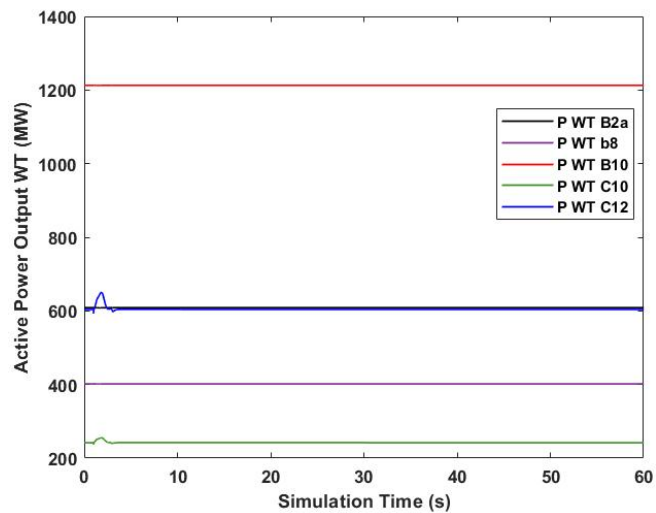


Figure 5.40: WTs' active power output - Load event area C - FFS by all SI means.

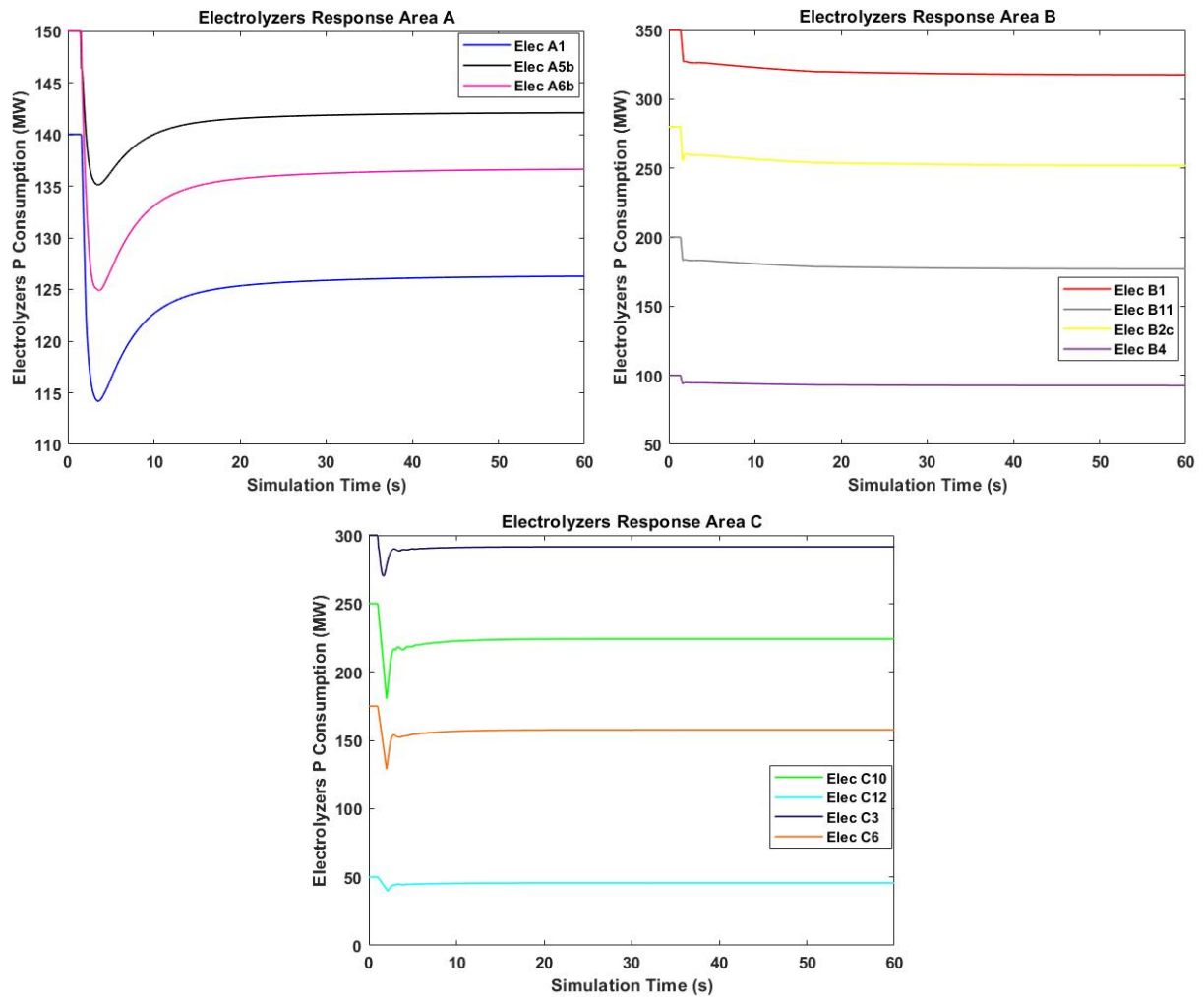


Figure 5.41: PEM Electrolyzers' power consumption - Load event area C -FFS by all SI means.

5.3. Results under problem formulation 2

In this section all the different active power events discussed in section 5.1 are applied again to the modified system. However, this time the frequency controllers of the various SI means such as HVDC links, electrolyzers and WTs are tuned with respect problem formulation 2 presented in section 4.3. The latter one aims at the minimization of the displacements of the dynamic trajectories of the speeds of each of the interconnected areas. In each of the events, different groups of FCRs are activated to provide support to the grid to evaluate the importance of each one of them. The frequency responses of the affected areas per case and per event are compared and the best achieved one is analyzed in detail considering the participation of the different elements on the frequency regulation with respect to their location and the impact on the neighboring areas.

5.3.1. Loss of largest generating unit in area C (C7G)

In this section and similarly to 5.2.1, at the 1st s of simulation a loss of 960MW corresponding to the loss of the largest generating unit in area C (SGU C7G) is performed leading to a critical under-frequency event. If no FFS is provided by any means of SI the frequency drops to low levels as explained in section 5.2.1 able to trigger the activation of protection devices and UFLS schemes and lead to cascading outages. For comparison reasons, if no protection schemes are activated to sustain the deviation the response of area C can be observed in Figure 5.1. As a result, in this case FFS is more than necessary to avoid the system collapse.

Frequency support can be provided either just by different combinations of local electrolyzers and WTs or by modifying the power flows on the HVDC links to enable sharing of the disturbance among the interconnected areas. In the former case, and due to the magnitude of the disturbance the best response is achieved utilizing all the available local means at their maximum capability as explained in 5.2.1 and can be observed in Figure 5.2. In this case, the frequency responses remain the same and only the calculation of the OF is performed under the guidelines of problem definition 2. On the contrary, when HVDC links are considered in the FFS scheme, the tuning of the parameters of the participating elements is different and is achieved by the minimization of OF2 with the aid of the MVMO algorithm. The best achieved frequency responses of the affected areas considering the different combinations of SI sources under the latter tuning method can be observed in Figure 5.42, whereas detailed results per case can be found in Table 5.11.

Table 5.11: Frequency response results - Loss of SGU C7G - FFS local and inter-area means (OF2).

MEANS OF FFS	Local WTs	Local Electrolyzers	Local WTs + Electrolyzers	HVDC links	HVDC links + WTs	HVDC links + Elec	HVDC links + WTs + Elec
OF2: Best Fitness Evaluation Value (60s)	18.5579	8.941	3.60	5.9327	5.3527	4.8228	4.2817
F _c nadir (Hz)	47.18	48.77	49.45	49.23	49.44	49.38	49.56
F _c steady state (Hz)	49.14	49.73	49.73	49.84	49.83	49.82	49.9

From the comparison of the best achieved responses of the affected area, it can be observed that when all the available means of SI are tuned to face the imbalance, the best response in terms of nadir and steady state deviation is obtained. Considering the rest cases, it is clear that results of similar quality are obtained when WTs provide their support, although the time limitation of their support leads to frequency dips after 15s when not combined with other means. When only HVDC links provide support to area C, the frequency response shown in red is characterized by significant changes as new setpoints are applied only once per simulation and are not based on the instantaneous Δf . However, in all cases at which the different SI sources are used with respect to the modified power flows, the frequency remains within the normal operating state limits.

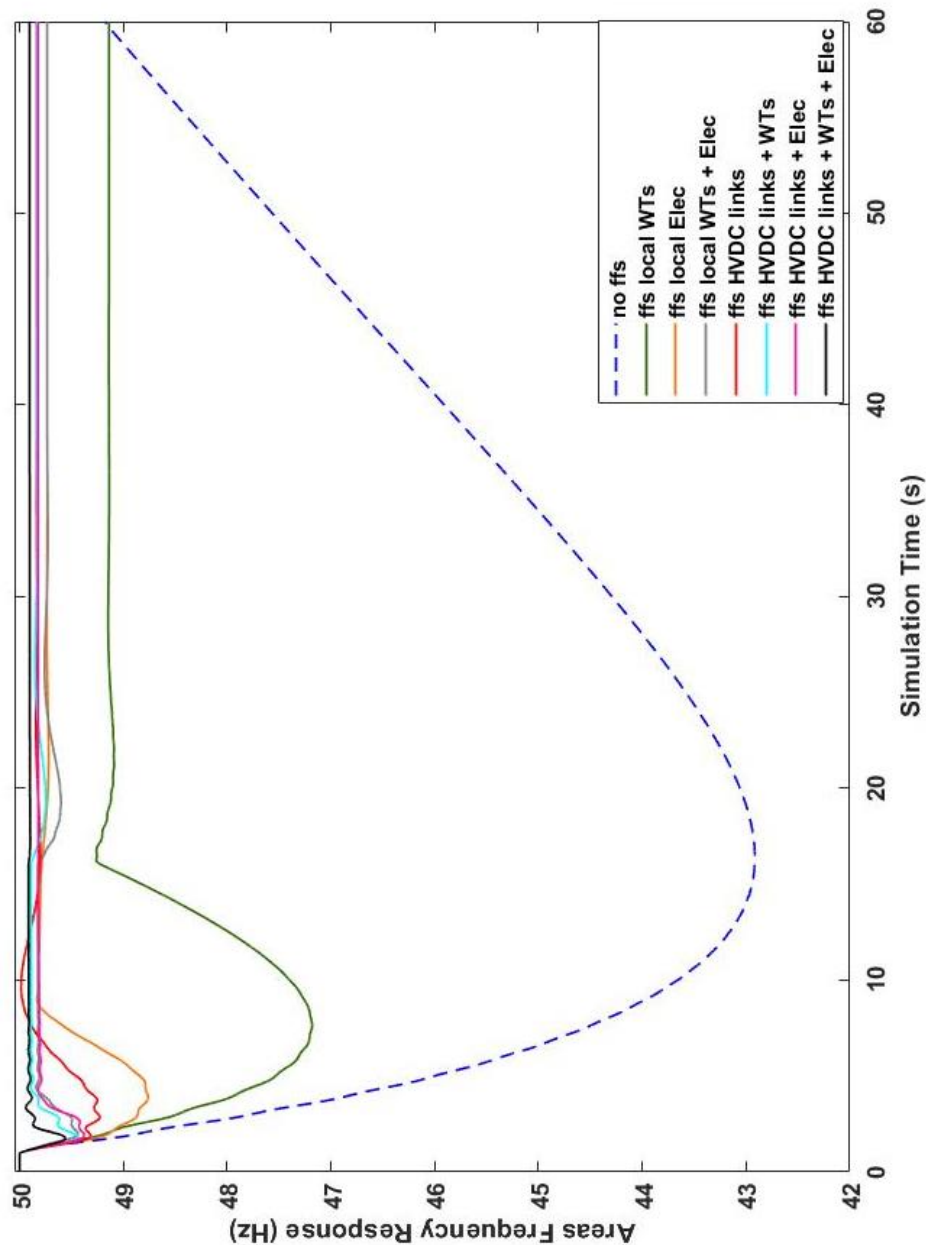


Figure 5.42: Frequency response area C - Loss of SGU C7G - FFS by local and inter-area means (OF2).

As far as the values of the best achieved fitness evaluations is concerned, it can be observed that the best value is achieved when only the local means of SI are utilized, followed by the case which achieves the best frequency response when all installed means of SI are activated. That is due to the fact that in the former case, the OF2 value is calculated based only on the local dynamic displacements of the speed, whereas in the latter case, deviations in all 3 areas contribute to the calculated value. Hence, the value of OF2 should be carefully examined with respect to the variables participating in the calculation process. The areas' frequency response when all the available means of FFS are utilized can be observed in Figure 5.43. As observed, during the first seconds of simulation the responses in the 3 areas are very close having activated the HVDC links. Before that period only the local units in area C provide their support and thus the frequency in area C experiences a worse RoCof and nadir. Frequency in area A is significantly affected as it shoulders the support and falls to 49.77Hz before stabilizing at 49.85Hz. Area B is not so significantly affected stabilizing with the aid of the local

units at 49.96Hz. Regarding the response of the HVDC links, as it is expected power injections to area C increase to tune down the imbalance. HVDC link AC experiences the largest change(Figure 5.44) increasing by 400MW its steady state power flow at a rate of 890MW/s, whereas HVDC link BC reverses the direction of the power flow to inject 55MW in area C. Also, a minor modification is applied in the link AB, aiming at reduced impact on area B with the aid of area A.

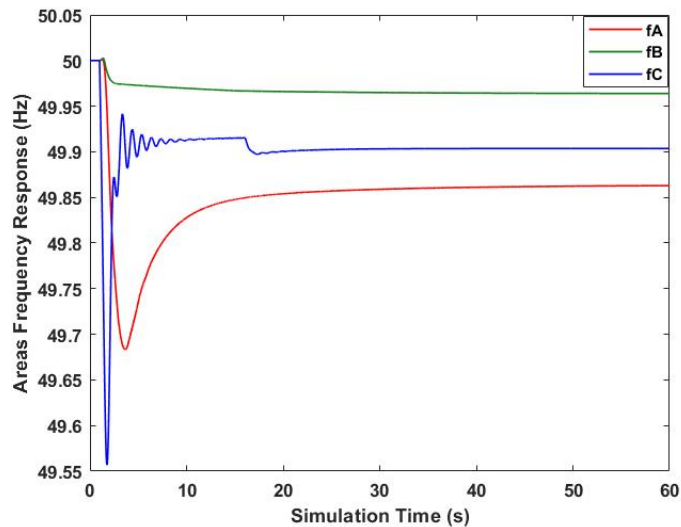


Figure 5.43: Areas' frequency response - Loss of SGU C7G - FFS by all SI means (OF2).

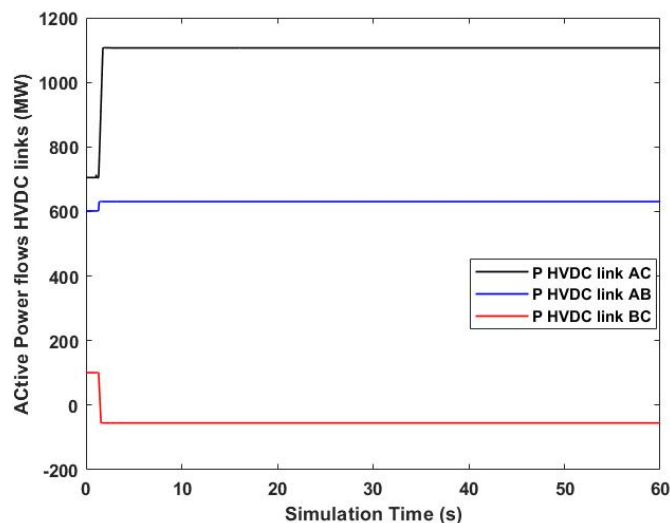


Figure 5.44: Active Power Flows HVDC links – Loss of SGU C7G - FFS by all SI means (OF2).

Regarding the response of the electrolyzers shown in Figure 5.45, in the affected area, they all experience a significant linear change in their consumption after some μ s following the disturbance. Their support is essential for this first period before the activation of the other inter-area means and the HVDC links. When the latter are activated, their demand restores quickly before experiencing a second small modification due to the changes in the WTs output. Units close to WTs experience a larger change in their consumption. Similar to previous cases, electrolyzers in area A and B are activated to support the local areas to mitigate the shared imbalance after 0.3s. Units closer to the CCPs of the HVDC links AC and AB which have significant changes in their power flows, experience the most significant change which decreases with the reduction of the Δf .

However, due to their unlimited in time supporting capability, their steady state consumption remains below its nominal value. Finally, WTs installed in area C, as observed in Figure 5.46 inject power when the local frequency drops below 49.95Hz based on the frequency deviation and their capacity for 15s before returning to their nominal output. In area B, no significant changes are observed since the frequency never falls out of the deadband zone of their controllers.

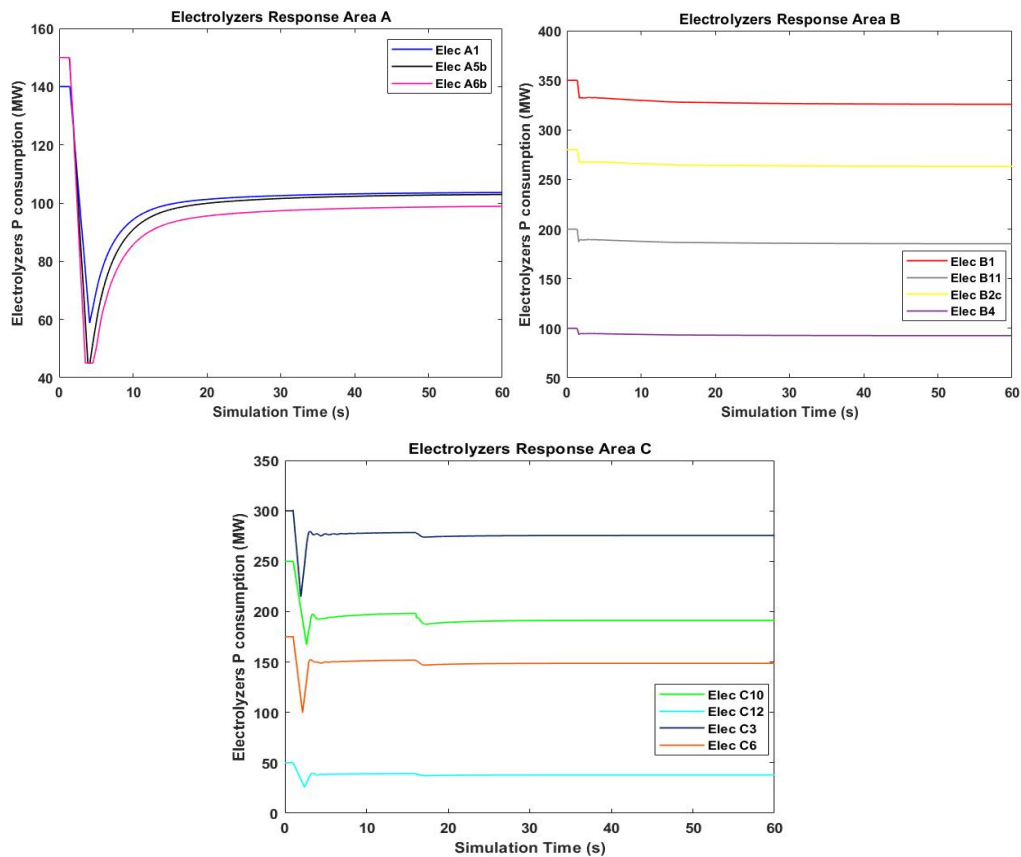


Figure 5.45: PEM Electrolyzers' power consumption - Loss of SGU C7G - FFS by all SI means (OF2).

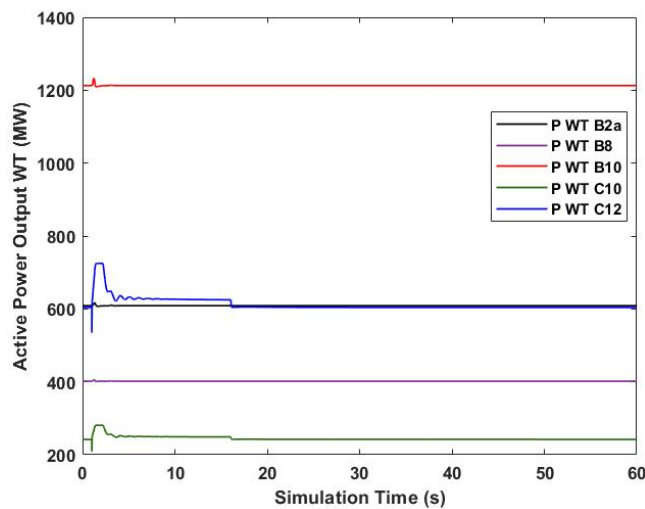


Figure 5.46: WTs' active power output - Loss of SGU C7G - FFS by all SI means (OF2).

5.3.2. Loss of largest generating unit in area A (A1aG)

In this section the same active power event with section 5.2.2, loss of SGU A1aG, is applied to the modified system. However, in this case the tuning of the supplementary frequency controllers is based on the MVMO algorithm under problem formulation 2. Applying the same event means that when no FFS response is provided by any means of SI, the frequency response will remain the same with the one shown in Figure 5.8, leading to a nadir of 48Hz followed by a steady state deviation of 400mHz. Furthermore, similar to Figure 5.9 would be the response of the system when local electrolyzers in area A are activated to provide their support operating at their maximum capability because of the magnitude of the disturbance. However, in this case the fitness evaluation is performed based on OF2 and thus the calculated value is equal to 4.3335.

On the other side of the coin, the frequency response in the 3 interconnected areas is expected to change in the scenarios at which modifications are applied to HVDC links power flows and in the inter-area means of SI as the corresponding parameters are selected under problem formulation 2. Considering all the different available groups of SI sources like in section 5.2.2 the frequency response of the affected area in each case can be observed in Figure 5.47. As it is clear, the frequency response in area A both in terms of maximum instantaneous deviation and steady state value improves with the increasing number of supporting means. Hence, the best frequency response is obtained when all HVDC links, electrolyzers and WTs in 3 areas are cooperatively tuned to support the grid. In the latter case, the frequency drops to 49.66Hz and stabilizes at a level of 49.92Hz, preserving the frequency within the normal operating state limits. Detailed information about the simulation results can be observed in Table 5.12. As it is clear, no significant difference in the frequency response and the best achieved fitness evaluation is observed when HVDC links and electrolyzers are acting together or independently from the WTs, as no WTs are installed in area A that experiences the main event.

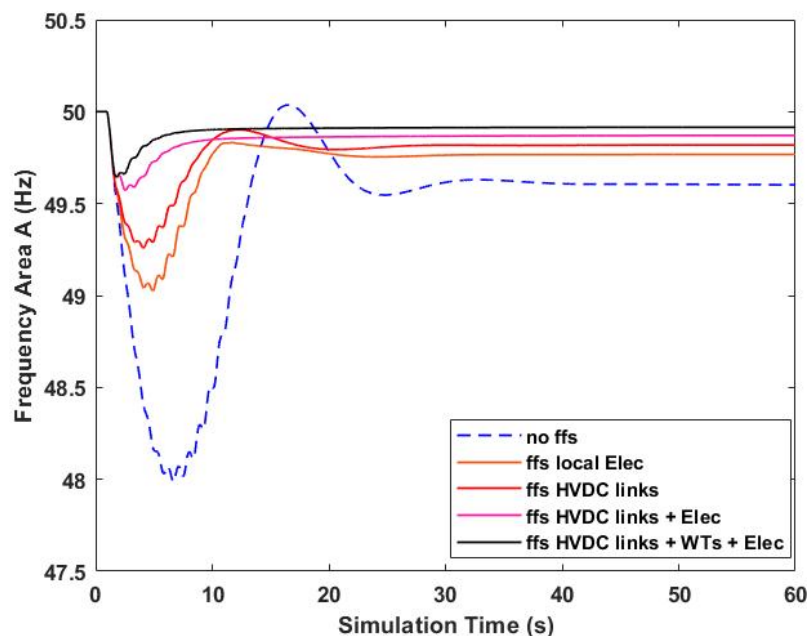


Figure 5.47: Frequency response area A - Loss of SGU A1a - FFS by local and inter-area means (OF2).

Table 5.12: Frequency response results -Loss SGU A1aG- FFS by local and inter-area means (OF2)

MEANS OF FFS	Local Electrolyzers	HVDC links	HVDC links + Electrolyzers	HVDC links + Electr. + WTs
OF2: Best Fitness Evaluation Value (60s)	4.3335	2.6387	1.4079	1.3875
F_A nadir (Hz)	49	49.26	49.6	49.66
F_A steady state (Hz)	49.77	49.82	49.87	49.92

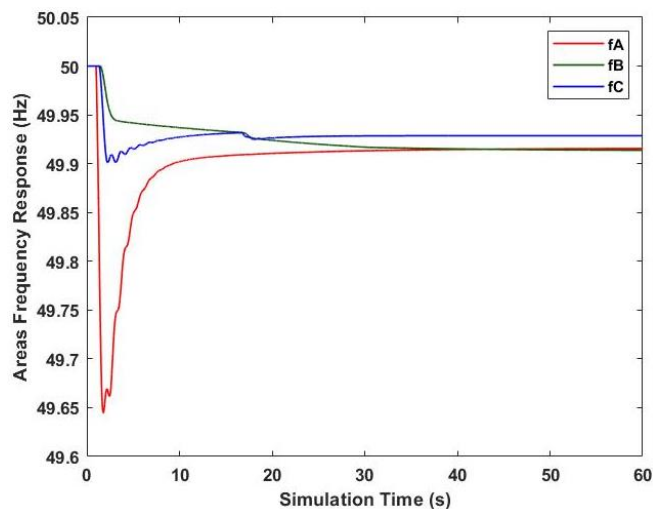


Figure 5.48: Areas' frequency response - Loss of SGU A1aG - FFS by all SI means (OF2).

In case of the best achieved result, the one that all the installed means of SI provide their support, the frequency in the 3 areas and the corresponding response of the various elements can be observed in Figure 5.48 to Figure 5.51. As it can be observed, the 3 areas effectively share the active power imbalance and sustain the frequency deviation achieving improved RoCof, nadir and steady state deviation due to the very fast response of the SI units. The frequency in the supporting areas starts to drop after 0.3s considered for the activation of the HVDC links, but it stabilizes close to 49.91Hz. In fact, when the HVDC links are activated, power exports from area A to other areas reduce to sustain the deviation as observed in Figure 5.50. Area B experiences the most significant drop of 390MW at a rate of 540 MW/s to support area A, whereas export to area C is also reduced by 140MW at a rate of 780MW/s. As area B experiences the most significant change in its imports, the optimization algorithm also modifies the power flow in the link BC to increase the power injection from area C. Electrolyzers in area A are almost instantaneously acting against the deviation when the event occurs. As it can be observed in Figure 5.49, unit A1 installed at the affected bus is the one that shoulders the imbalance followed by electrolyzer A5b which is installed close to the CCP of the most affected HVDC link, AB. As the frequency in area A restores to a new equilibrium, the consumption of the electrolyzers stabilizes with unit A1 experiencing again the largest deviation due to its location and the unlimited in time supporting capability of these elements. In area B, support from electrolyzers starts when the imbalance is shared through the HVDC links. Since the CCP constitute the origin of the disturbance for area B, units B1 and B2c installed

closer experience the most significant change in their demand. Similarly, in area C electrolyzers close to buses C1 and C8 experience significant changes with respect to their supporting capacity. Finally, considering the response of WTs, since no WTs are installed in area A, the units in area B and C modify their output with respect to the Δf induced by the HVDC links modifications. Since, WTs controllers have a larger deadband zone compared to electrolyzers, their power output is not so significantly affected as observed in Figure 5.51, whereas the share of their support depends mainly on their installed capacity.

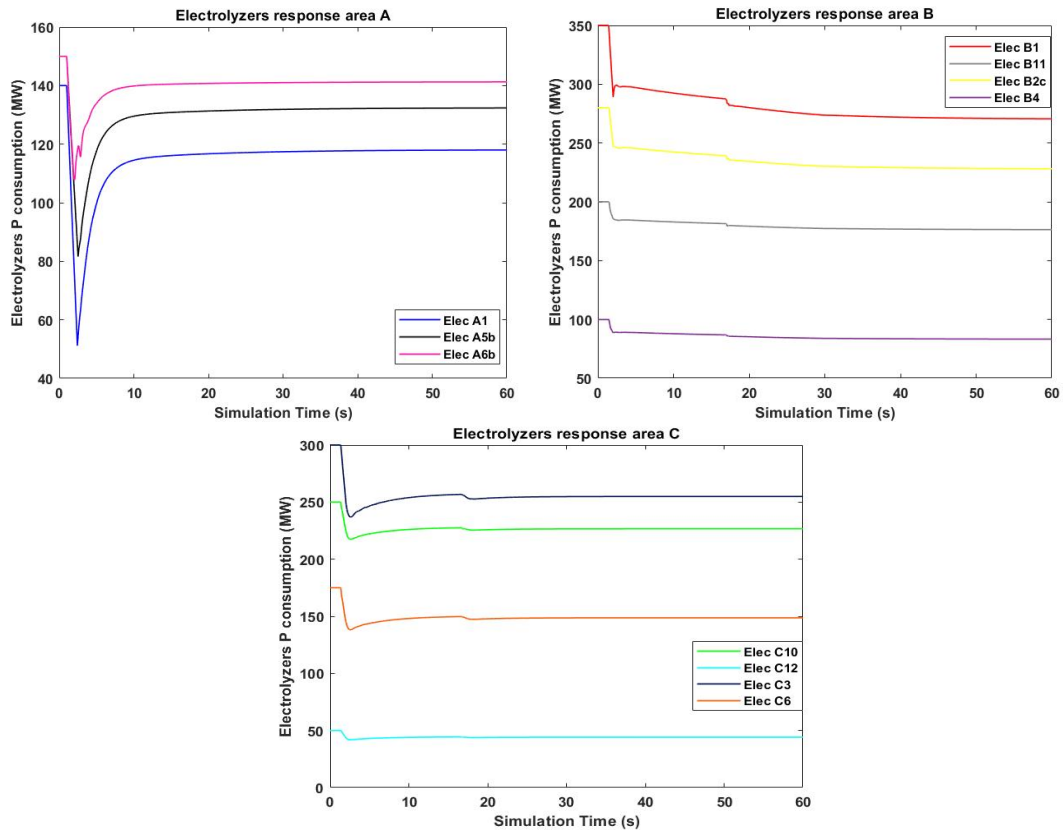


Figure 5.49: PEM Electrolyzers' power consumption - Loss of SGU A1aG -FFS by all SI means (OF2).

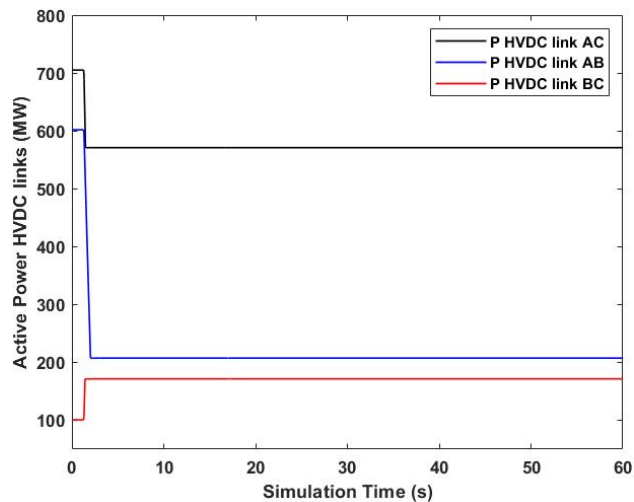


Figure 5.50: Active Power Flows HVDC links – Loss of SGU A1aG - FFS by all SI means (OF2).

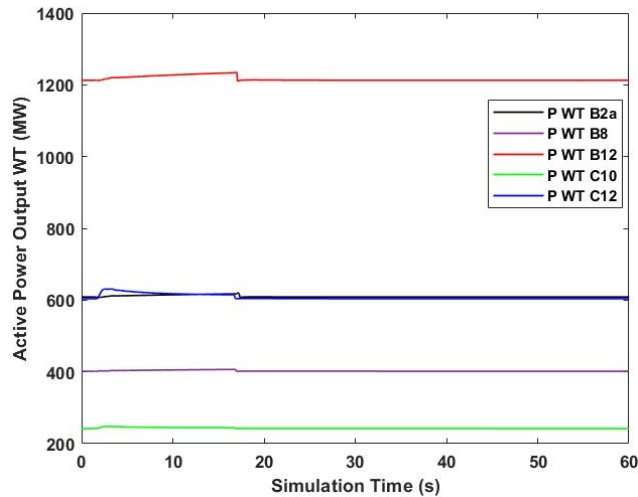


Figure 5.51: WTs' active power output - Loss of SGU A1aG - FFS by all SI means (OF2).

5.3.3. Loss of largest generating unit in area B (WTB10)

Similarly, to section 5.2.3 in this section WTB10 is set out of operation on the 1st s of simulation leading to an active power imbalance of 1200MW in area B. However, in this case the tuning of the frequency controllers of the various FFS elements is based on problem formulation 2. As expected, the frequency response of the system does not change from the one shown in Figure 5.15 and Figure 5.16 in the cases no FFS is provided or FFS is provided by the local means of SI operating at their maximum capability, respectively.

On the contrary, when HVDC links' power flows are modified and cooperate with the various means of SI in each area to offer FFS to area B, the tuning of the controllers is implemented with the aid of OF2 and thus different system responses are obtained. The best achieved frequency responses of area B in each case are presented in Figure 5.52. As it can be observed in the scenario at which all the installed means of SI are tuned cooperatively, the best response in the affected area is achieved. In this event, the role of the local electrolyzers and WTs has to be highlighted as the first ms following the disturbance they can effectively arrest the frequency drop occurring at very high rates. If not considered, support only from the HVDC links shown in red line is not provided quickly enough to effectively face an imbalance of such a magnitude under the low inertia conditions. Furthermore, in scenarios electrolyzers are used, their unlimited in time supporting capability leads to faster stabilization. Moreover, in the scenario only local means of SI are utilized, an acceptable frequency response shown in gray is obtained without affecting neighboring areas due to the large reserve capacity of FFS means in area B if they operate at their maximum capability and ramp rate. However, the only cases at which the frequency satisfies the normal operating state limits are those at which HVDC links and electrolyzers of all areas are supporting the grid with or without the additional injection from WTs. Detailed results of simulations can be observed in Table 5.13. As far as the best achieved fitness evaluation is concerned, it can be concluded that comparison is valid only when comparing scenarios with the same number of participating areas. In fact, when all 3 areas cooperate to mitigate the imbalance, the minimum value of OF2 is obtained when all means of SI are tuned, but in case only local means in area B are used without sharing the imbalance in neighboring areas a smaller value of OF2 is obtained. That is since the calculation of OF2 is based on the displacement of the speed of each area and thus the number of participating areas can significantly alter the OF2 value.

Consequently, the comparison of the best achieved fitness evaluation value must be carefully done based on scenarios with similar characteristics.

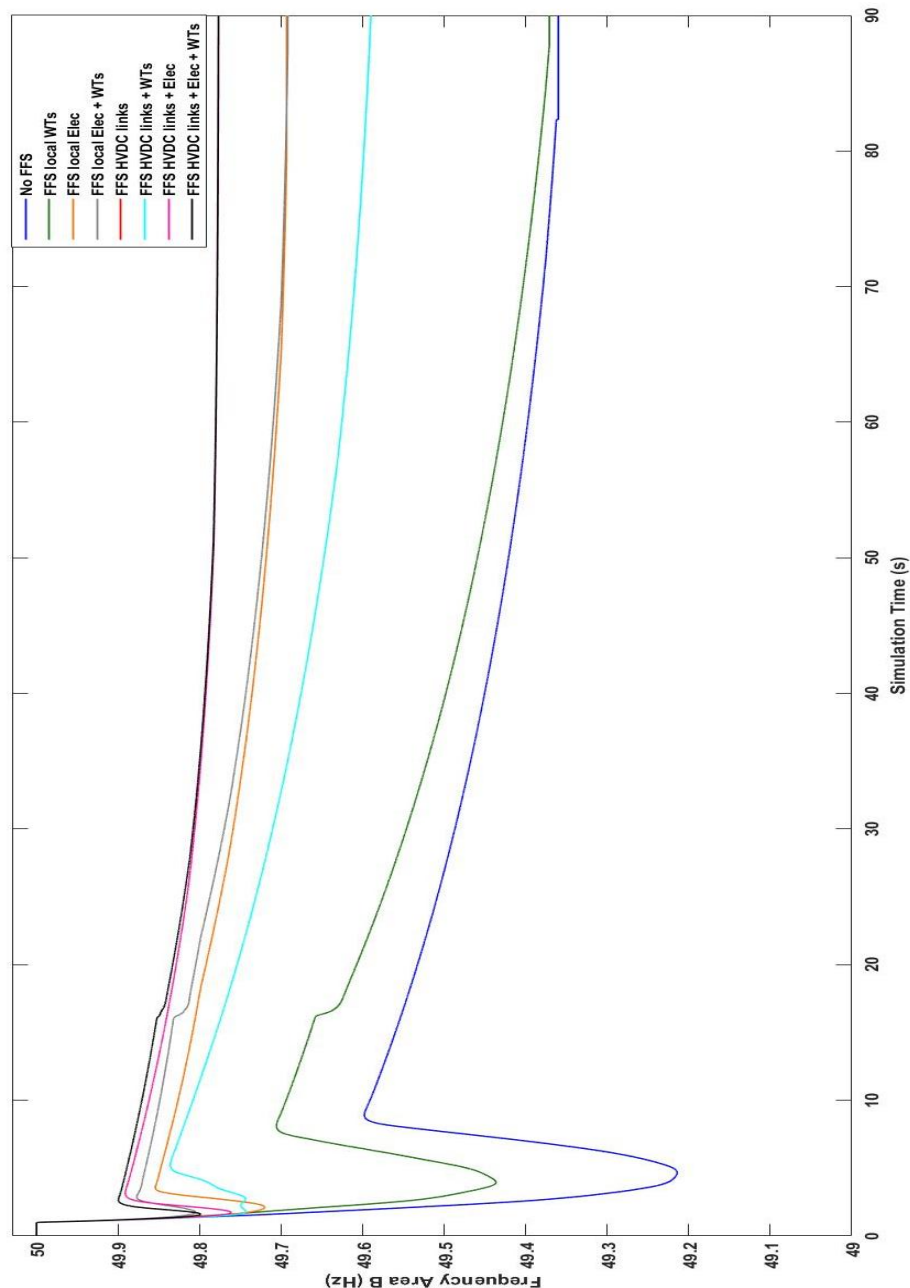


Figure 5.52: Frequency response area B - Loss of WTB10 - FFS by local and inter-area means (OF2).

Analyzing in further detail the scenario of the best frequency response in area B shown in black in Figure 5.52, the frequency responses of all the interconnected areas can be observed in Figure 5.53. As it can be seen, the utilized problem formulation tends to bring the responses of the 3 areas as close as possible the first seconds following the disturbance, trying to minimize and equalize the dynamic displacements. In this way not only an effective frequency containment is achieved but also, the frequency is preserved within the normal operating state bounds. However, it is clear that the steady state values of the frequencies do not converge. That is because this problem formulation focuses more on minimizing the rate of the displacement of the areas' speed and not directly the frequency deviation from its nominal value throughout the whole simulation.

Table 5.13: Frequency response results - Loss of WTB10- FFS local and inter-area means (OF2).

MEANS OF FFS	Local WTs	Local Electrolyzers	Local WTs + Electrolyzers	HVDC links	HVDC links + WTs	HVDC links + Elec	HVDC links + WTs + Elec
OF2: Best Fitness Evaluation Value (60s)	1.5661	1.06	0.6958	1.4887	1.3445	1.3187	1.06
F _B in.drop (Hz)	49.44	49.72	49.79	49.74	49.75	49.76	49.8
F _B steady state (Hz)	49.37	49.69	49.69	49.6	49.6	49.8	49.8

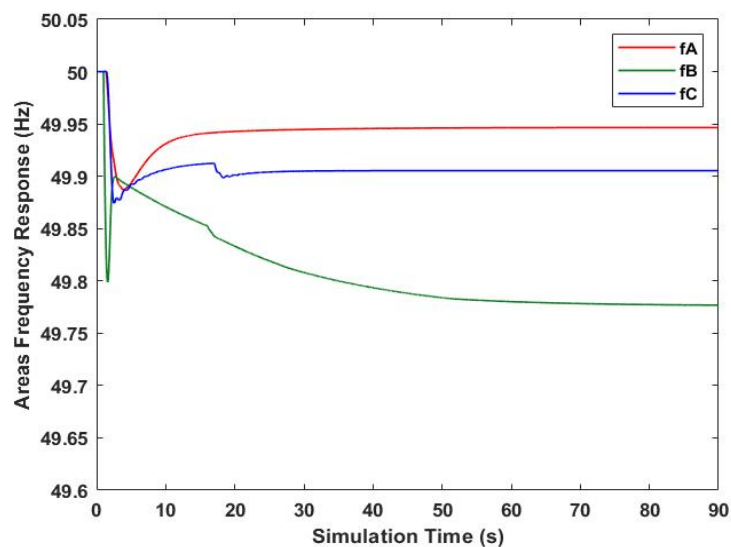


Figure 5.53: Areas' frequency response - Loss of WTB10 - FFS by all SI means (OF2).

Considering the response of the SI elements participating in the regulation, Figure 5.55 to Figure 5.56 can be observed. HVDC links AB and AC increase rapidly their injection to area C when activated. In fact, HVDC link BC shoulders the imbalance increasing its power flow by 350MW at a rate of 760MW/s, whereas area A increases the exports to both areas to support the affected area and to minimize the impact on area C. Electrolyzers in area B not only contribute the first seconds to the arrest of the initial RoCof but also to reach faster a stable point. The response of these units depends mainly in this case on their technical capabilities and less on the location of installation. In other areas electrolyzers are activated to mitigate the effect of the modifications on the HVDC links, with the units installed closer to the CCPs of the links to experience the most significant changes. Finally, WTs in area B are activated very fast due to the rapid initial drop and increase their active power output. Then, with respect to the frequency response, a second period of increasing injection is observed before the rapid return to the nominal value of the output after 15s of support. The latter effect leads to a second dip in the frequency handled by the electrolyzers and the remaining SGUs of the area. Finally, the response of the WTs to the disturbance is based mainly on the installed capacity of each unit.

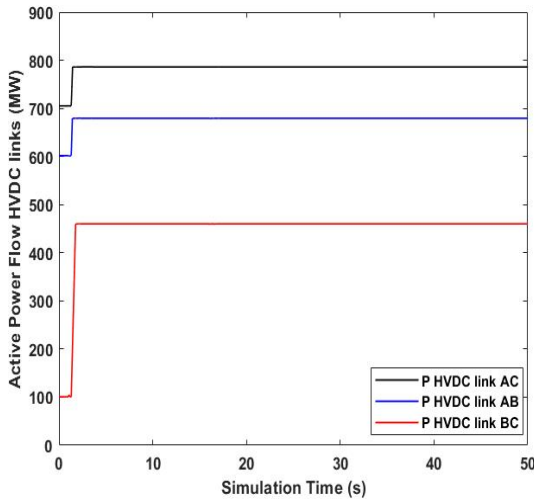


Figure 5.55: Active Power Flows HVDC links
Loss of WTB10 – FFS by all SI means (OF2).

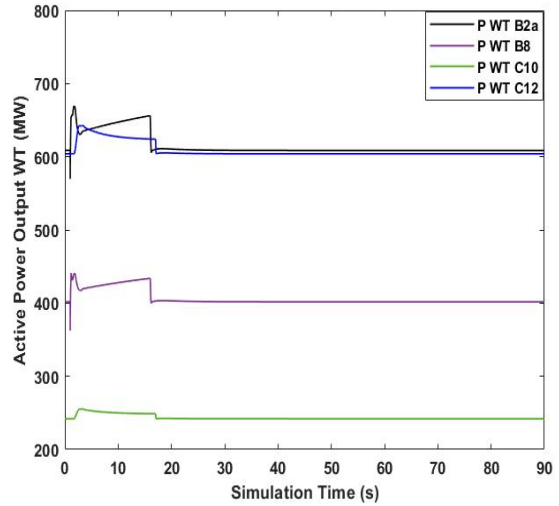


Figure 5.55: WTs' active power output –
Loss of WT B10 – FFS by all SI means (OF2).

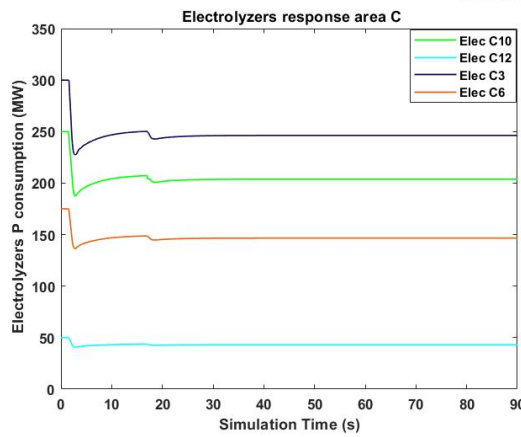
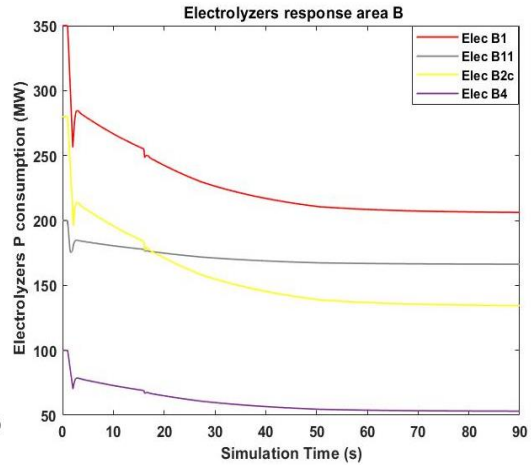
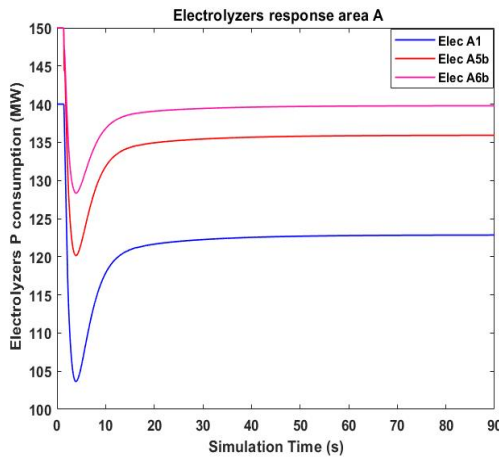


Figure 5.56: PEM Electrolyzers' power consumption - Loss of WTB10 - FFS by all SI means (OF2).

5.3.4. Load event area B

In this section the load event applied in section 5.2.4 takes place again on the 1st s of simulation to create an imbalance equal to 500MW in area B due to a step load increase at buses B8 and B10. Although no different frequency responses are expected in the scenarios only SGUs participate in the frequency containment or when only local units of SI operate at their maximum supporting capability against the imbalance, that is not the case with the rest of scenarios at which FFS units are acting cooperatively to sustain the deviations. That is due to the fact that in this case the tuning of their controllers is based on the minimization of OF2 with the aid of the MVMO algorithm as explained in chapter 4.

When all 3 areas participate in the frequency regulation, 4 different combinations of SI sources can be defined. Having optimally tuned the controllers' parameters and run the simulations the frequency responses of the affected area, area B, under the different scenarios are presented in Figure 5.57. As it can be observed, the best frequency response is obtained when either all the means of SI and the HVDC links support the grid to face the imbalance or at least HVDC links and electrolyzers cooperate. These 2 frequency responses exhibit minor differences since the frequency does not deviate significantly from the deadband zone of the WTs and thus their support is infinitesimal. The response is characterized by a period of high initial RoCof following the disturbance that is arrested when the electrolyzers are activated followed by a restoration period before stabilizing at 49.93Hz. In this case, the role of electrolyzers needs to be highlighted as they not only arrest the initial RoCof but also, they offer reduced drop and faster stabilization of the local frequency with the aid of local SGUs and the HVDC links modifications. If no adequate and fast support is provided, the frequency responses are characterized by a long restoration-stabilization period. Among the other responses, the scenario at which only the local electrolyzers and WTs are contributing to the imbalance without the aid of other areas leads to the 3rd best frequency response because of the very rapid response of these elements and the size of their supporting capability. Finally, it can be also observed that in cases WTs provide support in large magnitudes, the response is characterized by a 2nd frequency dip of large RoCof when the WTs output returns to its nominal value. The latter is perceived by the grid as a second active power imbalance that needs to be mitigated without any new modifications in the HVDC links flows. Detailed results of the frequency responses of each scenario can be observed in Table 5.14. Similarly, to the previous events under problem formulation 2 the value of OF2 is indicative of the best achieved frequency response only when the same number of areas are considered in the comparison process. As a result, the local means achieve a smaller value compared to the case that has the best response since the dynamic displacements of the speed in the former case are considered in a single area whereas in the latter case in 3.

In case all the means of SI in the 3 interconnected areas are acting against the imbalance, the response of the 3 areas obtained can be observed in Figure 5.58. As it is clear, the MVMO algorithm tries to tune the frequency controllers in a way to achieve the minimum change in the trajectories of the dynamic displacements of the speeds of the 3 areas and equalize them leading the responses at very close initial rates but has no direct effect on the minimization of the steady state error. In this way, it also achieves very close performance in steady state for areas A and C but not for area B which requires more time and sources to stabilize.

Table 5.14: Frequency response results - Load event area B- FFS local and inter-area means (OF2).

MEANS OF FFS	Local WTs	Local Electrolyzers	Local WTs + Electrolyzers	HVDC links	HVDC links + WTs	HVDC links + Elec	HVDC links + WTs + Elec
OF2: Best Fitness Evaluation Value (60s)	0.1105	0.089	0.07	0.3555	0.2213	0.1646	0.1398
F _B in.drop (Hz)	49.93	49.94	49.94	49.94	49.94	49.94	49.94
F _B steady state (Hz)	49.72	49.9	49.9	49.88	49.84	49.93	49.93

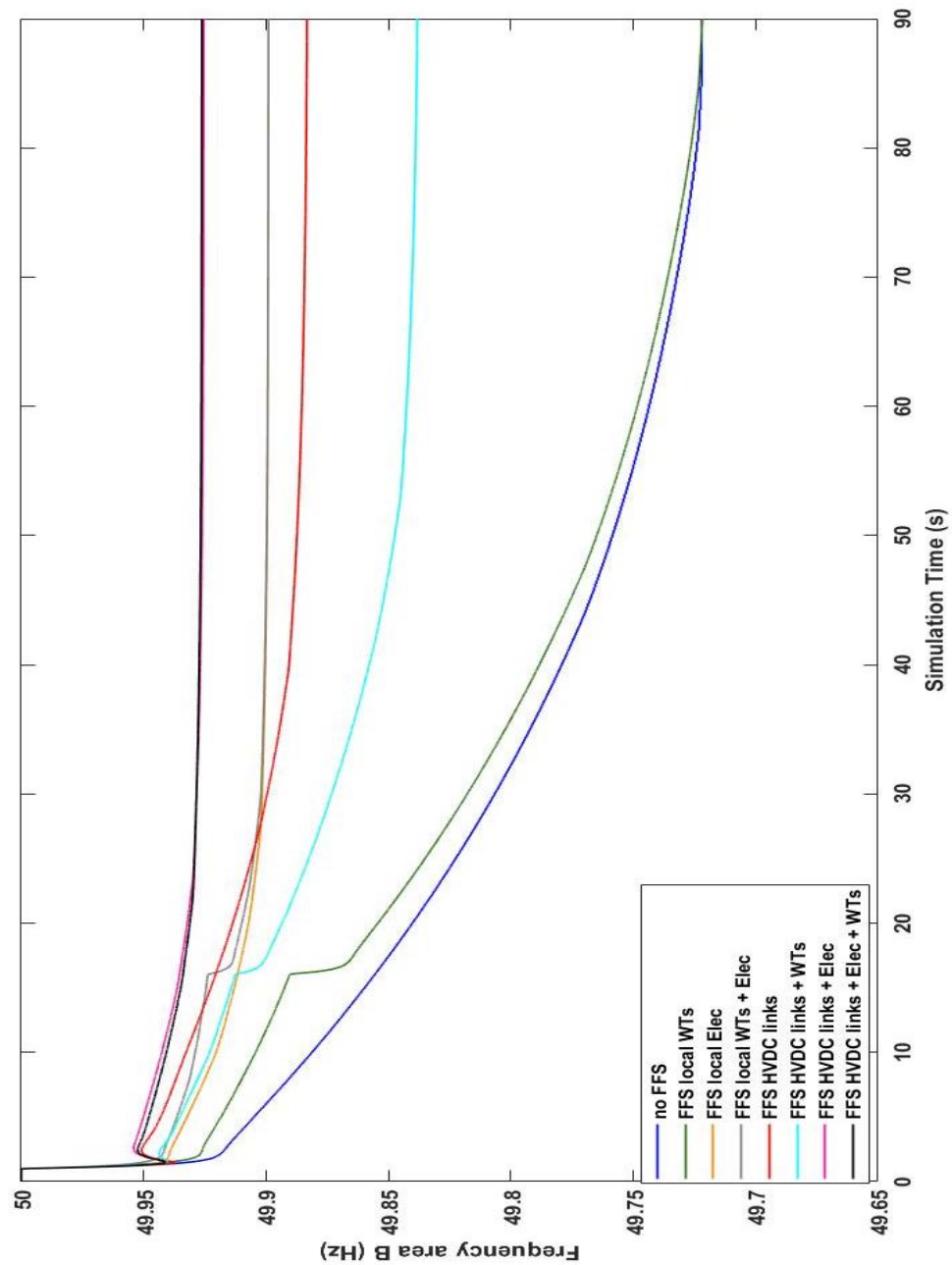


Figure 5.57: Frequency response area B - Load event area B - FFS by local and inter-area means (OF2).

In a deeper look at the responses of the participating to the FFS elements, HVDC link BC is the one that mainly injects power to area B increasing its power flow to 300MW, whereas link AB do not directly support area B but area C which is the main supporting area (Figure 5.59). Electrolyzers response in the affected area shown in Figure 5.60, is characterized by an initial rapid response to sustain the large initial drop followed by a period at which stabilization is pursued. Units closer to buses B8 and B10, depending also on their installed capacity, exhibit the most significant changes in their consumption. Electrolyzers in area A installed closer to the CCP with HVDC link AC mainly modified, are triggered to provide larger amounts of active power whereas unit A6b which is remotely installed remains unaffected due to its location and the magnitude of the imbalance shared. In area C, units C10 and C3 are those who due to their bid and location exhibit a significant initial change, whereas units C6 and C12 are not so significantly affected. Finally, in all areas where WTs are installed, no remarkable changes in their outputs are encountered since the frequency displacements are within their deadband zone. The latter confirms that the support from WTs in this event is not required and thus HVDC links and electrolyzers can effectively handle the imbalance.

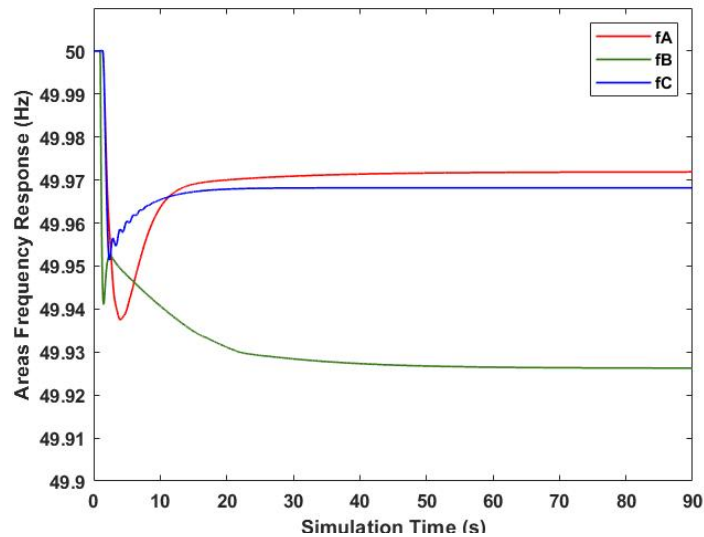


Figure 5.58: Areas' frequency response - Load event area B - FFS by all SI means (OF2).

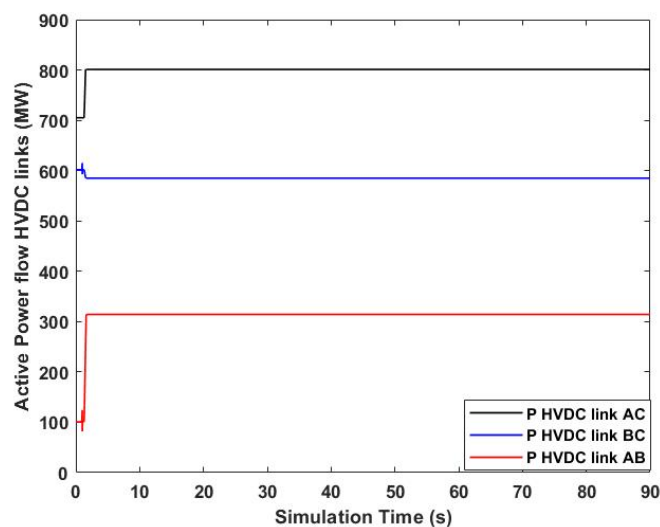


Figure 5.59: Active Power Flows HVDC links – Load event area B - FFS by all SI means (OF2).

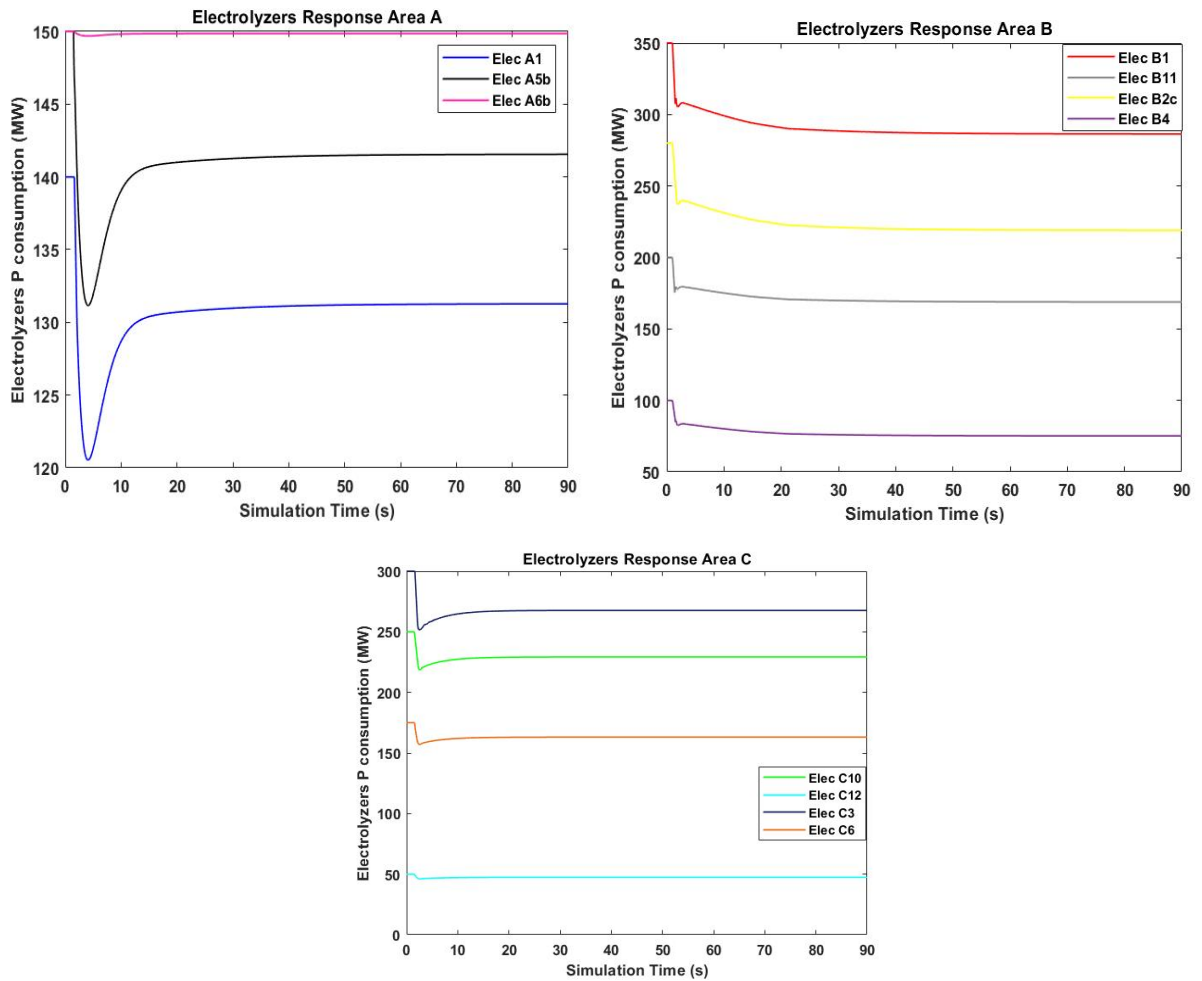


Figure 5.60: PEM Electrolyzers' power consumption - Load event area B -FFS by all SI means (OF2).

5.3.5. Load Event Area C

In this section a load event increasing the power consumption at buses C4 and C7 is performed at the 1st s of simulation leading to an active power imbalance of 370MW, that constitutes a 10% increase in the area's demand. The tuning of the controllers of the participating to the frequency regulation elements in this case is based on problem formulation 2. In case the imbalance is handled either by the local SGUs or any combination among the local means of SI, no differences are expected in the system's response with respect to Figure 5.35 and Figure 5.36 respectively as the participating elements operate at their maximum capability. In the worst-case scenario, the frequency in area C drops to 49.35Hz and restores to 49.73Hz with the aid of local SGUs.

When the various means of SI such as WTs and electrolyzers are supporting the grid in cooperation with the modified power flows on the HVDC links, tuning of the controllers depends on the minimization of OF2 and thus different responses are obtained. The best achieved frequency responses of the affected area C utilizing different groups of SI sources can be observed in Figure 5.61, whereas the complete results for the response in area C are presented in Table 5.15. The best result in terms of both frequency nadir and steady state deviation is obtained when all installed means of SI are cooperatively tuned against the imbalance. The latter response appears to have small differences from the scenario at which HVDC links and electrolyzers are only utilized with the second one to experience worse initial performance due to the lack of WTs support. Also, with

respect to the size of the disturbance, support by local means achieves one of the best responses when operating at maximum capability. Also, it is crucial to mention that the higher the support from WTs, the higher the second dip in the frequency after 15s that is characterized by a similar to the original RoCof if no other means provide rapid support after that time period. That highlights the drawback of considering only HVDC links and WTs as the former ones are only once modified per simulation and the latter ones provide limited in time. Finally, looking at the best achieved values of OF2 in Table 5.15, it is clear that their comparison is valid only when the same number of participating to the frequency regulation areas is considered.

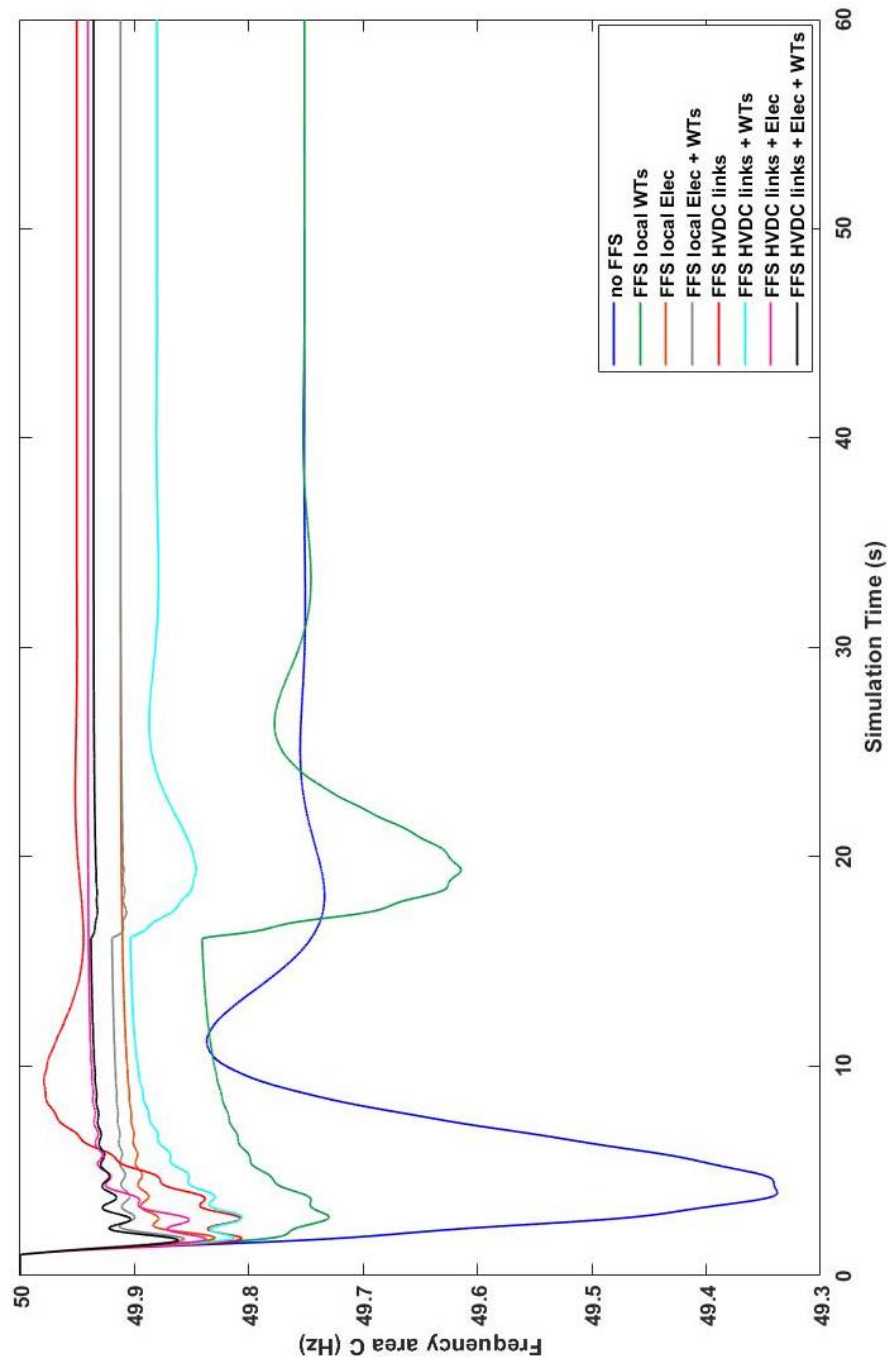


Figure 5.61: Frequency response area C - Load event area C - FFS by local and inter-area means (OF2).

Table 5.15: Frequency response results - Load event area C- FFS local and inter-area means (OF2).

MEANS OF FFS	Local WTs	Local Electrolyzers	Local WTs + Electrolyzers	HVDC links	HVDC links + WTs	HVDC links + Elec	HVDC links + WTs + Elec
OF2: Best Fitness Evaluation Value (60s)	0.7588	0.3226	0.2822	0.4645	0.4	0.3249	0.2932
F _c in.nadir (Hz)	49.62	49.83	49.86	49.81	49.81	49.84	49.86
F _c steady state (Hz)	49.75	49.91	49.91	49.95	49.85	49.94	49.94

Considering the scenario that all sources of SI are tuned against the imbalance, the areas' frequency response can be observed in Figure 5.62. In this case, the optimization solution tends to bring the initial RoCof of the 3 areas as close as possible to equalize the rate of change of the speed of each area and thus the frequency and in that way to minimize the nadir and steady state deviation. The latter however, leads the responses not to converge at close points as the deviations in the volume V occur during the first ms following the disturbance and thus the value of the OF2 does not increase during the stabilization period.

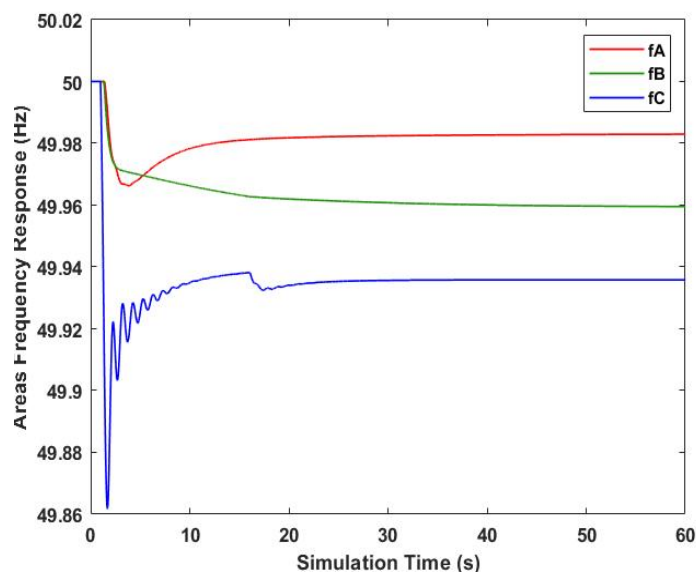


Figure 5.62: Areas' frequency response - Load event area C - FFS by all SI means (OF2).

In this scenario, HVDC links as expected are modified to inject more active power to area C. Thus, as shown in Figure 5.63, HVDC link AC increases the injection to area C by 100MW and link BC interrupts the exports from area C to area B to sustain the local deviations. The latter takes place at high rates of 800MW/s and 620MW/s respectively to mitigate the large initial RoCof. Electrolyzers in the affected area, are responsible to act rapidly before the activation of the HVDC links and sustain the initial drop. That is confirmed in Figure 5.64 and in fact the location of the electrolyzers plays a significant role as unit C3 installed close to the disturbance is more affected compared to the others. Electrolyzers in area A exhibit similar responses although the most remotely installed one unit, A6b, contributes the least. In area B, electrolyzers alter their consumption

to minimize the effect on that area too with electrolyzer B2c installed at the CCP of HVDC link BC to be the most affected one. Finally, WTs in area C as observed in Figure 5.65 provide their support for 15s, changing their outputs according to the frequency deviation and their installed capacity. On the other hand, WTs in area B remain unaffected as the frequency in area B remains within their deadband zone.

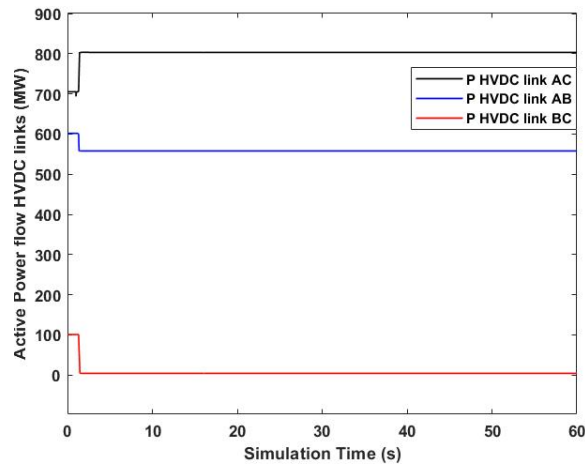


Figure 5.63: Active Power Flows HVDC links – Load event area C - FFS by all SI means (OF2).

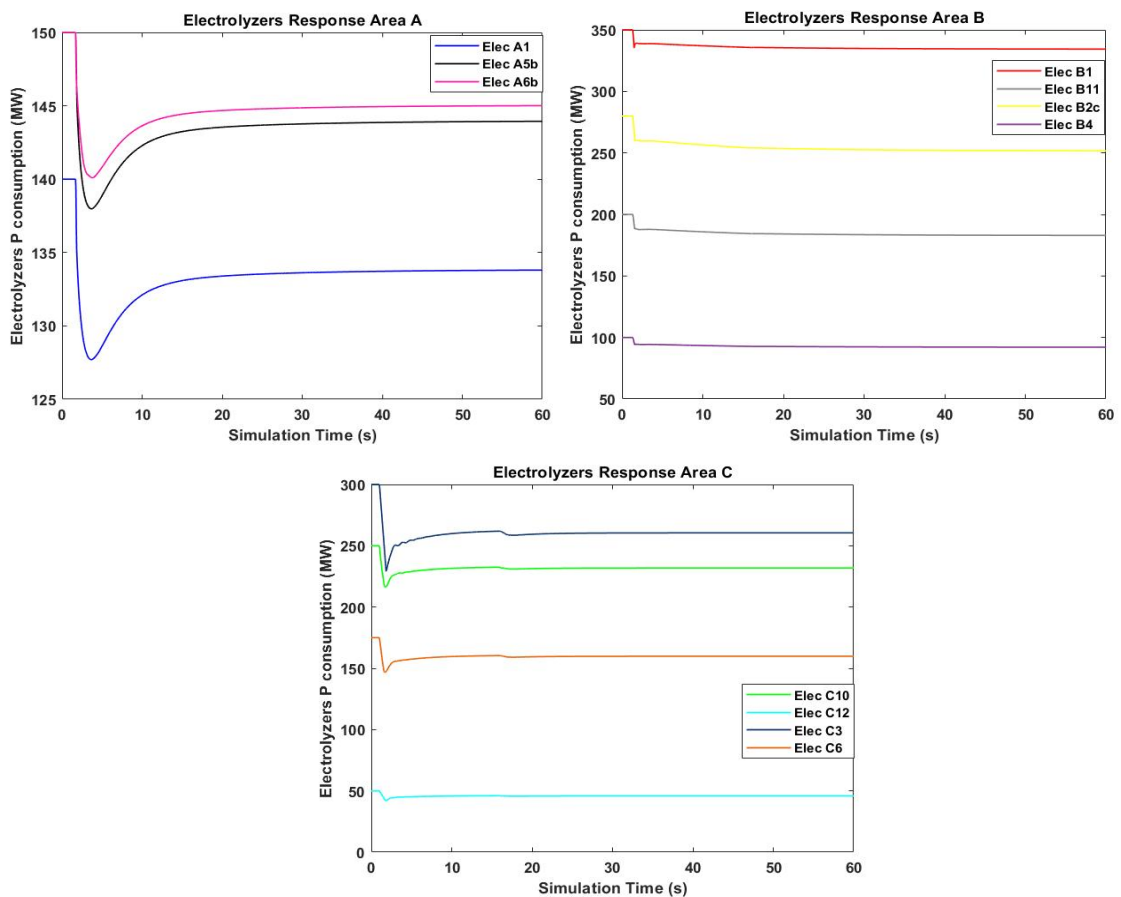


Figure 5.64: PEM Electrolyzers' power consumption - Load event area C -FFS by all SI means(OF2).

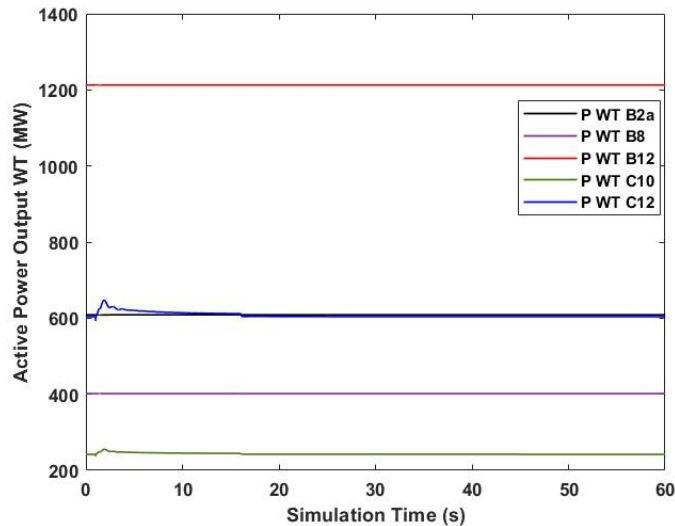


Figure 5.65: WTs' active power output – Load event area B - FFS by all SI means (OF2).

5.3.6. Load event area A

In this section, similarly to 5.2.5, a load event of 180MW takes place at bus A5a in area A. This event leads to a frequency deviation characterized by a nadir of 49.77Hz that stabilizes at 49.95Hz if no means of SI support the grid. The corresponding response can be observed in Figure 5.29. When support is provided by local electrolyzers in area A at their maximum capability, the frequency response of the system is also the same as in section 5.2.5. However, when multiple means of SI installed in all areas are tuned cooperatively against the imbalance under problem formulation 2 different frequency responses are obtained. Considering the various possible combinations, the best responses for area A can be observed in Figure 5.66 and the detailed simulation results in Table 5.16.

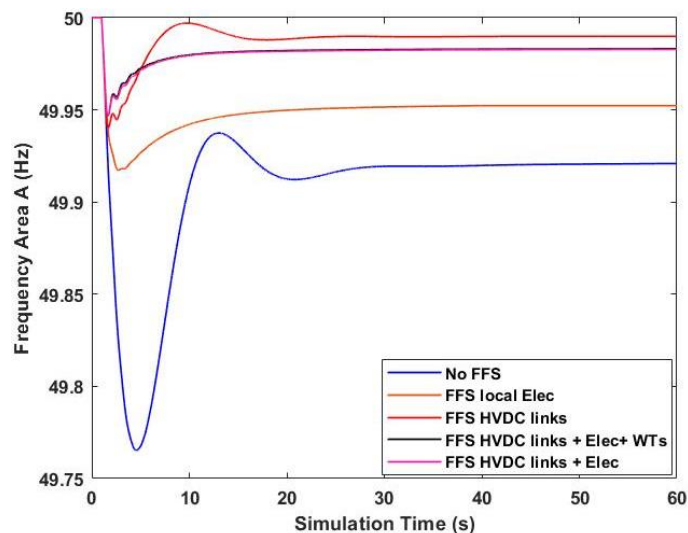


Figure 5.66: Frequency response area A - Load event area A - FFS by local and inter-area means (OF2).

As it is clear all the possible options considering the modified power flows in the HVDC links tuned with OF2 against the disturbance achieve improved results in terms of nadir and steady state deviation for the

affected area. However, as it can be concluded from the values OF2 in each scenario, the option at which only HVDC links are considered has a significant impact on the interconnected areas. In contrast, improved performance with minor differences is encountered when the latter one is combined with electrolyzers with or without the support from WTs. However, support from WTs is minor as no RES units are installed in area A and the shared imbalance in other areas does not trigger the activation of local WTs.

Table 5.16: Frequency response results - Load event area A- FFS local and inter-area means (OF2).

MEANS OF FFS	Local Electrolyzers	HVDC links	HVDC links + Electrolyzers	HVDC links + Electr. + WTs
OF2: Best Fitness Evaluation Value (40s)	0.0519	0.0685	0.0468	0.0464
F_A nadir (Hz)	49.92	49.94	49.95	49.98
F_A steady state (Hz)	49.95	49.99	49.95	49.98

The best achieved response regarding all the interconnected areas can be observed in Figure 5.67. As it is clear the 3 areas share the imbalance by equalizing the initial RoCofs of the areas' frequencies to sustain the deviation and effectively reach an equilibrium point close to 49.98Hz. In this scenario, to mitigate the frequency deviations, HVDC links power flows are modified according to Figure 5.68. As it can be seen, HVDC link AB mainly shoulders the imbalance and reduces the exports to area B to sustain the deviation. To mitigate the impact on area B, area C injects more power to area B to meet the local needs. Electrolyzers in area A are all activated to reduce their consumption against the imbalance that occurs at bus A5a. As it can be seen in Figure 5.69, all electrolyzers in area A exhibit a similar response to the imbalance independent from the location of installation. Electrolyzers installed in other areas react to the imbalance shared to sustain the local deviation with units closer to the CCPs of the HVDC links to be the most affected ones. Finally, the active power output of WTs does not present any notable difference due to the magnitude of the disturbance.

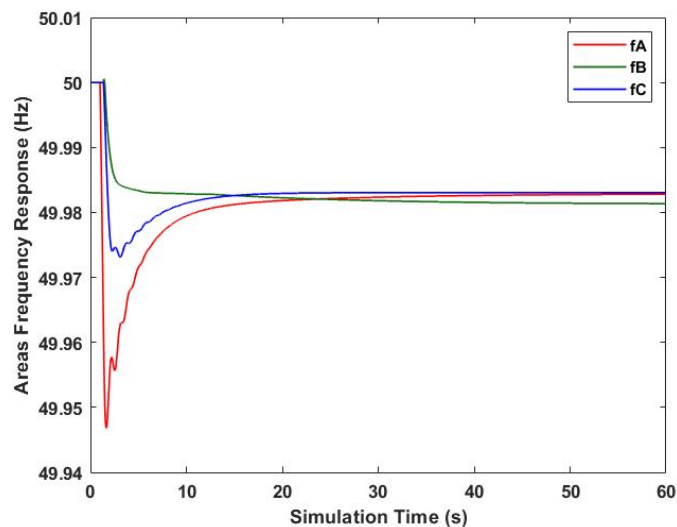


Figure 5.67: Areas' frequency response - Load event area A - FFS by all SI means (OF2).

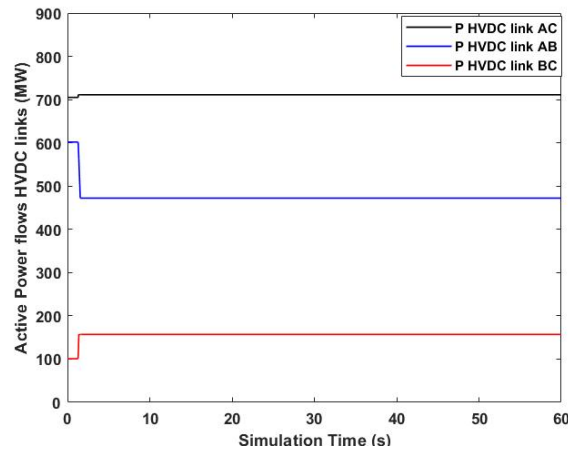


Figure 5.68: Active Power Flows HVDC links – Load event area A - FFS by all SI means (OF2).

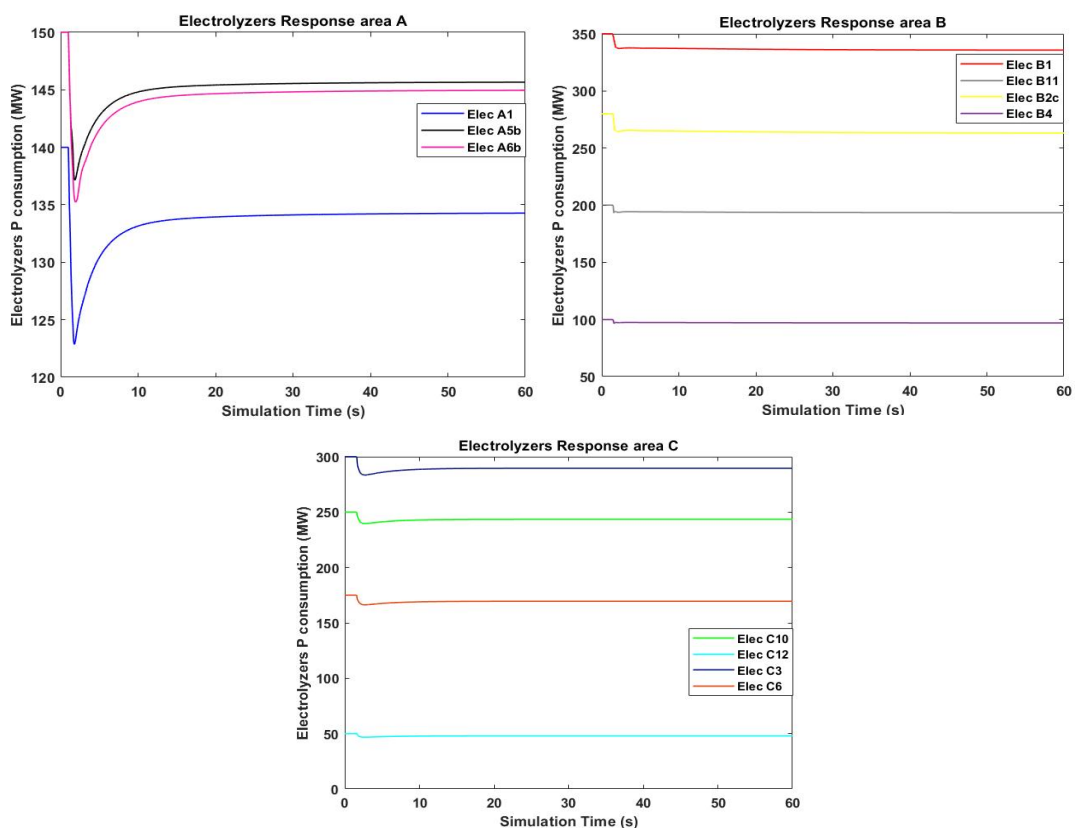


Figure 5.69: PEM Electrolyzers' power consumption - Load event area A - FFS by all SI means (OF2).

5.4. Simulation highlights

Having performed a set of extensive RMS simulations evaluating the performance of the control strategy and optimization methods proposed in this study the following points can be highlighted:

Regarding the sources of SI and frequency performance:

- In all active power events applied in different system areas and under both tuning strategies, the best frequency results in terms of maximum instantaneous frequency deviation, are obtained when all elements of FFS installed are cooperatively tuned against the imbalance. Indicative graphs of the maximum frequency deviation per event and OF can be observed in Figure F.1 and Figure F.2.

- The fast response of local means in each area such as electrolyzers and WTs is important for the initial arrest of the frequency in the affected area as modifications on the power flows of the HVDC links have a notable delay of 0.3s. In areas of low inertia characteristics this time delay is significant, and the role of local SI means is even more than important. The higher the local reserve capacity the better the response.
- In all active power events applied in different system areas and under both tuning strategies, the best frequency results in terms of steady state frequency deviation are obtained when all means of SI installed in the 3 areas are coordinated against the imbalance. Indicative plots of the steady state deviation of the frequency of the affected area per event and OF can be observed in Figure F.3 to Figure F.6.
- For significant active power events such as loss of large generating units, the reserve capacity of local means is not enough to achieve responses within the normal operating state bounds. In these cases, the local means can effectively achieve improved RoCof and nadir for the affected area and modifications on the HVDC links may help in achieving improved nadir, steady state deviation and faster stabilization. For smaller imbalances, like load events, local means of SI can achieve acceptable frequency responses when are tuned to operate at their maximum supporting capability in terms of bid and rate.
- WTs can only provide support for a limited amount of time equal to 15s. In most cases under significant active power events and low inertia conditions this period is not sufficient to restore the frequency in the affected area within the deadband zone of the WTs. Hence, WTs inject additional active power for 15s improving the initial system response and then return to their nominal output. The latter is perceived by the grid as a second imbalance that leads to a second frequency dip that needs to be handled by the remaining units of SI and the local SGUs. The larger the participation of the WTs against the imbalance in that period, the larger the impact on the frequency after its interruption.
- HVDC links are only modified once throughout the simulation considering their active power flows based on the minimization of the utilized OF. This means that they lack on real time regulation based on instantaneous deviations in contrast to electrolyzers and WTs. Hence, if not combined with other local means of SI in most cases worse response is obtained and insufficient regulation or periods of small over frequencies can be encountered. Also, if combined only with local WTs, after the WTs supporting period of 15s, HVDC links cannot help in the mitigation of the second frequency dip encountered. Furthermore, the introduced time delay of 0.3s for their activation may lead to ineffective support in the RoCof of the affected area under very low inertia conditions, highlighting the need of local FFS means. However, for significant active power events, the role of HVDC links is more than crucial for sharing the imbalance between areas and shouldering the frequency regulation.
- Electrolyzers are units that significantly improve the frequency response of the system in all areas. Their FFR can effectively maintain the initial frequency drop and help in the restoration process based on the instantaneous frequency deviations. When combined with HVDC links, this group can achieve frequency responses very close to the optimal ones. For smaller events electrolyzers shoulder the imbalance and achieve significantly improved responses with respect to their supporting capability and the technical characteristics of WTs. Since their regulation is based on the instantaneous deviations, abrupt changes in the sustainment and restoration periods are effectively avoided, whereas they can help in the mitigation of frequency dips induced by the limited in time support from WTs. When installed in supporting areas, they

effectively shoulder the mitigation of the impact of the shared imbalances at very fast rates. Also, in cases of very low inertia conditions, electrolyzers help the system to reach faster an equilibrium point due to their unlimited in time supporting capability. However, their unlimited in time support leads to permanent steady state deviations in their consumption that need SFC schemes to restore.

Regarding the performance of different problem formulations:

- Both problem formulations have been proven effective in the utilization of different sources of SI against commonly occurred critical active power imbalances no matter their magnitude or location of occurrence.
- Under both problem formulations when the magnitude of the disturbance is rather small compared to the available research space, the algorithm finds it more difficult to converge to a global rather than a local optimum. In these cases, the role of boundaries and initial vectors is important.
- Problem formulation 1 focusing on the mitigation of the frequency excursions of each area from its nominal value, can be effectively used in any type of study as the frequency can be measured at any system bus being a global variable. On the contrary, problem formulation 2 focuses on the mitigation and equalization of the rate of change of the speed dynamic displacements of each area. The calculation of the latter one depends on the speeds of SGUs of each area and thus this method cannot be used in areas with no SG.
- The value of OF1 is affected by the simulation time as it considers the integral of the instantaneous frequency excursions. Hence, since it directly controls both the transient and the steady state period, additional attention should be paid on the determination of a suitable simulation time to force the algorithm not to focus on the steady state rather in expense of the initial deviation. On the other hand, OF2 focuses more on the period the dynamic displacements occur and thus it is not affected by the simulation time. The latter characteristic assumes that equalization and mitigation of the initial displacements will also lead to the convergence of the steady state frequency of different areas, which is not directly controlled in this case. However, this is not always valid for areas of different characteristics and inertia conditions leading to poor steady state convergence.
- The value of OF1 is indicative of the response of the affected area and the impact on the supporting areas no matter the number of elements considered. Thus, the lower the value of OF1 the better the frequency response in the affected area and the lower the impact on the neighboring areas. On the contrary, that is not always the case with OF2, but it is only valid when comparing scenarios with the same number of areas. However, it is indicative of the performance in the scenarios the same number of areas considered. This shows the high impact of the number of participating areas on the displacements and on the value of OF2.
- Comparing the frequency of the affected area in the best achieved scenarios per event and OF, it can be concluded that OF1 achieves better performance in terms of nadir and steady state deviation for the affected area compared to OF2. Also, in most of the events under the tuning of OF1 the frequency of the interconnected areas converges to a closer point compared to when tuned under OF2. Indicative plots of the corresponding findings can be observed in Figure F.7 and Figure F.8. The latter result shows that the aim of OF2 to minimize the rate of change of the dynamic displacements may not lead to the best response for the affected area. In fact, OF2 tends to focus more on areas with the lowest inertia and thus higher RoCof than OF1, which may have a significant effect on the response of the affected area when the area

of the lowest inertia acts as a supporting one. Also, the indirect control of steady state deviation of OF2 in contrast to OF1 may lead to better responses in case of the latter method.

- Both objective functions converge at very fast rates close to an optimum value depending on the initial vector either provided by the user or randomly generated by the MVMO algorithm. OF2 has higher values than OF1 as it is based on the weight factors applied. Finally, even at large research spaces the MVMO algorithm can lead to OF minimization close to a local optimum. Indicative plots of the convergence of the algorithms OF and optimization variables under both problem formulations can be observed in Figure F.9 to Figure F.12.

Regarding the utilization of sources of SI with respect to the location per OF:

- Under both problem formulations, the imbalance tends to be shared among the areas and not to fully release the local means of SI first. If the latter is the preferable strategy for TSOs, then special constraints or initial vectors should be provided to the algorithm.
- Considering the utilization of HVDC links, in both problem formulations the direction of the power flows changes correctly aiming at increased active power injection to the affected area. The most affected HVDC links are those installed closer to the origin of the imbalance. As a result, HVDC links with CCPs closer to the imbalance are more significantly affected. Also, it can be observed that under OF1 HVDC links transfer in total more active power to the affected area than in OF2. Also, in all cases the area with the lowest inertia acts as a supporting area, OF2 tries to minimize the interactions with this area to avoid extensive displacements, which is not the case with OF1.
- In most cases the location of the electrolyzers is critical as the units closer to the disturbance exhibit a significant initial change in their power consumption and their steady state demand. Similar is the case in supporting areas with units closer to the CCPs of HVDC links to be more significantly affected. Of course, in all cases the available capacity of the corresponding units also plays a significant role apart from the location. Also, electrolyzers closer to WTs providing significant amounts of support face a second change in their consumption after 15s. Under OF2 it can be observed that the role of electrolyzers is more crucial compared to OF1. That is due to the fact that, electrolyzers are the units which are firstly activated to sustain the frequency deviation and thus they can arrest the initial RoCof and any other excursion occurring throughout the simulation. Also, due to the decreased participation of HVDC links in OF2 compared to OF1, electrolyzers tend to provide more active power in the former case rather than in the latter.
- Considering the utilization of WTs, it can be concluded that the main parameter that affects their response is their available reserve capacity with respect to the magnitude of the imbalance. The location of installation has not shown a significant role in the regulation due to the fact that the deadband zone of WTs is larger than the one of electrolyzers and thus in most of the cases frequency is first handled by the electrolyzers before the activation of WTs. For smaller in magnitude events the offer of WTs is infinitesimal while for large events is significant only for the first seconds following the disturbance. Finally, under OF2, extensive support from WTs both in terms of magnitude and time is avoided as the interruption of support by these units after 15s leads to a second change in the dynamic displacements of the areas speeds which has a higher impact on the value of OF2 rather than OF1. This is because OF2 focuses more on the rate of change, whereas OF1 on the deviation itself.

6 Conclusions & Future Work

This chapter provides a summary of the thesis project elaborated in the previous chapters, answers to the research questions formulated in chapter 1 and finally proposals for future research

6.1. Thesis summary

Converter based power systems forming today due to the energy transition, environmental policies and the emergence of new technologies induces significant challenges for the continuous, reliable, and stable operation of power systems. The new low inertia conditions encountered due to the decommissioning of SGUs by RES, the increasing utilization of HVDC technology for the asynchronous interconnection of systems and remotely installed RES, the introduction of controllable responsive demand units and the very fast and frequent switching of the PEIs form a rapidly evolving dynamic and volatile system putting in danger its stable operation. Among different challenges, frequency stability has been highlighted as one of the major concerns for TSOs.

Having as motivation the aforementioned, a model of a multi-area multi-energy hybrid HVDC/HVAC power system suitable for PSS studies representing a PE dominated power system of the future has been created in this thesis project in DPF 2020, a powerful software tool for dynamic stability studies. The latter system is a modified version of the original PST 16 benchmark system that consists of 3 areas asynchronously interconnected with the state-of-art MMC-based HVDC links. Furthermore, the generation mix of the 3 areas has been updated through the replacement of SGUs by fully decoupled WTs type 4 creating 3 areas of different generation and inertia characteristics. Moreover, 20% of the load demand of each area has been replaced by decoupled fully controllable PEM electrolyzers that are expected to constitute a significant amount of the hydrogen based future power consumption.

For the smooth interconnection of all these new introduced elements, PEI and more specifically VSCs have been utilized enabling the fast and independent control of their power outputs. The latter capability of these elements highlights the provision of FFS against commonly occurred active power imbalances of the local grid if their controllers are enhanced to respond to these phenomena. For this reason, the control structure of the converter stations of the HVDC links, WTs and PEM electrolyzers has been modified with the APG control strategy, a method able to control the amount and the rate of change of the active power output of these units with respect to the frequency response of the system following an active power imbalance. The modified system constitutes a great canvas for frequency stability studies in a multi-area multi-energy power system with the provision of FFS from various means of SI.

However, when multiple elements are simultaneously used against the same imbalance, coordination among them is more than necessary to avoid insufficient or over regulation of the target variable. Hence, a coordinated tuning of all the participating controllers of the means of SI should be performed. Based on that,

2 different problem formulations have been proposed in this study. Problem formulation 1 depends on the minimization of the frequency excursions occurring in the 3 interconnected areas following a significant active power imbalance from its nominal value of 50Hz. Problem formulation 2 on the other hand, aims at the minimization and equalization of the rate of change of the trajectories of the dynamic displacements of the speeds of each of the interconnected areas following a significant active power imbalance. The 2 different approaches have been developed in python script and utilize a python-based version of a powerful optimization metaheuristic algorithm, the MVMO algorithm to solve the optimization problem through the creation of a co-simulation environment between DPF and python.

Following that step, a set of significantly commonly occurred active power imbalances has been defined for each of the interconnected system areas that exhibit different generation, demand, structure and inertia characteristics. These events have been applied to the modified system to examine the control and tuning strategies through extensive time domain RMS simulations. The outcomes of these simulations highlight the effectiveness of the control strategy under the new operating conditions and the best tuning method for the participating controllers. Finally, the simulation results evince the group of SI sources that achieve the best frequency response of the system and the advantages and weaknesses of the elements responses to frequency excursions. In that way, not only the effectiveness of the control and tuning strategy is confirmed but also the importance of various elements against systems frequency instabilities has been highlighted.

6.2. Answers to research questions

Having followed the analyzed workflow, the research questions formulated in chapter 1 have been answered:

1. How the new PEI elements introduced to the original PST 16 benchmark system should be modelled for RMS simulations in DPF considering PSS studies?

Modelling of various elements in DPF depends on the scope, the level of accuracy required, and the time frame the phenomena of interest occur in each study. For PSS studies the time frame of interest is within ms to s since the power-frequency controllers act on the latter time frame and the dynamic response of the system following an active power disturbance evolves within the same period. Hence, modelling of MMC based HVDC links encompasses the modelling of the converter stations, the DC link and the interface with the grid. MMC converter stations can be represented with the AVM type 6 at which the AC side of the converter is modelled as a fully controllable voltage source considering only the fundamental frequency component and the DC side as a fully controllable current source based on the energy conservation equation in parallel to an equivalent capacitance of the SMs. The converters model is accompanied by its dynamic control system based on the current vector control strategy, outer active and reactive power controllers and supplementary loops for ancillary services. The DC link of the converter is represented by the lumped (Π) equivalent model of DC cables operating at a bipolar configuration. Finally, the interface with the grid is achieved through a phase reactor and a transformer through which the control of the power flows can be facilitated. In this study, the HVDC link model is based on a DPF template developed according to the guidelines of CIGRE. Modelling of the WTs type 4 in DPF can be achieved by the utilization of a static generator element of DPF representing the WT itself plus its dynamic control structure and the grid interface through a power transformer. The control

system of the WTs consists of all the necessary blocks representing the aerodynamic and mechanical part of the WT, the active and reactive power controllers, the pitch angle control system and finally the generator utilized. The output of the control structure is the current reference able to control the output of the static generator element. In this study the corresponding control system is based on the IEC 61400-27 standard, suitable for PSS studies. Finally, modelling of the PEM electrolyzers consists of the modelling of the electrolysis stack, the various losses, the balance of plant and the interface with the local grid plus its dynamic control system. However, for PSS studies the main variable of interest in the electrolyzers is the ramp rate at which its consumption changes with respect to frequency deviations. Thus, electrolyzers can be represented in DPF by a general load connected to the grid through a power transformer and its dynamic and frequency controllers. In this case the automatic load-frequency regulation of the general load should be deactivated.

2. What modifications should be done to the original PST 16 benchmark system to introduce MMC-based HVDC links, fully decoupled WTs and responsive demand units such as PEM electrolyzers?

Initially the original PST 16 benchmark system operates at various generation and loading scenarios. To enable the connection of the various PEIs of the introduced elements, the bus voltages and the equipment loading should remain within the normal operating limits. For this reason, a medium loading scenario has been selected. Interconnection of the areas through HVDC links is achieved when the power setpoints of the original power flow are provided to the converter stations of the HVDC link. One of the converters should operate in Vdc control mode whereas the other in P control mode to preserve the balance on the DC link. Also, the selected converter stations should be sized with respect to the expected power flows through the tie lines, whereas transformers should be of suitable rating and voltage ratio to offer interconnection to the local grid. Regarding the replacement of SGUs by WTs, the introduced elements should provide to the grid the same amount of active power as the replaced units to maintain the normal system power flows. Hence, the number of parallel WTs and transformers should be defined to transfer the required amount of power to the grid. Also, the transformers utilized should be of suitable power rating and voltage ratio to offer smooth interconnection. Finally, since it has been assumed that WTs do not provide reactive power to the grid during steady state, STATCOM devices can be introduced to offer the required amount of reactive power during steady state and support during dynamic simulations. Considering the introduction of PEM electrolyzers to the system, it should be implemented with respect to the existing load centers in order not to alter the existing power flows. Conventional loads should be deactivated and the electrolyzers should be sized with respect to their consumption and the expected losses of the transformers utilized. Having installed the new elements it should be assured that the expected power flows are obtained, the power flow converges, and the system can normally initialize for RMS time domain simulations of interest. Finally, it is important to be mentioned that all control systems contain measurement and PLL devices that should be offered connection to the local connection points to enable their correct operation and the execution of the time domain simulations.

3. What modifications should be done to the elements control systems to introduce the APG control scheme and enable FFS?

The goal of the APG control scheme applied is to control the magnitude and the rate of change of the active power setpoint or output of each element. These parameters should be accessible to be externally controlled through the python script that facilitates the optimization algorithm to offer proper tuning to achieve the best

frequency response. The active power change (ΔP) is applied to the existing active power setpoint of the P controllers of the corresponding elements whereas the control of the ramp rate is facilitated through externally controlled rate limiters. It is also crucial to be mentioned that the new active power setpoints and the ramp rates should always remain within the technical limits of the corresponding elements. In further detail, in HVDC links the active power change takes place once per simulation and is facilitated as a parameter event in the setpoint (P_{ref}) of the P controller of the converter station operating in P mode performed 0.3s following the applied disturbance and is externally controlled through python script. The rate limiter of the P_{ref} is also controlled through python to set the rate of interest and achieve the best frequency regulation. PEM electrolyzers are accompanied by a frequency droop controller that alters the output of the unit with respect to measured frequency deviations (Δf). Since, in this case regulation of the output is continuous, the magnitude of the active power change ΔP is controlled through the droop constant of the controller which corresponds to the available bid size of the electrolyzers. Considering the ramp rate of the demand that is controlled in through a rate limiter whose parameters are tuned through the python script. Finally, in WTs, a supplementary frequency droop controller is introduced to act upon the original active power setpoint with respect to measured frequency deviations. Similarly, to the electrolyzers, the magnitude of the change of the active power output (ΔP) is controlled through a droop constant representing the allowed additional active power output of the WT and the rate of change of the setpoint is controlled through a rate limiter. The parameters of these units are again controlled through the python script according to the guidelines of the optimization problem.

4. Which are the key parameters that affect the performance of the controllers, and which are the necessary input signals in each of the introduced elements?

Supplementary frequency controllers attached to electrolyzers and WTs are based on the measured Δf acting as droop controllers. For this reason, frequency measurement at the CCP of each of the corresponding elements should be provided as input. Also, as defined by the MVMO algorithm, tuning of the droop constant and the ramp rates is based on the frequency responses of the interconnected areas that should be also provided as inputs. On the other hand, frequency controller of the HVDC link changes the active power setpoint of the P controller only with respect to the frequency responses of the 3 interconnected areas. Characteristic parameters that affect the controller of the HVDC link are the introduced activation time delay and the proportional and integral gains of the P controller of the HVDC links that affects the linear response of the output to step changes and the ramp rate. Electrolyzers' frequency controllers are affected by the size of their deadband zone which determines the activation time of these units and the maximum allowed frequency deviation, which specifies the frequency threshold at which the full amount of the bid should be released to sustain the deviation. Finally, WTs' frequency controller is affected by the activation frequency threshold and the frequency release threshold similarly to the electrolyzers and also from the timer which specifies the maximum allowed period for which the WTs can alter their active power outputs against the encountered frequency deviations. The values of these parameters have been selected to be constant in all simulations and have been chosen according to regulations or previous research. Finally, the externally controlled through python parameters regarding the amount and the rate of change of the active power setpoints affect the response of the controllers and are selected with respect to the solution of the optimization problem and are always preserved within the acceptable technical limits.

5. How to optimally tune the controllers attached to the PEIs of the introduced elements to offer fast and well-coordinated active power – frequency support with the minimum required effort?

In this study 2 different problem formulations have been proposed to effectively tune the controllers of the system and achieve improved frequency responses. OF1 aims at the minimization of the frequency deviations in all interconnected areas from its nominal value of 50Hz, whereas OF2 aims at the minimization and equalization of the rate of change of the dynamic displacements of the speed of each area. Having tested both techniques under various commonly occurred active power imbalances and various different combinations of SI sources it can be concluded that OF1 offers improved performance as: a) it can be used in all cases no matter the share of non-synchronous units, b) achieves the best frequency performance in terms of nadir and steady state frequency deviation, c) effectively minimizes the impact on the neighboring areas, d) achieves convergence of the frequencies of the interconnected areas at a closer point compared to OF2, e) can properly tune the parameters of the controllers no matter the size of the optimization vector, the magnitude and the location of the disturbance and f) utilizes properly various sources of SI taking advantage of the characteristics of their responses to active power changes. OF2 can be also effectively utilized in most of the cases given the fact that SGUs exist in each of the participating areas. However, in cases the interconnected areas exhibit significantly different inertia levels, equalization of the ramp rates of the frequency excursions does not always lead to the best achieved frequency responses. Also, due to its inability to directly control the steady state frequency deviation it is characterized by worse frequency convergence compared to OF1. Finally, utilization of sources with limited in time supporting capability such as WTs that leads later to a second perturbation of the speeds is avoided under this OF. For all the reasons above, OF1 is considered as the best tuning method due to its performance, effectiveness, simplicity and extensive applicability.

6. What is the frequency stability profile of the system before and after applying the new control strategy? Has the frequency response improved and in what ways?

In the original PST 16 benchmark system, the frequency profile of the interconnected areas is based on the conventional SGUs and the power flows among the areas tie-lines. As a result, the total system is electromagnetically coupled, and a common global frequency characterizes its response and stability. The introduction of new elements led to the decoupling of the areas, the decommissioning of SGUs and the loss of conventional coupled load centers. Hence, the system is split to 3 different areas each of which has a different frequency and should be able to face commonly occurred disturbances under the new low inertia, reduced reserve capacity, volatile, fast and uncertain conditions. Without the support from non-synchronous sources of inertia, the different areas are regularly exposed to significant RoCofs and extensive frequency deviations able to trigger the activation of protection devices, UFLS schemes and lead to cascading outages or even blackouts. However, by applying the proposed control strategy, the areas can effectively cooperate utilizing not only the local means of SI, but also synchronous and non-synchronous sources of inertia installed in all system areas through the control of the power flows of the HVDC links. Consequently, acceptable frequency responses within the normal operating state limits can be achieved even for the most significant active power-frequency imbalances such as the loss of the largest generating unit in an area. Coordinated tuning against the imbalance ensures that insufficient or over regulation phenomena are avoided taking advantage of the capabilities of the element's responses. Hence, improved frequency responses in terms of

RoCof, maximum instantaneous and steady state deviation is achieved in combination with faster stabilization times and minimum impact on neighboring areas limiting the risk of operation of an area in expense of another.

6.3. Suggestions for future research

In this thesis, the research of fast and effective active power-frequency support extended from the modelling state to the optimization of the parameters of the frequency controllers of elements attached to the system. Although different aspects have been investigated and analyzed, various points constitute a great field for future research projects:

- **Elements accurate modelling:** In this thesis project the models of various introduced elements are based either on standards, guidelines, previous research and templates provided by institutions and DPF. These models are designed with respect to phenomena occurring at the time frame of ms to s and are suitable for time domain RMS simulation depicting mainly their responses to active power frequency imbalances. However, even more detailed models can be designed as the system dynamics become faster and more frequent and thus phenomena and responses taking place in shorter time frames can be also considered. Also, modelling of the various elements can be extended to include detailed representations of the PEIs used to interconnect the elements to the grid and thus capture their dynamic responses. Finally, in this study the representation of large in size elements was based on the modular design of smaller units in parallel connection, an assumption that is not always accurate enough to capture the dynamic behavior of larger units. Thus, further research can focus on the accurate design of dynamic models of large elements such as WTs or electrolyzers.
- **Application of other types of new technologies:** In this study the state-of-art most representative non-synchronous technologies have been used such as MMC-based HVDC links, fully decoupled type 4 WTs and PEM electrolyzers. However, various other new technologies such as PVs, EVs, ESS, microgrids, fuel cells, biomass units etc are also expected to have a significant share in the power system of the future. These elements are also characterized by increased levels of controllability, but they exhibit different dynamic responses compared to the considered ones due to their technical capabilities. For this reason, the provision of ancillary services from these elements and the cooperation and interaction between the analyzed and the new elements can be further investigated.
- **Dispatch and location:** In this study it has been assumed that the system operates at a medium loading conditions and the weather patterns remain constant. Also, the location of various introduced elements has been assumed to be constant at critical system points. The results of the current study have proven the role of the location of the various units of FFS with respect to the points various imbalances occur. However, the operation of the power system is characterized by time periods of different load demands, different generation mixes, time periods of increased or reduced renewable generation according to the availability of primary sources and uncertain reserve availability. For this reason, the dynamic response of the system and the effectiveness of various supporting means can be further investigated under different commonly occurred operating scenarios and weather conditions.
- **Enhancement of frequency controllers:** In this thesis it has been assumed that the HVDC links change their active power flows once per simulation depending on the solution of the optimization problems,

whereas the response of WTs and electrolyzers is based on the measured frequency deviation Δf and the droop constant and ramp rate determined by the MVMO algorithm. However, different frequency controllers have been proposed in literature that use different input signals such as derivative based frequency controllers and inertia emulation controllers. The effectiveness of this type of controllers can be further investigated in comparison to the proposed in this study strategy in systems of similar complexity and size to determine the most promising control strategy.

- **Optimization algorithm enhancement:** The MVMO optimization algorithm utilized in this study is a powerful algorithm that has shown great potential in various power system applications. However, it can be further improved with respect to the characteristic of each optimization problem. For example, various different sampling strategies may be implemented to achieve improved handling of the available research space and faster convergence closer to the global optimum. Furthermore, the investigation of the role of critical parameters of the mapping function against different optimization problems could lead to improved results and performance. Finally, the determination of specific mutating variables and the addition of precise termination criteria may lead to more sophisticated and purposeful solution approach.
- **Improvement of problem formulations:** In the current study the proposed problem formulations have shown great results achieving the optimal tuning of the controllers and thus enhanced frequency response. However, each of them has various weaknesses that can be further investigated to be diminished. Also, new problem formulations approaching the current problem from different perspectives or combining the existing formulations would be a field of great interest. Finally, according to various policies or strategies by TSOs, further research can focus on improving the proposed formulations by modifying weighting factors, adding constraints, initial vectors and penalties during the optimization process to guide the algorithm according to specific needs and achieve the strategy of interest.

References

- [1] J. Martinez, *Climate Change Impacts in Europe: Final Report of the PESETA Research Project*, Spain: Publications Office of the European Union, 2009.
- [2] United Nations, *Kyoto Protocol to the United Nations Framework on Convention on Climate Change*, Kyoto: United Nations, 1998.
- [3] United Nations, *Summary of Paris Agreement, United Nations Framework Convention on Climate Change*, Paris: United Nations, 2015.
- [4] European Commission, *The Road from Paris: Assessing the Implications of the Paris Agreement and Accompanying Proposal for a Council Decision on the Signing, on behalf of the European Union, of the Paris Agreement Adopted under the UNFCCC*, Brussels: European Commission, 2016.
- [5] European Commission, *A 2030 Framework for Climate and Energy Policies*, Brussels: European Commission, 2013.
- [6] European Commission, *The European Green Deal*, Brussels: European Commission, 2019.
- [7] European Commission, *A Clean Planet for all: A European Strategic long-term Vision for a Prosperous, Modern, Competitive and Climate Neutral Economy*, Brussels: European Commission, 2018.
- [8] K. Levin, D. Rich, K. Ross, T. Fransen and C. Elliott, *Designing and Communicating Net-zero Targets*, World Resources Institute, July 2020.
- [9] IRENA, *Global Energy Transformation: A Roadmap to 2050 (2019 edition)*, Abu Dhabi: International Renewable Energy Agency, 2019.
- [10] F. Blaabjerg, Y. Yang, K. Ma and X. Wang, "Power Electronics - The Key Technology for Renewable Energy System Integration," in *2015 International Conference on Renewable Energy Research and Applications (ICRERA)*, Palermo, Italy, 2015.
- [11] R. Choudhary, H. M. Suryawanshi, M. Chaudhari, G. Talapur and A. B. Shitole, "Modified Multilevel Topology for Grid Integration of High Power Solar PV System," in *2017 IEEE PES Asia-Pacific Power and Energy Conference (APPEEC)*, Bangalore, India, 2017.
- [12] J. Fang, H. Li, Y. Tang and F. Blaabjerg, "On the Inertia of Future More-Electronics Power Systems," *IEEE Journal of Emerging and Selected Topics in Power Electronics*, no. vol 4, pp. 2130-2146, December 2019.
- [13] P. K. Steimer, "Enabled by High Power Electronics - Energy Efficiency, Renewables and Smart Grids," in *The 2010 International Power Electronics Conference*, Sapporo, Japan, 2010.
- [14] B. Tourgoutian and A. Alefragkis, "Design Considerations for the COBRACable HVDC Interconnector," in *IET International Conference on Resilience of Transmission and Distribution Networks (RTDN 2017)*, Birmingham, UK, 2017.
- [15] P. L. Francos, S. Verdugo, H. F. Alvarez, S. Guyomarch and L. Loncle, "INELFE - Europe's First Integrated Onshore HVDC Interconnection," in *2012 IEEE Power and Energy Society General Meeting*, San Diego, CA, USA, 2012.

- [16] M. Migliori, S. Lauria, L. Michi, G. Donnini, B. Aluisio and C. Vergine, "Renewable Sources Integration Using HVDC in Parallel to AC Traditional System: The Adriatic Project," in *2019 AEIT HVDC International Conference (AEIT HVDC)*, Florence, Italy, 2019.
- [17] F. Qin, T. Hao, F. Gao, T. Xu, D. Niu and Z. Ma, "A Multiport DC-DC Modular Multilevel Converter for HVDC Interconnection," in *2020 IEEE Applied Power Electronics Conference and Exposition (APEC)*, New Orleans, LA, USA, 2020.
- [18] V. N. Sewdien, R. Chatterjee, M. V. Escudero and J. V. Putten, "System Operational Challenges from the Energy Transition," *CIGRE Science & Engineering*, no. vol 17, pp. 5-20, February 2020.
- [19] A. Halley, N. Martins, P. Gomes, D. Jacobson, W. Sattinger, Y. Fang, L. Haarla, Z. Emin, M. V. Escudero, S. A. D. Graaff, V. Sewdien and A. Bose, "Effects of Increasing Power Electronics Based Technology on Power System Stability: Performance and Operations," *CIGRE Science & Engineering*, no. Vol 11, pp. 5-17, June 2018.
- [20] A. P. Guera, D. Gusain, J. R. Torres, P. Palensky, M. v. d. Meijden and F. Gonzalez-Longatt, "Optimal Tuning of Active Power Gradient Control for Frequency Support in Multi-Energy Systems," in *2020 IEEE PES Innovative Smart Grid Technologies Europe (ISGT-Europe)*, The Hague, Netherlands, October 2020.
- [21] P. Kundur, J. Paserba, V. Ajjarapu, G. Andersson, A. Bose, C. Canizares, N. Hatziargyriou, D. Hill, A. Stankovic, C. Taylor, T. V. Cutsem and V. Vittal, "Definition and classification of power system stability IEEE/CIGRE joint task force on stability terms and definitions," *IEEE Transactions on Power Systems*, vol. 19, no. 3, pp. 1387-1401, 02 August 2004 June 2003.
- [22] N. Hatziargyriou, J. V. Milanovic, C. Rahmann, V. Ajjarapu, C. Canizares, I. Erlich, D. Hill, I. Hiskens, I. Kamwa, B. Pal, P. Pourbeik, J. J. Sanchez-Gasca, A. M. Stankovic, T. V. Cutsem, V. Vittal and C. Vournas, "Definition and Classification of Power System Stability Revisited & Extended," *IEEE Transactions on Power Systems*, 8 December 2020.
- [23] G. Trudel, J. Gingras and J. Pierre, "Designing a Reliable Power System: Hydro- Quebec's Integrated Approach," *Proceedings of the IEEE*, vol. 93, no. 5, pp. 907-917, 09 May 2005.
- [24] P. Kundur, *Power System Stability and Control*, McGraw-Hill Professional, 1st Edition, 1994.
- [25] L. Meegahapola, A. Squarezi, J. S. Bryant, M. Gu, E. R. Conde and R. B. A. Cunha, "Power System Stability with Power-Electronic Converter Interfaced Renewable Power Generation: Present Issues and Future Trends," *Energies* 2020, no. 13, 3 July 2020.
- [26] M. Yu, A. Dysko, A. Roscoe, C. Booth, R. Ierna, H. Urdal and J. Zhu, "Effects of Swing Equation-Based Inertial Response (SEBIR) Control on Penetration Limits of Non-Synchronous Generation in the GB Power System," in *International Conference on Renewable Power Generation*, Beijing, 2015.
- [27] ENTSO-E, *Rate of Change of Frequency (RoCoF) Withstand Capability*, Brussels: ENTSO-e, March 2017.
- [28] EirGrid and SONI, *DS3: Rate of Change of Frequency (RoCoF) Workstream*, EirGrid and SONI, 2011.
- [29] EirGrid and SONI, *Summary of Studies on Rate of Change of Frequency Events on the All-Island System*, EirGrid and SONI, August 2012.
- [30] C. Yongning, L. Yan, W. Zhen, L. Zhen, L. Hongzhi and Z. Zhankui, "Characteristics and Challenge on Large-Scale Renewable Energy Integration," in *2019 IEEE PES Innovative Smart Grid Technologies Asia*, Chengdu, China, 2019.
- [31] A. Abbou and A. Lazrak, "An Improved Control Strategy for DFIG Wind Turbine to Ride-Through Voltage Dips," in *2018 6th International Renewable and Sustainable Energy Conference (IRSEC)*, Rabat, Morocco, 2018.

- [32] DNV GL, *RoCoF Alternative Solutions Technology Assessment Final Report Phase 1*, London, UK: DNV GL, 2015.
- [33] P. Tielens, P. Henneaux and S. Cole, *Asset: Penetration of Renewables and Reduction of Synchronous Inertia in the European Power System - Analysis and Solutions*, EU; Tractebel; Ecofys; E3M-Lab, November 2018.
- [34] ENTSO-e, *System Dynamic and Operational Challenges*, Brussels: ENTSO-e, 2020.
- [35] EirGrid; SONI, *RoCoF Alternative & Complementary Solutions Project Phase 2*, EirGrid & SONI, 2016.
- [36] M. Rezkalla, M. Pertl and M. Marinelli, "Electric Power System Inertia: Requirements, Challenges and Solutions," *Electrical Engineering*, no. vol 100, pp. 2677-2693, December 2018.
- [37] M. Nedd, C. Booth and K. Bell, "Potential Solutions to the Challenges of Low Inertia Power Systems with a Case Study Concerning Synchronous Condensers," in *52nd International Universities Power Engineering Conference (UPEC)*, Heraklion, Greece, 2017.
- [38] K. Sun, K.-J. Li, W. Bao, Z.-d. Wang, Z. Liu, M. Wang and W.-J. Lee, "Frequency Compensation Control Strategy of Energy Storage in the Wind-energy storage Hybrid System for Improving Frequency Response Performance," in *2019 IEEE Industry Applications Society Annual Meeting*, Baltimore, MD, USA, 2019.
- [39] A. Junyent-Ferr, Y. Pipelzadeh and T. Green, "Blending HVDC-Link Energy Storage and Offshore Wind Turbine Inertia for Fast Frequency Response," *IEEE Transactions on Sustainable Energy*, vol. 6, no. 3, pp. 1059-1066, July 2015.
- [40] L. Meng, J. Zafar, S. K. Khadem, A. Collinson and K. C. Murchie, "Fast Frequency Response From Energy Storage Systems—A Review of Grid Standards, Projects and Technical Issues," *IEEE Transactions on Smart Grid*, vol. 11, no. 2, pp. 1566-1581, March 2020.
- [41] S. Debbarma, C. Hazarika and K. Singh, "Virtual Inertia Emulation from HVDC Transmission Links to Support Frequency Regulation in Presence of Fast Acting Reserve," in *2018 2nd International Conference on Power, Energy and Environment: Towards Smart Technology (ICEPE)*, Shillong, India, 2018.
- [42] A. Karaolanis, A. P. Guera, J. R. Torres, M. v. d. Meijden and A. Alefragkis, "Generic model of a VSC-based HVDC link for RMS simulations in PSS/E," in *10th IFAC Symposium on Control of Power and Energy Systems CPES 2018*, Tokyo, Japan, September 2018.
- [43] F. Sanchez, F. Gonzalez-Longatt and D. Bogdanov, "Impact Assessment of Frequency Support by Electric Vehicles: Great Britain Scenario 2025," in *2018 20th International Symposium on Electrical Apparatus and Technologies (SIELA)*, Bourgas, Bulgaria, 2018.
- [44] F. Alshehri, V. G. Suarez, J. R. Torres, A. P. Guera and M. v. d. Meijden, "Modelling and evaluation of PEM hydrogen technologies for frequency ancillary services in future multi-energy sustainable power systems," *Heliyon*, no. 5, pp. 1-24, April 2019.
- [45] W. Wang, A. Beddard, M. Barnes and O. Marjanovic, "Analysis of Active Power Control for VSC–HVDC," *IEEE Transactions on Power Delivery*, pp. 1978-1988, 3 June 2014.
- [46] O. D. Adeuyi, M. Cheah-Mane, J. Liang and N. Jenkins, "Fast Frequency Response From Offshore Multiterminal VSC–HVDC Schemes," *IEEE Transactions on Power Delivery*, no. vol 32, pp. 2442 - 2452, December 2017.
- [47] M. Yu, A. Dyško, C. D. Booth, A. J. Roscoe and J. Zhu, "A review of control methods for providing frequency response in VSC-HVDC transmission systems," in *2014 49th International Universities Power Engineering Conference (UPEC)*, Cluj-Napoca, Romania, 2014.

- [48] A. P. Guerra, J. R. Torres, A. v. d. Meer, M. v. d. Meijden and A. Alefragkis, "Influence of active power gradient control of an MMC-HVDC link on long-term frequency stability," in *2017 IEEE Power & Energy Society General Meeting*, Chicago, IL, USA, 2017.
- [49] F. Sanchez, F. Gonzalez-Longatt and D. Bogdanov, "Probabilistic Assessment of Enhanced Frequency Response Services Using Real Frequency Time Series," in *20th International Symposium on Electrical Apparatus and Technologies (SIELA)*, Bourgas, Bulgaria, 2018.
- [50] J. L. R. Torres, A. Perilla, E. Rakhshani, P. Palensky, M. A. A. M. v. d. Meijden and A. Alefragkis, "MIMO-based tuning of Active Power Gradient Control of VSC-HVDC links for Frequency Support," in *2019 2nd International Conference on Smart Grid and Renewable Energy (SGRE)*, Doha, Qatar, 2019.
- [51] ENTSO-e, *Load-Frequency Control and Performance, UCTE Operation Handbook Appendix A1*, ENTSO-e, 2004.
- [52] ENTSO-e, *The Italian 2003 Blackout Report*, Brussels: ENTSO-e, 2003.
- [53] ENTSO-e, *Final Report System Disturbance on 4 November 2006*, Brussels: ENTSO-e, 2006.
- [54] ENTSO-e, *Report on Blackout in Turkey on 31st March 2015*, Brussels: ENTSO-e, 2015.
- [55] ENTSO-e, *Continental Europe Significant Frequency Deviations - January 2019*, April: ENTSO-e, 2019.
- [56] European Commission, *Commission Regulation (EU) 2017/1485 of 2 August 2017 establishing a guideline on electricity transmission system operation*, Brussels: European Commission, 2017.
- [57] European Commission, *Commission Regulation (EU) 2017/2196 of 24 November 2017 establishing a network code on electricity emergency and restoration*, Brussels: European Commission, 2017.
- [58] TenneT TSO B.V, *FCR Manual for BSPs: Requirements and procedures for supply of FCR*, The Netherlands: TenneT TSO B.V, 2020.
- [59] European Commission, *Commission Regulation (EU) 2016/631 of 14 April 2016 establishing a network code on requirements for grid connection of generators*, Brussels: European Commission, 2016.
- [60] European Commission, *Commission Regulation (EU) 2016/1447 of 26 August 2016 establishing a network code on requirements for grid connection of high voltage direct current systems and direct current-connected power park modules*, Brussels: European Commission, 2016.
- [61] B. S. Abdulraheem and C. K. Gan, "Power System Frequency Stability and Control: Survey," *International Journal of Applied Engineering Research*, vol. 11, no. 8, pp. 5688-5695, 2016.
- [62] ENTSO-e RG-CE System Protection & Dynamics Sub Group, *Frequency Stability Evaluation Criteria for the Synchronous Zone of Continental Europe - Requirements and Impacting Factors*, Brussels: ENTSO-e, 2016.
- [63] F. M. Gonzalez-Longatt and J. L. R. Torres, *Modelling and Simulation of Power Electronic Converter Dominated Power Systems in PowerFactory*, Springer, Cham, 2020.
- [64] N. Mohan, T. Undeland and W. Robbins, *Power Electronics: Converters, Applications and Design*, John Wiley & Sons Inc, September 2002.
- [65] I. Erlich, A. Korai and F. Shewarega, "Control challenges in power systems dominated by converter interfaced generation and transmission technologies," in *2017 IEEE Power & Energy Society General Meeting*, Chicago, IL, USA, 16-20 July 2017.
- [66] M. H. Rashid, *Power Electronics Handbook*, Elsevier Inc., 2018.
- [67] N. Flourentzou, V. G. Agelidis and G. D. Demetriades, "VSC-Based HVDC Power Transmission Systems: An Overview," *IEEE Transactions on Power Electronics*, no. 24, pp. 592-602, March 2009.

- [68] J. Dorn, H. Gambach and D. Retzmann, "HVDC Transmission Technology for Sustainable Power Supply," in *9th International Multi-Conference on Systems, Signals and Devices*, Chemnitz, Germany, 2012.
- [69] M. Hannan, I. Hussin, P. J. Ker, M. Hoque, M. H. Lipu, A. Hussain, M. Rahman and C. a. F. Blaabjerg, "Advanced Control Strategies of VSC Based HVDC Transmission System: Issues and Potential Recommendations," *IEEE Access*, pp. 78352-78369, December 2018.
- [70] B. Gemmill, J. Dorn, D. Retzmann and D. Soerangr, "Prospects of multilevel VSC technologies for power transmission," in *2008 IEEE/PES Transmission and Distribution Conference and Exposition*, Milpitas, CA, Apr. 2008.
- [71] DlgSILENT, *PowerFactory Seminar HVDC and FACTS*, Gomaringen: DlgSILENT, 2018.
- [72] CIGRE Working Group B4.57, *Guide for the DEvelopment of Models for HVDC Converters in a HVDC Grid*, CIGRE, December 2014.
- [73] H. Saad, S. Denetière, J. Mahseredjian, P. Delarue, X. Guillaud, J. Peralta and S. Nguefeu, "Modular Multilevel Converter Models for Electromagnetic Transients," *IEEE Transactions on Power Delivery*, vol. 29, pp. 1481-1489, June 2014.
- [74] H. Saad, J. Peralta, S. Denetière, J. Mahseredjian, J. Jatskevich, J. A. Martinez, A. Davoudi, M. Saeedifard, V. Sood, X. Wang and a. A. M.-S. J. Cano, "Dynamic Averaged and Simplified Models for MMC-Based HVDC Transmission Systems," *IEEE Transactions on Power Delivery*, vol. 28, pp. 1723-1730, July 2013.
- [75] J. Peralta, H. Saad, S. Denetiere, J. Mahseredjian and S. Nguefeu, "Detailed and Averaged Models for a 401-Level MMC-HVDC System," *IEEE Transactions on Power Delivery*, vol. 27, pp. 1501-1508, July 2012.
- [76] M. P. Bahrman, "Overview of HVDC Transmission," in *2006 IEEE PES Power Systems Conference and Exposition*, Atlanta, GA, USA, 2006.
- [77] T. Shrivastava, A. Shandilya and S. Gupta, "Overview strategy of wind farm in VSC-HVDC power transmission," in *2016 IEEE 7th Power India International Conference (PIICON)*, Bikaner, India, 2016.
- [78] J. Kang, D. Kang, J. P. Lee, D. W. Yoo and J. W. Shim, "Design Procedure of MMC-HVDC System: Comprehensive Consideration of Internal and External Dynamics," *IEEE Access*, vol. 8, pp. 157437 - 157450, 21 August 2020.
- [79] A. Korompili, Q. Wu and H. Zhao, "Review of VSC HVDC connection for offshore wind power integration," *Renewable and Sustainable Energy Reviews*, vol. 59, pp. 1405-1414, June 2016.
- [80] Hydrogen Council, "Hydrogen Scaling up - A Sustainable Pathway for the Global Energy Transition," Nov. 2017.
- [81] S. S. Kumar and V. Himabindu, "Hydrogen production by PEM water electrolysis – A review," *Materials Science for Energy Technologies 2*, pp. 442-454, March 2019.
- [82] P. Ayivor, J. Torres, M. v. d. Meijden and R. v. d. P. a. B. Stouwie, "Modelling of Large Size Electrolyzer for Electrical Stability Studies in Real Time Digital Simulation," in *3rd International Hybrid Power Systems Workshop*, Tenerife, Spain, 2018.
- [83] TSO 2020 Activity 2 Final Report, "Stability Analysis of an International Electricity System Connected to Regional and Local Sustainable Gas Systems," 2019.
- [84] ITM Power, "ITM Power, World's Largest Hydrogen Electrolysis in Shell's Rhineland Re-finery," London, 2018.
- [85] McPhy- Driving Clean Energy Forward, "Power-to-Gas in Austria," 2017.
- [86] AkzoNobel, "AkzoNobel and Gasunie Looking to Convert Water into greenHydrogen Using Sustainable Electricity," 2018.

- [87] B. W. Tuinema, E. Adabi, P. Ayivor, V. G. Suárez, L. L., A. Perilla, Z. Ahmad, J. Torres, M. v. d. Meijden and P. Palensky, "Modelling of large-sized electrolyzers for real-time simulation and study of the possibility of frequency support by electrolyzers," *IET Generation, Transmission & Distribution*, vol. 14, no. 10, pp. 1985-1992, 13 May 2020.
- [88] J. Eichman, K. Harrison and M. Peters, "Novel Electrolyzer Applications: Providing More Than Just Hydrogen," National Renewable Laboratory (NREL), September 2014.
- [89] T. M. Letcher, *Wind Energy Engineering: A Handbook for Onshore and Offshore Wind Turbines*, Elsevier Academic Press, 2017.
- [90] M. Zaaijer and A. Viré, *Introduction to wind turbines: Physics and Technology : Course Reader*, Delft: TU Delft, 2019.
- [91] EMTIP, "Renewable energy," EMTIP, [Online]. Available: <https://www.emtip.com/applications/renewable-energy-systems>.
- [92] Y. Duan and R. Harley, "Present and future trends in wind turbine generator designs," in *2009 IEEE Power Electronics and Machines in Wind Applications*, Lincoln, NE, USA, 2009.
- [93] K. Burman, D. Olis, V. Gevorgian, A. Warren and R. Butt, "Integrating Renewable Energy into the Transmission and Distribution System of the U.S. Virgin Islands," NREL, 2011.
- [94] E. Camm, M. R. Behnke, O. Bolado, M. Bollen, M. Bradt, C. Brooks, W. Dilling, M. Edds, W. J. Hejidak, D. Houseman, S. Klein, F. Li, J. Li, P. Maibach, T. Nicolai, J. Patiño, S. V. Pasupulati, N. Samaan, S. Saylor, T. Siebert, T. Smith, M. Starke and R. Walling, "Characteristics of Wind Turbine Generators for Wind Power Plants," in *2009 IEEE Power & Energy Society General Meeting*, Calgary, AB, Canada, 2009.
- [95] P. Pourbeik, A. Ellis, J. Sanchez-Gasca, Y. Kazachkov, E. Muljadi, J. Senthil and D. Davies, "Generic stability models for type 3 & 4 wind turbine generators for WECC," in *2013 IEEE Power & Energy Society General Meeting*, Vancouver BC Canada, 2013.
- [96] R. Nelson, *Full-Converter Wind Turbine Technology*, Siemens Energy, 2014.
- [97] F. Gonzalez-Longatt and J. L. R. Torres, *Advanced Smart Grid Functionalities Based on PowerFactory*, Springer, 2018.
- [98] A. D. Hansen and I. D. Margaris, "Type IV Wind Turbine Model," DTU Wind Energy, 2014.
- [99] IEC, "International Standard IEC 61400-27-1: Part 27-1: Electrical simulation models – Wind turbines," IEC, Geneva, Switzerland, 2015.
- [100] S. P. Teeuwssen, *Phd Dissertation: Oscillatory Stability Assessment of Power Systems using Computational Intelligence*, Duisburg-Essen, Germany: Technische Universität Duisburg-Essen, 2005.
- [101] DlgSILENT GmbH, *DlgSILENT PowerFactory 2020 User Manual*, Gomarigen, Germany, 2020.
- [102] DlgSILENT GmbH, *DlgSILENT PowerFactory Application Guide: Dynamic Modelling Tutorial DlgSILENT Technical Documentation*, Gomarigen, Germany, 2013.
- [103] F. M. Gonzalez-Longatt and J. Torres, *PowerFactory Applications for Power System Analysis*, Delft, The Netherlands: Springer, 2014.
- [104] L. Ruttledge, N. W. Miller, J. O'Sullivan and D. Flynn, "Frequency Response of Power Systems With Variable Speed Wind Turbines," *IEEE Transactions on Sustainable Energy*, pp. 683-691, October 2012.
- [105] IEEE, *1110-2019 IEEE Guide for Synchronous Generator Modeling Practices and Parameter Verification with Applications in Power System Stability Analyses*, IEEE, March 2020.

- [106] DlgSILENT GmbH, *Technical Reference Synchronous Machine PowerFactory 2020*, Gomaringen Germany: DlgSILENT GmbH, February 2020.
- [107] IEEE Standards Association, *IEEE Recommended Practice for Excitation System Models for Power System Stability Studies (IEEE Std 421.5-2016)*, New York, USA: IEEE, 2016.
- [108] IEEE Power System Dynamic Performance Committee, Power System Stability Subcommittee, Task Force on Turbine-Governor Modeling, *Dynamic Models for Turbine-Governors in Power System Studies (PES-TR1 Technical Report)*, IEEE, January 2013.
- [109] IEEE, "Dynamic Models for Steam and Hydro Turbines in Power System Studies," *IEEE Transactions on Power Apparatus and Systems*, pp. 1904-1915, November 1973.
- [110] DlgSILENT GmbH, *PowerFactory 2020 Technical Reference PWM Converter*, Gomaringen, Germany: DlgSILENT GmbH, February 2020.
- [111] DlgSILENT GmbH, *PowerFactory 2020 Technical Reference General load*, Gomaringen, Germany: DlgSILENT GmbH, 2020.
- [112] Energynautics GmbH, *Type 3 and Type 4 Wind Turbine and Wind Park Models Model Documentation version 7*, Darmstadt, Germany: Energynautics GmbH, 2016.
- [113] E. Rakhshani, J. Torres, P. Palensky and M. d. v. Meijden, "Determination of Maximum Wind Power Penetration Considering Wind Turbine Fast Frequency Response," in *2019 IEEE Milan PowerTech*, Milan, Italy, 2019.
- [114] J.L.R.Torres and I. Erlich, "Hybrid Single Parent-Offspring MVMO for Solving CEC2018 Computationally Expensive Problems," in *2018 IEEE Congress on Evolutionary Computation (CEC)*, Rio de Janeiro, Brazil, 8-13 July 2018.
- [115] E. Rakhshani, D. Gusain, V. Sewdien, J. L. R. Torres and M. A. M. M. v. d. Meijden, "A Key Performance Indicator to Access the Frequency Stability of Wind Generation Dominated Power System," *IEEE Access*, no. 7, pp. 130957 - 130969, 10 September 2019.
- [116] DlgSILENT GmbH, *DlgSILENT PowerFactory Application Guide Python Tutorial*, Gomaringen, Germany: DlgSILENT GmbH.
- [117] W. R. Institute, *Climate Analysis Indicators Tool: Global Manmade GHS emissions by sector 2013*, 2017.

APPENDICES

A DQ Transformation

Generally, in power systems currents and voltages are represented as sinusoidal time varying waves in the three phases A,B,C. However, using these signals to perform calculations or control actions such as in the case of current vector strategy in VSCs is more than challenging. For this reason, in such complex cases, voltages and currents are transformed from the ABC frame to the d-q frame. In this way, the information of the 3 phase system voltages and currents are stored into DC signals that are more easily controlled, enabling the utilization of the commonly used PID controllers. Furthermore, calculations are more easily performed and independent control of active and reactive power can be achieved by controlling the d and q components of the current respectively. To perform this transformation two steps are required: the Clarke and the Park transformation.

The idea behind the famous Clarke transformation also called $\alpha\beta 0$ transformation, is to project the vector of the voltage and the current from the ABC frame to a two-dimensional stationary frame as observed in Figure A.1. The outcome of this transformation is a rotating vector with respect to a stationary 2-axes frame, the $\alpha\beta$ frame, under balanced conditions. Through this transformation the problem dimensions reduce from 4 (A,B,C and time) to 3 (α,β , time). Equation A.1 and Equation A.2 describe the mathematical representation of the normal and inverse Clarke transformation.

$$\begin{bmatrix} X_\alpha \\ X_\beta \end{bmatrix} = \frac{2}{3} \begin{bmatrix} 1 & -\frac{1}{2} & -\frac{1}{2} \\ 0 & \frac{\sqrt{3}}{2} & -\frac{\sqrt{3}}{2} \end{bmatrix} \begin{bmatrix} X_A \\ X_B \\ X_C \end{bmatrix} \quad \text{Equation A.1}$$

$$\begin{bmatrix} X_A \\ X_B \\ X_C \end{bmatrix} = \begin{bmatrix} 1 & 0 \\ -\frac{1}{2} & \frac{\sqrt{3}}{2} \\ -\frac{1}{2} & -\frac{\sqrt{3}}{2} \end{bmatrix} \begin{bmatrix} X_\alpha \\ X_\beta \end{bmatrix} \quad \text{Equation A.2}$$

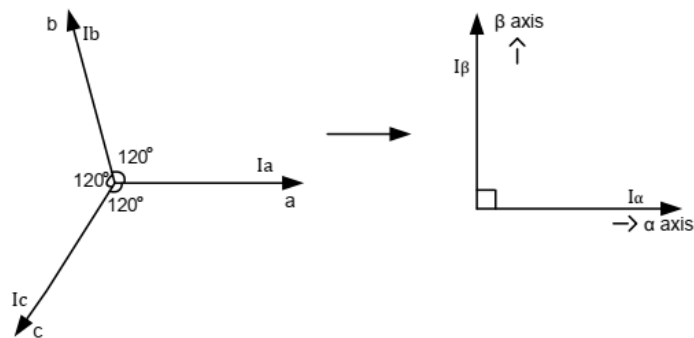


Figure A.1: Clarke Transformation.

Having obtained a rotating vector on a stationary axis, Park transformation can be utilized to obtain a stationary vector with respect to a rotating frame. The later one rotates at the synchronous speed of the grid achieved through phase locked loop (PLL). In fact, PLL is responsible to obtain the measurement of the voltage at the CCP and generate angle θ , the angle between dq and ABC reference frames. The output of the last transformation is a DC signal decomposed in 2 axes d and q and can be easily controlled with respect to specific reference points. The diagram representing the park transformation can be observed in Figure A.2 and the mathematical representation of the normal and inverse Park transformation in Equation A.3 and Equation A.4 respectively. Finally, the dimensions of the problem have reduced from 4 (A,B,C, time) to 2 (d,q) as observed in Figure A.3.

$$\begin{bmatrix} X_d \\ X_q \end{bmatrix} = \begin{bmatrix} \cos\theta & \sin\theta \\ -\sin\theta & \cos\theta \end{bmatrix} \begin{bmatrix} X_\alpha \\ X_\beta \end{bmatrix} \tag{Equation A.3}$$

$$\begin{bmatrix} X_\alpha \\ X_\beta \end{bmatrix} = \begin{bmatrix} \cos\theta & -\sin\theta \\ \sin\theta & \cos\theta \end{bmatrix} \begin{bmatrix} X_d \\ X_q \end{bmatrix} \tag{Equation A.4}$$

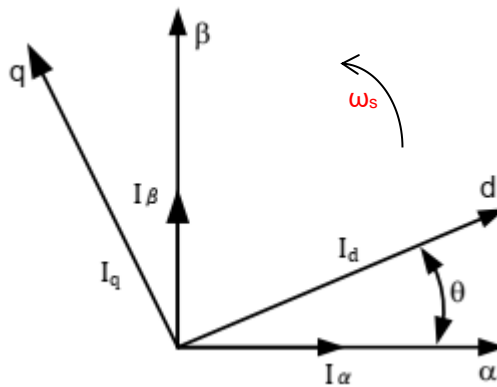


Figure A.2: Park Transformation.

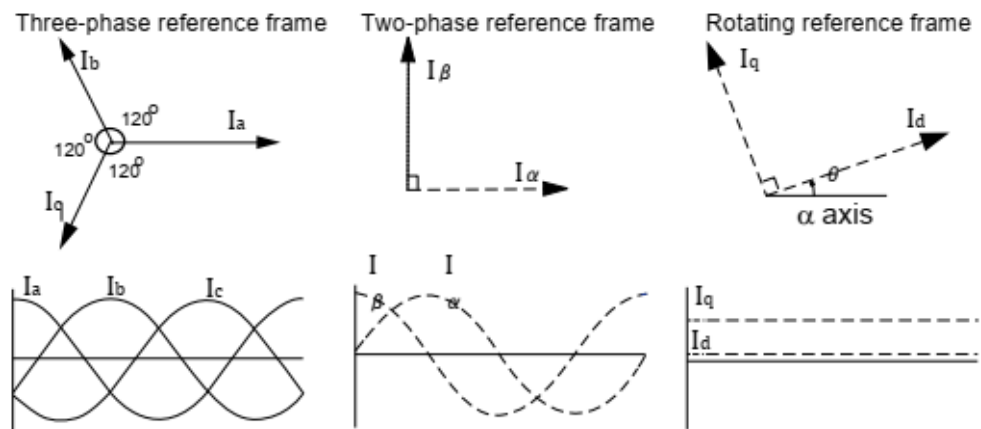


Figure A.3: Reference frames and signals after transformation.

Finally, the applied transformations serve the optimum goal to control the power at every instant. Based on that the instantaneous power theory, the instantaneous power in each of the reference frames can be expressed as in Equation A.5. Finally, in the dq frame of interest, through the Clarke and park transformations, the active and reactive power can be described from Equation A.6 and Equation A.7 respectively.

$$\overline{S(t)} = S_{\alpha\beta}(t) = S_{dq}(t) \quad \text{Equation A.5}$$

$$P = U_d I_d + U_q I_q \quad \text{Equation A.6}$$

$$Q = U_d I_q - U_q I_d \quad \text{Equation A.7}$$

Aligning $u(t)$ with d-axis (meaning that $u_q=0$) we obtain the final set of equations, which show that the active and reactive power can be independently controlled by controlling the i_d and i_q respectively.

$$u(t) = u_d(t) + U_q(t) \xrightarrow{U_q(t)=0} U(t) = U_d(t) \quad \text{Equation A.8}$$

$$P = U_d I_d \quad \text{Equation A.9}$$

$$Q = U_d I_q \quad \text{Equation A.10}$$

B Synchronous Generators Models

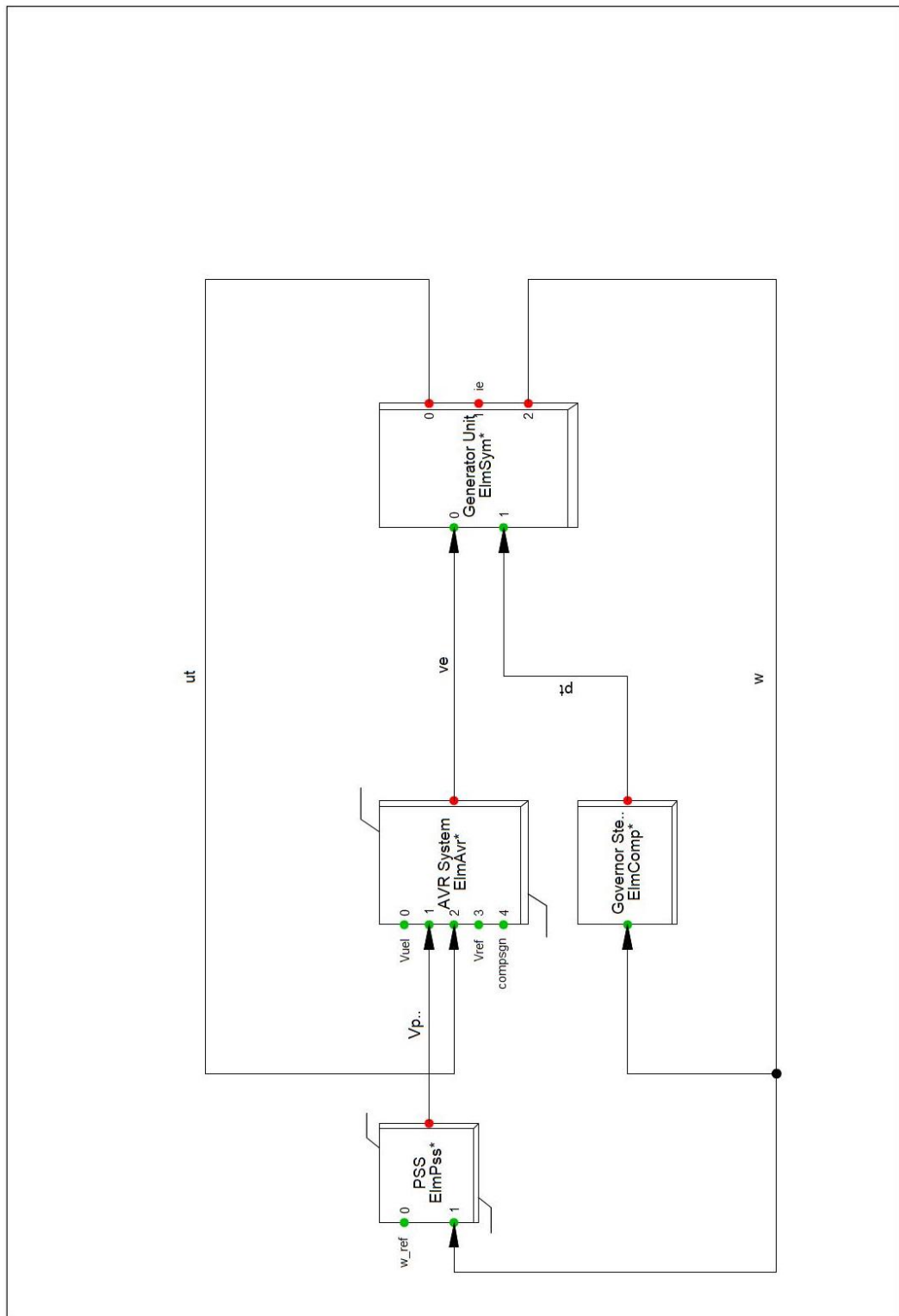


Figure B.1: SGU Composite Frame.

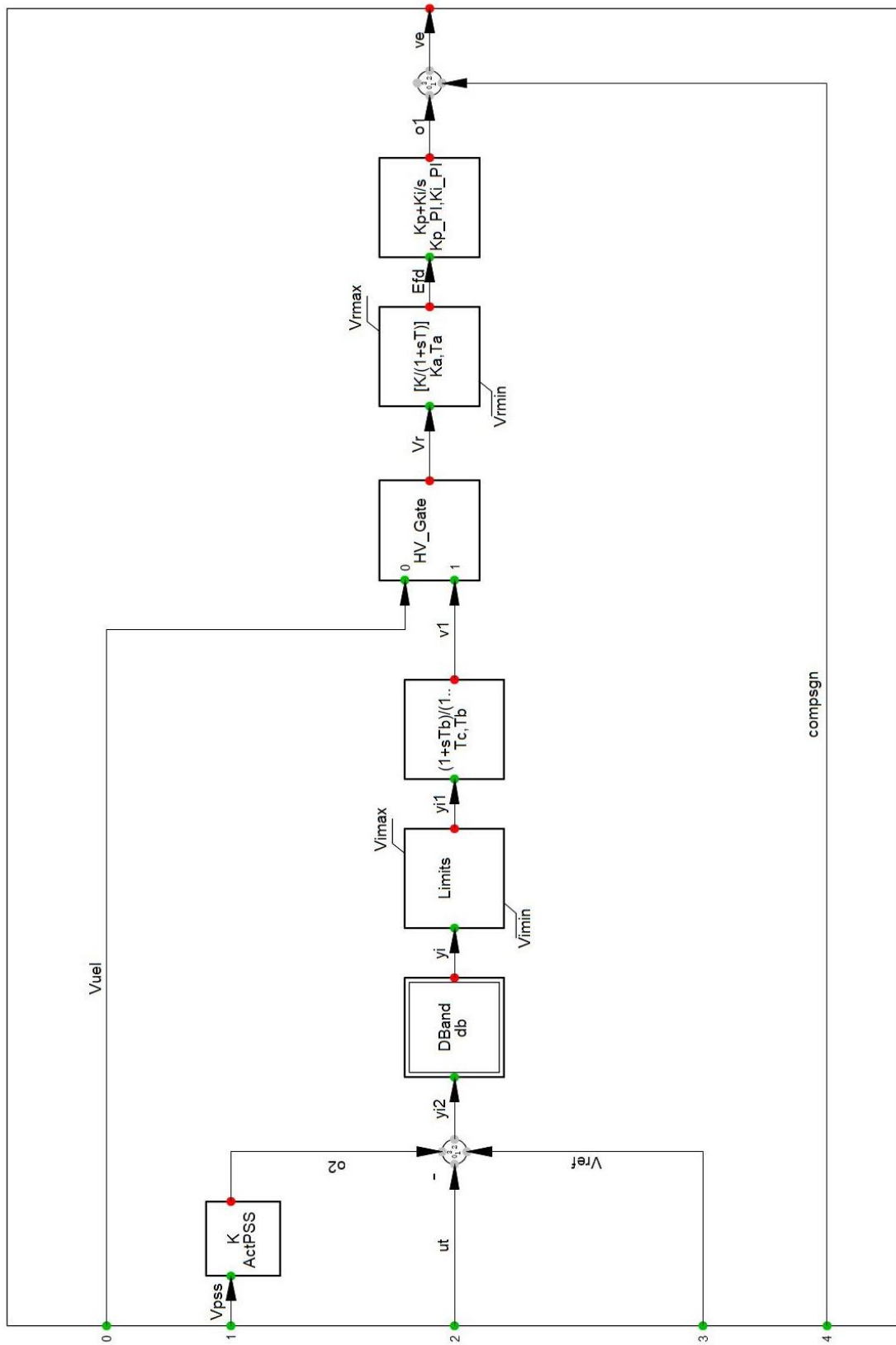


Figure B.2: SGU excitation system IEEEAC4A block diagram.

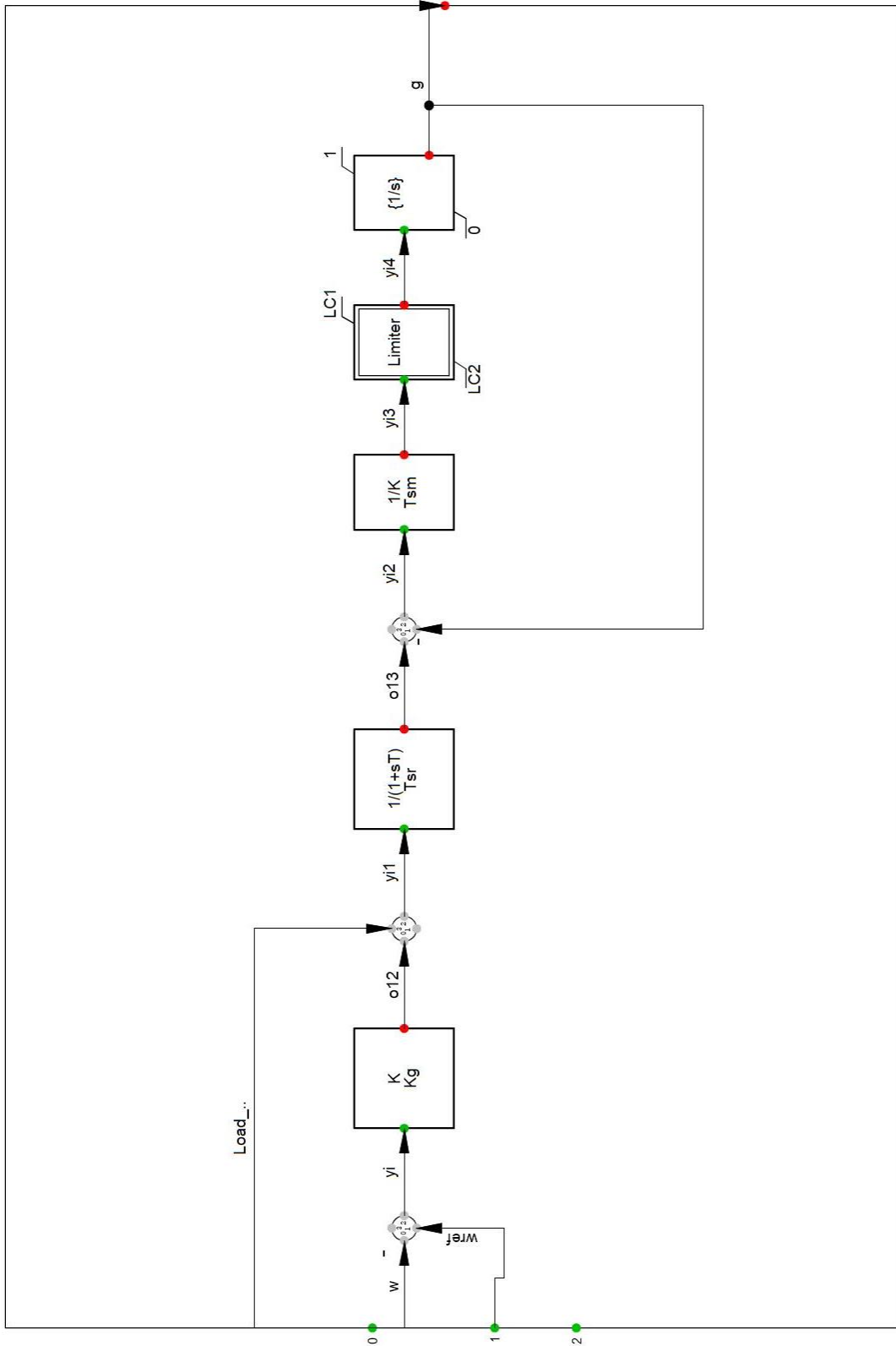


Figure B.3: SGU Turbine Model IEEE1.

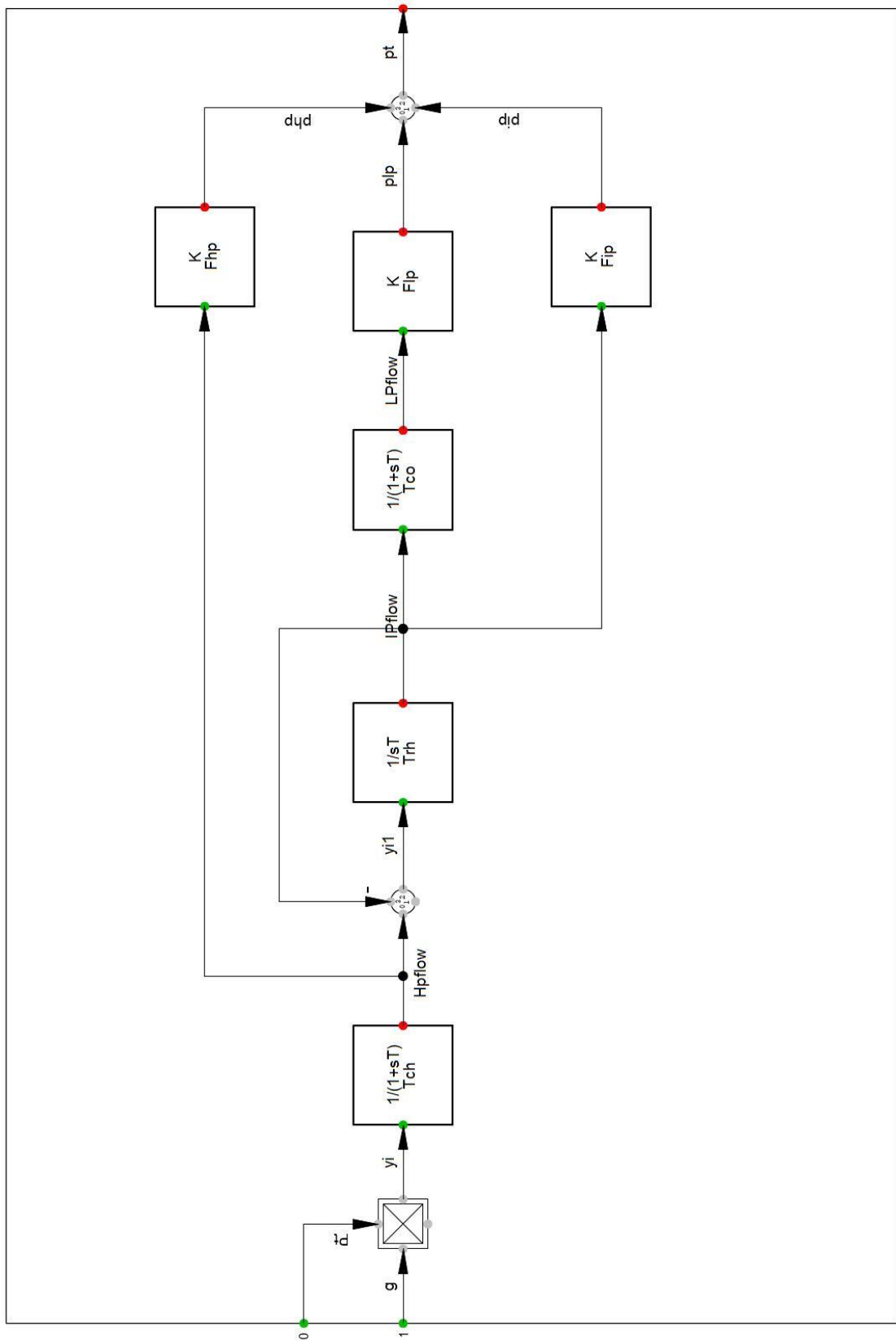


Figure B.4: SGU Governor Model IEEE G1.

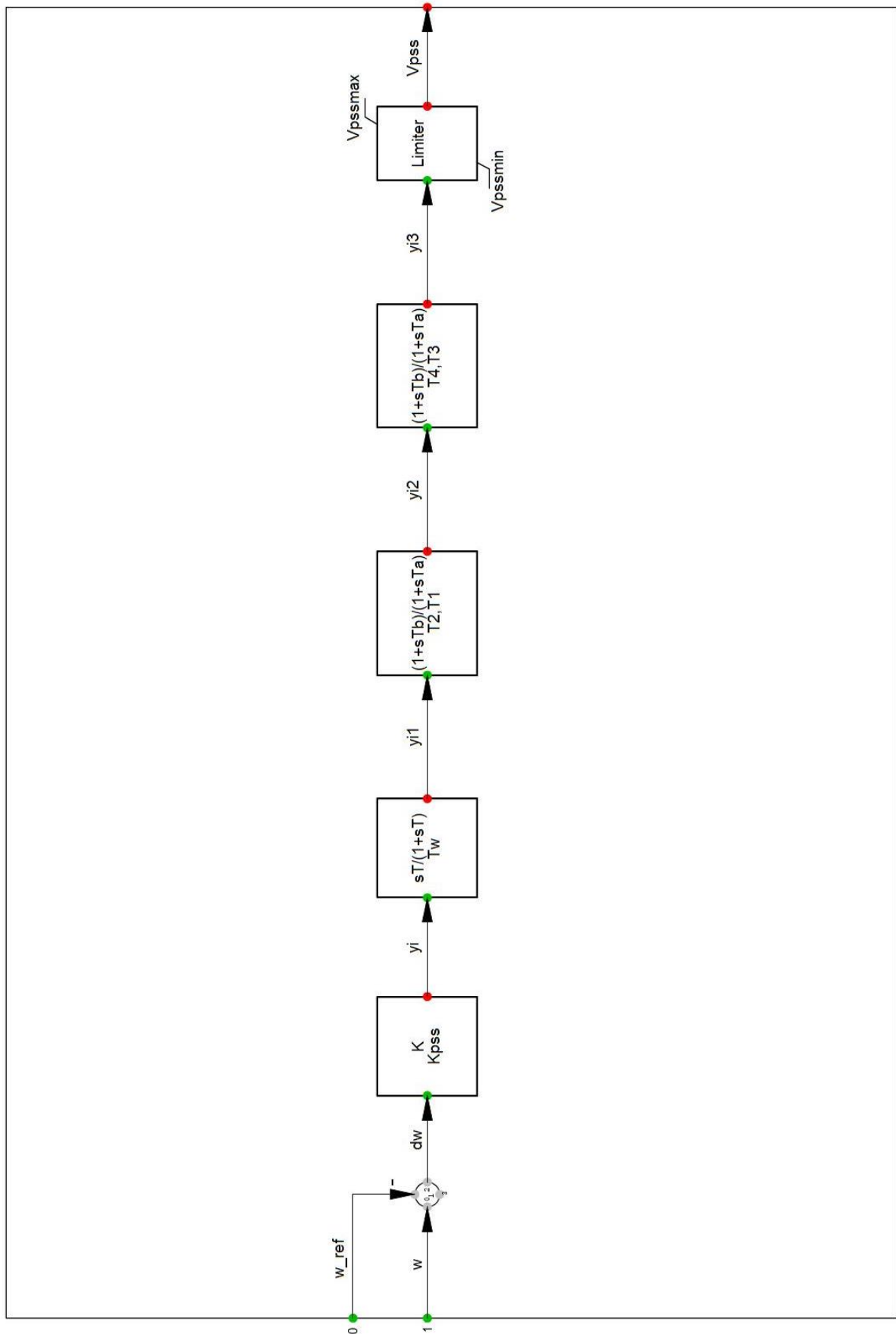


Figure B.5: SGU simple PSS block diagram.

C MMC-HVDC Interconnection Link Models

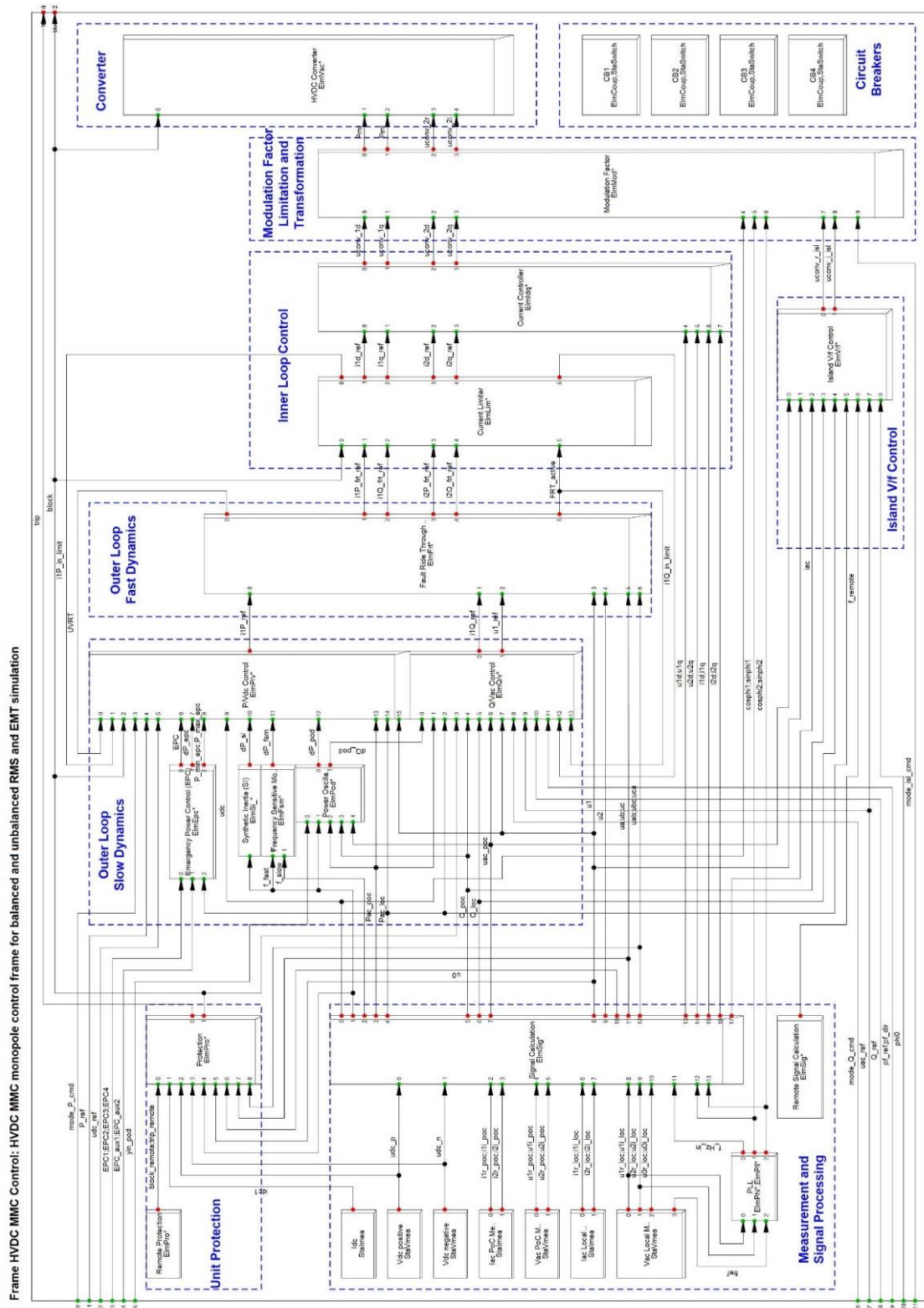


Figure C.1: HVDC interconnection link Composite Frame [72].

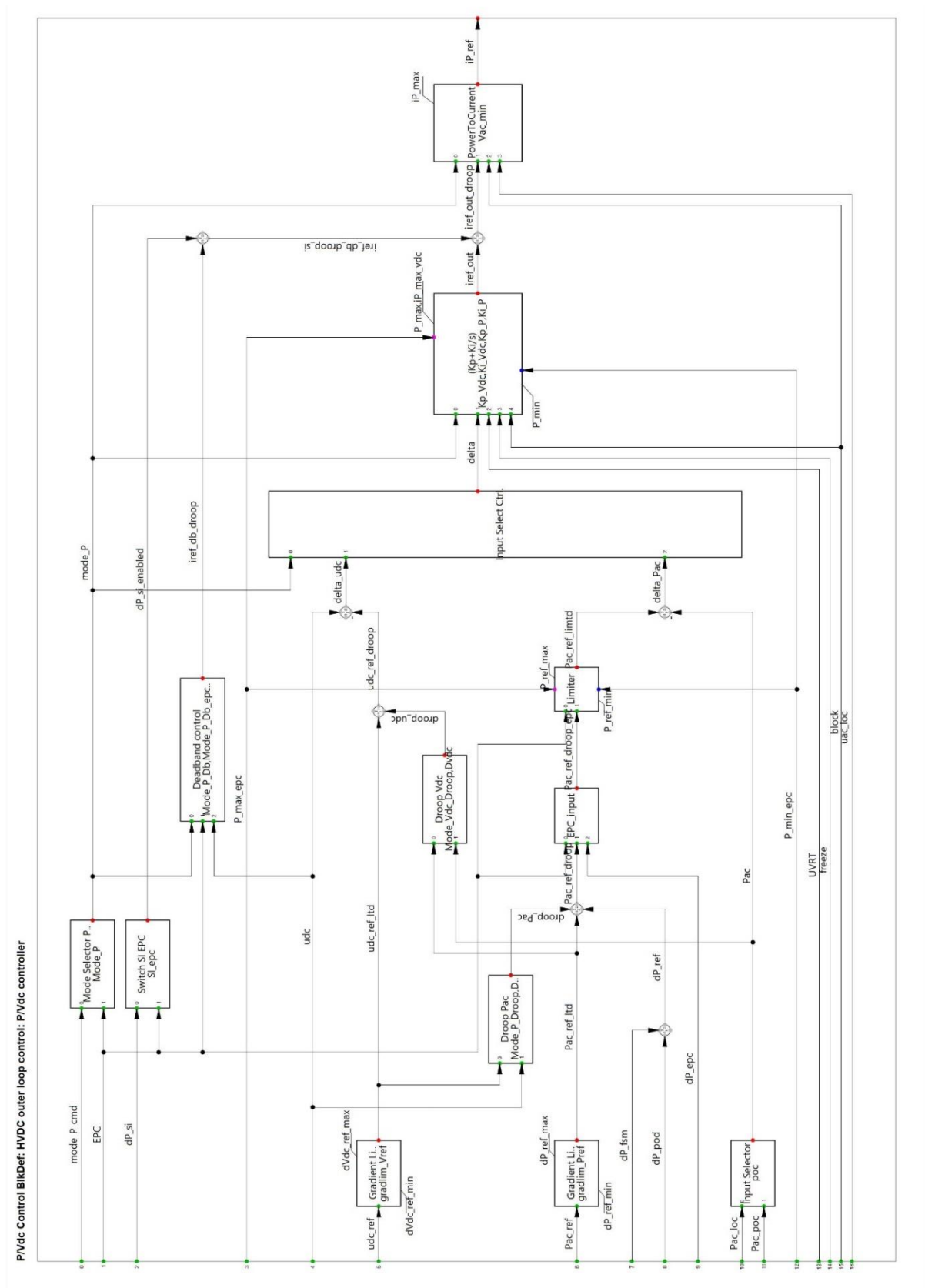


Figure C.2: P/Vdc Controller of MMC HVDC link block diagram [72].

D WT PowerFactory Models

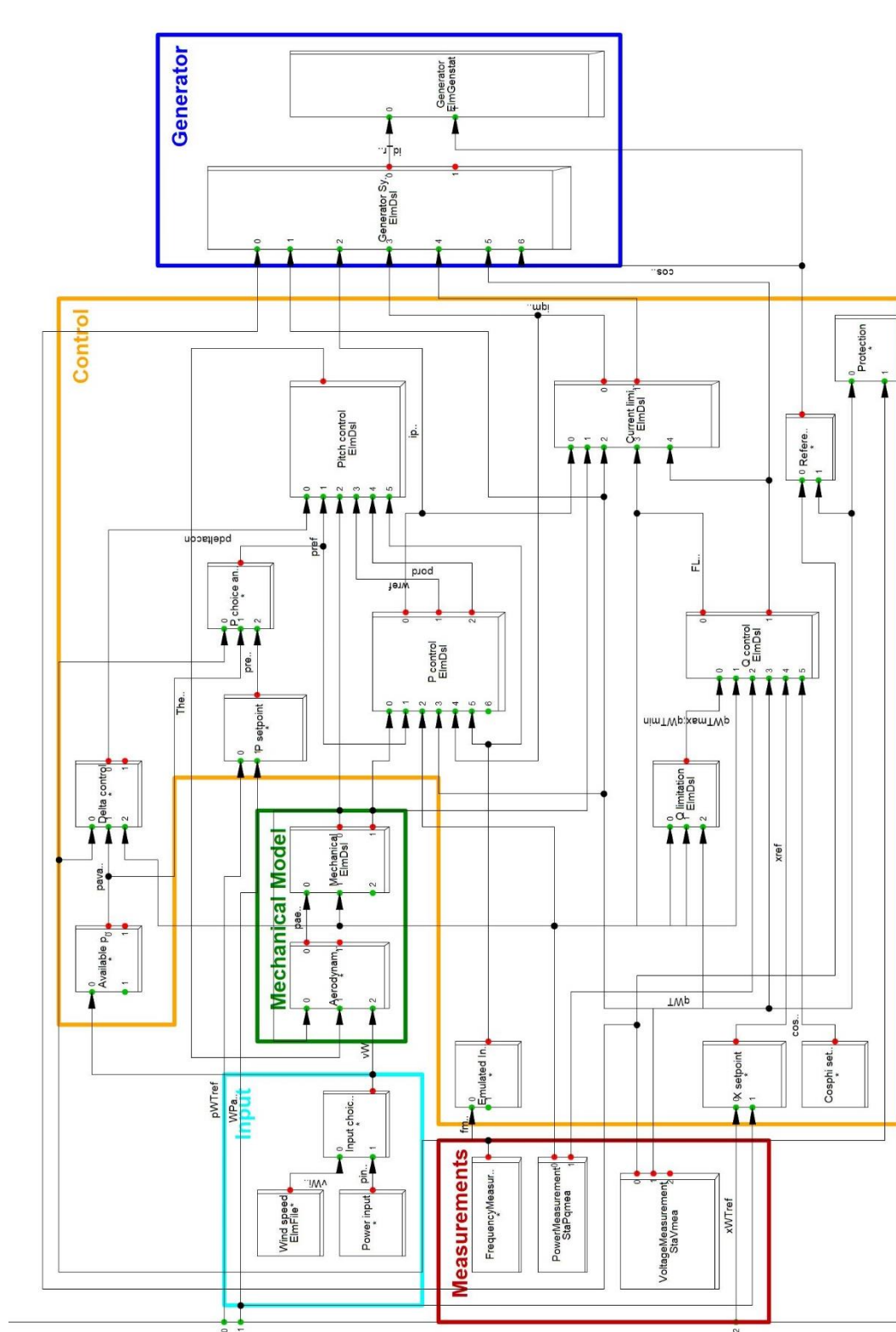


Figure D.1: WT Composite Frame DPF [115].

E Python Scripts

MVMO algorithm definition – MVMO class

```

import numpy as np, pandas as pd #imports the necessary python modules numpy and pandas
import time
class MVMO(): #generation of the MVMO algorithm class
    def __init__(self, iterations=1000, num_mutation=1, population_size=5, logger=True, app=None):
        self.app = app
        self.iterations = iterations
        self.num_mutation = num_mutation
        self.population_size = population_size
        self.logger = logger
# Definition of the initialization function for the MVMO algorithm. The user may specify the number of iterations,
#the number of mutate variables, the archive size and the DPF platform. If not, predefined values applied.
    def mvmo(self, obj_fun, bounds, cons, x_initial):
# Definition of the mvmo function. This function can be called, and the user should provide as inputs the
#objective function, the bounds, any possible constraints and an initial vector.
        convergence = []
        min_b, max_b = np.asarray(bounds).T # variables containing the max and min bounds
        diff = np.fabs(min_b - max_b) #contains the difference between the max and min of each variable
        D = len(bounds) # Calculation of the size of the optimization vector D
        solutions_d = pd.DataFrame()
        metrics_d = {} #Creates the archive saving the best candidate solutions and its statistical data
        if x_initial:
            x0 = (np.asarray(x_initial) - min_b) / (max_b - min_b)
        else:
            x0 = np.random.uniform(size=D)
# This loop utilizes as initial vector provided by the user or creates a new one of size D with random variables
#within the normalized range [0,1]
            x0_denorm = min_b + x0 * diff #candidate vector is denormalized to perform the fitness evaluation
# evaluate initial fitness considering the input objective function
            a = obj_fun(x0_denorm.tolist())
#check if constraints are met
            sol_good = self.constraint_check(x0_denorm.tolist(), cons)
            print(sol_good)
            if sol_good:
                fitness = round(a, 4)
            else:
                fitness = 1e10 #penalty for constraint violation

```

```

    convergence.append(fitness)
# fills the archive with fitness evaluation value, the solution vector, mean, shape, and d-factor
    solutions_d[fitness] = x0.tolist()
    metrics_d['mean'] = 0.5 * np.ones(D) # initial metric is set to 0.5 for mean
    metrics_d['variance'] = 0.5 * np.ones(D)
    for i in range(self.iterations):
        if self.logger:
            x_parent = solutions_d.loc[:, min(solutions_d.columns)].tolist()
# In every iteration the algorithm sets as parent solution the best solution achieved so far depending on the
#best fitness evaluation value. The variable x_parent is updated to contain the best optimization vector
            idxs = np.random.choice(list(range(len(bounds))), self.num_mutation)
# The idxs variable is created to randomly select which of the optimization variables of the parent
# solution vector will be modified. The number of the mutated variables is provided as input.
# Then for all the optimization variables to be mutated the parameters of the mapping function are calculated
# according to [117]. Then a new solution is generated.
            for idx in idxs:
                # mean
                x_bar = metrics_d['mean'][idx]
                xi_star = np.random.uniform(0, 1, 1)[0]
                var = metrics_d['variance'][idx]
                scaling_factor = 1 + 1/self.iterations * (20 - 1)
                # print(min(var,1e-5))
                s_old = -np.log(var) * scaling_factor
                if xi_star < 0.5:
                    s_new = s_old/(1 - x_bar)
                    hm = x_bar - x_bar/(0.5*s_new + 1)
                    hf = x_bar * (1 - np.exp(-xi_star * s_new))
                    hc = (x_bar - hm) * 2 * xi_star
                    xi_new = hf + hc
                else:
                    s_new = s_old/x_bar
                    hm = (1 - x_bar)/(0.5*s_new + 1)
                    hb = (1 - x_bar) / ((1 - xi_star) * s_new + 1) + x_bar
                    hc = hm * 2 * (1 - xi_star)
                    xi_new = hb - hc
            x_parent[idx] = xi_new
# The offspring solution has been generated and the corresponding optimization variables are saved in x
# The generated solution is within the normalized range [0,1] and needs to be denormalized to perform the
#fitness evaluation of the new solution.

```

```

        x_denorm_t = min_b + np.asarray(x_parent) * diff
        x_denorm = x_denorm_t.tolist()
# Fitness evaluation of the new solution
        a = obj_fun(x_denorm)
        if not a:
            continue
# Constraints Check
        sol_good = self.constraint_check(x_denorm, cons)
        if sol_good:
            fitness = round(a, 4)
        else:
            fitness = 1e10 #penalty for constraint violation
# If the new solution vector has achieved a better fitness evaluation, the archive is updated. The size of archive
#remains constant.
        if fitness >= max(solutions_d.columns) or fitness in list(solutions_d.columns):
            convergence.append(convergence[-1])
        else:
            solutions_d[fitness] = x_parent
            if len(solutions_d.columns) > self.population_size:
                solutions_d.pop(max(solutions_d.columns))
            convergence.append(min(solutions_d.columns))
# Same for the archive containing the statistical data of the optimization variables.
        metrics_d['variance'] = [
            np.var(solutions_d.iloc[x, :]) for x in range(len(solutions_d))]
        metrics_d['mean'] = [
            np.mean(solutions_d.iloc[x, :]) for x in range(len(solutions_d))]
        res = min_b + np.asarray(solutions_d.loc[:, min(solutions_d.columns)].tolist()) * diff
# res variable contains the optimization vector that achieved the best fitness evaluation so far denormalized
# Finally, at the output of the mvmo function the variables to be returned are the optimization vector that
#achieved the best fitness evaluation until the termination criteria reached, the convergence data, the value of
#the best fitness evaluation and the archive containing the best stored vectors
        return [convergence[-1], res], convergence, solutions_d
def constraint_check(self, solution, constraints):
    if len(constraints) == 0:
        return True
    else:
        X = solution
        for key, value in constraints.items():
            if key != 'func':

```

```

v = eval(value)
if key == 'ineq' and v >= 0:
    return False
elif key == 'eq' and v != 0:
    return False
else:
    return True
else:
    return value(X)

```

constraint_check function of the mvmo class can be called through the corresponding class to validate that #the **x** does not violate a predefined constraint. The inputs of these function are the solution vector of interest #and the constraint and return a true/false value.

```

def optimize(self, obj_fun, bounds, constraints={}, x0=False):
    t1 = time.time()
    self.res, self.conv, self.sol = self.mvmo(
        obj_fun=obj_fun, bounds=bounds, cons=constraints, x_initial=x0)
    t2 = time.time()
    if self.logger:
        sep = '*' * 50
        print("\n")
        print(sep)
        print(f"Optimal Solution found in {round(t2-t1, 2)}s")
        print(sep)
        print(f"\nFinal Objective Function Value: {self.res[0]}.")
        print(f"Optimal Objective Function Value at: {self.res[1]}.")
    return self.res, self.conv, self.sol

```

optimize can be called through the main python script to perform the optimization algorithm and solve the #optimization problem. It has as inputs the objective function, the boundaries for each of the optimization #variables, constraints and an initial solution vector. Inside this function the mvmo() function is utilized.

```

def plot(conv): # plot() function can be used to plot the results of interest in python
    import matplotlib.pyplot as plt
    plt.plot(conv, "C2", linewidth=1)
    plt.ylabel("Objective Function Fitness")
    plt.xlabel("Iterations")
    plt.title("Convergence Plot")
    plt.legend()
    plt.tight_layout()
    plt.show()

```

Problem Formulation 1 – Python main script- Full extend optimization vector

This python script refers to the main script that can be executed to create the co-simulation environment between DPF 2020 and Python 3.8 and run the mvmo algorithm with respect to the problem definition 1 as described in section 4.2. In this script, x is at its full extend, meaning that all the possible parameters of interest in the different network elements (WTs, PEM electrolyzers and HVDC links) are going to be optimized simultaneously. If the user wants to take advantage of a part of the available FCRs, the corresponding optimization variables should be excluded.

Initially the necessary modules will be imported to enable the co-simulation.

```
import sys
```

```
sys.path.append("C:\\Program Files\\DlG SILENT\\Power Factory 2020 SP1\\Python\\3.8")
```

```
import powerfactory as pf
```

```
sys.path.append("C:\\Users\\georg\\Desktop\\myoptimization")
```

```
import mvmo
```

```
from mvmo import MVMO
```

```
import numpy as np
```

```
from numpy import loadtxt
```

```
import pandas as pd
```

```
app = pf.GetApplication() # contains the information about the powerfactory platform and offers access
```

```
app.ClearOutputWindow() # Before the start of simulation output window of the DPF platform is cleared
```

Next step is to create lists containing the optimization data for each of the optimization variables

Data for the HVDC links ΔP and APG of the HVDC links

```
OptimData_APG_AB = []
```

```
OptimData_DP_AB = []
```

```
OptimData_APG_AC = []
```

```
OptimData_DP_AC = []
```

```
OptimData_APG_BC = []
```

```
OptimData_DP_BC = []
```

#Data for the electrolyzers bid and Page of the electrolyzers

```
OptimData_B_A1 = []
```

```
OptimData_APG_A1 = []
```

```
OptimData_B_A5b = []
```

```
OptimData_APG_A5b = []
```

```
OptimData_B_A6b = []
```

```
OptimData_APG_A6b = []
```

```
OptimData_B_B1 = []
```

```
OptimData_APG_B1 = []
```

```
OptimData_B_B11 = []
```

```
OptimData_APG_B11 = []
```

```
OptimData_B_B2 = []
```

```

OptimData_APG_B2=[]
OptimData_B_B4 =[]
OptimData_APG_B4=[]
OptimData_B_C10 =[]
OptimData_APG_C10=[]
OptimData_B_C12 =[]
OptimData_APG_C12=[]
OptimData_B_C3 =[]
OptimData_APG_C3=[]
OptimData_B_C6 =[]
OptimData_APG_C6=[]
#Data for WT pemuinmax and gradW of the WTs
OptimData_APG_WTC10=[]
OptimData_K_WTC10=[]
OptimData_APG_WTC12=[]
OptimData_K_WTC12=[]
OptimData_APG_WTB2=[]
OptimData_K_WTB2=[]
OptimData_APG_WTB8=[]
OptimData_K_WTB8=[]
OptimData_APG_WTB10=[]
OptimData_K_WTB10=[]
# Definition of a system path at which any export files will be saved.
  Pathtowrite = r'C:\Users\georg\Desktop\myoptimization'
# To modify the parameters of interest with candidate values of the optimization variables, access to the
#corresponding DPF objects has to be gained. Also, the user should be able to modify the events of interest.
#One of them is the parameter event created to modify the active power setpoint of the HVDC links. Hence,
#access should be gained initially to the active study case folders, then to the list of events and then to the
#event of interest and stored to a specific variable.
FolderStudyCase=app.GetProjectFolder("study")
  StudyCases=FolderStudyCase.GetContents('*.IntCase')
  ListCases=StudyCases[0]
  ListEvents = ListCases.GetContents('*.EvtParam',1)
  for x in ListEvents:
    if x.loc_name[:12]=='AP_Event_AB':
      Event_AB=x
    if x.loc_name[:12]=='AP_Event_AC':
      Event_AC=x
    if x.loc_name[:12]=='AP_Event_BC':

```

```

Event_BC=x
# the script should also gain access to functions to execute the initial conditions and the RMS simulation. Also,
#having defined the result variables of interest within DPF, the results following a simulation are stored in a
#DPF result object. To obtain these results the corresponding result object should be accessed.
Case = app.GetActiveStudyCase()
CalcInIt=app.GetFromStudyCase("ComInc") # Initial Conditions
comSim = app.GetFromStudyCase("ComSim") # RMS Simulation
comRes = app.GetFromStudyCase("ComRes")
res = Case.GetContents("*.ElmRes")[0] # Result object of DPF in the active case study
# Fitness Evaluation in problem formulation 1 as explained in section 4.2 depends on the frequency of each
#area measured at any point within each area. Also, it can be provided by the electrical frequency measured
#at the output of a generating unit within the area. The corresponding result variables in order to be utilized in
#python should be first accessed, then stored into a csv file in a suitable form. The csv file can be then read
#by python script to perform the calculations of interest.
# Gain access to the SGUs of interest in each area
GC14 = app.GetCalcRelevantObjects('C14G.ElmSym')[0]
GA1a = app.GetCalcRelevantObjects('A01aG.ElmSym')[0]
GA03 = app.GetCalcRelevantObjects('A03G.ElmSym')[0]
GB3 = app.GetCalcRelevantObjects('B03G.ElmSym')[0]
# Print to a CSV file all the results from selected variables that has to do with the time, speed of generators
#and frequencies in the required form. The CSV is stored in a specific path in the system. Depending on the
#(PC) system characteristics ',' and ';' options may differ. Refer to the python tutorial of DPF for further details.
comRes.pResult = res
comRes.iopt_exp = 6 # to export as csv
comRes.f_name = Pathtowrite + '\RESULTSG' + '.csv'
comRes.iopt_sep = 1 # to use the system separator
comRes.col_sep = ','
comRes.dec_Sep = '.'
comRes.iopt_locn = 0
comRes.ciopt_head = 0
comRes.iopt_honly = 0 # to export data and not only the header
comRes.iopt_csel = 1 # export only selected variables
comRes.iopt_tsel=0
# Select the variables to be exported
resObj=[None,None,None,None]
resElms=[res,GA03,GB3,GC14]
resVars=['b:tnow','s:xspeed','s:xspeed','s:xspeed']
# Perform the simulation and obtain the results
comRes.resultobj = resObj# Export selected

```

```

comRes.element = resElms
comRes.variable = resVars
Calclnit.Execute() #calculates initial conditions
comSim.Execute() #calculated the rms simulation
comRes.Execute() #produces the results and saves it into a csv file

```

##Definition of a function containing the OF1 described in section 4.2

```

# objective function 1 has as input a candidate optimization vector .In its full extend D=38
def objective_function(x):
# x given as input to the objective function is matched with the corresponding optimization variables
    APRR_AB,DeltaP_AB,APRR_AC,DeltaP_AC,APRR_BC,DeltaP_BC,B_A1,APGe_A1,B_A5b,
APGe_A5b,B_A6b,APGe_A6b,B_B1,APGe_B1,B_B11,APGe_B11,B_B2,APGe_B2,B_B4,
APGe_B4,B_C10,APGe_C10,B_C12,APGe_C12,B_C3,APGe_C3,B_C6,APGe_C6,APG_WTC10,K_WTC10
,APG_WTC12,K_WTC12,APG_WTB2,K_WTB2,APG_WTB8,K_WTB8,APG_WTB10,K_WTB10 = x
# Based on the lists containing the values of the optimization variables, the lists are appended with the
#candidate variables
    OptimData_APG_AB.append(APRR_AB)
    OptimData_DP_AB.append(DeltaP_AB)
    OptimData_APG_AC.append(APRR_AC)
    OptimData_DP_AC.append(DeltaP_AC)
    OptimData_APG_BC.append(APRR_BC)
    OptimData_DP_BC.append(DeltaP_BC)
    OptimData_B_A1.append(B_A1)
    OptimData_APG_A1.append(APGe_A1)
    OptimData_B_A5b.append(B_A5b)
    OptimData_APG_A5b.append(APGe_A5b)
    OptimData_B_A6b.append(B_A6b)
    OptimData_APG_A6b.append(APGe_A6b)
    OptimData_B_B1.append(B_B1)
    OptimData_APG_B1.append(APGe_B1)
    OptimData_B_B11.append(B_B11)
    OptimData_APG_B11.append(APGe_B11)
    OptimData_B_B2.append(B_B2)
    OptimData_APG_B2.append(APGe_B2)
    OptimData_B_B4.append(B_B4)
    OptimData_APG_B4.append(APGe_B4)
    OptimData_B_C10.append(B_C10)
    OptimData_APG_C10.append(APGe_C10)
    OptimData_B_C12.append(B_C12)
    OptimData_APG_C12.append(APGe_C12)

```

```

OptimData_B_C3.append(B_C3)
OptimData_APG_C3.append(APGe_C3)
OptimData_B_C6.append(B_C6)
OptimData_APG_C6.append(APGe_C6)
OptimData_APG_WTC10.append(APG_WTC10)
OptimData_K_WTC10.append(K_WTC10)
OptimData_APG_WTC12.append(APG_WTC12)
OptimData_K_WTC12.append(K_WTC12)
OptimData_APG_WTB2.append(APG_WTB2)
OptimData_K_WTB2.append(K_WTB2)
OptimData_APG_WTB8.append(APG_WTB8)
OptimData_K_WTB8.append(K_WTB8)
OptimData_APG_WTB10.append(APG_WTB10)
OptimData_K_WTB10.append(K_WTB10)

```

Access should also be gained to the controllers of interest and to the corresponding common models. Hence,
#access is gained in the active power controllers of the HVDC links, to the electrolyzers' frequency controllers
#and to the frequency controllers of the WTs

```
DslModels=app.GetCalcRelevantObjects("*.ElmDsl")
```

```
for DSL in DslModels:
```

```
    if DSL.loc_name == 'P/Vdc Control CA':
```

```
        APCtrl_CA = DSL
```

```
    if DSL.loc_name == 'P/Vdc Control CB':
```

```
        APCtrl_CB=DSL
```

```
    if DSL.loc_name == 'P/Vdc Control BA':
```

```
        APCtrl_BA=DSL
```

```
    if DSL.loc_name == 'Electrolyser Droop A1':
```

```
        ele_A1=DSL
```

```
    if DSL.loc_name == 'Electrolyser Droop A5b':
```

```
        ele_A5b=DSL
```

```
    if DSL.loc_name == 'Electrolyser Droop A6b':
```

```
        ele_A6b=DSL
```

```
    if DSL.loc_name == 'Electrolyser Droop B1':
```

```
        ele_B1=DSL
```

```
    if DSL.loc_name == 'Electrolyser Droop B11':
```

```
        ele_B11=DSL
```

```
    if DSL.loc_name == 'Electrolyser Droop B2':
```

```
        ele_B2=DSL
```

```
    if DSL.loc_name == 'Electrolyser Droop B4':
```

```
        ele_B4=DSL
```

```

if DSL.loc_name == 'Electrolyser Droop C10':
    ele_C10=DSL
if DSL.loc_name == 'Electrolyser Droop C12':
    ele_C12=DSL
if DSL.loc_name == 'Electrolyser Droop C3':
    ele_C3=DSL
if DSL.loc_name == 'Electrolyser Droop C6':
    ele_C6=DSL
if DSL.loc_name == 'Frequency Control WTB10':
    WTB10=DSL
if DSL.loc_name == 'Frequency Control WTB8':
    WTB8=DSL
if DSL.loc_name == 'Frequency Control WTB2':
    WTB2=DSL
if DSL.loc_name == 'Frequency Control WTC10':
    WTC10=DSL
if DSL.loc_name == 'Frequency Control WTC12':
    WTC12=DSL

# Having gained access to the events and controllers of interest the corresponding parameters are modified
#with the candidate optimization variables of interest.
APCtrl_CA.dP_ref_max = APRR_AC # changes APG in the P/Vdc controller of A-C HVDC link
APCtrl_CA.dP_ref_min= -APRR_AC # same for downwards
APCtrl_CB.dP_ref_max = APRR_BC # changes APG in the P/Vdc controller of B-C HVDC link
APCtrl_CB.dP_ref_min= -APRR_BC # same for downwards
APCtrl_BA.dP_ref_max = APRR_AB # changes APG in the P/Vdc controller of A-B HVDC link
APCtrl_BA.dP_ref_min= -APRR_AB #same for downwards
Event_AB.value = str(DeltaP_AB/2000) #changes the P_ref of the P/Vdc controller of AB
# HVDC link through the parameter event. Division by 2000 as controllers work in pu.
Event_AC.value = str(DeltaP_AC/2000) # same for the AC HVDC link
Event_BC.value = str(DeltaP_BC/2000) # same for the BC HVDC link
# Changing the bid size of each of the electrolyzers in the common models and the APGe
ele_A1.FCR_bid=B_A1
ele_A1.grad=APGe_A1
ele_A5b.FCR_bid=B_A5b
ele_A5b.grad=APGe_A5b
ele_A6b.FCR_bid=B_A6b
ele_A6b.grad=APGe_A6b
ele_B1.FCR_bid=B_B1
ele_B1.grad=APGe_B1

```

```

ele_B11.FCR_bid=B_B11
ele_B11.grad=APGe_B11
ele_B2.FCR_bid=B_B2
ele_B2.grad=APGe_B2
ele_B4.FCR_bid=B_B4
ele_B4.grad=APGe_B4
ele_C10.FCR_bid=B_C10
ele_C10.grad=APGe_C10
ele_C12.FCR_bid=B_C12
ele_C12.grad=APGe_C12
ele_C3.FCR_bid=B_C3
ele_C3.grad=APGe_C3
ele_C6.FCR_bid=B_C6
ele_C6.grad=APGe_C6
# Changing the pemuinmax and gradW of the common model of each of the contributing WTs to FFS
WTC10.gradW=APG_WTC10
WTC10.pemuinmax=K_WTC10
WTC12.gradW=APG_WTC12
WTC12.pemuinmax=K_WTC12
WTB2.gradW=APG_WTB2
WTB2.pemuinmax=K_WTB2
WTB8.gradW=APG_WTB8
WTB8.pemuinmax=K_WTB8
WTB10.gradW=APG_WTB10
WTB10.pemuinmax=K_WTB10
# Perform the simulation and obtain the results
CalcInit.Execute() #calculates initial conditions
comSim.Execute() #calculated the rms simulation
comRes.Execute() #produces the results and saves it into a csv file in the suitable form
csvFile = pd.read_csv(Pathtowrite + '\RESULTSG' + '.csv', delimiter=',', header=None) #read the csv
# Match the information in the csv file with the parameters of interest
time = csvFile.iloc[:,0].to_numpy().astype(np.float) #read time from csv and make i into float
fA= csvFile.iloc[:,1].to_numpy().astype(np.float)
fB= csvFile.iloc[:,2].to_numpy().astype(np.float)
fC= csvFile.iloc[:,3].to_numpy().astype(np.float)
# Definition of the objective function
# fA,fB,fC variables are multiplied by 50 as in the csv file are stored in pu.
a=abs((fA*50-50)**2)+abs((fB*50-50)**2)+abs((fC*50-50)**2)
total_objective=np.trapz(abs(a),time)

```



```
import mvmo
from mvmo import MVMO
import numpy as np
from numpy import loadtxt
import pandas as pd
app = pf.GetApplication() # the app variable contains the information about powerfactory and offers access
app.ClearOutputWindow() # Before the start of simulation output window of the DPF platform is cleared
# Next step is to create lists containing the data for each of the optimization variables
# Data for the HVDC links ΔP and APG of the HVDC links
OptimData_APG_AB = []
OptimData_DP_AB = []
OptimData_APG_AC = []
OptimData_DP_AC = []
OptimData_APG_BC = []
OptimData_DP_BC = []
#Data for the electrolyzers bid and APGe of the electrolyzers
OptimData_B_A1 =[]
OptimData_APG_A1=[]
OptimData_B_A5b =[]
OptimData_APG_A5b=[]
OptimData_B_A6b =[]
OptimData_APG_A6b=[]
OptimData_B_B1 =[]
OptimData_APG_B1=[]
OptimData_B_B11 =[]
OptimData_APG_B11=[]
OptimData_B_B2 =[]
OptimData_APG_B2=[]
OptimData_B_B4 =[]
OptimData_APG_B4=[]
OptimData_B_C10 =[]
OptimData_APG_C10=[]
OptimData_B_C12 =[]
OptimData_APG_C12=[]
OptimData_B_C3 =[]
OptimData_APG_C3=[]
OptimData_B_C6 =[]
OptimData_APG_C6=[]
#Data for WT pemuinmax and gradW of the WTs
```

```

OptimData_APG_WTC10=[]
OptimData_K_WTC10=[]
OptimData_APG_WTC12=[]
OptimData_K_WTC12=[]
OptimData_APG_WTB2=[]
OptimData_K_WTB2=[]
OptimData_APG_WTB8=[]
OptimData_K_WTB8=[]
OptimData_APG_WTB10=[]
OptimData_K_WTB10=[]
# Definition of a system path at which any export files will be saved.
  Pathtowrite = r'C:\\Users\\georg\\Desktop\\myoptimization'
# To modify the parameters of interest with candidate values access to the corresponding DPF objects has to
#be gained. Also, the user should be able to modify the events of interest. Hence, access should be gained to
#the active study case folders, then to the list of events and then to the event of interest.
  FolderStudyCase=app.GetProjectFolder("study")
  StudyCases=FolderStudyCase.GetContents('*.IntCase')
  ListCases=StudyCases[0]
  ListEvents = ListCases.GetContents('*.EvtParam',1)
  for x in ListEvents:
    if x.loc_name[:12]=='AP_Event_AB':
      Event_AB=x
    if x.loc_name[:12]=='AP_Event_AC':
      Event_AC=x
    if x.loc_name[:12]=='AP_Event_BC':
      Event_BC=x
# Apart from the parameter events of interest, the python script should also gain access to the functions able
#to execute the initial conditions and the RMS simulation of interest and then access and store the results of
i#nterest in a csv file.
  Case = app.GetActiveStudyCase()
  CalcInit=app.GetFromStudyCase("ComInc")
  comSim = app.GetFromStudyCase("ComSim")
  comRes = app.GetFromStudyCase("ComRes")
  res = Case.GetContents('*.ElmRes')[0]
# To perform the fitness evaluation as explained in Problem formulation 2 in section 4.3, the speed of each of
#the electromagnetically decoupled areas ( $\omega_A, \omega_B, \omega_C$ ) should be calculated. In a multi-machine system the
#calculation of these parameters can be either based on the average speed of the participating SGUs [20] or
#based on the COI of each of the interconnected areas [116]. In both cases the speed response of the active
#SGUs of the system when an imbalance occurs should be obtained following the simulation. Thus, access to

```

```

#the corresponding SGUs parameters should be gained and the results of interest should be stored in a csv
#file. In case of an active power event that includes a loss of a SGU, the latter one should be excluded
#Access Generating Units Area A
    GA03 = app.GetCalcRelevantObjects('A03G.ElmSym')[0]
    GA01a= app.GetCalcRelevantObjects('A01aG.ElmSym')[0]
    GA01b= app.GetCalcRelevantObjects('A01bG.ElmSym')[0]
    GA02a= app.GetCalcRelevantObjects('A02aG.ElmSym')[0]
    GA02b= app.GetCalcRelevantObjects('A02bG.ElmSym')[0]
    GA06= app.GetCalcRelevantObjects('A06G.ElmSym')[0]
#Access Generating Units Area B
    GB03 = app.GetCalcRelevantObjects('B03G.ElmSym')[0]
    GB02b = app.GetCalcRelevantObjects('B02bG.ElmSym')[0]
#Access Generating Units Area C
    GC14 = app.GetCalcRelevantObjects('C14G.ElmSym')[0]
    GC02 = app.GetCalcRelevantObjects('C02G.ElmSym')[0]
    GC07 = app.GetCalcRelevantObjects('C07G.ElmSym')[0]
# Print to a CSV file all the results from selected variables that has to do with the time and speed
    comRes.pResult = res
    comRes.iopt_exp = 6 # to export as csv
    comRes.f_name = Pathtowrite + '\RESULTSG' + '.csv'
    comRes.iopt_sep = 1 # to use the system separator
    comRes.col_sep = ','
    comRes.dec_Sep = '.'
    comRes.iopt_locn = 0
    comRes.ciopt_head = 0
    comRes.iopt_honly = 0 # to export data and not only the header
    comRes.iopt_csel = 1 # export only selected variables
    comRes.iopt_tsel=0
#Select the variables that would be exported in the CSV file in the specified form. The result variables should
#be also defined within DPF.
    resObj=[None,None,None,None,None,None,None,None,None,None,None]
    resElms=[res,GA03,GA01a,GA01b,GA02a,GA02b,GA06,GB03,GB02b,GC02,GC07,GC14]
    resVars=['b:tnow','s:xspeed','s:xspeed','s:xspeed','s:xspeed','s:xspeed','s:xspeed','s:xspeed','s:xspeed','s:x
speed','s:xspeed','s:xspeed',]
# Perform the simulation and obtain the results
    comRes.resultobj = resObj# Export selected
    comRes.element = resElms
    comRes.variable = resVars
    CalcInit.Execute() #calculates initial conditions

```

```
comSim.Execute() #calculated the rms simulation
comRes.Execute() #produces the results and saves it into a csv file
```

##Definition of a function containing the OF2 described in section 4.4

```
# The objective function has as input the candidate x. Based on that fitness evaluation will be performed.
```

```
def objective_function(x):
```

```
    APRR_AB,DeltaP_AB,APRR_AC,DeltaP_AC,APRR_BC,DeltaP_BC,B_A1,APGe_A1,B_A5b,APGe_A5b,
    B_A6b,APGe_A6b,B_B1,APGe_B1,B_B11,APGe_B11,B_B2,APGe_B2,B_B4,APGe_B4,B_C10,APGe_C10,
    B_C12,APGe_C12,B_C3,APGe_C3,B_C6,APGe_C6,APG_WTC10,K_WTC10,APG_WTC12,K_WTC12,AP
    G_WTB2,K_WTB2,APG_WTB8,K_WTB8,APG_WTB10,K_WTB10=x
```

```
# the solution vector given as input to the objective function is matched with the corresponding variables
```

```
# In each iteration the lists containing the values of the optimization variables are appended with the new
```

```
#candidates. Each one of the following corresponds to a specific optimization variable.
```

```
    OptimData_APG_AB.append(APRR_AB)
    OptimData_DP_AB.append(DeltaP_AB)
    OptimData_APG_AC.append(APRR_AC)
    OptimData_DP_AC.append(DeltaP_AC)
    OptimData_APG_BC.append(APRR_BC)
    OptimData_DP_BC.append(DeltaP_BC)
    OptimData_B_A1.append(B_A1)
    OptimData_APG_A1.append(APGe_A1)
    OptimData_B_A5b.append(B_A5b)
    OptimData_APG_A5b.append(APGe_A5b)
    OptimData_B_A6b.append(B_A6b)
    OptimData_APG_A6b.append(APGe_A6b)
    OptimData_B_B1.append(B_B1)
    OptimData_APG_B1.append(APGe_B1)
    OptimData_B_B11.append(B_B11)
    OptimData_APG_B11.append(APGe_B11)
    OptimData_B_B2.append(B_B2)
    OptimData_APG_B2.append(APGe_B2)
    OptimData_B_B4.append(B_B4)
    OptimData_APG_B4.append(APGe_B4)
    OptimData_B_C10.append(B_C10)
    OptimData_APG_C10.append(APGe_C10)
    OptimData_B_C12.append(B_C12)
    OptimData_APG_C12.append(APGe_C12)
    OptimData_B_C3.append(B_C3)
    OptimData_APG_C3.append(APGe_C3)
    OptimData_B_C6.append(B_C6)
```

```
OptimData_APG_C6.append(APGe_C6)
OptimData_APG_WTC10.append(APG_WTC10)
OptimData_K_WTC10.append(K_WTC10)
OptimData_APG_WTC12.append(APG_WTC12)
OptimData_K_WTC12.append(K_WTC12)
OptimData_APG_WTB2.append(APG_WTB2)
OptimData_K_WTB2.append(K_WTB2)
OptimData_APG_WTB8.append(APG_WTB8)
OptimData_K_WTB8.append(K_WTB8)
OptimData_APG_WTB10.append(APG_WTB10)
OptimData_K_WTB10.append(K_WTB10)
```

Apart from the modifications in the events, modifications should be applied to the common models of the #frequency controllers of the HVDC links, the electrolyzers and the WTs. Hence, access should be gained to #the corresponding DPF objects and to be assigned to python variables

```
DslModels=app.GetCalcRelevantObjects("*.ElmDsl")
```

```
for DSL in DslModels:
```

```
    if DSL.loc_name == 'P/Vdc Control CA':
```

```
        APCtrl_CA = DSL
```

```
    if DSL.loc_name == 'P/Vdc Control CB':
```

```
        APCtrl_CB=DSL
```

```
    if DSL.loc_name == 'P/Vdc Control BA':
```

```
        APCtrl_BA=DSL
```

```
    if DSL.loc_name == 'Electrolyser Droop A1':
```

```
        ele_A1=DSL
```

```
    if DSL.loc_name == 'Electrolyser Droop A5b':
```

```
        ele_A5b=DSL
```

```
    if DSL.loc_name == 'Electrolyser Droop A6b':
```

```
        ele_A6b=DSL
```

```
    if DSL.loc_name == 'Electrolyser Droop B1':
```

```
        ele_B1=DSL
```

```
    if DSL.loc_name == 'Electrolyser Droop B11':
```

```
        ele_B11=DSL
```

```
    if DSL.loc_name == 'Electrolyser Droop B2':
```

```
        ele_B2=DSL
```

```
    if DSL.loc_name == 'Electrolyser Droop B4':
```

```
        ele_B4=DSL
```

```
    if DSL.loc_name == 'Electrolyser Droop C10':
```

```
        ele_C10=DSL
```

```
    if DSL.loc_name == 'Electrolyser Droop C12':
```

```

    ele_C12=DSL
if DSL.loc_name == 'Electrolyser Droop C3':
    ele_C3=DSL
if DSL.loc_name == 'Electrolyser Droop C6':
    ele_C6=DSL
if DSL.loc_name == 'Frequency Control WTB10':
    WTB10=DSL
if DSL.loc_name == 'Frequency Control WTB8':
    WTB8=DSL
if DSL.loc_name == 'Frequency Control WTB2':
    WTB2=DSL
if DSL.loc_name == 'Frequency Control WTC10':
    WTC10=DSL
if DSL.loc_name == 'Frequency Control WTC12':
    WTC12=DSL
# Having gained access to the events and controllers of interest the corresponding parameters are modified
#as explained in Chapter 3 with the candidate optimization variables of interest.
    APCtrl_CA.dP_ref_max = APRR_AC # changes APG in the P/Vdc controller of A-C HVDC link
    APCtrl_CA.dP_ref_min=-APRR_AC # same for downwards
    APCtrl_CB.dP_ref_max = APRR_BC # changes APG in the P/Vdc controller of B-C HVDC link
    APCtrl_CB.dP_ref_min=-APRR_BC # same for downwards
    APCtrl_BA.dP_ref_max = APRR_AB # changes APG in the P/Vdc controller of A-B HVDC link
    APCtrl_BA.dP_ref_min=-APRR_AB # same for downwards
    Event_AB.value = str(DeltaP_AB/2000) #changes the P_ref of the P/Vdc controller of AB
# HVDC link through the parameter event. Division by 2000 as controllers work in pu.
    Event_AC.value = str(DeltaP_AC/2000) # same for the AC HVDC link
    Event_BC.value = str(DeltaP_BC/2000) # same for the BC HVDC link
# Changing the bid size of each of the electrolyzers in the common models and the APG e
    ele_A1.FCR_bid=B_A1
    ele_A1.grad=APGe_A1
    ele_A5b.FCR_bid=B_A5b
    ele_A5b.grad=APGe_A5b
    ele_A6b.FCR_bid=B_A6b
    ele_A6b.grad=APGe_A6b
    ele_B1.FCR_bid=B_B1
    ele_B1.grad=APGe_B1
    ele_B11.FCR_bid=B_B11
    ele_B11.grad=APGe_B11
    ele_B2.FCR_bid=B_B2

```

```
ele_B2.grad=APGe_B2
ele_B4.FCR_bid=B_B4
ele_B4.grad=APGe_B4
ele_C10.FCR_bid=B_C10
ele_C10.grad=APGe_C10
ele_C12.FCR_bid=B_C12
ele_C12.grad=APGe_C12
ele_C3.FCR_bid=B_C3
ele_C3.grad=APGe_C3
ele_C6.FCR_bid=B_C6
ele_C6.grad=APGe_C6
# Changing the pemuinmax and gradW of the common model of each of the contributing WTs to FFS
WTC10.gradW=APG_WTC10
WTC10.pemuinmax=K_WTC10
WTC12.gradW=APG_WTC12
WTC12.pemuinmax=K_WTC12
WTB2.gradW=APG_WTB2
WTB2.pemuinmax=K_WTB2
WTB8.gradW=APG_WTB8
WTB8.pemuinmax=K_WTB8
WTB10.gradW=APG_WTB10
WTB10.pemuinmax=K_WTB10
# Perform the simulation and obtain the results
CalcInit.Execute() #calculates initial conditions
comSim.Execute() #calculated the rms simulation
comRes.Execute() #produces the results and saves it into a csv file in the suitable form
#Having performed the simulation, the results stored in the csv need to be read by python to perform the
fitness evaluation
csvFile = pd.read_csv(Pathtowrite + '\RESULTSG' + '.csv', delimiter=',', header=None) #reads csv
# To perform the fitness evaluation through the calculation of the objective function, the generators' speed
#should be read from the csv file and matched to the corresponding python variables.
time = csvFile.iloc[:,0].to_numpy().astype(np.float) #read time from csv and make i into float
wGA03= csvFile.iloc[:,1].to_numpy().astype(np.float) # speed of SG A03
wGA01a= csvFile.iloc[:,2].to_numpy().astype(np.float) # speed of SG A01a
wGA01b= csvFile.iloc[:,3].to_numpy().astype(np.float) # speed of SG A01b
wGA02a= csvFile.iloc[:,4].to_numpy().astype(np.float) # speed of SG A02a
wGA02b= csvFile.iloc[:,5].to_numpy().astype(np.float) # speed of SG A02b
wGA06= csvFile.iloc[:,6].to_numpy().astype(np.float) # speed of SG A06
wGB03= csvFile.iloc[:,7].to_numpy().astype(np.float) # speed of SG B03
```

```

wGB02b= csvFile.iloc[:,8].to_numpy().astype(np.float) # speed of SG B02b
wGC02= csvFile.iloc[:,9].to_numpy().astype(np.float) # speed of SG C02
wGC07= csvFile.iloc[:,10].to_numpy().astype(np.float) # speed of SG C07
wGC14= csvFile.iloc[:,11].to_numpy().astype(np.float) # speed of SG C14
# Then, the user should select which assumption will be used: Area's frequency based on the average speed
#of the active SGUs of each area or based on the COI of each area. The part of the code that will not be used
#should be commented.
### Average Areas Speed – Frequency
# Only the actively operating SGUs should be included in the calculation. If loss of SGUs is considered as
#event, the corresponding SGU should be excluded from the calculations.
wA=(wGA03+wGA01a+wGA01b+wGA02a+wGA02b+wGA06)/6 #Average speed in area A.
# Include only actively participating generators throughout the RMS simulation
wB=(wGB03+wGB02b)/2 #Average speed in area B. Include only participating generators
wC=(wGC02+wGC07+wGC14)/3 #Average speed in area C.Include only participating generators
### Utilizing the COI assumption for areas speed – frequency.
#If this assumption is used the part “Average Areas Speed – Frequency” above should be commented. Only
#the actively operating SGUs should be included in the calculation. If loss of SGUs is considered as event, the
#corresponding SGU should be excluded from the calculations.
# Information about the SGUs Rating and Inertia Constant: Hydro generating units have a power
# rating of 220MVA and an inertia constant of 6.900002s and are installed in buses A1a, A1b, A2a, A2b, A3.
#Coal based thermal power plants have a rating of 247MVA and an inertia constant of 6.999998s and are
#installed in buses A6, C2, C7, C14. Finally, nuclear based SGUs have a power # rating of 259MVA and an
#inertia constant of 10.5s and are installed at buses B2b and B3.
wA=((5*220*6.900002*wGA01a+5*220*6.900002*wGA01b+5*220*6.900002*wGA02a+2*220*6.900002*
wGA03+2*247*6.999998*wGA06)/(5*220*6.900002+5*220*6.900002+5*220*6.900002+2*220*6.900002+2*
247*6.999998))
wB=((6*259*10.5*wGB03+6*259*10.5*wGB02b)/(6*259*10.5+6*259*10.5))
wC=((5*247*6.999998*wGC02+6*247*6.999998*wGC07+4*247*6.999998*wGC14)/(5*247*6.999998+6*
247*6.999998+4*247*6.999998))
#Having found the angular speed - frequency in each area, then the volume v can be calculated
v=wA*wB*wC
# The goal of this OF2 is to minimize the volumetric changes of the volume v.
d_volume=np.gradient(v,time) #calculation of the rate of change of the volume v at every instant of the
#simulation. This rate of change of the volume v (d_volume) is a new function that needs to be minimized
#throughout the complete simulation time.
objective1=np.trapz(d_volume,time) #minimization of the rate of change of the volume v
# The next step according to section 4.3 is to assure that the minimization of the objective function is subjected
#to  $dwA/dt = dwB/dt = dwC/dt$ . The latter one is facilitated in the following script lines
dwA=np.gradient(wA,time) # calculation of the speed derivative in area A

```


F Frequency Responses

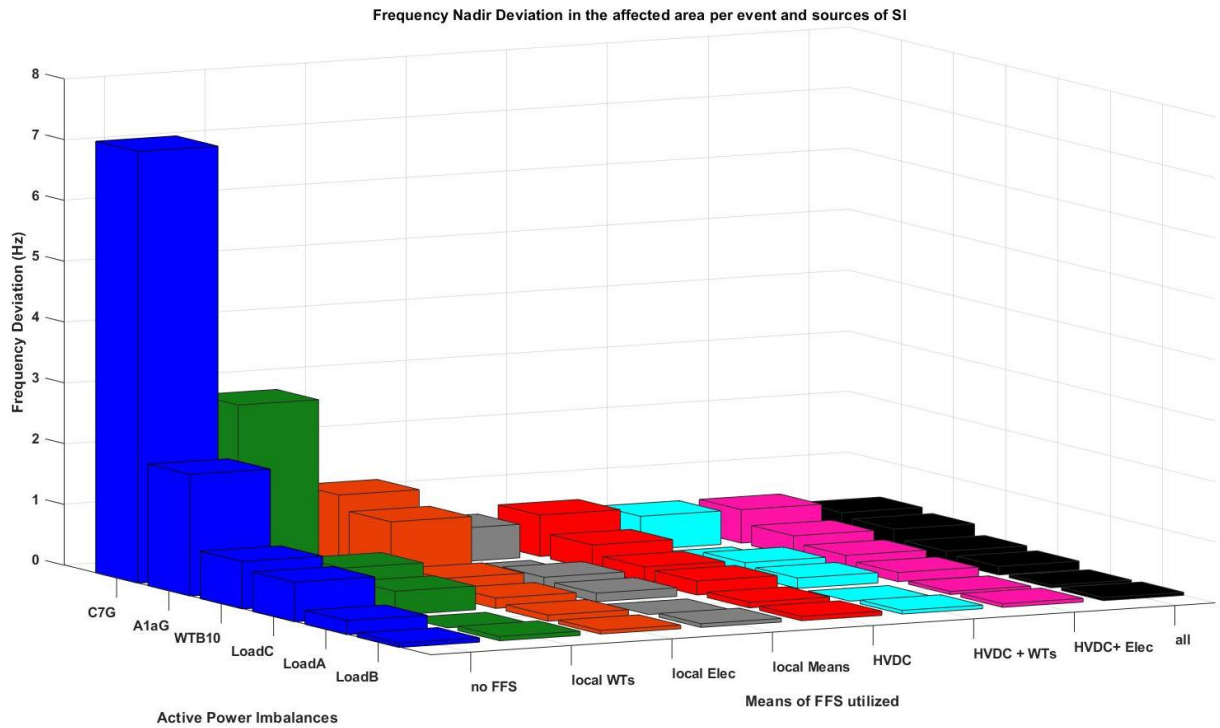


Figure F.1: Frequency nadir deviation per event and group of SI sources tuned under problem formulation 1.

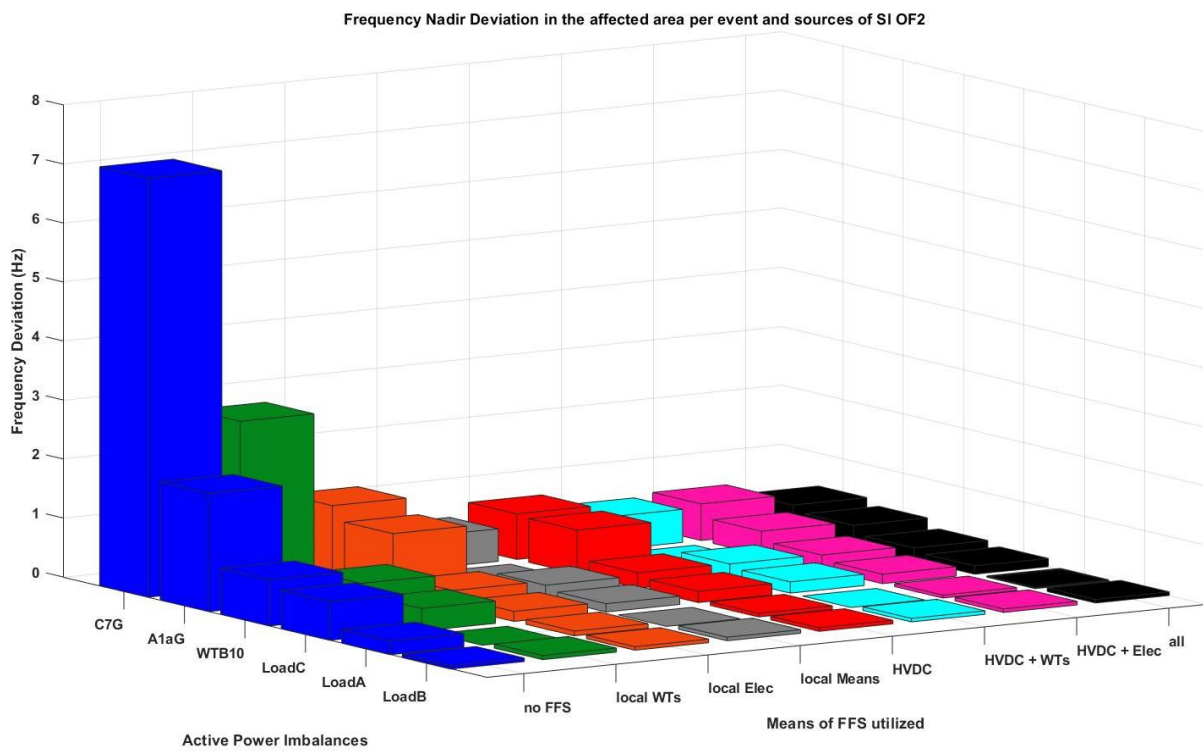


Figure F.2: Frequency nadir deviation per event and group of SI sources tuned under problem formulation 2.

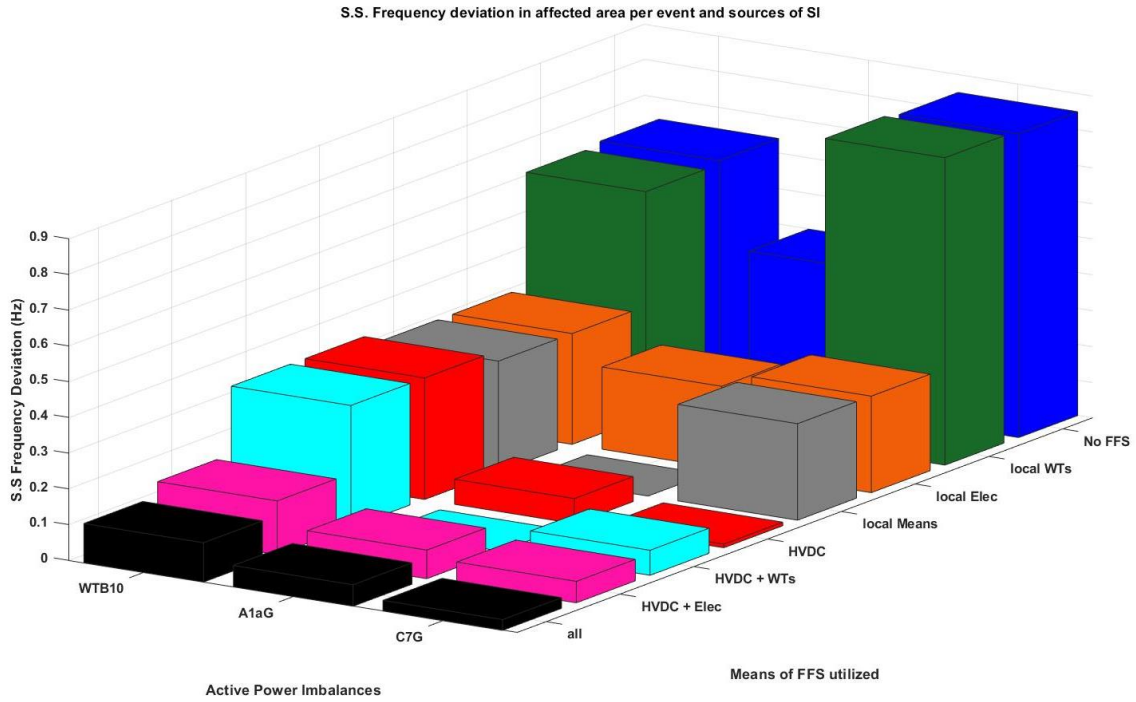


Figure F.3: Steady state frequency deviation of the affected area per event and group of SI sources tuned under problem formulation 1 – Loss of generating units' events .

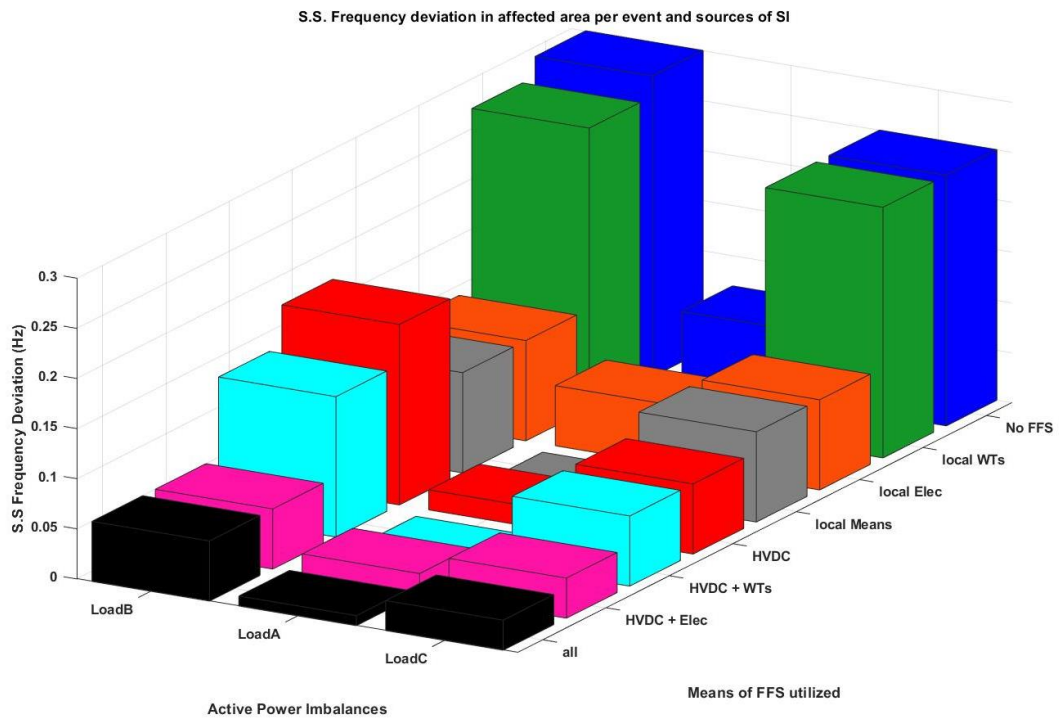


Figure F.4: Steady state frequency deviation of the affected area per event and group of SI sources tuned under problem formulation 1 – Load under-frequency events.

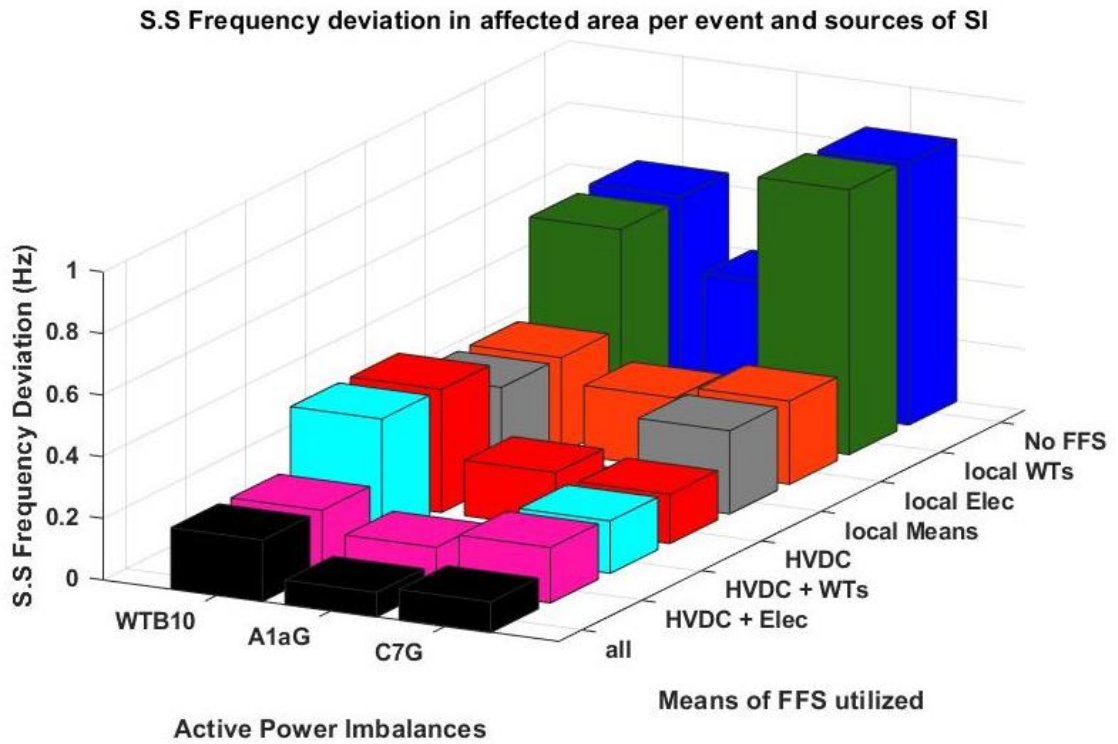


Figure F.5: Steady state frequency deviation of the affected area per event and group of SI sources tuned under problem formulation 2 – Loss of generating units' events .

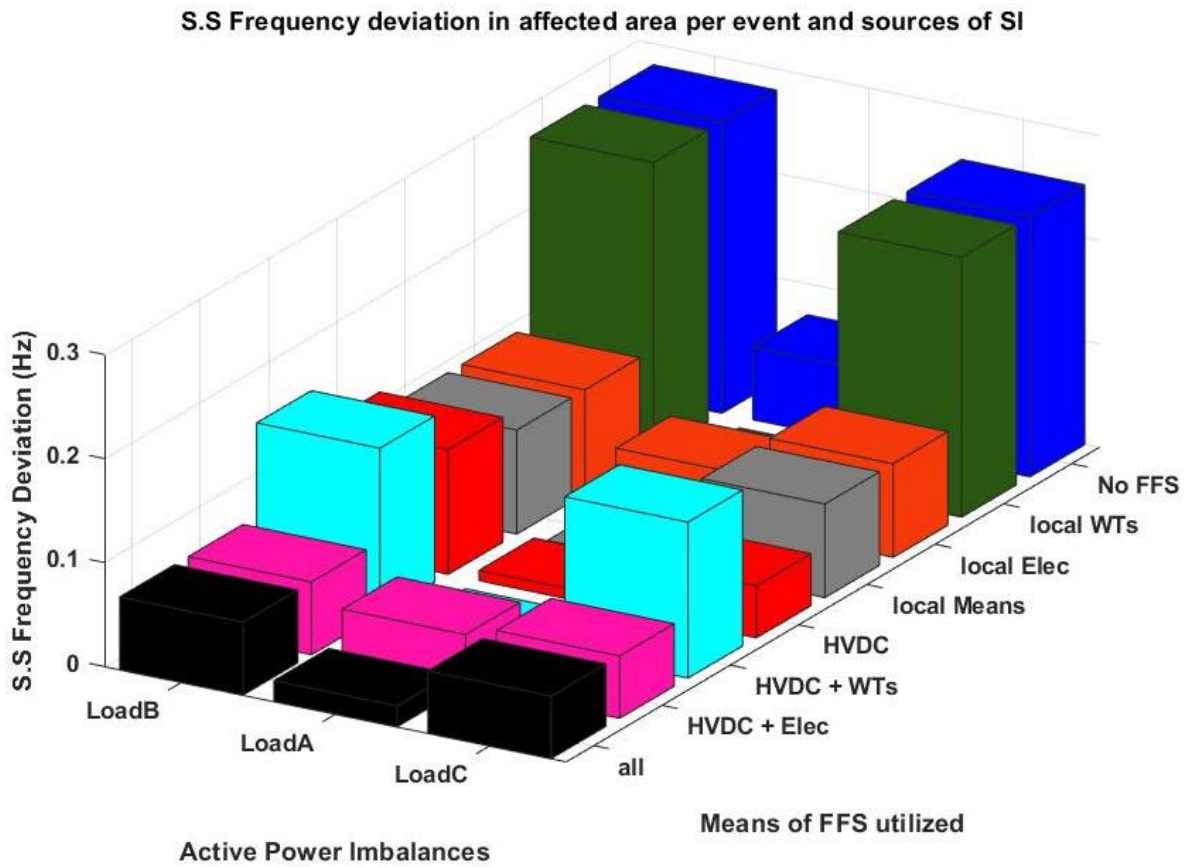


Figure F.6: Steady state frequency deviation of the affected area per event and group of SI sources tuned under problem formulation 2 – Load under-frequency events.

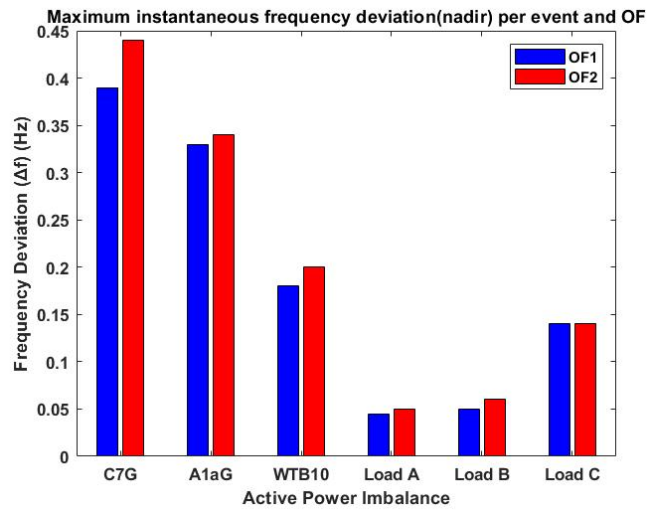


Figure F.7: Maximum initial deviation (nadir) per event and OF under the best achieved frequency response of the affected area.

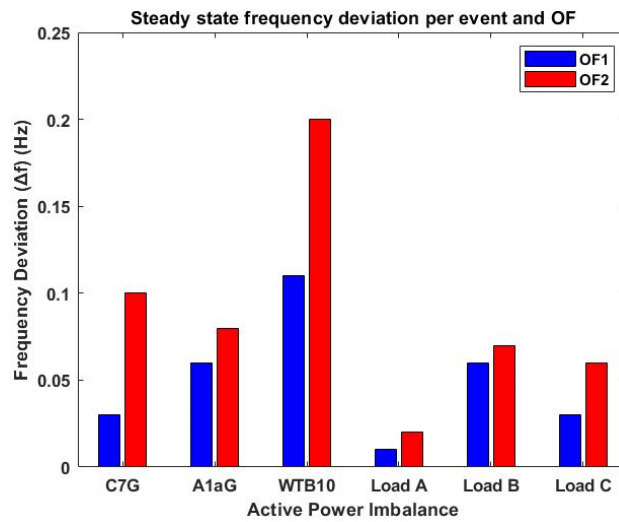


Figure F.8: Steady state frequency deviation per event and OF under the best achieved frequency response of the affected area.

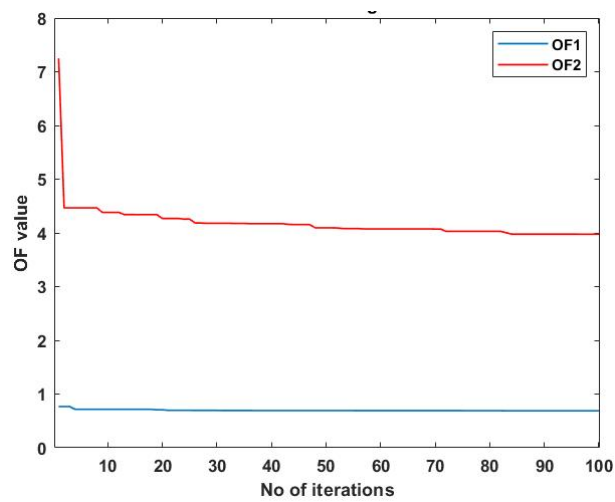


Figure F.9: MVMO algorithm- Objective Functions convergence plot per problem formulation- Loss C7G.

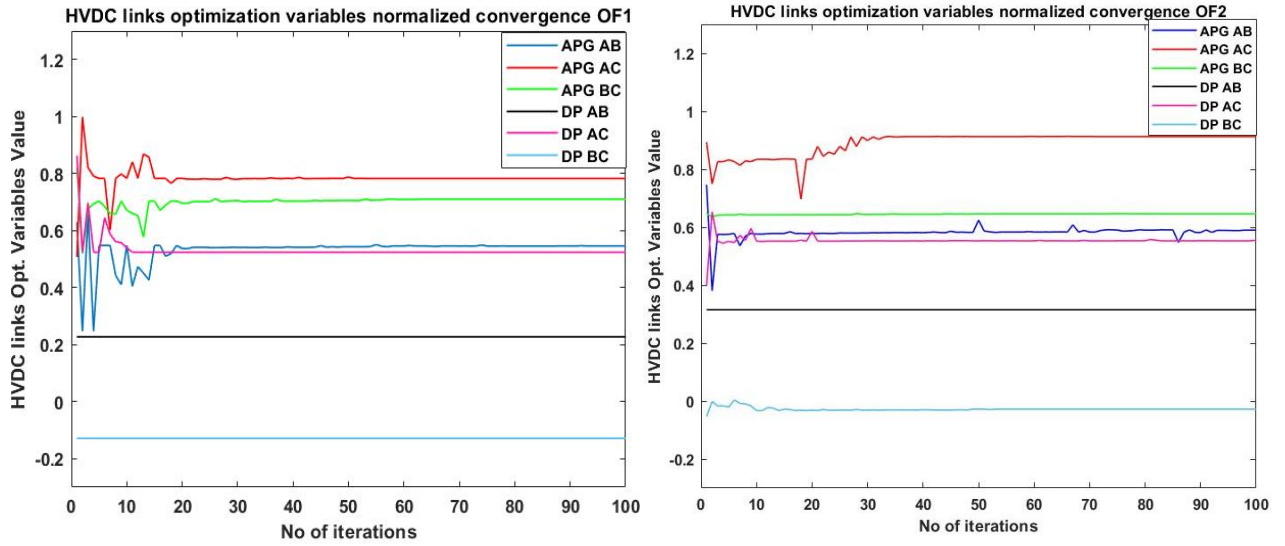


Figure F.12: HVDC links optimization variables convergence per OF - Loss C7G.

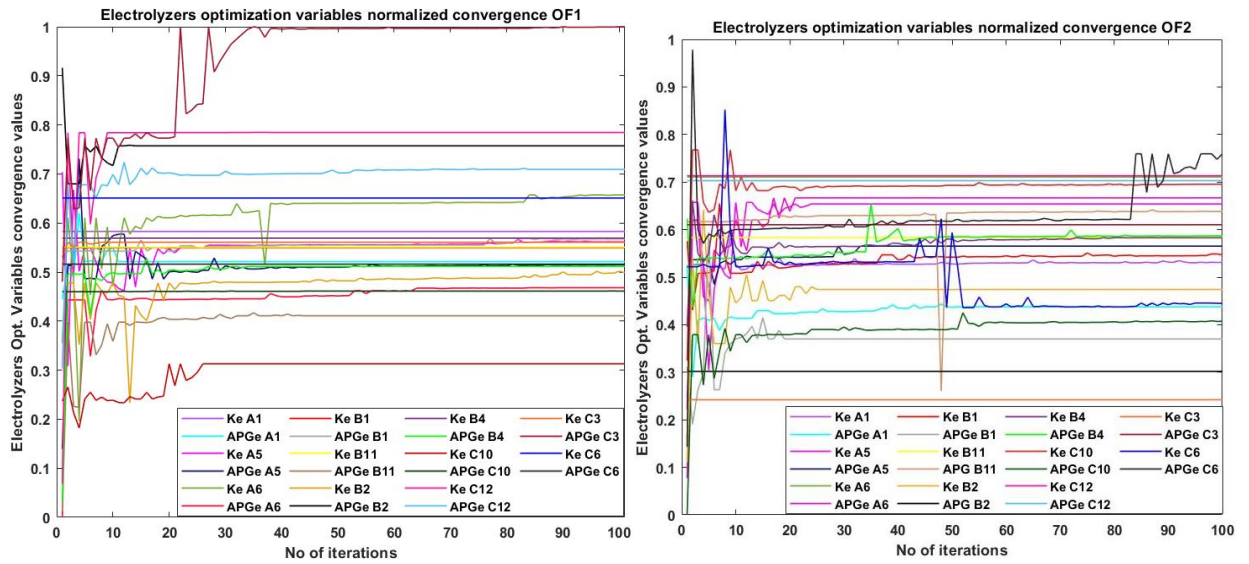


Figure F.11: Electrolyzers optimization variables convergence per OF - Loss C7G.

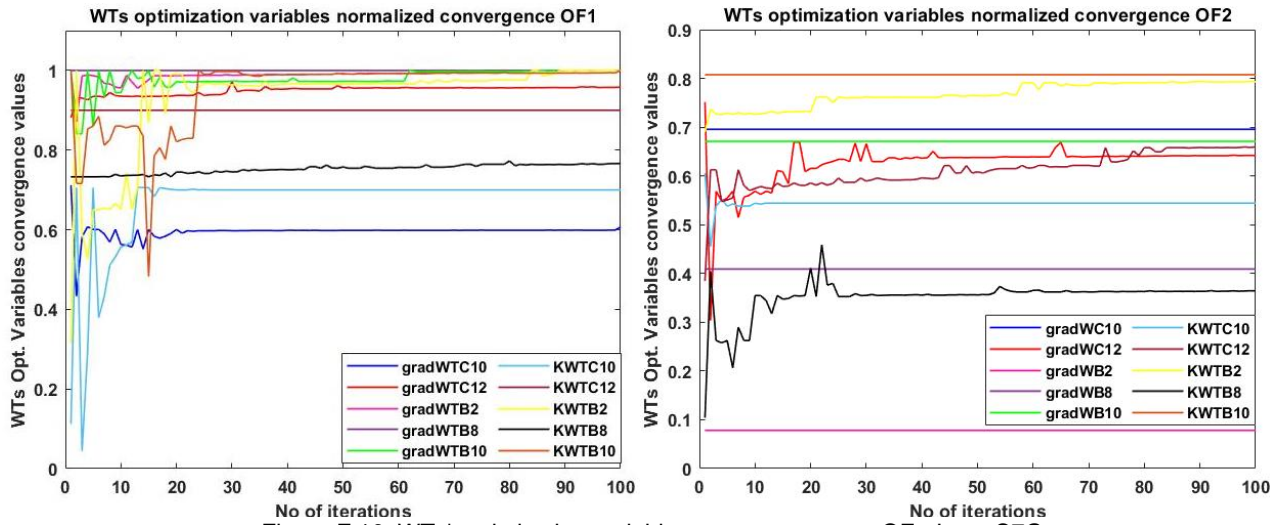


Figure F.10: WTs' optimization variables convergence per OF - Loss C7G.